Lithosphere Removal in the Central Andes: Reconciling Seismic Images and Elevation History

by

Olivia A. Henderson

A thesis submitted in partial fulfillment of the requirements for the degree of

Master of Science

in

Geophysics

Department of Physics
University of Alberta

ABSTRACT

The central Andes (18° - 26°S) is an active Cordilleran orogen, formed through the subduction of the Nazca oceanic plate beneath the South American continent. Despite significant tectonic crustal shortening and thickening (60 -70 km), deep seismic imaging indicates a thin to absent mantle lithosphere beneath the central Andean plateau (Altiplano-Puna plateau). In order to explain this as well as regional geological observations (e.g. widespread mafic volcanism, and along-strike timing variations in uplift across the plateau), lithosphere removal has been proposed to have occurred within the central Andean system within the last 20 Ma.

Conditions within Cordilleran systems, such as the central Andes, can produce density inversions (i.e. roots) within the plateau mantle lithosphere, including: changing pressure-temperature conditions induced by subduction, crustal tectonic shortening, and cyclical magmatic processes. The presence of gravitationally unstable mantle lithosphere drives its removal. Motivated by these observations, the present study uses thermal-mechanically coupled geodynamic models in order to study gravitational removal of single and multiple dense roots within an active subduction zone setting, representative of the central Andes. Both lithosphere removal via large-scale coherent delamination and localized Rayleigh-Taylor (RT)-type instabilities are investigated. Emphasis is placed on i) the dynamics and timing of removal events, ii) the topographic response to lithosphere removal, and iii) the predicted seismic velocity structures generated as lithosphere removal proceeds.

In general, subduction-induced flow aids the removal process, perturbing the lithosphere and entraining the foundering material to remove it from the system. For the modelled lithospheric structure, delamination causes mantle lithosphere to coherently peel away from the overlying crust towards the subducting oceanic slab. The numerical modelling experiments show this delamination occurs within 5 – 12 m.y., resulting in 0.5 – 0.7 km isostatic uplift, with removal proceeding faster for

decreased root density and increased mantle lithosphere strength (i.e. dehydrated conditions). In comparison, RT-type instabilities of greater density and decreased strength are more readily destabilized. Mantle lithosphere is locally removed within 2 – 12 m.y., and the root's down-going trajectory is largely dependent on its relative position to the trench and the rate at which is descends. Note that lithosphere removal of a single RT instability results in local uplift of 0.5 km, whereas destabilization of multiple roots positioned across the extent of the plateau causes regional uplift of 1 – 1.2 km.

This study shows that present-day lithosphere structure across the Altiplano-Puna plateau can be reproduced through episodes of gravitationally driven lithosphere removal. Overall, for both removal mechanisms (i.e. delamination and Rayleigh-Taylor-type instabilities), predicted seismic velocity structures are able to reconcile previously identified upper mantle velocity anomalies to a certain degree, supporting the idea that low velocity zones beneath the central Andean plateau represent high temperature areas of thinned mantle lithosphere. However, regardless of the manner of removal, the resulting surface uplift is limited to ~1 km, suggesting the modern Altiplano-Puna plateau topography is likely not solely linked to removal-induced isostatic and dynamic elevation changes.

ACKNOWLEDGEMENTS

This research was supported by a CGS-M grant from Natural Sciences and Engineering Research Council of Canada (NSERC).The finite-element code (SOPALE) employed in this study was developed by Philippe Fullsack, with additional modifications by Douglas Guptill (Dalhousie University, Halifax, Canada). The numerical models in this study were run using Compute Canada (WestGrid) computational resources. And finally, I would like to thank Dr. Claire Currie for helpful comments and advice throughout the course of this project.

TABLE OF CONTENTS

LIST OF TABLES

LIST OF FIGURES

CHAPTER 1 : INTRODUCTION

1.1 Statement of problem

The Andean Cordillera of South America is a typical example of an active convergent plate margin where oceanic lithosphere descends beneath continental lithosphere, a process called subduction. Specifically, the central Andes (18°-26°S) is the highest and widest region of the Andean Cordillera, with some of the thickest crust on Earth, and, as a result, is an ideal place to study the nature of tectonically thickened crust in an orogenic system. Numerous studies have shown that the thick crust (60-70 km) and high elevation (~4 km) of the central Andean plateau are linked to the large amount of tectonic shortening in the central Andes (e.g. Isacks, 1988; Lamb *et al*., 1997; Allmendinger *el al.*, 1997). Typically orogenesis results in shortening of the crust and produces dense mantle lithospheric roots that protrude into the asthenosphere. However, for many orogens, including the Andes, geophysical and geological observations indicate that mantle lithosphere is spatially heterogeneous, being anomalously thin or absent (Myers *et al.*, 1998; Beck and Zandt, 2002; Schurr *et al.*, 2006; Beck *et al*., 2015; Ryan *et al*., 2016). It is postulated that lower portions of the thickened lithospheric mantle, and possibly lower crust, can be removed by convective flow triggered by lateral temperature gradients, by compositional contrasts that result in density inversions, or by thermal instabilities resulting from the initial crustal shortening of orogenesis. Geophysical studies only provide a snapshot of present-day subsurface structure. Furthermore, numerical modelling studies to date have mostly only investigated idealized generic systems, ignoring the regional dynamics of a subduction zone that characterizes a system such as the central Andes (e.g. Göğüş and Pyslywec, 2008; Valera *et al*., 2011; Krystopowicz and Currie, 2013). This thesis utilizes the insights provided by seismic imaging in order to investigate and reconcile, through numerical modelling, the conceptual models of lithosphere removal that have been proposed to explain geological and geophysical observations. The results of this body of work provide insights to determine the dynamics behind a static picture and to constrain the timing of the proposed lithosphere removal within the central Andes.

1.2 Subduction zones and orogenesis

Subduction zones are important factories within the system of plate tectonics on Earth, and key in maintaining its equilibrium. Inherently, subduction zones are non-steady state systems as many factors interact to determine their dynamics and overall evolution. The process of subduction involves one lithospheric plate descending beneath another due to a density contrast. In an oceanic setting, oceanic lithosphere sinks beneath the continental plate, delivering sediment and water to the mantle (Stern, 2002) (Figure 1.1). This results in the modification of the mantle composition and the generation of melting and magmatism (Billen, 2008). The oceanic plate is dense due to its cool temperature relative to the mantle and subsequent metamorphic phase changes in the crust, creating negative buoyancy as it descends, known as the slab-pull force. The sinking of lithosphere at these destructive margins provides most of the force needed to drive the plate motion and spreading at mid-ocean ridges (Forsyth and Uyeda, 1975; Turcotte and Schubert, 2002). However, from a kinematic perspective, there is a balance between driving and resisting forces controlling subduction, which vary spatially and temporally. The magnitude of slab-pull force depends on the density and, as a result, the age of the sinking lithosphere; notably, this slab-pull force can be counteracted by resistance produced by the viscous mantle against the down-going slab (Becker and Faccenna, 2009). Additionally, the strength of both the overlying plate and the descending lithospheric plates opposes bending at the trench (a feature that is a direct manifestation of underthrusting oceanic lithosphere), and in combination with frictional plate-coupling at shallow depths, subduction is resisted (Stern, 2002; Billen, 2008). The relative importance of each force depends on the details of the subduction history. The net force balance as a result varies with depth, subduction rate, duration of subduction, age of the involved lithosphere, and mechanical properties (Arcay, 2012). As the lithosphere descends during subduction it experiences increasing temperature and pressure gradients. This is responsible for several petrologic processes including melting, dehydration, and metamorphic phase changes which result in an increase in density of the sinking slab as well as changes in the compositional and rheological structure of the subduction system as a whole (King, 2001; van Keken, 2003; Karato, 2010; Burov 2011). All of these factors and feedbacks affect the local balance of forces and the thermal evolution, which have a direct feedback on the viscosity and strength of both the descending slab and the overriding lithosphere.

From a dynamical point of view, the motions of the lithospheric plates are part of the mantle convection system (Becker and Faccenna, 2009). When subduction occurs, it causes the cold dense lithospheric slab to be circulated within the mantle. This essentially allows the circulation of the cooler

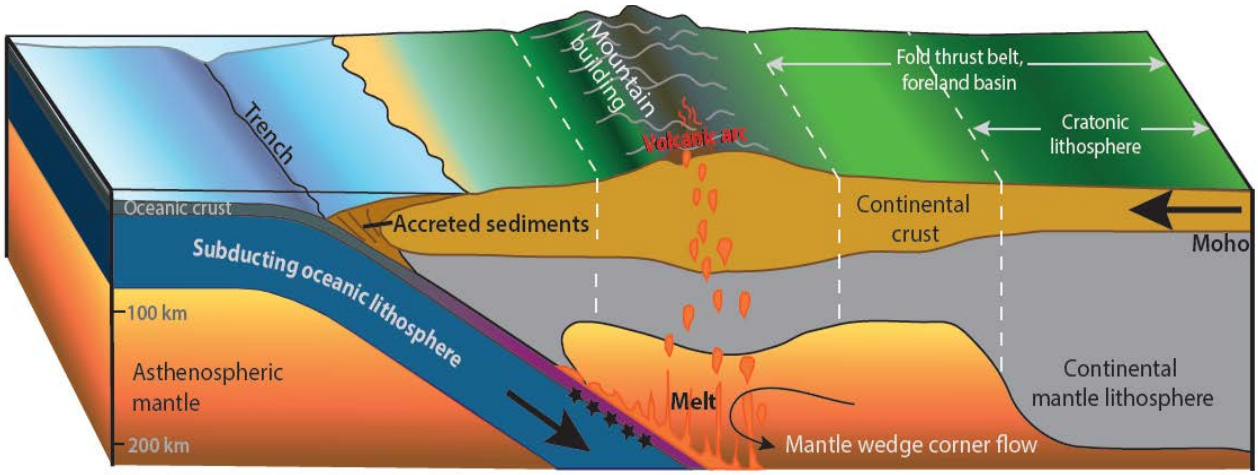

Figure 1.1 Conceptual model of an idealized subduction zone, where oceanic lithosphere descends beneath the continental lithosphere. Dehydration of the oceanic crust introduces volatiles to the system, lowering the solidus temperature of sublithospheric mantle material resulting in arc magmatism. A resulting linear trend of volcanos builds parallel to the trench of the subduction zone. Mountain building initiates when the converging plates are sufficiently coupled to allow compressional stresses to be transmitted into the interior of the upper plate. This orogenic load, which is enhanced by the downward pull of the mantle wedge flow (dynamic topography), results in flexure of the continental lithosphere and creates a retroarc foreland basin. The Wadati-Benioff zone of seismicity is planar along the oceanic slab, as indicated by star symbols ★.

near-surface material to occur, leading to the modification of the thermal field (King, 2001; Stern, 2002; Abers *et al*., 2006). Within the slab itself, advection transports isotherms to greater depths, however thermal diffusion limits their extent as the slab heats up (Riedel and Karato, 1997; Turcotte and Schubert, 2002). The simplest model for flow in the mantle in regards to its interaction with the descending slab involves two-dimensional corner flow, with viscous coupling between the slab and the overlying mantle resulting in slab-parallel flow just above the slab and horizontal convergence-parallel flow just beneath the overriding plate (Billen and Gurnis, 2001; Stern, 2002; van Keken, 2003; Manea and Gurnis, 2007) (Figure 1.1). Effectively, corner flow is induced by the down-dip motion of the slab, generating a zone of viscous deformation between the descending slab and the overriding plate that defines the mantle wedge. A low viscosity zone develops within the mantle wedge due to high temperatures, high strain rates, and high volatile content introduced by the dehydration reactions from the subducting oceanic crust and sediments (Schmidt and Poli, 1998), leading to thermal buoyancy. The low pressures induced by the flow tend to lift the slab up beneath the overriding plate thereby offsetting

the tendency of gravity to align the slab with the vertical (Billen and Gurnis, 2001; van Keken, 2003). Furthermore, the viscosity of the wedge links the negative buoyancy force of the sinking slab to the surface (van Keken, 2003). Therefore, subduction dynamics depend on the buoyancy of the subducting plate, the viscosity structure of the mantle, and coupling between the subducting and overriding plate.

Oceanic lithosphere will sink once it is turned down onto the sublithospheric mantle (i.e. the asthenosphere); however, it is unclear how subduction is actually initiated. There are a few possibilities: compression may exploit the weakness in the contact zone at passive margins with oceanic against continental lithosphere, at a transform fault or at an inactive segment in a mid-ocean ridge system (Van der Pluijm and Marshak, 2002). The sinking slab will exert a slab-pull force on the rest of the plate which will drive the subduction process. Typically, the oceanic plate continues to subduct beneath continental lithosphere as long as the rocks remain denser than the adjacent mantle at a given depth (Turcotte and Schubert, 2002; Billen, 2008). Spatial and temporal variations in slab strength and the history of subduction, including absolute plate motions, determine whether the slab sinks directly into the lower mantle or whether it becomes trapped in the transition zone of the mantle (410-660 km depth) (Riedel and Karato, 1997; Billen, 2010). The strength of the slab relative to the surrounding mantle depends on the dominant deformation mechanism which in turn depends on the thermal structure and strain rate of the overall system. Down-going lithosphere can retain its separate thermal and mechanical identity to a considerable depth until sufficient heat has been transferred to it from the mantle to increase its temperature to that of its surroundings. Thus the descending slab can maintain negative buoyancy, and can exist lower in the mantle. The subduction zone in the central Andes is an example where the slab stagnates at the transition zone, eventually entering the lower mantle (e.g., Kárason and van der Hilst, 2000; Scire *et al.*, 2015).

Orogenesis occurs at convergent plate margins and involves intra-plate shortening, crustal thickening, and topographic uplift (Stern, 2002). Non-collisional orogenesis results from ocean-continent convergence where plate motions and the other factors controlling subduction lead to compression within the overriding plate. Mountain building initiates where the upper continental plate experiences compression and the converging plates are sufficiently coupled to allow compressional stresses to be transmitted into the interior of the upper plate, causing shortening (Turcotte and Schubert, 2002). Studies of subduction zones in general suggest that the stress regime in the overriding plate is influenced by the rate and age of subducting oceanic lithosphere (Uyeda and Kanamori, 1979; Jarrard, 1986). Among the most important of the other factors are the strength of the inter-plate coupling at the

trench, and the internal structure and rheology of the continental plate. In particular, where continental lithosphere is relatively hot and weak, strain tends to delocalize and shortening is distributed across zones that can be over a thousand kilometers wide; this can be observed in the central Andes of South America.

Another distinctive feature of subduction and the accompanying orogenesis is the development of a volcanic arc, a trend of volcanos that builds parallel to the trench of the subduction zone (Figure 1.1). Volcanism arises from partial melting of the asthenosphere, triggered by the dehydration and resulting release of volatiles from the slab at 50 to 150 km depth (Hildreth and Moorbath, 1988; Stolper and Newman, 1994; Schmidt and Poli, 1998). Down-going lithospheric mantle can remain hydrated to a depth of tens of kilometers as a result of the normal faulting associated with the bending of the plate as it approaches the subduction zone, as well as the presence of hydrous minerals within the oceanic crust (Billen, 2008). A generalized model of arc magmatism involves heat being transferred to the descending slab, resulting in temperature gradients such that the asthenosphere in the vicinity of the slab becomes cooler and more viscous than the surrounding areas, particularly, near the upper part of the slab. This more viscous asthenosphere is then dragged down with the slab causing less viscous mantle to flow in behind it (i.e. mantle wedge corner flow). It is the interaction of this down-welling mantle with aqueous fluids rising from the sinking slab that is thought to produce partial melting of the mantle. It is this addition of water that lowers the solidus temperature of the mantle wedge, generating partial melt that rises to the surface, erupting to form volcanoes (e.g. Stern, 2002; Van der Pluijm and Marshak, 2002). Moreover, some melts may result from the reduction of pressure, known as decompression partial melting, that occurs if material rises quickly enough so that little heat is lost (Sisson and Bronto, 1998). The process of arc volcanism is how continental crust is generated at present-day (Turcotte and Schubert, 2002).

Seismicity within the descending oceanic slab is the diagnostic expression of subduction zones, being a direct manifestation of how deformation is accommodated at the convergent plate margin. Subduction zones are characterized by earthquakes that are shallow near the intersection of the plate boundary with the surface, but increase with depth in the direction of convergence (Stern, 2002). This seismicity-depth relationship defines the dipping slab of lithosphere, and this planar zone of earthquakes is known as the Wadati-Benioff zone (Figure 1.1). The descending plate experiences either down-dip compression or extension (Figure 1.2b). Isacks and Molnar (1969) have suggested that the distribution of stress type in the seismic zone may result from the degree of resistance experienced by

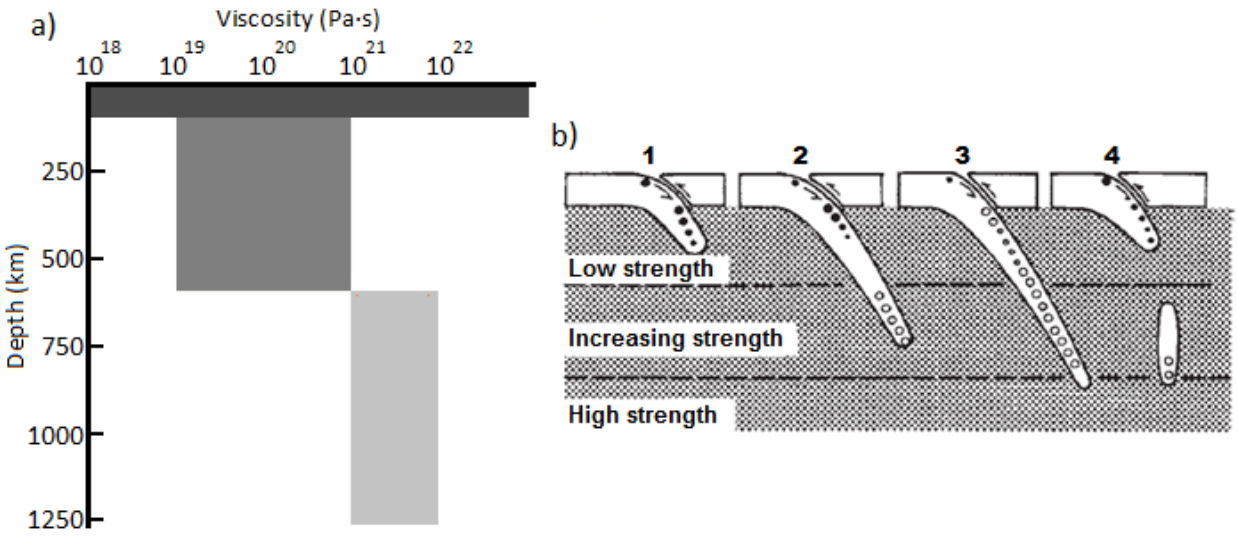

Figure 1.2 **a)** Viscosity structure as a function of depth for Earth's mantle (based on Karato, 2010). **b)** Model of stress distributions in the descending lithosphere within a subduction zone. Solid circles and open circles are extensional and compressional stress, respectively, down-dip (modified from Isacks and Molnar, 1969). Refer to text for explanation.

the plate during its descent and Spence (1987) has described this resistance in terms of the net effect of ridge-push and slab-pull forces. As the oceanic plate begins to sinks through the upper mantle it experiences down-dip tension as its descent is unimpeded. However, once the bottom of the plate approaches the lower mantle, which exhibits an order of magnitude increase in viscosity (Figure 1.2a), its descent is resisted and, as a result, the leading tip is thrown into compression. Molnar *et al.* (1979) deduced the length of the Benioff zone depends on the depth to which the subducting oceanic lithosphere maintains a relatively cold central core; therefore, the downward deflection of isotherms, and hence, the length of the seismic zone, is proportional to both the rate of subduction and the product of convergence rate and age (Turcotte and Schubert, 2002).

Superimposed on this large-scale stress field are local stresses associated with plate flexure and metamorphic phase changes within the oceanic plate. As the descending slab heats up, unstable hydrous minerals begin to undergo dehydration, causing the oceanic plate to demonstrate brittle behaviour at high temperatures as pore pressures increase and pre-existing faults reactivate (e.g. Kirby *et al.*, 1990; Kirby, 1995; Kirby *et al.*, 1996). Faulting by this process, referred to as dehydration embrittlement, can occur at 400 km depth as long as temperatures remain below 700°C , conditions that

can exists due to the presence of metastable olivine within the cold central core of the subducting slab (Rubie and Ross, 1994; Riedel and Karato, 1997; Billen, 2008).

The angle at which the oceanic plate descends beneath the continental plate can exhibit different values, and subsequently can affect the dynamics of subduction, associated petrological processes, as well as crustal shortening exhibited in the overriding continental plate (e.g. Dickinson and Synder, 1978; Bird, 1988; Kay and Mpodozis, 2001; 2002). In normal subduction zones the angle of subduction is on the order of 30°; however, in the case of flat or near horizontal subduction, the descending slab shallows to ~5° at ~ 100 km depth and extends for several hundred kilometers inland before descending more steeply into the underlying mantle. It is proposed that these flat slab geometries are attributed to several factors including the age of the subducting oceanic slab (a young slab likely would exhibit greater buoyancy), metastable basalt, the absolute motion of the plates and the relative motion of the trench, the viscosity of the mantle wedge (low viscosity regions acting to enhance slab flattening by reducing viscous resistance), and the presence of buoyant thick aseismic ridges on the descending oceanic plate (e.g. Jarrard, 1986; Gutscher *et al.*, 2000; van Hunen et al., 2002; 2004; Manea and Gurnis, 2007; Manea *et al.*, 2012). As a subducting oceanic plate transitions to a shallow subduction angle, sublithospheric mantle is displaced in the direction of subduction. This can result in the cooling of the overriding plate (Dumitru et al., 1991), as well as the cessation of frontal volcanic arc activity and the subsequent migration of magmatism into the back-arc (e.g. Trumbull *et al.*, 2006; Kay and Coira, 2009). Moreover indications of flat slab subduction can be discerned from the geochemical analysis of regional igneous rocks, as chemical components from the evolving slab, the mantle wedge, and the overlying crust affect overall magma composition (Kay and Mpodozis, 2001; 2002).

1.3 Tectonic and geologic setting of the Andes

1.3.1 Plate tectonic history of the Andean orogeny

The Andean Cordillera is a mountain chain that extends along the western continental margin of South America; in its entirety, it is one of the largest mountain belts in the present-day world. Morphologically continuous, the chain exceeds 7500 m in length, covering a distance much greater than its width, with notable variations in both topography and crustal structure across its extent (Dewey and Lamb, 1997; McQuarrie *et al.*, 2005). The Andean Cordillera is the result of compressional strain associated with the subduction of the oceanic Nazca plate beneath the continental South American plate. In particular, the central Andes (18°-26°S) is the highest and widest region of the Andean

Cordillera, and is thought to be the result of Cenozoic tectonic shortening and thickening of the continental lithosphere (Isacks, 1988; Ramos, 1988; Horton *et al.*, 2001; DeCelles and Horton, 2003; McQuarrie *et al.*, 2005).

The structure setting of the Andean margin is the result of a complex tectonic evolution. Beginning in the Paleozoic, the Andean margin was subjected to several episodic deformational stages when accretionary tectonics dominated (i.e. progressive addition of crustal terranes to the paleo-Andean margin of the South American plate) (Ramos, 2009). Moreover, the Paleozoic recorded the Pampean, Famatinian and Gondwanan orogenies, all of which are the sequential precursors to the modern Andean orogeny (Ramos, 1988). During the Late Jurassic and Early Cretaceous, the margin of South America was characterized by either a non-compressive or an extensional regime (Mpodozis and Ramos, 1989). At this time, most of the margin lay below sea level as a series of extensional barkarc and marginal basins formed above a subduction zone (Mpodozis and Allmendinger, 1993; Mora *et al.*, 2006). It is believed that the distribution and rheology of the pre-Cretaceous crustal domains and orogenies have affected later Andean deformation (Isacks 1988; Ramos, 1988; Piñán-Llamas and Simpson, 2006).

The Andean tectonic cycle began during the Mesozoic, at ~200 Ma, in association with the breakup of Pangea and the opening of the Southern Atlantic Ocean, as constrained by the regional geochemical record (Franz *et al*., 2006; Oncken *et al.,* 2006; Ramos, 2009). The subduction zone observed today was initiated during a period of convergence during the Early Jurassic, with the Farallon oceanic plate descending beneath the margin of the South American continental plate (Ramos, 1988). Since that time, the subduction zone has evolved in the same general orientation, as neither terrane accretion nor significant tectonic rearrangements have influenced this area since the Paleozoic (Ramos, 1988; Franz *et al.*, 2006; Piñán-Llamas and Simpson, 2006). However, at ~25 Ma, the Farallon plate split into the present-day Cocos and Nazca plates (Cande and Leslie, 1986), resulting in a change from oblique to nearly orthogonal convergence between the Nazca plate and South America. This led to changes in subduction geometry which accelerated crustal thickening, shortening and uplifting (McQuarrie *et al.*, 2005). Finally, the modern Andean tectonic setting was established in the mid-late Cenozoic, causing the central Andes to have risen significantly in last 50-30 million years. There is still debate as to whether the pulse of tectonism responsible for the modern Andean orogeny initiated in the late Oligocene-early Miocene (25-30 Ma) (Isacks, 1988; Sempere, 1995; Allmendinger, 1997; Lamb and Hoke 1997), or as early as the late Cretaceous – early Paleocene time (~ 65 Ma) (Horton *et al.*, 2001; DeCelles and Horton, 2003; McQuarrie *et al.*, 2005). Regardless, at present, subduction of the Nazca plate, approximately 45

Ma in age at the trench (Müller *et al.*, 2008), continues at a convergence rate of ~ 7 cm yr^{-1} in the central Andean region (Oncken *et al.*, 2006).

As defined by seismicity, the subduction of the Nazca plate under the central Andes (18°-26°S) currently occurs at an angle of ~30° to a depth of ~300 km in the upper mantle (Hayes *et al.*, 2012; Scire *et al.*, 2015), falling within the range of 'normal' subduction (refer to section 1.2). However, the geometry of the subducting Nazca plate varies along strike when considering the Andean orogen as a whole, with flat slab subduction observed in the northern Andes (Peruvian flat slab, 5°-14°S) and in the southern Andes (Chilean-Pampean flat slab, 30°-33°S) (Ramos and Folguera, 2009; Hayes et al., 2012). The origin of the shallower segments has been attributed to the subduction of the Nazca Ridge (a bathymetric high on the Nazca plate thought to have been formed by volcanism from the Easter-Salas hotspot (Ray *et al.*, 2012)) and the Juan Fernandez Ridge (a chain of volcanic seamounts and islands), respectively (e.g. Yañéz *et al.*, 2001; Trumbell *et al.*, 2006; Kay and Coira, 2009). Despite the present-day central Andes exhibiting a steep subduction angle of ~30 °, temporal and spatial variations in volcanism and surface deformation across the region has led previous studies to infer former episodes of flat slab subduction: occurring beneath the Altiplano between ~40 – 18 Ma, and beneath the Puna between 18 – 12 Ma (e.g. Hoke and Lamb, 2007; Kay and Coira, 2009; Ramos and Folguera, 2009; Lamb, 2016) (discussed more in Chapter 4). Furthermore, these studies suggest that petrological processes related to the changes in the geometry of the subducting Nazca slab (i.e. hydration and crustal thickening) can result in a local region of gravitationally unstable mantle lithosphere and can serve to trigger a subsequent lithosphere removal event (discussed further in section 1.4.1).

1.3.2 Central Andes

The Andean Cordillera is subdivided based on geologic evolution, crustal thickness, and active tectonism (Ramos, 2009). The central Andes (18°-26°S) have the highest average elevations, the greatest width, and thickest crust of the Andean Cordillera (Allmendinger *et al.*, 1997; Lamb and Hoke, 1997; Beck and Zandt, 2002; McQuarrie *et al.*, 2005). Characteristically, the geology of the central Andes is subdivided into several north-south morphotectonic zones (Figure 1.3). From west to east, this includes the Precordillera (the remnant of a Mesozoic arc), the Western Cordillera (the modern volcanic arc), the Altiplano plateau (a relatively flat internally draining basin of high elevation, connected to the southern Puna plateau), the Eastern Cordillera (a bivergent fold thrust belt that rises abruptly from the Altiplano-

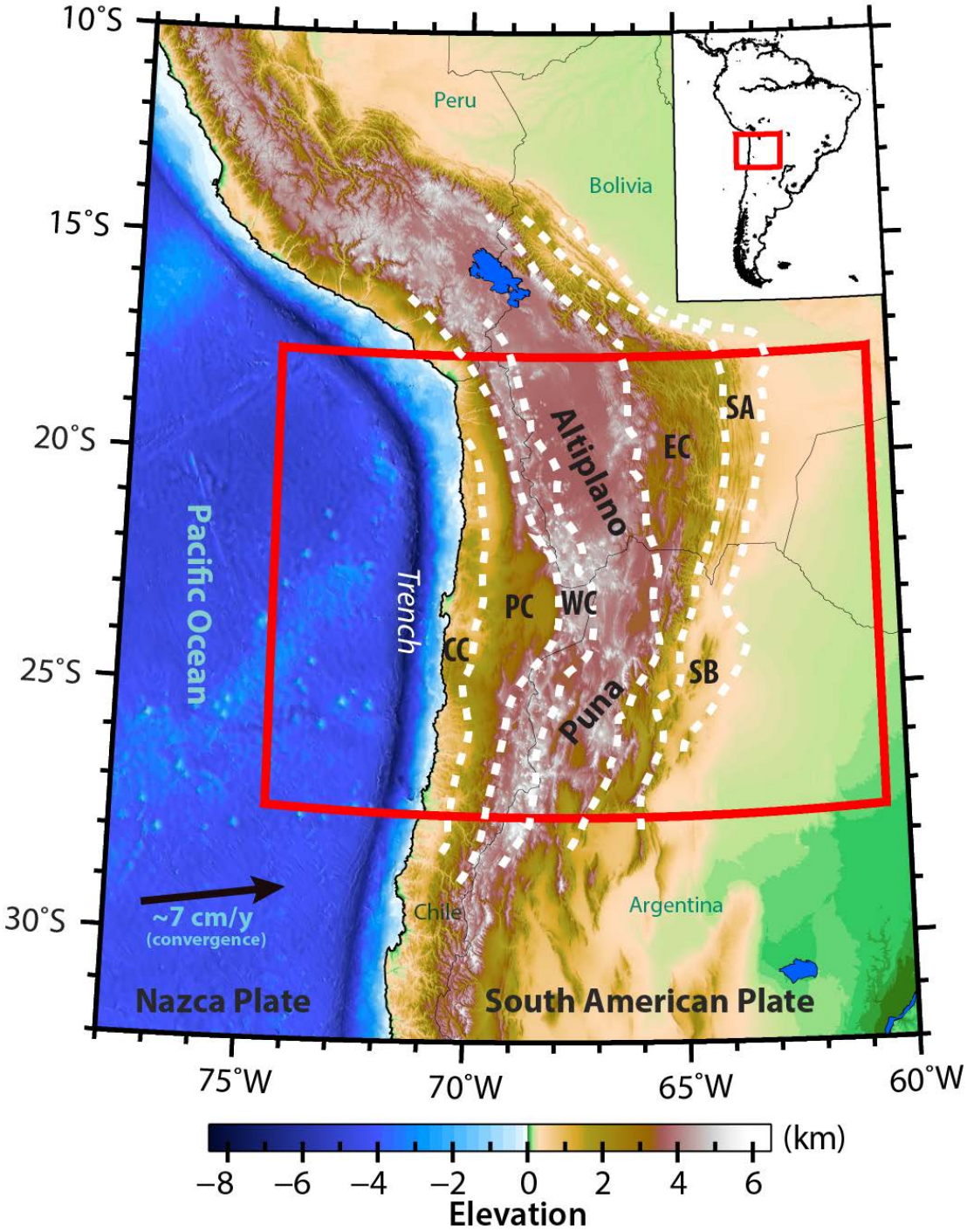

Figure 1.3 Elevation map of the central Andes, South America, with boundaries between morphotectonic zones shown with dashed lines: **CC** –Coastal Cordillera, **PC** – Pre-Cordillera, **WC** – Western Cordillera, **Altiplano** and **Puna** plateau (4 km average elevation), **EC** – Eastern Cordillera, **SA** – Subandean Zone, **SB** – Santa Barbara System. The area of investigation for this study is outlined in red.

Puna to elevations as high as 6.4 km), the Subandean zone (the active fold and thrust belt), and the Chaco Plain (a low elevation foreland basin created through flexural accommodation associated with the fold and thrust belt tectonic loading) (e.g. Kley, 1996; McQuarrie *et al.*, 2005).

The central Andean plateau, an area of high elevation greater than 3 km high, and a maximum width of 400 km (Figure 1.3), is the highest plateau in the world associated with abundant arc magmatism and is second only to Tibet in height and extent. Unlike the Tibetan plateau, which is a product of the collisional Himalayan orogeny, the central Andean plateau was uplifted in the absence of continental collision or terrane accretion, and is a direct product of crustal thickening and shortening associated with ocean-continent plate convergence. It encompasses three of the eastern morphotectonic zones: the Western Cordillera, Altiplano-Puna plateau, and the Eastern Cordillera (Isacks, 1988; Lamb and Hoke, 1997; McQuarrie *et al.*, 2005). At its surface the both the Altiplano- and the Puna- plateau are characterized by several localized sedimentary basins (diameter of ~100 km) (McQuarrie *et al.*, 2005; Horton, 2012), and contain broad, internally drained areas of low relief and records little surface erosion. However, the Puna is broken in several contractional basins and ranges unlike the broad flat Altiplano basin that is covered by several large salars (Allmendinger *et al.*, 1997). Furthermore, the Puna is on average 0.5 – 1 km higher elevation than the Altiplano (e.g. Isacks, 1988; Allemendinger *et al.*, 1997), and exhibits more widespread volcanism, though the Altiplano too exhibits Miocene to Pliocene ignimbrite centres towards its southern end (Allmendinger *et al.*, 1997; Kay and Coira, 2009).

The evolution of surface topography in an orogen provides information about the dynamics of the deep lithosphere. The high elevations and large amount of tectonic shortening recorded in the central Andes correspond to large regions of extreme crustal thicknesses (60 -70 km) (Isacks, 1988; Beck *et al.*, 1996; Beck and Zandt, 2002; McQuarrie, 2005; Ryan *et al.*, 2016). In order to conserve mass, shortening of the upper crust should be accompanied by thickening of the deeper mantle lithosphere. However, geophysical and geological observations of the central Andes indicate that present-day mantle lithosphere below the thickened crust is spatially heterogeneous, being anomalously thin or absent (e.g. Beck and Zandt, 2002; Schurr *et al.*, 2006; Beck *et al.*, 2015). Similar observations have been made concerning the presence of a mafic lower crust. In particular, Beck and Zandt (2002) proposed that original mafic lower crust of the Altiplano was removed due to crustal shortening and subsequent eclogitization, else if still present has seismic properties of mantle and is not readily discernible. The implication of that interpretation is an overall weak felsic crust supporting the high elevations of the

Altiplano. Moving southward, the higher elevations exhibited by the Puna could also reflect differences in crustal structure, possibly due to removal as well, including the underlying mantle lithosphere (e.g. Whitman *et al.*, 1996; Schurr *et al.*, 2006; Beck *et al.*, 2015).

1.4 Lithosphere removal in the central Andes

1.4.1 Physical drivers of gravitational lithosphere removal

Lithosphere removal can arise due to a contrast in material properties between the lithosphere and sublithospheric mantle, primarily driven by the negative buoyancy of the mantle lithosphere (Bird, 1978; 1979). It involves the rapid descent of relatively cool and dense mantle lithosphere into the less dense sublithospheric mantle. Causes for this density inversion can be attributed to differences in temperature, compositional contrasts, or a phase change (mafic granulite facies to eclogite facies) (e.g. Kay and Kay, 1993). As a direct result of the geothermal gradient, where temperature is a function of depth, mantle lithosphere is cooler and therefore denser than the underlying material; this thermal contraction can be further destabilized by localized lithospheric thickening associated with plate convergence (e.g. Houseman and Molnar, 2003). Compositional contrasts can occur due to melt differentiation that takes place during the ascension of mantle-derived mafic magma (e.g. Hildreth and Moorbath, 1988; Austrheim, 1991; Ducea and Barton, 2007; Lee *et al.*, 2010), which can arise as hydrous melt or supercritical fluids are released from a subducting oceanic slab (Peacock, 1993). Due to multi-stage fractional crystallization (i.e. melt differentiation) (e.g. Lee *et al.*, 2006), mafic peroxenite magma may exist within the mantle lithosphere below the Moho, as the buoyant components of the magma separate and rise through the crust. As a result, the residual magma can evolve to an eclogitic composition, creating a zone of high density, and possibly lower strength than the surrounding mantle lithosphere. (Figure 1.4) (Austrheim *et al.*, 1997; Saleeby *et al.*, 2003; Elkins-Tanton, 2007; Ducea *et al.*, 2015). Jull and Kelemen (2001) find that lower crustal and mantle compositions that result from magmatism are likely to exceed the mantle density by 50 to 250 kg m-3 at the same temperature. It has been proposed in a conceptual model that mantle lithospheric removal caused by this type of magmatic root generation, especially within Cordilleran orogenic systems such as the Andean margin, occurs cyclically; it involves stages of root –generation, –removal, and –system-recharge where magmatically-triggered roots form and founder on timescales of 25-50 million years (DeCelles *et al.*, 2009; 2015). Note that water released during slab dehydration can also be re-adsorbed by adjacent anhydrous rocks in

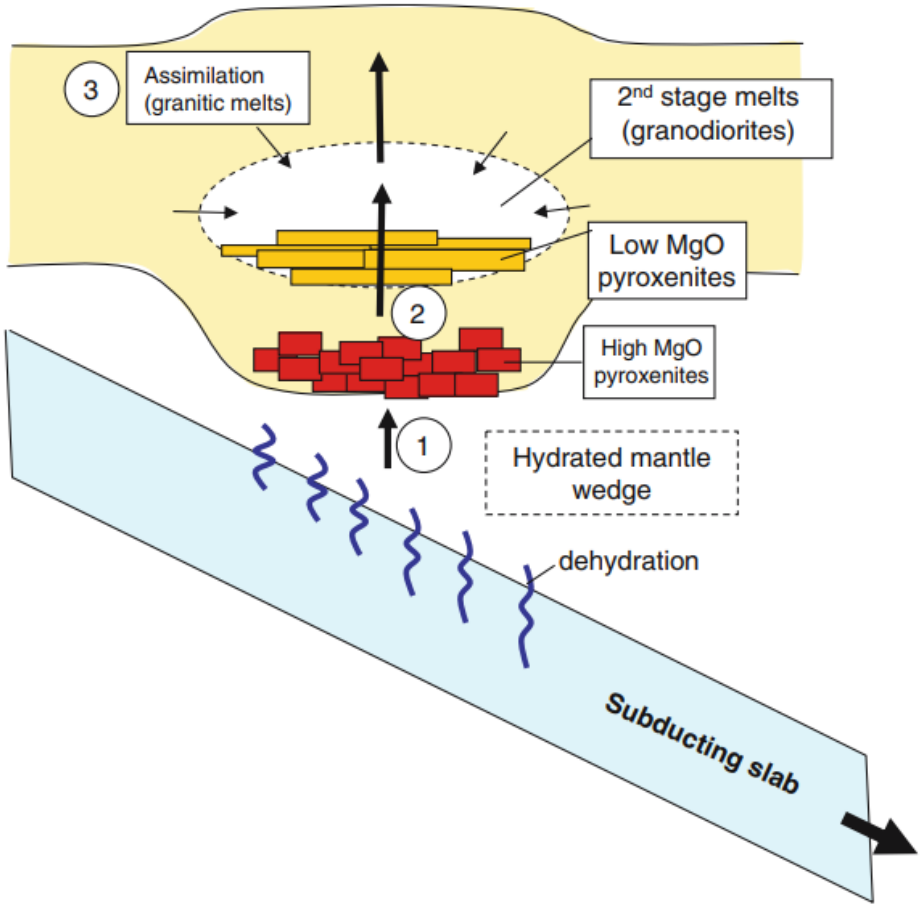

Figure 1.4 Schematic diagram showing the multi-stage melt differentiation resulting from dehydration of unstable hydrous minerals derived from the subducting oceanic slab. The end result is the formation of a dense residuum near the base of the crust **1.** Hydrous basalts are formed within the wet mantle wedge, and rise to intrude the base of the overriding lithosphere. The decreased temperatures and pressure allow for the crystallization of mafic material (High MgO pyroxenites). **2.** Increased buoyancy allows for the derivative melt to rise and pond beneath the lower crust, denser portions becoming negatively buoyant. This fractional crystallization (creating low Mgo pyroxenites) in combination with subsequent melting and (**3.**) assimilation of the surrounding crustal rocks can generate more felsic melts that continue to rise. This melt generation can cause compositional and rheological contrasts that serve to trigger gravitational instabilities within the lithosphere. From Lee *et al.* (2006).

secondary hydration reactions (Austrheim *et al.*, 1997). This can drive rapid eclogitization and sudden density changes not directly related to melt ascension (Leech, 2001). Lithosphere removal can be further induced through tectonic thickening of the crust. This results in lithospheric material being pushed to higher pressure-temperature conditions, and this may trigger a phase change with the mafic lower crust. Of most importance is the eclogite phase change which is marked by the appearance of garnet and a rapid density increase of the crust; this can create crustal densities that are higher than mantle density (e.g. Kay and Kay, 1993; Leech, 2001). This phase change can therefore drive decoupling of the lower crust and mantle lithosphere from the overlying crust (e.g. Krystopowicz and Currie, 2013).

For removal driven only by the thermally-induced density contrast, removal is generally limited to the lowermost lithosphere, owing to the strong temperature-dependence of typical mantle rheologies (e.g. Conrad and Molnar, 1999; Göğüş and Pyslywec, 2008). Previous studies numerically examining lithosphere removal for Newtonian rheology shows that for dry olivine rheology, only the lower 50-60% of the mantle lithosphere may be removed, while for wet olivine, removal may involve more than 80% of the mantle lithospheric thickness (Houseman and Molnar, 1997; Molnar *et al.*, 1998). The amount of mantle lithosphere removed is modulated by increasing density contrasts and melt content; in some cases a compositional density contrast of only 1% is sufficient to drive a gravitational instability, making the viscosity of the dense material the dominant limiting factor controlling the formation of the instability (e.g. Elkins-Tanton, 2005; 2007). Nonetheless, the growth of a gravitational instability develops exponentially once triggered, which ultimately results in the removal of a large fraction of the mantle lithosphere (e.g. Houseman & Molnar 1997; Conrad 2000; Houseman and Molnar, 2003; Elkins-Tanton, 2007). The presence of high density material in the deep crust and shallow mantle lithosphere due to both metamorphic and magmatic eclogite can, therefore, drive the removal of the full thickness of mantle lithosphere (e.g. Krystopowicz and Currie, 2013).

Regardless of its cause, gravitational removal alters the density structure of the lithosphere, and is generally accompanied by an isostatic readjustment and a vertical deflection of the Earth's surface once the density anomaly is detached. During removal itself, a downward normal stress is exerted on the overlying material, and this is typically expressed as subsidence of the surface, except in cases where the crust is weak and can be thickened by the stresses associated with removal (Neil and Houseman, 1999; Wang and Currie, 2017). Geological and geophysical observations that support the presence of lithosphere removal include regional uplift due to an isostatic readjustment (which can be inferred from unconformities or offsets in the surficial sedimentation patterns), increases in heat flow as hot mantle

upwells and replaces the foundered lithospheric material, a reduction of mantle seismic velocities as cool lithosphere is replaced by hotter mantle, and mafic volcanism (revealed by geochemical analysis of preserved lava flow). However, lithosphere removal events are of short duration, and the resulting thermal and mechanical structures are fleeting, and, therefore, difficult to record and preserve in the geologic record (Göğüş and Pyslywec, 2008).

There are several proposed removal mechanisms, including *ablation* (subduction related removal), *Rayleigh-Taylor-type instabilities* (gravitational instabilities resulting in piecewise 'drip' removal) (Houseman *et al.*, 1981; Houseman and Molnar 1997), and *delamination* (coherent removal of mantle) (Bird, 1979; Morency and Doin, 2004). Continuous removal through the process of ablation involves the entrainment of continental mantle lithosphere that is in close proximity to the descending oceanic slab (Figure 1.5a). This occurs at a rate that balances the orogenic shortening of the crust (Pope and Willet, 1998), and therefore results in steady removal of continental lithosphere. Rayleigh-Taylor-type instabilities stem from the perturbation of the interface between the mantle lithosphere and the underlying mantle, causing its deviation from a level surface (Houseman *et al.*, 1981; Houseman and Molnar, 1997). This results in a differential pressure profile along the interface, and a release of potential energy modulated by the dynamics of surface tension, viscosity and compressibility, culminating with the gravitational 'drip' removal of mantle lithosphere (Houseman and Molnar, 1997) (Figure 1.5b,c). The interface irregularity can be induced by any lateral variation in thermal structure that perturbs the lithosphere-asthenosphere boundary (LAB), such as tectonic shortening or arc magmatic processes (Houseman *et al.*, 1981; Kay and Kay, 1993; Conrad and Molnar, 1997; Houseman and Molnar, 1997; Elkins-Tanton, 2007). Gravitational forces and resisting viscous forces determine the rate at which density instabilities in the lithosphere grow (Conrad and Molnar, 1997). This 'drip'-style of removal produces observable near-circular deflection of the surface directly above the high density root as it detaches (Neil and Houseman, 1999; Pysklywec and Beaumont, 2004; Göğüş and Pysklywec, 2008; Wang *et al.*, 2015).

In contrast, delamination is used to describe largescale removal of mantle lithosphere as a coherent slab that detaches along a weaker plane along its top edge. Numerical models of delamination show that this style of removal produces a wave of surface uplift and subsidence that migrates with the detachment point of the removal (Sobolev *et al.*, 2006; Göğüş and Pysklywec, 2008; Krystopowicz and Currie, 2013). Krystopowicz and Currie (2013) show that delamination can be sub-classified into two specific styles of removal based on the relative strength of the mantle lithosphere: i) retreating

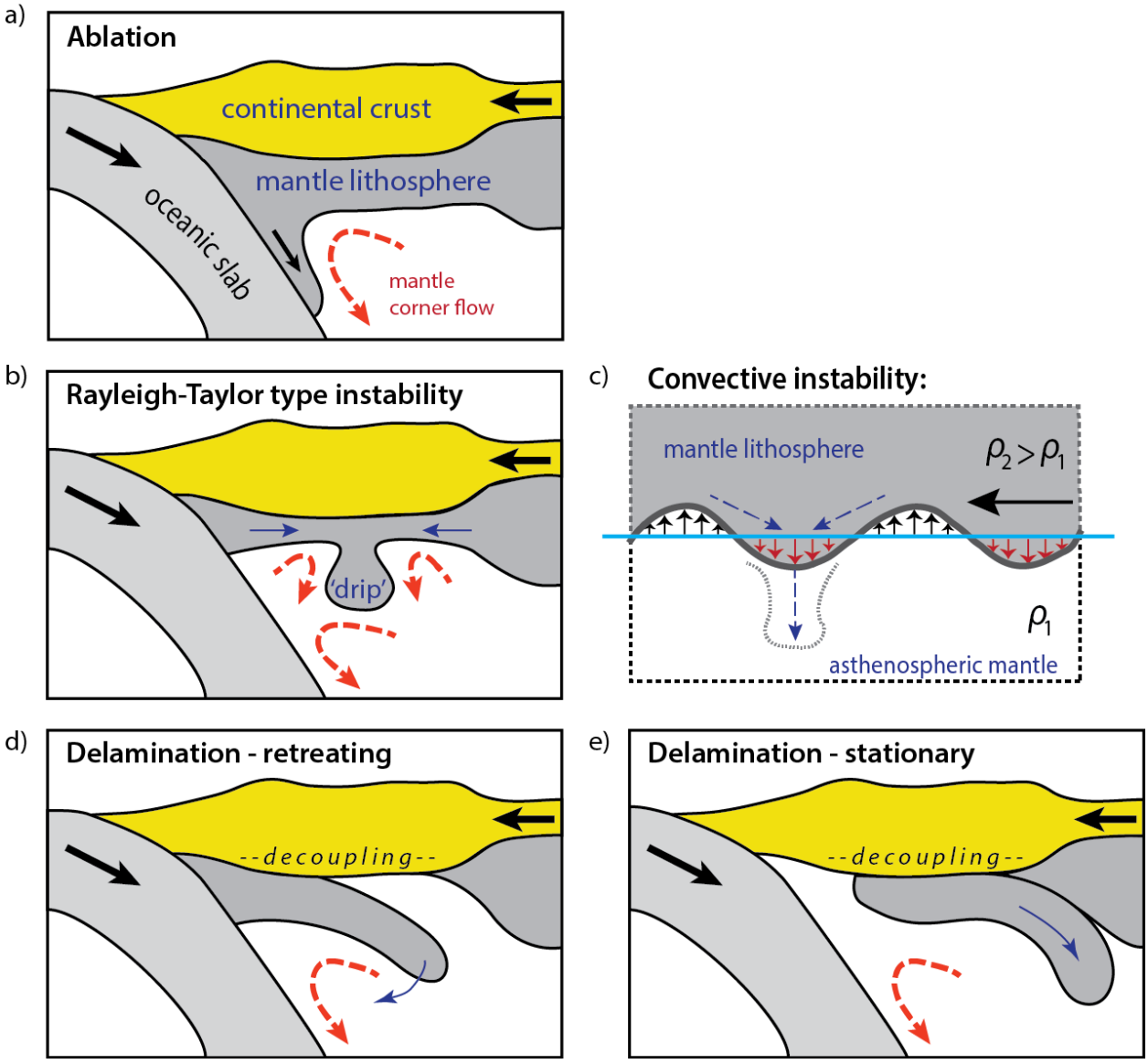

Figure 1.5 Proposed styles of lithosphere removal: **a)** Continuous removal by way of ablation, where viscous drag from the subducting plate entrains the mantle lithosphere of the overriding plate. **b)** Removal through convective instabilities, known as Rayleigh-Taylor (RT) -type, which results in 'drip'-like removal. A schematic of the mechanism that generates RT-type removal events along the lithosphere-asthenosphere boundary is depicted in **c)**, whereby a density (ρ) contrast is present between the two layers of mantle material, with its interface perturbed from a level surface resulting in a differential pressure profile (indicated by the arrows). RT type instabilities result from local increases in potential energy along said profile. **d)** and **e)** depict coherent and largescale removal of mantle lithosphere, either peeling back away from the crust or sinking vertically between the site of initiation, respectively.

(Figure 1.5d) and ii) stationary (Figure 1.5e). Both styles lead to complete removal of orogenic mantle lithosphere, where a *retreating* mode has weak mantle lithosphere peeling away from the crust at a migrating detachment point, and a *stationary* mode results in removal of strong mantle lithosphere proceeding rapidly, sinking vertically beneath the site of delamination initiation. Previous studies have demonstrated that delamination requires a weak zone in the crust, which may relate to a rheological weakness associated with hydration (Schott and Schmeling, 1988; Göğüş and Pysklywec, 2008), or to high Moho temperatures (e.g. Meissner and Mooney, 1998), or to lower crustal eclogitization and densification (Krystopowicz and Currie, 2013).

In summary, both Rayleigh-Taylor-type instabilities and delamination rely on the generation of a gravitational instability that can be generated through numerous petrological and/or tectonic processes; however it is possible to differentiate the different styles of removal through patterns of surface deformation, uplift and magmatism (Göğüş and Pyslywec, 2008; Krystopowicz and Currie, 2013). Observations of this type have been made in the central Andes and will be discussed in section 1.4.2.

1.4.2 Observations of removal in the central Andes

Numerous studies have stated that the thick crust (60-70 km) and high elevation of the central Andean plateau are linked to the large amount of tectonic shortening in the central Andes (e.g. Isacks, 1988; Beck *et al.,* 1996; Lamb *et al.*, 1997; Allmendinger *et al.*, 1997). Shortening of the crust should be accompanied by thickening of the deeper mantle lithosphere in order to respect conservation of mass. However, both geophysical and geological observations for the Andes indicate that mantle lithosphere is spatially heterogeneous, being anomalously thin or absent (Myers *et al.*, 1998; Beck and Zandt, 2002; Schurr *et al.*, 2006; Kay and Coira, 2009; Ryan *et al.*, 2016).

Recent deep seismic data collected covering the central Andes provide unprecedented imaging of the present-day lithospheric structure at depth (Figure 1.6a) (e.g. Myers *et al.*, 1998; Beck and Zandt, 2002; Schurr *et al.*, 2006; Heit *et al.*, 2008; Ryan *et al.*, 2016). In particular, anomalous seismic velocities have been observed in tomographic images beneath the plateau in the northern central Andes, reflective of large lateral variations in the upper mantle structure (Dorbath *et al.*, 1991; Dorbath and Granet, 1996; Myers *et al.*, 1998). In the mantle, seismic velocity depends primarily on the temperature, with composition being a second-order effect (e.g. Goes *et al.*, 2000; 2012; Cobden *et al.*, 2008); regions of anomalously high velocities indicate lower temperatures. Below the central part of the Altiplano plateau (~21°S), higher seismic velocities observed within the shallow mantle suggest thicker lithosphere

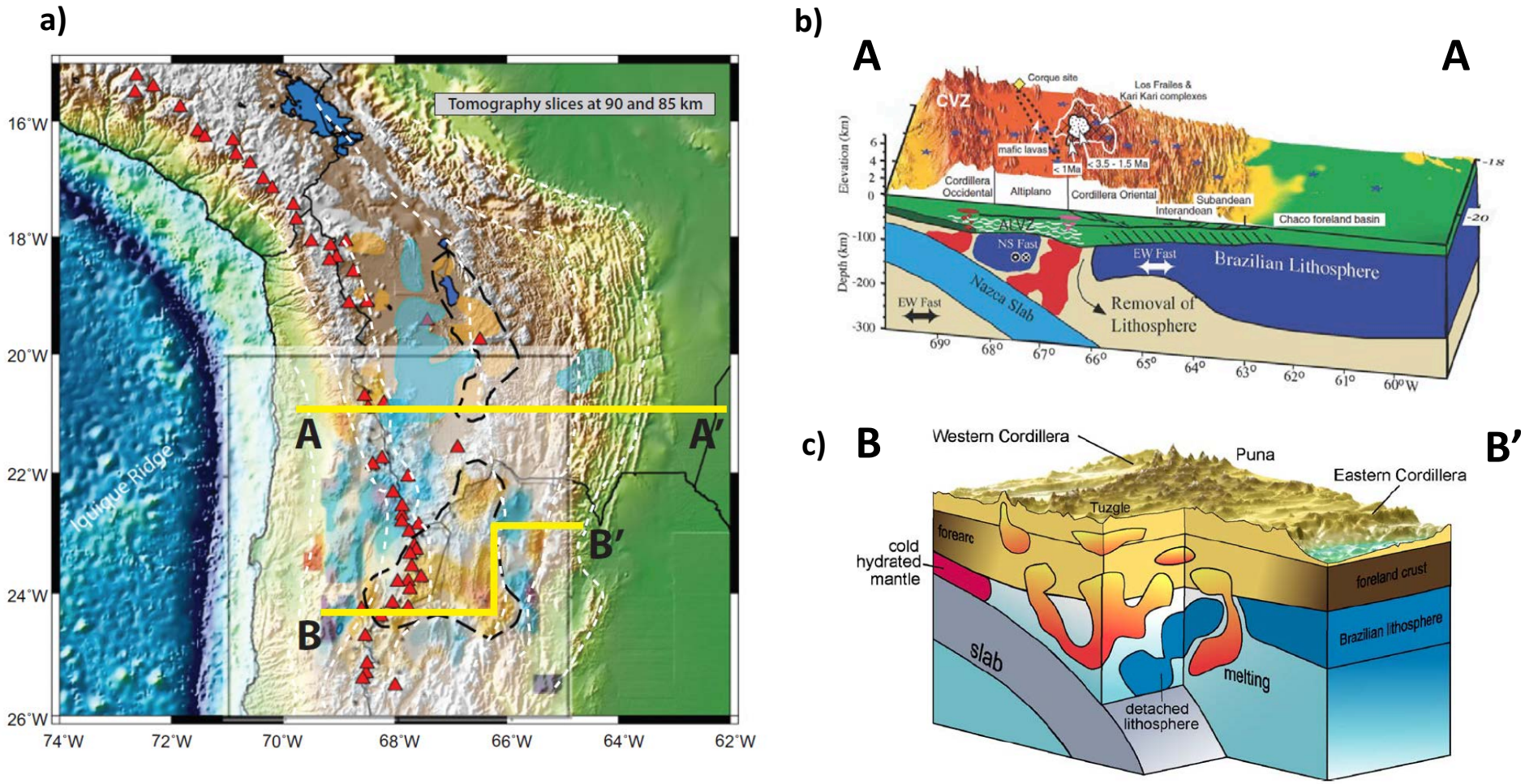

Figure 1.6 **a)** P-wave tomography slices of the central Andes at 85 – 90 km depth, highlighting areas of lithosphere removal. Blue: areas with P-wave velocity >8.1 km s^{-1}; yellow: <7.9 km s^{-1} (modified from Kay and Coira, 2009). Cross-sections **b) A-A'** and **c) B-B'** correspond to conceptual models of removal proposed in the Altiplano- Puna- plateau, respectively, where red and blue regions are based on seismic tomography observations (Myers *et al.*, 1996; Beck and Zandt, 2002; Schurr *et al.*, 2006).

(Figure 1.6b). Here, the lithosphere-asthenosphere boundary (LAB) is imaged at ~130 km (Heit *et al.*, 2008). However, moving eastward, where low velocities zones and high attenuation in the shallow mantle have been recorded beneath the Eastern Cordillera, the corresponding LAB has shallowed, imaged at ~100 km depth (Myers *et al.*, 1998; Heit *et al.*, 2008). The LAB depth increased to the east beneath the Subandean range, imaged at 170 km depth, suggesting that there is a window where the mantle lithosphere has been locally thinned beneath the northern Altiplano and Eastern Cordillera boundary, with the thick lithosphere below the centre of the central Andean plateau largely preserved (Figure 1.6a).

Observations change southward, where it is postulated that the mantle lithosphere has been completely removed beneath the Puna plateau; this may explain why despite having thinner crust (55-60 km), the Puna region sits at a ~ 1 km higher elevation relative to the northern Altiplano (Yuan *et al.*, 2000; Schurr *et al.*, 2006; Bianchi *et al.*, 2012; Beck *et al.,* 2015). Low velocities and high attenuation are observed throughout the crust and shallow mantle of the entire plateau region in this area (Schurr *et al.*, 2006; Bianchi *et al.*, 2012; Beck *et al.*, 2015) (Figure 1.6c). Specifically, Schurr *et al.* (2006) presented tomographic images of high-velocity zones at ~150 km depth under the Puna plateau, 30 -100 km in diameter, in the shallow upper mantle sitting atop of the descending oceanic slab. These are interpreted to be pieces of detached upper plate lithosphere (Schurr *et al.*, 2006; Sine *et al.*, 2008; Saleeby *et al.*, 2012). Balanced cross-sections reveal that shortening is less in the southern Puna (~25°-30°S) than in the northern Altiplano (~18°S–21°S), decreasing from as much as 250 – 330 km to less than 100 km (Allmendinger *et al.*, 1997; Baby *et al.*, 1997; Elger *et al.*, 2005; McQuarrie *et al.*, 2005; Oncken *et al.*, 2006), making the Altiplano theoretically more prone to detachment. Yet, tomographic images suggest that under the Puna, mantle lithosphere is mostly removed and that under the Altiplano the lithospheric mantle lid is mostly preserved, although there are localized area that appear to have experienced piecewise removal (Myers *et al.*, 1998; Schurr *et al.*, 2006; Saleeby *et al.*, 2012; Ryan *et al.*, 2016).

In addition to seismic imaging, examination of surficial geology gives an indication of subsurface lithospheric thinning processes in the central Andes. Geochemical analysis of Andean volcanics reveals a complex magmatic history between 30 – 10 Ma, with volcanism originally concentrated at the volcanic arc in the Western Cordillera and then migrating westward to cover the majority of the central Andean plateau (Trumbull *et al.*, 2006; Kay and Coira, 2009). This magmatic activity cannot be linked to normal tectonic processes and the mafic composition of the igneous rocks suggests they were sourced from deeper mantle magma compared to typical arc magmas, supporting the scenario of mantle lithosphere

removal beneath the plateau and its replacement by an influx of hot mantle material near the base of the crust (Kay and Kay, 1993; Gao *et al.*, 2004; Elkins-Tanton, 2007; Hoke and Lamb, 2007; Kay and Coria, 2009; Ducea *et al.*, 2013). In the last 10 Ma, volcanism has shifted back to the Western Cordillera, while orogenic deformation propagated eastward to the foreland area (Trumbull *et al.*, 2006; McQuarrie *et al.*, 2005).

Geologic evidence for removal can also be observed within the stratigraphic record. At its surface the central Andean plateau is characterized by several localized sedimentary basins (diameter of ~100 km) (McQuarrie *et al.*, 2005; Horton, 2012). Many of these basins have experienced subsidence and crustal contraction, followed by surface uplift and crustal extension (Carrapa *et al.*, 2011; DeCelles *et al.*, 2015). The formation of these basins cannot be directly linked with regional orogenic deformation, and have a sedimentation history that spans 10-20 million years (DeCelles *et al.*, 2015). DeCelles *et al.* (2015) proposes that these basins are caused by formation and removal of dense lower lithosphere. Numerical modelling of lithosphere removal in the presence of thick orogenic crust presented in Wang *et al*. (2015) shows that these basins can occur due to lithosphere removal with the main control on the amount of deflection being the viscous coupling between the high-density-lithospheric-root and surface. Furthermore, to produce surface deflection over a width of ~100 km, the near surface rocks must be relatively weak.

Recent paleoelevation studies examining the Altiplano region performed by Garzione *et al.* (2006) and (2008) suggest that the central Andean plateau underwent a large episodic pulse of uplift in the last 10 Ma, resulting in a greater than 1.5 km increase in elevation. Based on multiple proxies of elevation, including oxygen isotopic composition of carbonates deposited in the northern Altiplano, paleobotany, sedimentation and volcanism, it has been proposed that this rapid surface uplift was in response to the removal of 80 – 140 km thick mantle lithosphere beneath the Eastern Cordillera. This would lead to basal heating of the crust and magmatism between 10 and 6 Ma, which is a period that corresponds to a time of mafic and felsic magmatism in the region.

There are currently three competing hypotheses concerning lithosphere removal in the central Andes:

(1) Uplift across the central Andes is consistent with crustal shortening and periodic loss of upper-plate lithosphere (e.g. McQuarrie *et al.*, 2005; Barke and Lamb, 2006). Material is removed by thermal thinning and viscous drag of the lithospheric mantle by the subducting Nazca plate, i.e.

ablation (Tao and O'Connell, 1992; Pope and Willet, 1998). The removal is then a natural by-product of the compressional tectonic setting and surface erosion, and allows for contraction to shorten and thicken the remaining crust (Isacks, 1988). However, removal by ablation alone likely does not cause localized gaps with the plateau mantle lithosphere, which are observed in current seismic images of the Altiplano and southern Puna (e.g. Heit *et al.*, 2008; Scire *et al.*, 2015).

(2) Piecewise removal of the mantle lithosphere via Rayleigh-Taylor-type gravitational instabilities, likely localized in the region with the largest amount of shortening. Tomographic imaging and receiver functions reveal the central Andean plateau crust has seismic velocities consistent with a felsic to intermediate bulk composition, with a lack of mafic lower crust and mantle lithosphere across much of the plateau (Myers *et al.*, 1998; Beck and Zandt, 2002; Yuan *et al.*, 2002; Beck *et al.*, 2015; Ryan *et al.*, 2016). Note that eclogitized lower crust is difficult to distinguish from mantle lithosphere as they have similar seismic velocities (Beck and Zandt, 2002; Schurr *et al.*, 2006), and the observations suggest that neither are present in many areas. The thick crust observed across the central Andean plateau could reach the critical depth within the eclogite stability field to experience the phase change (~45 km depth). This metamorphic phase change results in densification that can trigger local lithosphere removal (Beck and Zandt, 2002; Krystopowicz and Currie, 2013; Beck *et al.*, 2015; Ryan *et al.*, 2016). An alternate idea to explain localized removal involves magmatic cyclical process associated with Cordilleran settings (DeCelles *et al.*, 2009; 2015), involving: i) generation of eclogitic residues due to magmatism triggered by slab dehydration processes, ii) melt differentiation that leads to localized density inversions within and below the lower crust (e.g. Lee *et al.*, 2006; 2010), iii) mantle lithosphere removal of the gravitationally unstable eclogite-rich residuum, and iv) the cycle being rejuvenated as new mantle lithosphere is introduced by the underthrusting of craton mantle lithosphere. Removal triggered by magmatic reactions notably does not require shortening. In either case, the presence of dense metamorphic or magmatic eclogite in the deep crust and/or shallow mantle lithosphere may induce gravitational instability, and the removal of the lower crust and mantle lithosphere below much of the plateau is supported by the low velocity zones near the base of the crust, as imaged seismically (Myers *et al.*, 1998).

(3) Catastrophic, large-scale delamination of an extremely dense lower crust and mantle lithosphere during the last 6-10 million years, as suggested by paleoelevation studies (e.g.

Garzione *et al.* 2006; 2008). Again, the driver for removal would come from metamorphic or magmatic eclogite; as noted above, previous geodynamic studies have shown that the density increase associated with cool lithosphere temperatures is expected to allow for only the lower 30-60% of the mantle lithosphere to be removed (e.g. Houseman and Molnar, 1997; Molnar *et al.*, 1998) whereas delamination requires removal of the full thickness of mantle lithosphere, with or without the lower crust. In contrast to RT-type instabilities, delamination involves lithosphere removal as a coherent slice beneath the plateau region of the central Andes (Kay and Kay, 1993; Garzione *et al.*, 2006; 2008; Kay and Coira, 2009).

It is important to note that the aforementioned hypotheses of lithosphere removal within the central Andes are essentially endmember conceptual models. Within a mature subduction zone, a combination of subduction-induced ablation, and either RT-type instabilities, or delamination occurs (possibly induced via a RT-type instability). This is discussed further in Chapter 3, when model results are presented and discussed.

1.5 Thesis objectives and organization

1.5.1 Objectives

To date, most previous geodynamic modelling studies have provided insights into lithospheric removal within idealized and generic models (i.e. parameters and geometries not based on any specific setting/location) (e.g. Göğüş and Pyslywec, 2008; Krystopowicz and Currie, 2013; Wang *et al.*, 2015). In this thesis, thermally-mechanically coupled geodynamic models are used to provide insights into lithosphere removal within an active subduction zone setting, with the parameterization based on that of the central Andes. Focus is placed on the geodynamic evolution of the central Andes during the last 10 – 20 m.y., a period over which rapid uplift has been proposed to have occurred in response to catastrophic mantle lithosphere removal (e.g. Garzione *et al.,* 2008). In the models, crustal shortening stemming from orogenesis is assumed to have already occurred, and this study addresses the dynamics of mantle lithosphere removal beneath tectonically thickened crust.

The objectives of this thesis are:

(1) To test various removal scenarios in order to provide insights into the dynamics that have created lithosphere structure given by geophysical surveys (e.g. seismic tomography). Lithospheric removal via delamination and Rayleigh-Taylor-type instability are investigated, with particular attention paid to the modulating effect of mantle flow induced by the adjacent subducting plate. These two styles of lithosphere removal are emphasized in this study as several recent geophysical and geologic studies employ these mechanisms in order to explain identified localized gaps with the mantle lithosphere, rapid largescale removal events, as well as rapid surface uplift (e.g. Myers *et al.*, 1998; Schurr *et al.*, 2006, Heit *et al.*, 2008; Garzione *et al.*, 2008). Note that subduction-induced ablation occurs within all models due to the tectonic setting; however, it is not the main focus of this study.

(2) To constrain the rheological and compositional factors that control the timing of the lithosphere removal and relate these to the proposed central Andean removal events.

(3) To examine the surface deflection and uplift implications of lithosphere removal within in active subduction zone setting. This would aim to aid in the reconciliation of recent paleoaltimetry studies that have yielded contradicting results for the central Andes, revealing high topography much earlier than expected (e.g. Puna plateau, Canavan *et al.*, 2014), or very young kilometre-scale uplift (e.g. Altiplano plateau, Garzione *et al.*, 2008).

(4) To use the thermal-mechanical models to predict the mantle seismic structure, in order to understand the origin of seismic anomalies in published seismic tomography models that have been attributed to the founding of mantle lithosphere.

1.5.2 Thesis organization

The current chapter (Chapter 1) provides the background information concerning the tectonic setting of the central Andes, as well as a discussion of possible drivers of lithospheric removal. Moreover, a summary of relevant regional geophysical observations is also provided, with particular focus on the current competing hypotheses of lithosphere removal in the central Andes. A detailed description of the parameterization of the numerical models and the overall modelling procedure is given in Chapter 2, which first details the governing equations for the finite element code used in this study (SOPALE). In Chapter 3, the evolution of a series of numerical models are presented and discussed in terms of their overall dynamics, for lithosphere removal through both delamination and Rayleigh-Taylor-type instability. Chapter 4 compares model results to proposed conceptual models of central Andean lithosphere removal, constrained primarily by deep seismic imaging. Chapter 5 focuses on the surface observations associated with lithosphere removal; derivative products of the models, specifically surface elevation profiles and mantle seismic structure are presented and compared to published topography and seismic observations for the central Andes. Finally, the conclusions of this thesis, as well as recommendations for future work, are provided in Chapter 6.

CHAPTER 2 : METHODOLOGY

In this study, two-dimensional numerical models are used in order to examine the dynamics, timing, and surface expressions of lithospheric removal within an Andean- Cordilleran-type subduction system. For this, the finite element numerical code SOPALE is used, with a model set-up that is a simplified representation of the natural system with the central Andes. SOPALE, a code developed at Dalhousie University (Fullsack, 1995), has been widely applied to studies of lithosphere dynamics on time scales typical of subduction and orogenesis, i.e., 10^4-10^8 years (e.g. Fullsack, 1995; Beaumont *et al.*, 2006; Currie *et al.*, 2007; Currie and Beaumont, 2011; Krystopowicz and Currie, 2013; Currie *et al.*, 2015; Wang and Currie, 2015). It has also been verified for numerical accuracy in applications related to the thermal-mechanical behaviour of the crust and upper mantle (Fullsack, 1995; Pysklywec *et al.*, 2002; Buiter *et al.*, 2006). In this chapter, the numerical code SOPALE (governing equations, boundary conditions, material properties) and modelling assumptions are discussed, the initial model setup and geometries are introduced, and the modelling procedure is presented.

2.1 Governing equations and Arbitrary Eulerian-Lagrangian method in the SOPALE code

This study uses two-dimensional thermal-mechanically coupled viscous-plastic numerical models to investigate the dynamics of lithosphere removal within a subduction zone setting. The thermal-mechanical evolution of the geodynamic system is solved based on the equations of conservation of momentum, mass, and energy. All governing equations are solved using a finite element code, SOPALE, which serves as a forward modelling tool. Material deformation, such as subduction, is driven by imposed velocity boundary conditions (discussed in section 2.5.1) and internal buoyancy forces, limited by the material viscosity, and is computed using an Arbitrary Eulerian–Lagrangian (ALE) finite element solution (Fullsack, 1995). SOPALE initializes a 2D domain geometry and spatial properties and fields (thermal, rheological, density, boundary conditions, etc.), and proceeds to perform a sequence of incremental motion computations to move and deform material, solving for the thermal evolution over time. The mechanical and thermal fields are as a result of the feedback between the thermal field, mechanical properties (e.g. viscosity, density), and the redistribution of radioactive heat-producing materials.

The ALE method consists of two representations for the material continuum, one based on marker particles, the Lagrangian grid (i.e. the "material domain" that tracks mechanical and thermal material properties, as well as material deformation history), and the other based on the fixed computational space, the Eulerian grid (i.e. the "spatial domain" in which the governing equations are solved). A particular sequence of steps defines the basis of the ALE method, iterated over a prescribed time step. The Eulerian grid serves as the reference frame where all governing equations are solved in order to obtain the velocity, pressure, and temperature at each timestep. The Eulerian grid is continually modified to track the external boundaries of the model domain by adjusting to the current position of the surface boundary, held fixed horizontally. The material domain, defined by a Lagrangian 'cloud' consisting of a set of marker particles/points prescribed with thermal-mechanical material properties, is then updated with particles being advected along material trajectories utilizing the Eulerian velocity field. The Eulerian grid is then updated to match the new material distribution. This allows for the Lagrangian motion and fields to be honoured and to be coupled to the Eulerian calculation of flow. Moreover, the Lagrangian particles are used to update the Eulerian material properties for the computation of the thermal-mechanical field in the following time step. This modelling approach allows for large amounts of deformation to be simulated at relatively low computational expense. Furthermore, the Eulerian grid permits a free top surface allowing for development of topography. Full details of SOPALE are given by Fullsack (1995) and Beaumont *et al.* (2006).

The models used in this study are regional scaled cross-sections, through the subduction zone setting of the central Andes, oriented perpendicular to the trend of the trench and approximately in the direction of plate convergence. It is assumed the evolution of the lithosphere – upper mantle system occurs under conditions of plain-strain, implying material deformation does not occur perpendicular to the plane of the model, material incompressibility, and a Reynolds number of zero. The Reynolds number is inversely proportional to viscosity, defining the ratio of inertial forces to viscous forces in a fluid. In the case of modelling the lithosphere – upper mantle system, assuming a Reynolds number of zero is justified due to the high material viscosities ($>10^{19}$ Pa·s) within the system, and due to the dominance of viscous forces (Reynolds number ~0). Therefore, the system can be modeled as a creeping viscous flow (Fullsack, 1995).

In SOPALE, the evolution of the geodynamic system is solved based on the equations of conservation of momentum, mass, and energy. The conservation of momentum is represented by the Stokes equation of creeping flow for a continuous medium (Equation 2.1) under the assumption of

incompressibility (Equation 2.2). It is calculated within the creeping flow limit where inertial forces are negligible compared to viscous resistance and gravitational forces. This force balance equation is solved in two dimensions, as given by,

$$-\frac{\partial P}{\partial x_j} + \eta_{eff}\frac{\partial}{\partial x_i}\left(\frac{\partial v_j}{\partial x_i} + \frac{\partial v_j}{\partial x_j}\right) + \rho g_j = 0 \qquad \text{Equation 2.1}$$

$$\textit{where} \quad \frac{\partial v_j}{\partial x_j} = 0 \qquad \text{Equation 2.2}$$

where *P* is the pressure (mean stress), x_i x_j are spatial coordinates, η_{eff} is the effective viscosity, v_i and v_j are the two velocity components with associated strain rates, $\dot{\varepsilon}_{ij}$, and stress, σ_{ij}, ρ is the density, and g_j is the vertical acceleration due to gravity. The system is solved for the unknown velocity components according to the imposed boundary conditions and mass conservation. The associated stress tensor is expressed,

$$\sigma_{ij} = -P\delta_{ij} + 2\eta_{eff}\varepsilon_{ij} = -P\delta_{ij} + \sigma'_{ij} \qquad \text{Equation 2.3}$$

where $\sigma'_{ij} = 2\eta_{eff}\varepsilon_{ij}$ is the deviatoric stress tensor and $\dot{\varepsilon}_{ij}$ is the strain rate tensor, given by,

$$\dot{\varepsilon}_{ij} = \frac{1}{2}\left(\frac{\partial v_i}{\partial x_j} + \frac{\partial v_j}{\partial x_i}\right)) \qquad \text{Equation 2.4}$$

The thermal field is modelled by accounting for temperature changes due heat generation and heat transport through diffusion and advection. The energy balance is then,

$$\rho c_p\left(\frac{\partial T_K}{\partial t} + v_i\frac{\partial T_k}{\partial x_i}\right) = \underbrace{k\frac{\partial}{\partial x_i}\frac{\partial T_K}{\partial x_i}}_{\textit{Conductive heat flux}} + \underbrace{\sigma'_{ij}\varepsilon_{ij}}_{\textit{Shear heat production}} + \underbrace{v_2\alpha g T_K \rho}_{\textit{Adiabatic production/ consumption}} + \underbrace{A}_{\textit{Volumetric radioactive heat production}} \qquad \text{Equation 2.5}$$

where T_K is temperature, c_p is the specific heat, *k* is the thermal conductivity, σ'_{ij} is the deviatoric stress tensor, α is the volumetric thermal expansion coefficient, v_2 is the vertical velocity, and *A* is the heat production per unit volume. Shear heating is included with the assumption made that all dissipated mechanical energy associated with deformation is converted to heat. In particular, the shear heating term connects the thermal field to the mechanical domain: it involves heat being produced, diffused (limited by the material thermal conductivity) and transported advectively (via the mechanically determined velocity), which ultimately affects the system rheology that in turn affects the mechanical behaviour of the system. Furthermore, the mechanical and thermal systems are coupled through the temperature dependence of viscosity and density.

2.2 Formulation of material properties

2.2.1 Material rheology and strength

On the timescale of millions of years, Earth rheology is generally studied utilizing a continuum mechanics approach that describes macroscopic relationships between stress and strain and their time derivatives. In this study, all materials in the numerical models have a viscous-plastic rheology (Bingham material), having both plastic (brittle) and viscous/ductile (power law creep) properties. Note, the following rheological laws treat the materials as a fluid and not solid, allowing the model to capture large deformation at geological timescales and enabling the use of continuum mechanics equations. The deformation mechanism, plastic or viscous, depends on ambient conditions. At and above the yield stress, material deformation occurs through frictional plastic (brittle) failure, and below yield the material deforms through ductile flow. In SOPALE, frictional-plastic deformation is modelled as viscous creep by defining a viscosity that places the state of stress on yield (Fullsack 1995; Willett, 1999; Beaumont *et al.*, 2006). In the brittle regime, all materials modelled have a pressure-dependent Drucker-Prager failure criterion, given by,

$$(J_2')^{1/2} = Psin\phi_{eff} + C_0 cos\phi_{eff} \quad \text{Equation 2.6}$$

$$Psin\phi_{eff} = P(1-\lambda)sin\phi \quad \text{Equation 2.7}$$

where $J_2' = \frac{1}{2}\sigma_{ij}'\sigma_{ij}'$ is the second invariant of the deviatoric stress tensor, P is the pressure (mean stress), C_0 is the cohesion, and ϕ_{eff} is the internal angle of friction. Equation 2.7 defines ϕ_{eff} to include the dry internal angle of friction (ϕ), the effects of pore fluid pressure where λ is the Hubbert-Rubey fluid pressure ($\lambda = P_f/P$, where P_f is the pore fluid pressure). Note pore fluid pressure weakens the material by reducing the frictional coefficient.

In the ductile regime, when the stress is less than the frictional-plastic yield stress, deformation is modelled by a thermally activated power-law rheology,

$$\eta_{eff}^{v} = \frac{f}{W_s}(B^*)(I_2')^{(1-n)/n} exp\frac{Q+PV^*}{nRT_K} \quad \text{Equation 2.8}$$

$$\textit{where} \quad B^* = 2^{(1-n)/n}3^{-(n+1)/2n}A^{*-1/n} \quad \text{Equation 2.9}$$

where η_{eff}^{v} is the effective viscosity, *f* is a viscosity scaling factor, W_s is a strain-weakening factor (discussed in section 2.2.2), $\dot{I}_2' = \frac{1}{2}\dot{\varepsilon}_{ij}'\dot{\varepsilon}_{ij}'$ is the second invariant of the deviatoric strain rate tensor, R is the universal gas constant (8.3145 J mol^{-1} K^{-1}), T_K is temperature in Kelvin, and *P* is pressure (mean stress). The pre-exponential viscosity parameter (B^*), the stress exponent (*n),* the activation energy (Q),

and the activation volume (V^*) are rheological parameters derived from laboratory experiments. In order to convert the pre-exponential factor, *A* in Equation 2.9, from uniaxial laboratory conditions to the 2D plain strain conditions used in the model (e.g. Ranalli, 1987), another constant B^* is defined. Note, thermally activated power-law dislocation creep is believed to be the primarily mode of deformation in the upper mantle (Karato and Wu, 1993; Hirth and Kohlstedt, 2003), where it governs convective flow. Deformation is accommodated at the microscopic level by the movement of defects within the lattice structure, and at sufficiently high temperatures both dislocation glide and climb occur, which allows steady-state creep to be facilitated. Moreover seismic observations suggest that diffusion creep (n=1) becomes the dominant mechanism in the lower mantle, where less seismic anisotropy is detected and temperatures are higher (Karato, 1981; Karato, 2010).

The effective viscosities are linearly scaled utilizing the constant *f* in Equation 2.8, in order to approximate variations in rheological parameters that occur due to the gap between laboratory conditions and studies of geological deformation in terms of time- and space-scales. Laboratory-derived flow laws are determined based on deformation of individual rock samples, and at strain rates that need to be extrapolated to that of typical geological values (laboratory studies conducted at 10^{-6}-10^{-3} s^{-1}, with geological strain rates at 10^{-12}-10^{-16} s^{-1}) (Karato, 2010; Burov, 2011). The space-scale issue can be important for plastic properties, where anisotropy and heterogeneity are highly influential factors (Karato, 2010). Furthermore, rheology is affected by numerous factors not incorporated in laboratory based equations, and variations in strength can occur due to minor variations in composition, water content, strain rates or deformation mechanism, or the presence of melt. Therefore, in order to simplify the construction and interpretation of the models, while still providing reasonable variations in material strengths, the approach outlined in Beaumont *et al.* (2006) is used. The reference rheologies for the model materials are based on a set of laboratory flow laws, parameterized and tested in many previous numerical studies examining lithospheric dynamics (e.g. Beaumont *et al.*, 2006; Warren *et al.*, 2008; Currie and Beaumont, 2011; Currie *et al.,* 2015) (discussed in section 2.3). The effective viscosities captured in the model can then be scaled without altering temperature and pressure dependence. This method simplifies the modelling procedure, removing the need to change the flow law parameters individually to vary the strength of materials.

2.2.2 Strain induced deformation mechanisms

Under conditions of strain, materials can undergo strain-softening or –hardening processes that lead to lithosphere mechanical weakening or strengthening, respectively. As a result, layer thickness and strength, play important roles in controlling the systems resistance to deformation or, contrastingly, the localization of strain and deformation. In the upper layers of the lithosphere, variations strength occur in response to pore fluid pressure variations, infiltration of fluids, changes in strain rate, and mineral reactions (Sibson, 1990; Bos and Spiers, 2002; Huismans and Beaumont, 2003; Warren *et al.*, 2008). Strain-induced weakening is specified in the model by linear changes in the effective angle of internal friction for brittle deformation and in the effective viscosity for viscous deformation. Specifically, following values used in previous models, strain-softening within the brittle domain is included in the model by decreasing the value of ϕ_{eff} in Equation 2.6 linearly from 15° to 2° as the accumulated strain increases from 0.5 to 1.5 (e.g., Beaumont *et al.*, 2006; Huismans and Beaumont, 2003; Warren *et al.*, 2008; Liu, 2014).

Viscous strain-weakening, W_s, proceeds through a linear decrease in effective viscosity by a factor of 10 to 100 over an accumulated strain range of 2 to 5 for oceanic crust in the current model. Viscous strain-weakening represents the combined effects of reaction- and strain-weakening mechanisms that occur during ductile deformation (Warren *et al.*, 2008). Note high temperature dislocation creep is accompanied by thermally activated softening processes in order to reach steady-state deformation, with these processes also known as recovery mechanisms. This allows crystal defects to continue to glide at constant stress and maintain low energy configurations. Other potential weakening mechanisms include, but are not limited to, strain-induced grain size reduction, increase in temperature, metamorphic reactions, and infiltration of volatiles and melt. Note these mechanisms are poorly constrained at geologic conditions.

2.2.3 Density

All materials have a temperature-dependent density, given by,

$$\rho(T) = \rho_0[1 - \alpha(T - T_0)] \qquad \text{Equation 2.10}$$

where ρ_0 is the reference density at temperature T_0, and α is the volumetric thermal expansion coefficient.

2.3 Model set-up

2.3.1 Initial geometries

The models in this study are set-up to characterize, the dynamics of lithosphere removal beneath the central Andes within the time period of 10 – 20 Ma. The model parameterization is intentionally simplified to capture first-order features of this region, including a mature subduction zone, thick continental crust of the plateau, and stable craton including a retroarc foreland basin. The fixed computational domain is 200 km wide, extending from the surface to 660 km depth. The Eulerian mesh has 250 elements horizontally (8 km width), and 108 stratified elements vertically, with 56 elements in the upper 140 km (2.5 km height), and 52 elements in the following 520 km (10 km in height) (Figure 2.1.a). The Lagrangian 'cloud' is coincident with the right side of the model domain, but extends to the left of the Eulerian grid, allowing for the introduction of oceanic material as subduction occurs. Prior to any deformation, this Lagrangian mesh is 5024 km wide, with the same vertical resolution parameters as the Eulerian mesh. During model initialization, additional Lagrangian particles are injected such that the mesh is three times more dense, in order to better resolve the distribution of materials. Note that this cross-sectional domain is assumed to be oriented approximately parallel to the direction of convergence between the South American and Nazca plates.

Prior models of lithosphere removal have generally neglected to include the dynamics associated with subduction and its influence on the thermal and mechanical fields of the system. Therefore, in order to incorporate a subduction zone, oceanic lithosphere reflective of the Nazca plate (age ~45 Ma at the trench) is specified within this modelling study. The oceanic plate is 80 km thick, comprising of 7.5 km thick crust underlain by 72.5 km mantle lithosphere (Figure 2.1b). Tassara *et al.* (2006) and Tassara and Echaurren (2012) report that the Nazca Plate oceanic crust thickness close to the continental margin is within the global average of 7 +/- 1 km estimated by White *et al.* (1992) and Bown and White (1994). Age predicted lithosphere-asthenosphere boundary depths, from the same studies, result in ~ 80 km plate thickness, as do the density-derived modelled values. Sodoudi *et al.* (2011) estimates the Nazca plate to be ~50 km thick, based on teleseismic receiver function analysis. To reconcile available data as well as the error bounds of the thickness estimates, the value of 80 km for the mantle lithosphere suggested by Tassara *et al.* (2006) was used in the models. This thickness also ensures that the base of the plate coincides with element boundaries within the model domain. A diagonal boundary dipping at ~30° defines the boundary between the oceanic and the continental lithosphere, where a rheologically weak 'seed' is emplaced in order to aid in subduction initiation

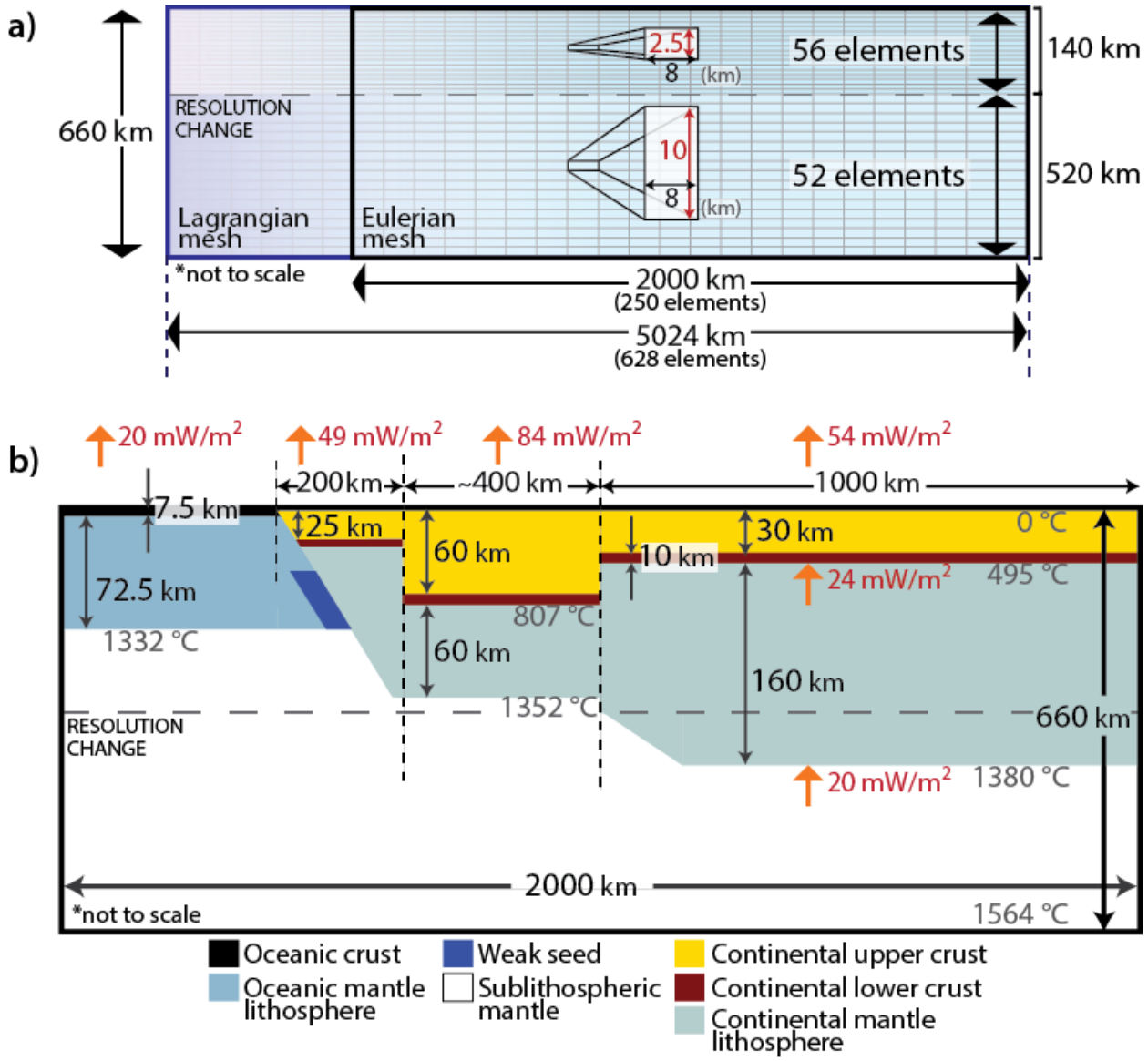

Figure 2.1 Model design and initial geometry, displayed within the Eulerian space. **a)** Schematic of resolution parameterization of both the Lagrangian and Eulerian mesh. **b)** Dimensions of initial geometries: *Pre-cordillera* spans 200 km from the interface with oceanic lithosphere; *Plateau* region spans ~400 km, exhibiting 60 km (+10 km lower crust) thick crust, assuming crustal shortening stemming from orogenesis has already occurred; *Craton* region spans the remaining 1000 km to the right edge of the model domain. The initial thermal structure is indicated in terms of interface temperatures (black) and layer heat flux (red).

(discussed in section 2.6). This plate boundary is set at 400 km from the edge of the model domain. Note water loading is neglected here.

The geometric dimensions of the continental lithosphere are specified based on seismic receiver function studies, which provide unprecedented constraints on the crustal thicknesses in the central Andean region (e.g. Beck and Zandt, 2002; Yuan, 2002; Ryan *et al.*, 2016). The continent is stratified into three-layers: upper-, lower- crust, and mantle lithosphere. Laterally, the continent is subdivided into three adjacent regions which are analogous to the central Andean lithospheric structure (Figure 1.3): (1) the Pre-cordillera that is adjacent to the plate margin and trench, (2) the Plateau region, including the Western and Eastern Cordilleras, with ~400 km width, and (3) the Craton region that encompasses the foreland basin and extends to the 2000 km wide boundary of the model domain (Figure 2.1b). The Pre-cordillera region is comprised of 25 km upper crust, underlain by 10 km lower crust and mantle lithosphere that extends to 130 km depth. The Plateau region is characterized by the extreme upper crustal thickness of 60 km, underlain by 10 km thick lower crust and 60 km mantle lithosphere. This 130 km thick lithosphere reflects the range suggested by Whitman *et al*., 1996 for the plateau, with values of 100 – 150 km found below the Altiplano and values several tens of kilometers thinner beneath the Puna. Finally, the Craton consists of 35 km thick upper crust (Assumpção *et al.*, 2002), underlain by 10 km lower crust and mantle lithosphere that extends to 200 km depth. All upper crustal thicknesses reflect the depth to Moho values specified in Beck *et al.* (1996), Yuan *et al.* 2000, 2002; Beck and Zandt (2002), and Ryan *et al.* (2016). Moreover, the craton values are calibrated to available estimates of the Brazilian craton, including a global map of lithospheric thickness based on long-period (>50 s) surface waves (McKenzie *et al.*, 2015) that indicates ~200 km thick cratonic lithosphere. As the Craton region is >500 km from the subduction zone, its lithosphere thickness is expected to have little effect on mantle wedge pressures and slab dynamics. Notably, crustal shortening stemming from orogenesis is assumed to have already occurred, as the removal of mantle lithosphere and its implications to the system as a consequence of this crustal thickening is the primary focus of this study. The development of an orogeny above a subduction zone remains an area of active research that is outside the scope of this work.

2.4 Material parameterization

2.4.1 Mechanical properties

Following previous studies (e.g. Beaumont *et al.*, 2006; Krystopowicz and Currie, 2013; Currie *et al.*, 2015), material mechanical properties are based on several well-constrained laboratory derived

viscous rheologies (Table 2.1). Recall, these base rheologies are then scaled a factor of *f* in order to approximate changes in strength due to the effect of the variations in composition and water content (Hirth and Kohlstedt, 2003; Beaumont *et al.*, 2006; Karato, 2010). Within the continent, the rheological structure has a laterally uniform three-layer crust: upper-, lower- crust, mantle lithosphere. Note that the thickness of each layer varies between each continental region (Figure 2.1). This layering is designed to incorporate continental margin-type crust, with an upper crust that is dominated by quartz-rich sedimentary rock underlain by a more intermediate mafic lower crust. The continental upper crust is assigned wet quartzite (Gleason and Tullis, 1995) scaled by $f = 5$ to approximate material stronger than its pure base rheology. It is assigned a reference density of 2900 kg m^{-3} to reflect a silica-rich composition. The lower continental crust uses the parameters of dry Maryland diabase (Mackwell *et al.*, 1998), with $f = 0.1$, assuming the crust is hydrated, and, therefore, weaker than the base rheology. This

Table 2.1: Material parameters used in reference model

	Continental upper crust	Continental lower crust	Continental mantle lithosphere	Oceanic crust	Oceanic mantle lithosphere	Sublithospheric mantle
Plastic rheology						
$\boldsymbol{c_0}$ (MPa)	2	0	0	0	0	0
$\boldsymbol{\phi_{eff}}$	15° - 2°	15° - 2°	15° - 2°	15° - 2°	15° - 2°	15° - 2°
Viscous rheology						
$\boldsymbol{f}$	5	0.1	10	0.1	10	1
$\boldsymbol{A}$ (Pa^{-n} s$^{-1)}$	1.1 x 10^{-28}	5.05 x 10^{-28}	3.91 x 10^{-15}	5.05 x 10^{-28}	3.91 x 10^{-15}	3.91 x 10^{-15}
$\boldsymbol{B}^*$ (Pa s$^{1/n}$)	2.92 x 106	1.92 x 10^5	1.91 x 10^5	1.92 x 10^5	1.92 x 10^4	1.92 x 10^4
$\boldsymbol{n}$	4.0	4.7	3.0	4.7	3.0	3.0
$\boldsymbol{Q}$ (kJ mol^{-1})	223	485	430	485	430	430
$\boldsymbol{V}^*$ (cm^3 mol^{-1})	0	0	10	0	10	10
Thermal values						
$\boldsymbol{k}$ (W m^{-1} K^{-1})**	2.25	2.25	2.25	2.25	2.25	2.25
$\boldsymbol{A}$ (W m^{-3})	1.0	0.4	0	0	0	0
$\boldsymbol{c_p}$ (J kg^{-1} K^{-1})	750	750	1250	750	1250	1250
Density						
$\boldsymbol{\rho_0}$ (kg m^{-3})	2900	3000	3250	3080	3250	3250
$\boldsymbol{T_0}$ (°C)	900	900	1340	0	1340	1340
$\boldsymbol{\alpha}$ (K^{-1})	3.0 x 10^{-5}	3.0 x 10^{-5}	3.0 x 10^{-5}	3.0 x 10^{-5}	3.0 x 10^{-5}	3.0 x 10^{-5}
Eclogite						
$\boldsymbol{\rho_0}$ (kg m^{-3})	–	–	–	3350	–	–
$\boldsymbol{T_0}$ (°C)	–	–	–	500	–	–

** Thermal conductivities reported are for temperature below 1352°C (within the lithosphere), above which $\boldsymbol{k}$ increases linearly from 2.25 W m^{-1} K^{-1} to 50 W m^{-1} K^{-1} at 1362°C.

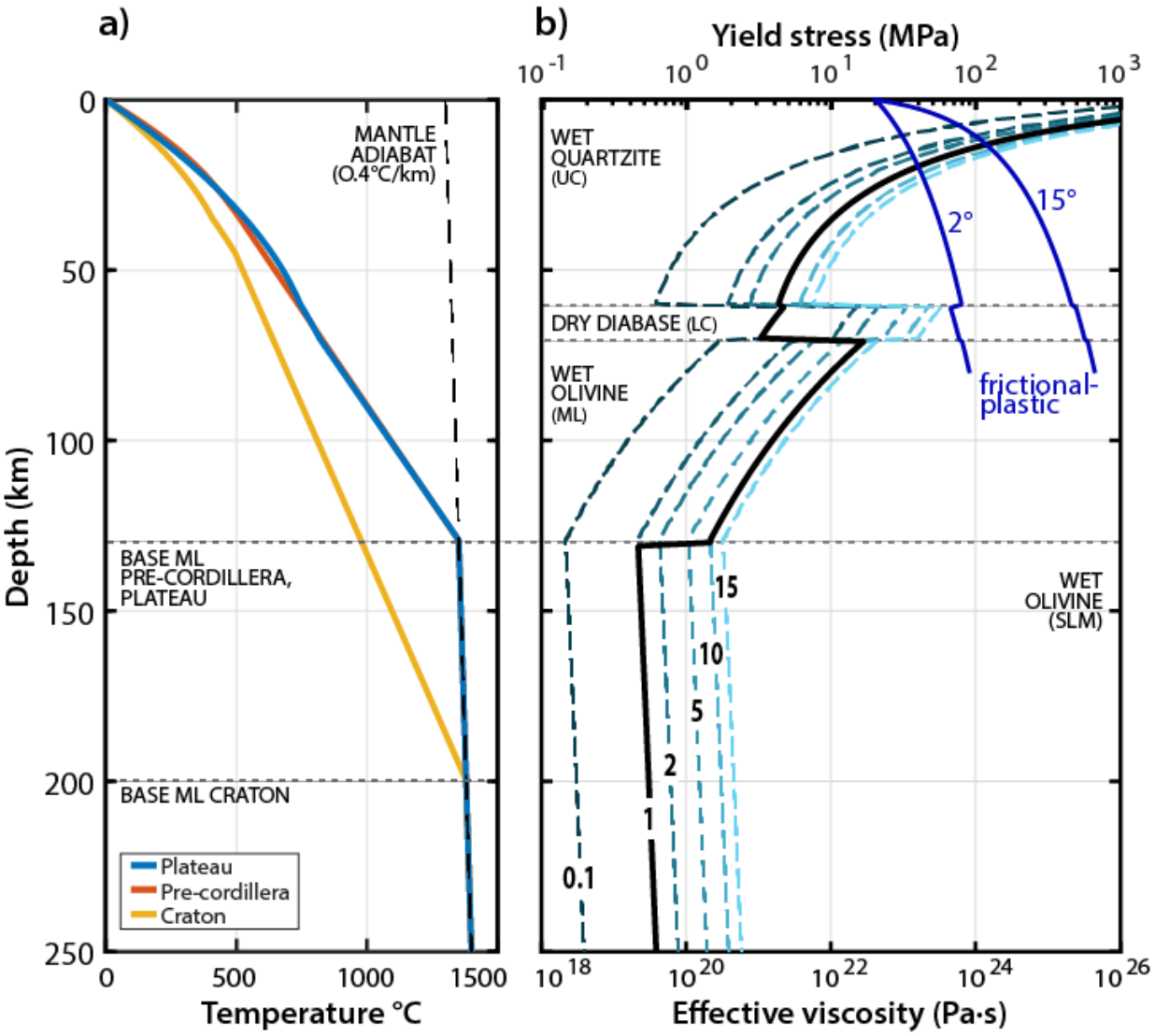

Figure 2.2 **a)** Initial thermal structure of the model for the three continental regions, with each geotherm of the different regions intersecting with the mantle adiabat at the base of the mantle lithosphere. This reflects the boundary between conductive lithosphere and convective mantle. **b)** Lithosphere strength profile for the *Plateau* region, reflecting its thermal structure. Blue lines show frictional-plastic yield stress for unsoftened (ϕ=15°) and softened (ϕ=2°) material. Dashed lines show the effective viscosity various scaling factors (*f=0.1, 1, 2, 5, 10, 15)*, calculated using the initial thermal structure and a constant strain rate of 10^{-15} s^{-1}. Note that strain rate varies during model evolution. The thick black line shows the composite strength profile for the reference model, reflecting the various material assignments: wet quartzite for upper crust (UC) (Gleason and Tullis, 1995), dry Maryland diabase (Mackwell *et al.*, 1998) for the lower crust (LC), and wet olivine (Karato and Wu, 1993) for both the mantle lithosphere (ML) and sublithospheric mantle (SLM).

lower crustal material is more mafic than the overlying material, and it prescribed a reference density of 3000 kg m^{-3}. Note, the oceanic crust utilizes the same rheology as the continental lower crust, for a similar rationale, but is assigned a slightly larger reference density of 3080 kg m^{-3}. Finally, all mantle is assigned a wet olivine rheology (Karato and Wu, 1993), with f=1 for the sublithospheric mantle, and f = 10 for both the continental and oceanic mantle lithosphere. It is assumed that the mantle lithosphere is more depleted and dehydrated in comparison to the fertile and water-saturated sublithospheric mantle, and therefore, is 5 – 10 times more viscous than its underlying counterpart (Hirth and Kohlstedt, 2003). The reference density of the mantle is 3250 kg m^{-3} and is consistent with the density of fertile upper mantle. Olivine flow laws are generally used to simulate the rheology of the upper mantle, as olivine is believed to be the most abundant and strength limiting mineral in the upper mantle pyrolytic composition (Karato and Wu, 1993; Hirth and Kohlstedt, 2003; Karato, 2010). Note the mantle lithosphere and sublithospheric mantle material assignments are equivalent except for the viscous scaling factor, thus allowing for removal to be triggered by buoyancy contrasts and gravitational instabilities imposed within the model (discussed in section 2.6). The composite strength profile for the Plateau region, based on initial thermal structure, is shown in Figure 2.2b. This profile also highlights the effect of scaling the base rheologies.

2.4.2 Thermal properties

Thermal properties are listed in Table 2.1 for each material, all falling within the expected range of crustal and mantle materials (e.g. Jaupart and Mareschal, 2003). Radiogenic heat production A is 1.0 W m^{-3} and 0.4 W m^{-3} in the upper- and lower- crust, respectively (Pollack and Chapman, 1997). There is no radiogenic heat production in the oceanic crust or mantle. Moreover, all materials are assigned a thermal conductivity of 2.25 W m^{-1} K^{-1} at temperatures below 1352°C. At higher temperatures, the thermal conductivity increases to 50 W m^{-1} K^{-1} at 1362°C. This primarily affects sublithospheric mantle and is used in order to maintain a nearly constant heat flux at the base of the lithosphere, as well as to produce an adiabatic temperature gradient of 0.4 °C/km in the sublithospheric mantle. The high conductivity simulates heat transfer by a convecting mantle without the need to model upper mantle convection explicitly (Pysklywec and Beaumont, 2004).

2.4.3 Phase changes

In all models, a metamorphic phase change to eclogite is included for oceanic crust. Upon subduction, the descending oceanic lithosphere encounters higher temperature and pressure conditions, and, as a result, the oceanic crust begins to dehydrate through a series of metamorphic mineral reactions. In nature, hydrous basalt and gabbro are metamorphosed progressively to blueschist, amphibolite, and finally eclogite (Hacker *et al.*, 2003). At each transformation, water is released, and the density of the crust increases, with the final eclogite transition marking the greatest density change. Therefore, to include this phase change to first-order, the transformation from basalt to eclogite for the oceanic crust is incorporated into the models. Stable conditions for the eclogite facies conditions exist at temperatures >500°C and pressures >1.2 GPa (Figure 2.3) (Hacker, 1996; Hacker *et al.*, 2003). This stability field supports seismological studies that suggest that the eclogite facies is generally not an important part of subducted crust until depths of ~50–200 km (Abers, 2000).

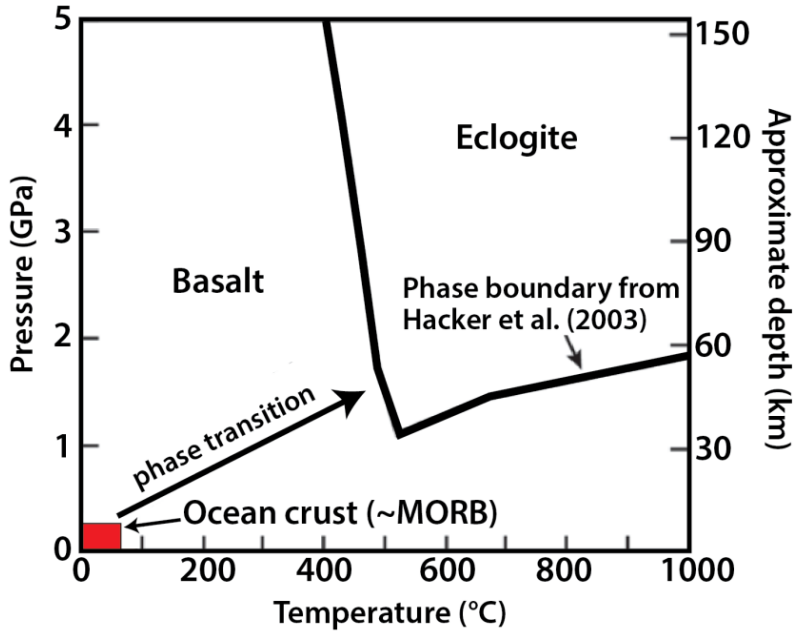

Figure 2.3 Pressure-temperature stability field of basalt and eclogite (from Hacker *et al.*, 2003). The red region shows the initial pressure-temperature conditions for the oceanic crust for the models in this study. During subduction, pressure and temperature increase, and as conditions enter the eclogite stability field the oceanic crustal material takes on material properties of eclogite (modified from Liu, 2014).

Eclogite is mafic rock predominantly consisting of garnet and omphacitic clinopyroxene (Coleman *et al*., 1965). The geophysical importance of eclogite is that it represents the highest density commonly attained by crustal rocks. Omphacite and garnet have densities of 3200 – 3400 kg m^{-3} and 3600 – 4000 kg m^{-3}, respectively, a marked increase in density compared to that of typical basalt at ~3000 kg m^{-3} (Hacker, 1996). The phase change to eclogite represents a shift from positive to negative buoyancy relative to the sublithospheric mantle, which has a density of ~3250 kg m^{-3}. The density of eclogitized rocks depends on their initial composition, the ambient thermal and pressure conditions, and the history of deformation. Field and experimental data suggest that eclogitized oceanic crust may be 50 – 250 kg m^{-3} denser than mantle (e.g. Bousquet *et al.*, 1997; Jull and Kelemen, 2001). Therefore, the transformation to eclogite enhances the negative buoyancy of the descending lithosphere and contributes to the slab-pull force acting on the oceanic plate. The baseline parameters for the eclogite material in the reference model are given in Table 2.1, and differ from those of the oceanic crust only in terms of their reference density value, such that the eclogite phase change corresponds to a density increase of ~300 kg m^{-3} (at the same temperature).

This phase change is achieved by tracking and comparing the temperature and pressure of the oceanic crust with that of eclogite (Figure 2.3); once the crust enters the eclogite stability field, its density is increased. During the phase changes the incompressibility equation is modified to that of mass conservation: $\partial\rho/\partial t = -\partial(\rho v_i)/\partial x_i$, (Warren *et al.,* 2008). This accounts for the minor volume change associated with the densification, and its effect on the buoyancy and velocity field. An additional force, ΔP, compresses material locally and only during the model time step when the phase change occurs, thereby ensuring mass conservation. This excess pressure, $\Delta P = \Delta\rho/\beta_v\rho$, is calculated utilizing the viscous bulk modulus of the material, β_v, and the fractional change in density corresponding to the phase change, $\Delta\rho/\rho$.

Note that the interest of this study is restricted to the dynamics occurring within upper mantle (<410 km depth). As a result phase changes and specific rheological processes associated with the transition zone (410 – 660 km depth) are not incorporated. These are, however, briefly discussed within section 6.2.

2.5 Boundary conditions

2.5.1 Mechanical boundary conditions

The mechanical boundary conditions imposed on the model are summarized in Figure 2.4. In particular, they include a free surface top boundary (zero stresses) to allow for topographic growth, a closed free slip bottom lower boundary, and imposed horizontal velocities on both side boundaries; the side boundaries are free slip (zero tangential stress). To drive convergence, as well as subduction, the horizontal velocities are imposed onto the full length of the continental and oceanic lithosphere. The velocities are determined by examining both the historic convergence between the Nazca and South American plates, and the present-day velocity of the plates themselves. Convergence for the last 35 Ma between the two plates is provided by Somoza (1998), which gives an average value for the last 20 Ma of ~10 cm y^{-1}. The South American plate drifted westward during this time, with this acceleration caused by the continued opening of the South Atlantic and the slowing motion of Africa during the Miocene. This westward drift has remained nearly constant for the last ~ 50 Ma, averaging a value of ~2.5 cm y^{-1} at the latitude range of 18-22°S for the last 20 Ma (Silver *et al.*, 1998). Furthermore, this

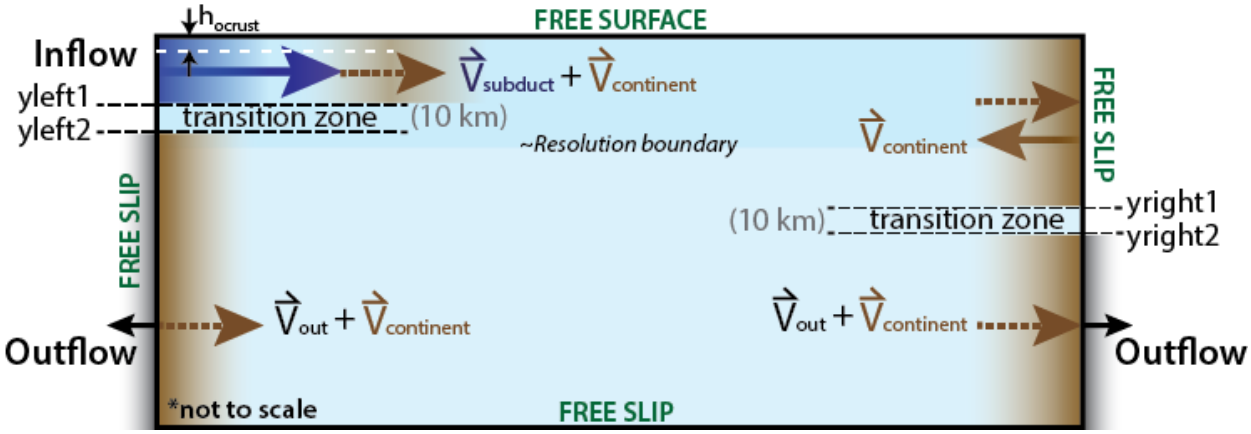

Figure 2.4 Mechanical boundary conditions imposed on the models. Velocities are imposed on the length of the side boundaries of the model domain, including an inflow ($\vec{V}_{subduct}$) and outflow ($\vec{V}_{out}$) component. The models are set in the continental reference frame, therefore all inflow and outflow components have $\vec{V}_{continent}$ added to their values (see text). Between the inflow and outflow regions there is a transition zone, a prescribed 10 km between *yleft1*-*yleft2* and *yright1*-*yright2*, where the inflow velocity ($\vec{V}_{subduct} + \vec{V}_{continent}$) linearly becomes the outflow velocity. h_{ocrust} refers to the thickness of the oceanic crust used in Equation 2.11, where the thickness of the mantle lithosphere is equal to the difference between *yleft1* and h_{ocrust}.

westward drift is believed to be equivalent to the rate of motion of the trench owing to the retreat of the subducting Nazca plate. In order to run the models within the continental reference frame, the continental velocity, $\vec{V}_{continent}$, which is equivalent to this westward drift of South America, is added to all vertical boundaries. Ultimately, absolute velocities of 7.5 cm y^{-1} and 2.5 cm y^{-1} are imposed on the oceanic and continental lithosphere, respectively, summing to the average convergence proposed of 10 cm y^{-1} for the last 20 Ma (Somoza, 1998), and also reflecting past and present-day absolute velocities of the respective tectonic plates.

It is necessary to impose a small outflow velocity $\vec{V}_{out}$ to the side boundaries of the sublithospheric mantle in order to maintain a constant mass in the model as subduction occurs. There is a linear transition between the two velocity conditions that takes place within a prescribed 10 km zone on each side boundary, as depicted in Figure 2.4. This outflow velocity is dependent on the inflow velocity of the incoming oceanic plate, as well as the thickness and density of the material being introduced to the model (refer to section 2.6.1 for specific values employed at various stages in the modelling procedure). Defining this input = output relationship, the outflow velocity $\vec{V}_{out}$ can be determined by,

$$\vec{V}_{subduct}\left((\rho_{Ocrust} \times h_{Ocrust}) + \left(\rho_{OML} \times (y_{left1} - h_{Ocrust})\right)\right) = \vec{V}_{out}\left(\rho_{sublith} \times (y_{left2} + y_{right2})\right)$$

Inflow = Outflow Equation 2.11

where $\vec{V}_{subduct}$ is the subducting rate of the oceanic plate, ρ_{Ocrust} is the reference density for the oceanic crust, h_{Ocrust} is the thickness of the oceanic crust, ρ_{OML} is the reference density for the oceanic mantle lithosphere, y_{left1} is the base of the oceanic lithosphere, $\vec{V}_{out}$ is the mass balancing outflow velocity, $\rho_{sublith}$ is the reference density of the sublithospheric mantle material, and y_{left2} and y_{right2} are depths at the top of the transition zone on corresponding sides of the model domain. Furthermore, the lithostatic pressure at the base of the model is monitored adjacent to the right edge of the Eulerian domain (element 245), where the velocity field is relatively stable. If the pressure fluctuates, the outflow velocity is dynamically modified in order to keep the mass in the model constant by maintaining an average basal pressure within the model.

2.5.2 Thermal boundary conditions

Thermal boundary conditions imposed on the models are: a fixed basal and top temperature, 1564 °C ($z = 660$ km) and 0 °C respectively, a heat flux of 0 mW m^{-2} on the side boundaries of the

sublithospheric mantle (i.e. insulating boundaries), and prescribed temperatures on the side boundaries for the oceanic and cratonic lithosphere. In particular, the initial thermal structure of the continental portion of the model is calculated via the one-dimensional steady-state conductive heat equation (Equations 2.12, 2.13) based on a fixed surface and basal temperature. The geotherm for a given continental region depends on prescribed surface heat flow (constrained by surface heat flow values observed within the central Andes (e.g. Springer, 1999)), the vertical distribution of heat production source, and the variation of thermal conductivity with depth (Pollack and Chapman, 1997; McKenzie *et al.*, 2005). Therefore, for each compositional layer of the lithosphere of thickness dz_n, the top temperature T_{n-1} and heat flow q_{n-1} of the layer are used to calculate the basal temperature T_n and heat flow q_n. The oceanic lithosphere side boundary is given an oceanic geotherm, utilizing the same surface temperature constraint of 0 °C, and exhibiting a linear temperature gradient from the base of the crust to the base of the lithosphere, 1332 °C ($z = 80$ km). For both the continental and oceanic materials, the base of the lithosphere is defined as the intersection of the conductive lithospheric geotherm with a mantle adiabat that has a potential temperature of 1300 °C and an adiabatic gradient of 0.4 °C km^{-1}. Note the thermal conductivity (k) and radiogenic heat production (A) values are given in Table 2.1 in section 2.4, and all fall within the expected range for crustal and mantle materials (e.g. Jaupart and Mareschal, 2003).

$$T_n(z) = T_{n-1} + \frac{q_{n-1} dz_n}{k_n} - \frac{A_n {dz_n}^2}{2k_n} \qquad \text{Equation 2.12}$$

$$q_n = q_{n-1} - A_n dz_n \qquad \text{Equation 2.13}$$

The resulting thermal field is generating using surface heat flows of 20 mW/m^2, 49 mW/m^2, 84 mW/m^2, 54 mW/m^2 for the oceanic plate, Pre-cordillera, Plateau and Craton regions, respectively, as shown in Figure 2.1. These values are comparable to the measured and modelled surface heat flow values for the central Andean region from Springer and Forster (1998) and Springer (1999).

2.6 Modelling procedure

2.6.1 Modelling procedure for removal

The modelling procedure for this body of work is carried out in four phases: (1) Isostasy, (2) Subduction initiation, (3) Relaxation, (4) Removal. In Phase 1, the initial conditions including material geometries (sections 2.3.1, 2.4.1) and the 2D thermal field (sections 2.4.2, 2.5.2) are set up. The mechanical boundary conditions are static as no horizontal velocities are imposed on the system. The

main purpose of this phase is for materials to come into equilibrium by adjusting isostatically, a direct result of the temperature and reference density assignments of the stratified lithospheric material (Table 2.1). This adjustment results in an elevation profile with four distinct features: an oceanic basin of ~3.6 km depth (recall water loading is neglected), a slight continental rise, a 400 km wide plateau ~2.9 km in height, and a foreland basin at an elevation of ~0 km that extends to the right lateral edge of the model domain (Figure 2.5).

Phase 2 is used to establish a mature subduction zone setting, which is then used as the 'initial' conditions for the following removal experiments. This is achieved by imposing a horizontal velocity along the length of the oceanic lithosphere of 5 cm y^{-1} and 0 cm y^{-1} along the continental boundary (corresponding $\vec{V}_{out}$= ~0.39 cm y^{-1}, refer to section 2.5.1). It is necessary to provide some form of decoupling between the subducting and overriding plates in order to allow for one-sided subduction to take place. A locus of deformation that leads to the oceanic lithosphere descending beneath the continent is achieved by emplacing a rheologically weak 'seed' along the diagonal boundary between the oceanic and continental lithosphere, which is assigned the material properties of wet quartzite with a scaling factor *f = 1*. This weak material is subsequently carried deep into the model domain with the descending slab has no effect on model evolution thereafter. Note that during this phase, the strength of the continental lithosphere is increased by an order of magnitude in order to ensure that it remains static as the oceanic material sinks. In this phase, the models use a timestep of 1000 years, until 400 km convergence. This results in a slab geometry reflective of a typical steep dip subduction zone (dip ~30 – 40°) (e.g. Stern, 2002; Turcotte and Schubert, 2002), and is characteristic of the central Andes within the last 20 Ma (e.g. DeCelles *et al.*, 2009; Ramos, 2009) (Figure 2.5). At the end of this phase, the elevation profile includes a ~6 km deep trench (subduction hinge) and a more defined continental shelf.

Phase 3 is carried out as an intermediate step to allow the model to equilibrate to new conditions imposed on the system at a smaller timestep, before Phase 4 occurs. Each timestep is 100 years in length, and this stage is run until 50 km of convergence has occurred. Side boundary velocities are altered to reflect the convergence of the Nazca and South American plates (discussed in section 2.5.1), with 7.5 cm y^{-1} and 2.5 cm y^{-1} imposed on the oceanic and continental lithosphere, respectively (corresponding $\vec{V}_{out}$= ~0.78 cm y^{-1}, refer to section 2.5.1). . This phase also allows for the continental material to vertically re-adjust as its scaling factors are those presented in Table 2.1(section 2.4). This allows for the plateau region of the continent to 'relax' and its morphology to flatten out. This is also the stage where dense bodies of various geometries are imposed within the continental mantle lithosphere

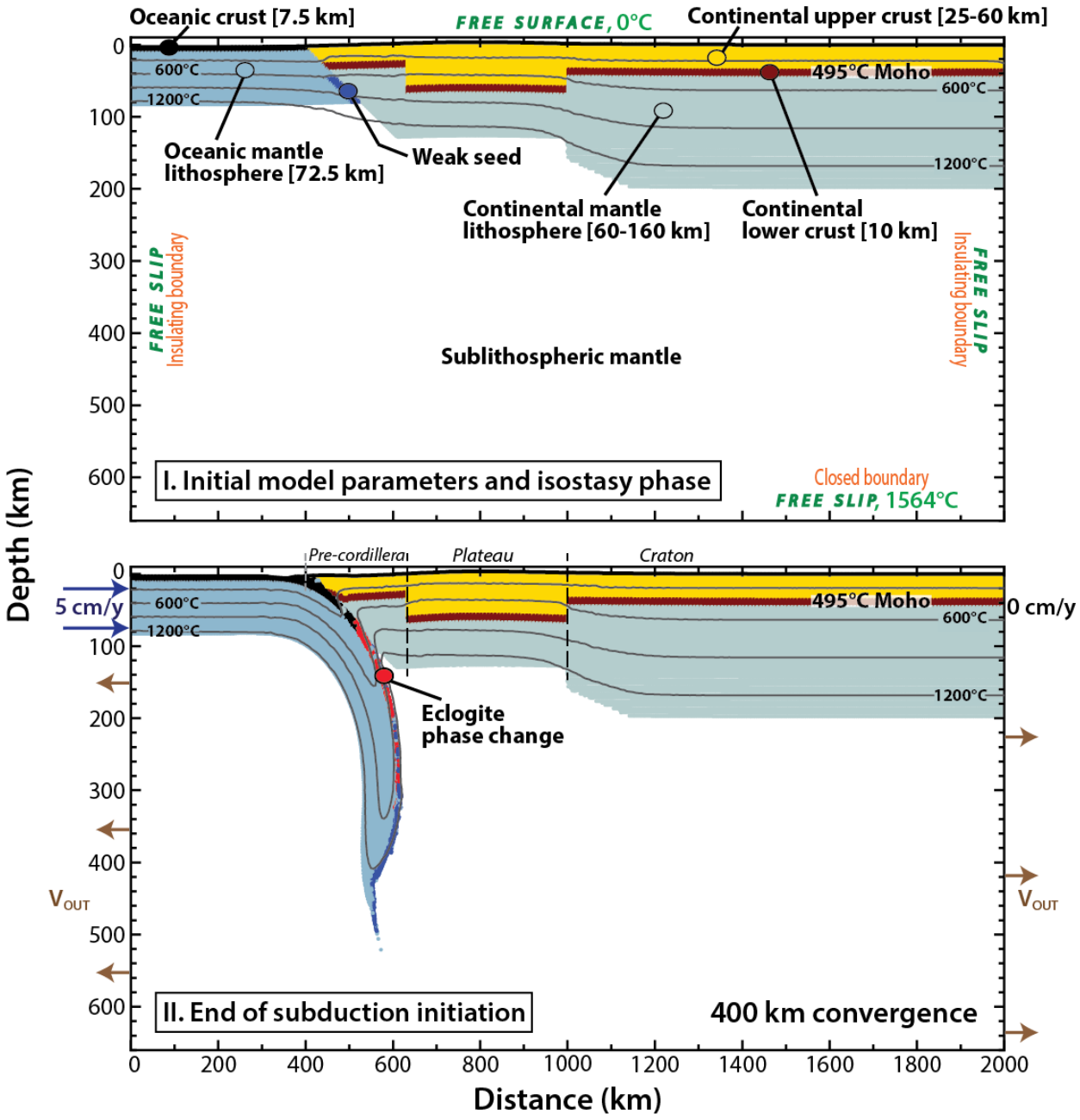

Figure 2.5 Phase1 (initial conditions) and Phase2 (subduction initiation) of the modelling procedure. Thermal-mechanical boundary conditions are shown and remain constant throughout both phases. Subduction initiation is carried out until 400 km convergence is achieved. Material colours are the same as those shown in Figure 2.1.

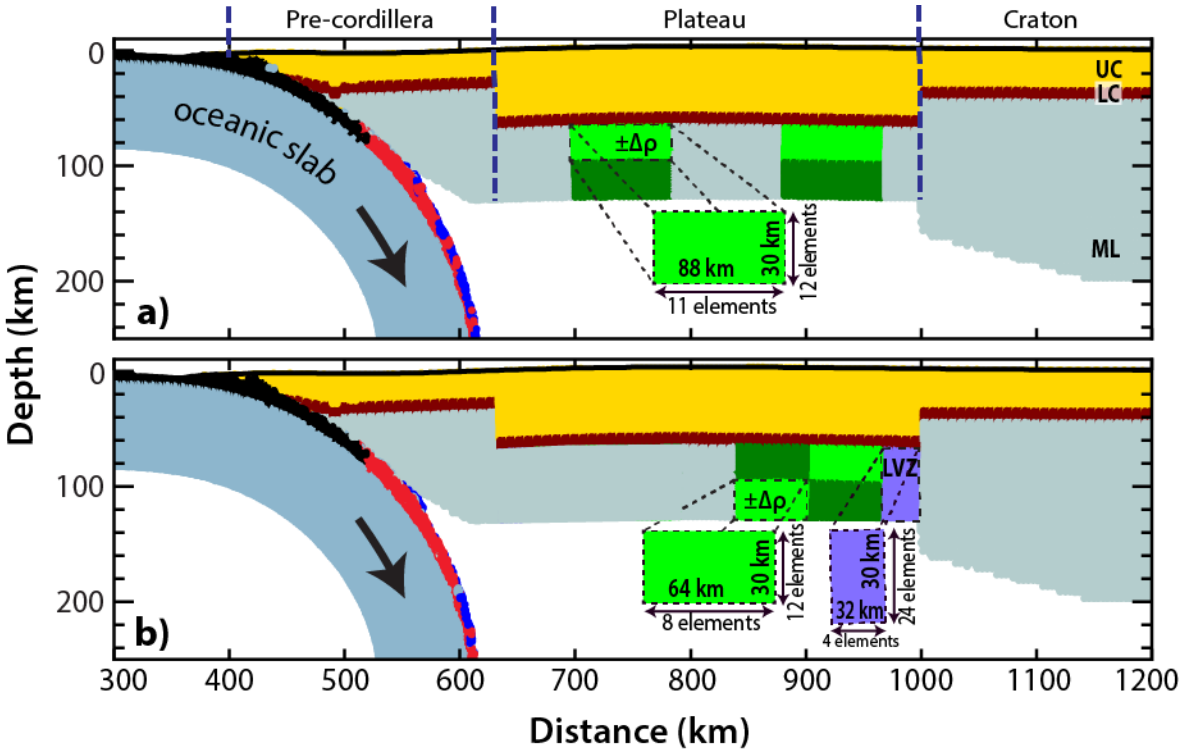

Figure 2.6 Geometries of the dense blocks introduced in Phase 3 of the models, simulating a contrast between mantle lithosphere and sublithospheric mantle material within the system. **a)** Geometry for removal via Rayleigh-Taylor-type instabilities, with roots imposed beneath the lower crust. **b)** Geometry for delamination utilizing the lower crust as the decoupling agent between the crustal and lithospheric mantle material. A low viscosity zone (**LVZ**) is imposed to the right of the dense root, prescribed a value between 10^{19}-10^{21} Pa·s. Each dense root ($\pm\Delta\boldsymbol{\rho}$) is **a)** 11 x 12 elements, **b)** 8 x 12 elements, and any combination of the available four imposed blocks can be activated to test various sizes and magnitudes of density inversions. Refer to Figure 2.1 and 2.5 for colour coding of materials.

beneath the plateau in preparation for Phase 4 (Figure 2.6), and thus the model must adjust to the introduction of these bodies. These dense bodies, referred hereafter as roots, are representative of compositional contrasts stemming from possible melt differentiation or eclogitization of the mantle lithosphere beneath the plateau, of which both have been postulated to trigger lithosphere removal (section 1.4.1). Variations in the model geometry allow for two styles of removal to be tested: Rayleigh-Taylor-type instabilities and delamination. Rayleigh-Taylor- type removal is examined by introducing dense roots beneath the lower crust (Figure 2.6a), spanning 30 km x 80 km each. As described in section 1.4.1, delamination requires a weak zone surrounding the dense body, in order for a coherent slab of

lithosphere to remove. In the models, delamination style removal is investigated utilizing the lower crust as the decoupling agent, as well as imposing a low viscosity zone (LVZ) within the mantle lithosphere (Figure 2.6b). The LVZs are assumed to be a zone prone to ductile flow due to one of the following: an inherited feature from the previous terrane accretion period of the regional history, or a possible lateral compositional variation or thermal contrast as the lithosphere transitions into the stable Precambrian Brazilian craton. Moreover, a weak lower crust may arise from either a felsic composition or hydration of the crust owing to its location above a mature subduction zone (e.g., Krystopowicz and Currie, 2013). Here, the lower crust is sufficiently weakened due to thermal effects as a direct consequence to the pre-thickened upper crust, and, as a result, no imposed low viscosity along the top interface of the mantle lithosphere is required to trigger coherent removal, unlike some previous studies (e.g. Göğüş and Pyslywec, 2008; Wang and Currie, 2015). Delamination is triggered by introducing dense roots beneath the lower crust (Figure 2.6b), spanning 30 km x 64 km, in combination with the LVZ. In the case of both the delamination and RT-type models, the dimensions of the imposed roots result in the formation of perturbation wavelengths typical of lithosphere, which range from 40 – 90 km, and can be increase to 100 to 200 km when temperature-induced density perturbations are disregarded due to the effects of thermal diffusion (e.g. Conrad and Molnar, 1997). As eclogitization likely occurs heterogeneously in nature, the imposition of roots within the mantle lithosphere can represent localized eclogite-rich zones adjacent to unaltered material (Austrheim *et al.*, 1997).

Finally, in Phase 4, the removal of the dense bodies is modelled; this is the main focus of the current study with the previous phases being used to generate the required model geometry (i.e. an active subduction zone and the presence of the dense roots). At this point 450 km convergence has occurred. In Phase 4, a timestep of 1000 years is used, and the models are run for 10 to 20 m.y. In the remainder of this thesis, model times are reported as "elapsed model time", in m.y., relative to the beginning of Phase 4, i.e. 0 m.y. corresponding to the start of Phase 4. This phase of modelling examines the timescales and dynamics of the foundering mantle lithosphere and its effects on the overlying continent (e.g. surface deflection). In order to simulate a wide-ranging of thermal and compositional conditions, as well as assorted degrees of hydration, the viscous strength is varied over a range of f=1 to f=20 (i.e. weak, hot and/or hydrated to strong, cool, dehydrated). This is enhanced by varying the root density, increasing the density contrast with the surrounding mantle by 25 – 150 kg m^{-3}. An additional sensitivity analysis was run specifically on the LVZ in the delamination models over a range of values typical of that observed in the upper mantle (see section 1.3.1), for similar reasons. The imposed

velocities remain the same as in Phase 3, and the activated dense bodies are allowed to influence the system for an extended model runtime. The results of the numerical experiments are presented in the next chapter (Chapter 3).

2.6.2 Model calibration

A sensitivity analysis was carried out in order to determine a basic reference model that emulates the central Andean subduction zone. This reference model serves as the baseline model on which the removal experiments are carried out. Due to the juxtaposition of thick felsic upper crust of the Plateau region (60 km) and the thin upper crust of the Pre-cordillera (25 km) there exists an innate weakness at the boundary between the two regions. This needs to be understood and calibrated to ensure model stability; otherwise plate convergence would localize deformation in this area, which is inconsistent with central Andean tectonics. A series of model tests were run to determine how to stabilize the continent. This was accomplished by altering the initial thermal structure and the thickness layering of the Plateau region, in order to adjust the effective viscosity profile with depth to ensure the interface no longer registered as a zone of weakness. The activation volume of the mantle, which represents the pressure dependence of the thermally activated power-law creep, was also varied over the range of 10 – 15 cm^3 mol^{-1} in order to adjust the viscosity of the deep sublithospheric mantle, and thereby the resistance of the slab as it descended to greater depths. This sensitivity analysis resulted in the 60-10-60 km layering of the upper- , lower- crust, and mantle lithosphere, respectively, in the Plateau region as the final geometries, within the range of thickness values recorded by previous studies (50 – 70 km) (e.g. Beck *et al.*, 1996; Beck and Zandt, 2002; Yuan *et al.,* 2002; Ryan *et al.*, 2016). Additionally, a relatively cool geotherm within the upper crust is favoured in order to establish an upper crust with a minimum effective viscosity of 10^{20} Pa·s at its base (Figure 2.2b). If the effective viscosity is less than 10^{20} Pa·s, a locus of deformation occurs at the interface with the Plateau region and back-arc extension proceeds as the system evolves. Furthermore, activation volume values greater than 12 cm^3 mol^{-1} results in trench advance, and the cannibalization of the Plateau region as the model proceeds. These higher values result in higher effective viscosities for all mantle material, which increases the resisting force against the descending oceanic lithosphere consequently transmitting stress up-dip through the slab, where it too remains highly viscous and strong; as a result, plate convergence causes deformation in the thick (weak) Plateau crust. Therefore, an activation volume value of 10 cm^3 mol^{-1} was favoured. Conversely, adjusting the initial thermal structure to a warmer configuration, at any mantle

activation volume tested, results in back-arc extension and trench retreat. This warmer parameterization also exploits the weak interface created by the thick felsic crust of the plateau. The final result is a stable subduction zone, and the system set-up within the continental reference frame (as discussed in section 2.5.1) with a stationary trench to serve as the baseline model of lithosphere removal experiments. Within this geometry, the dense bodies are introduced and viscosity structure is altered in order to study the dynamics of removal.

2.7 Observations of removal

The geodynamic models serve as a tool to be able to examine the associated surface expressions and resulting seismic structures that arise due to lithospheric removal, reflecting two objectives of this thesis. This make direct use of the free surface boundary condition within the SOPALE code, as well as the thermal and pressure fields calculated at each timestep of the model evolution. This section describes the manner in which the topography was isolated from the models, and the seismic velocity conversion was carried out.

2.7.1 Surface observations associated with lithospheric removal

Surface topography can be a diagnostic feature associated with mantle lithospheric removal (e.g. Göğüş and Pyslywec, 2008). Here, elevation profiles were extracted by isolating the topography created in each model. The upper boundary of the model is stress-free (Figure 2.4), and therefore it moves vertically in response to the underlying dynamics, including both isostatic changes and dynamic effects generated by lithosphere and mantle deformation. At each time step, the elevation profile for the model can be obtained by extracting the position of the top node for each element column within the Eulerian mesh. It is also possible to plot the temporal variation in elevation of a specific point in time, in order to assess the direct evolution of the surface associated with removal. These results are discussed in Chapter 5.

2.7.2 Seismic conversion methodology

2.7.2.1 Perple_X and the extraction of seismic velocities

Seismic velocity in the mantle depends on the local composition, temperature and pressure conditions. As the numerical models provide information about the evolving temperature and pressure fields, it is possible to convert the model results into maps of mantle seismic velocity, to provide a first-

order view of how lithosphere removal may look in seismic tomography images. The method used to carry out this conversion consists of three steps: (1) generation of phase diagrams for a given mantle composition within a chosen range of temperatures and pressures (depths), (2) calculation of the anharmonic (i.e. elastic) moduli for each mineral phase allowing the determination of the corresponding velocities, (3) correction of these anharmonic velocities for the effects of anelasticity (i.e. attenuation). This methodology has been developed through many other studies that have successfully reconciled continental V_p, V_s, shear attenuation, and surface heat constraints (e.g. Goes *et al.*, 2000; Cobden *et al.*, 2008; van Wijk *et al.*, 2008; 2010; Goes *et al.*, 2012).

Steps (1) and (2) are carried out with the Perple_X program package (Connolly, 1990; Connolly and Petrini, 2002). This package employs a Gibbs free-energy minimization algorithm and the mantle mineral parameter database of Stixrude and Lithgow-Bertelloni (2011). Note the same mineral physics data are used in all stages of the forward calculation, from defining the mineral phase relations to computing the seismic velocities. The Stixrude and Lithgow-Bertelloni (2011) thermodynamic database is derived from a largescale global inversion of experimental and first-principles theoretical data; it is appropriate to 400 km depth, and, therefore, well suited to characterize the upper mantle domain of the lithospheric models of this body of work.

Table 2.2: Bulk chemical compositions tested in this study (mol%)

Composition	SiO_2	MgO	Al_2O_3	FeO	CaO	*Reference*
Pyrolite	38.66	48.53	1.80	5.72	3.50	Sun (1982)
Harzburgite	36.22	57.42	0.48	5.44	0.44	Irifune & Ringwood (1987)
MORB	53.82	13.64	10.13	8.80	13.60	Perrillat *et al.* (2006)
Eclogite	52.54	16.31	9.88	6.70	14.58	Griffin *et al.* (1999)
Archon	38.05	56.48	0.49	4.46	0.52	Griffin *et al.* (2009)
Tecton (weight%)	44.83	40.09	3.53	8.19	3.12	Griffin *et al.* (2009)

Six different bulk chemical compositions that are considered (Table 2.2), expressed in terms of relative proportions (in mol%) of the Ca-Mg-Fe-Al-Si system. The mantle, on a gross scale, is believed to be chemically homogenous, with the aforementioned oxides making up more than 98% of MORB-source mantle (pyrolite). As a result, these oxides are also a good representation of the more depleted compositions like harzbugite and those of continental mantle lithosphere (Archon, Proton, etc. from Griffin et al., 2009). Perple_X uses these compositions do determine the mineral phases present at each

pressure-temperature condition. For this study, phase diagrams were created with Perple_X for the temperature range of 0°C (z=0 km) to 1565°C (z=~660 km) and pressure range of 0 GPa to 15.5 GPaa, corresponding to the temperatures and pressures (depths) of the mantle materials in the models. Then, Using the third-order Birch-Murnaghan equation of state (refer to Stixrude & Lithgow-Bertelloni, 2005 for details), the bulk and shear moduli are calculated for each mineral phase. The elastic parameters for each mineral are extrapolated to high temperature and pressures so that they are defined at each point in the phase diagram. This is done within PerPle_X employing a Grüneisen thermal extrapolation in conjunction with a third-order finite-strain equation to extrapolate pressure. The anharmonic seismic velocities are then computed using these elastic moduli, with the overall seismic velocity at each P-T point in the phase diagram given by the weighted average of the constituent minerals. These reported velocities,

$$V_p = \left[\frac{K_B + (\frac{4}{3}\mu_B)}{\rho}\right]^{1/2} \quad \text{Equation 2.14}$$

$$V_s = \left[\frac{\mu_B}{\rho}\right]^{1/2} \quad \text{Equation 2.15}$$

reflect bulk aggregate moduli (K_B and μ_B) and density (ρ) determined utilizing a Voight-Reuss-Hill averaging scheme. Note, at upper mantle conditions, the choice of equation of state has a relatively small effect as long as the extrapolation is consistent with available data at higher pressure and temperature conditions (e.g. Jackson and Ridgen, 1998; Cobden *et al.*, 2008). The reader is directed to Perple_X documentation for more details on these calculations (Connolly 1990; Connolly 2005); (http://www.perplex.ethz.ch).

The final result from Perple_X is a plot of the seismic velocities (V_p and V_s) as a function of pressure and temperature for each mantle composition. These are the velocity at infinite frequency, or the anharmonic velocity. Within the Earth, strain energy is transmitted through the subsurface via seismic waves that propagate by elastic deformation of the rock through which they travel. However, in general, mantle silicates also exhibit a small amount of viscous, or permanent, deformation due to the passing of said seismic waves, resulting in the corresponding reduction of the amplitude of the seismic wave. This seismic attenuation is quantified by the quality factor Q, which is inversely proportional to the attenuation. Moreover, attenuation also affects the velocity of the seismic wave, and, therefore, it is necessary to correct the anharmonic velocities (from step 2) for the effects of attenuation (anelasticity). This correction cannot be neglected as it is strongly temperature dependent, and, therefore, significantly influences seismic velocities in the mantle, especially at temperatures greater than 900 °C

(Karato, 1993). Following Sobolev *et al.* (1996), Goes *et al.* (2000), van Wijk *et al.* (2008, 2010), and Goes *et al.* (2012), a partly empirical attenuation correction is used. This is done first by calculating the S-wave Q, (Q_S, Equation 2.16) and the P-wave Q, (Q_P, Equation 2.19) , and then using these to correct the anharmonic velocities (Equation 2.21). The relevant equations are,

$$Q_s(T,z) = Q_0\omega^a exp\frac{agT_m(P)}{T} \quad \text{Equation 2.16}$$

$$g = \frac{H(P)}{RT_m(P)} \quad \text{Equation 2.17}$$

$$T_m(P) = 1086 - 5.7P_{GPa} + 390lnP_{GPa} \quad \text{Equation 2.18}$$

$$Q_p{}^{-1} = (1-L)Q_K{}^{-1} + LQ_s{}^{-1} \quad \text{Equation 2.19}$$

$$L = \frac{4}{3}(\frac{V_s}{V_p})^2 \quad \text{Equation 2.20}$$

$$V_{anelastic} = V_{anharmonic}[1 - \frac{Q^{-1}}{2\tan(\pi a/2)}] \quad \text{Equation 2.21}$$

where Q_0 is the pre-factor constant, ω is the seismic frequency, a is a constant describing the frequency dependency of attenuation, g is a dimensionless thermal scaling factor that is a function of the activation enthalpy $H(P)$ and the melting temperature $T_m(P)$ (Karato, 1993), P is pressure (in GPa), and T is temperature (°C) at the corresponding depth of P. All corresponding values of these parameters are given in Table 2.3. In particular, the value of the ω parameter is chosen to describe the mean frequency content of the teleseismic data available within the central Andean literature (e.g. Myers *et al.*, 1998; Schurr *et al.*, 2006; Scire *et al.*, 2015). Furthermore, consistent with seismic observations, a bulk attenuation Q_K is assumed to be large and constant (Durek and Ekstrom, 1996; Cammarano *et al.*, 2003). Finally, Equation 2.16 extrapolates to high pressures utilizing the Herzberg *et al.* (2000) anhydrous solidus relationship (Equation 2.18), providing a simple way to parameterize the poorly constrained pressure dependence of the mantle activation volume and enthalpy (Karato, 1993; Sobolev *et al.*, 1996). The corrected velocity is finally computed utilizing Equation 2.21 (Minster and Anderson, 1981), where P-wave and S-wave velocities (V_p and V_s) use the corresponding attenuation correction. Only isotropic velocities are considered here as constraints on anisotropic elastic constraints and anisotropic attenuation are much more limited.

Table 2.3: Anelasticity parameters (Equations 2.16 – 2.21)

Depth	Q_0	a	ω (Hz)	g	Q_K
0-400 km	0.1	0.15	0.4	40	1000

2.7.2.2 Conversion of model domain to seismic velocity structure

The above procedure provides the P-wave and S-wave velocities of the mantle as a function of pressure and temperature. These are then used to convert the thermal and pressure fields from the geodynamic models into plots of seismic velocity. Multiple starting bulk mantle compositions were considered (refer to Table 2.2) in the previous section) based on the material assignments made in the model (refer to section 2.4.1). Griffin *et al.* (1999) and (2009) document the relationship between the mantle lithosphere composition and the tectono-thermal age of the overlying crust, distinguishing the craton (archon composition) as being the most depleted. In order to calibrate the choice of starting compositions for the model domain conversion to seismic structure, the seismic velocity for the six bulk compositions in Table 2.2 were compared at different depths. Figure 2.7 reveals a negligible contrast between the velocities produced by pyrolite, harzburgite, and the assorted mantle lithosphere compositions (Archon, Tecton) for depths within the upper mantle (<400 km). Moreover, previous studies have revealed that differences in seismic velocity for a pyrolytic and harzburgitic compositions are small except where seismically very slow plagioclase is stable (shallower than ~30 km depth) (Cobden et al., 2008; Goes et al., 2012). As a result, to a first-order approximation, the pyrolite composition was chosen for the conversion of the geodynamic models to seismic velocity. Note that Figure 2.7 shows that increased eclogitic content results in increased P- and S- velocities of ~0.4 km s-1 and ~0.12 km s-1, respectively, and its presence would serve to increase the observed seismic velocities. The predicted seismic velocity structures produced from the model output files are discussed in Chapter 5.

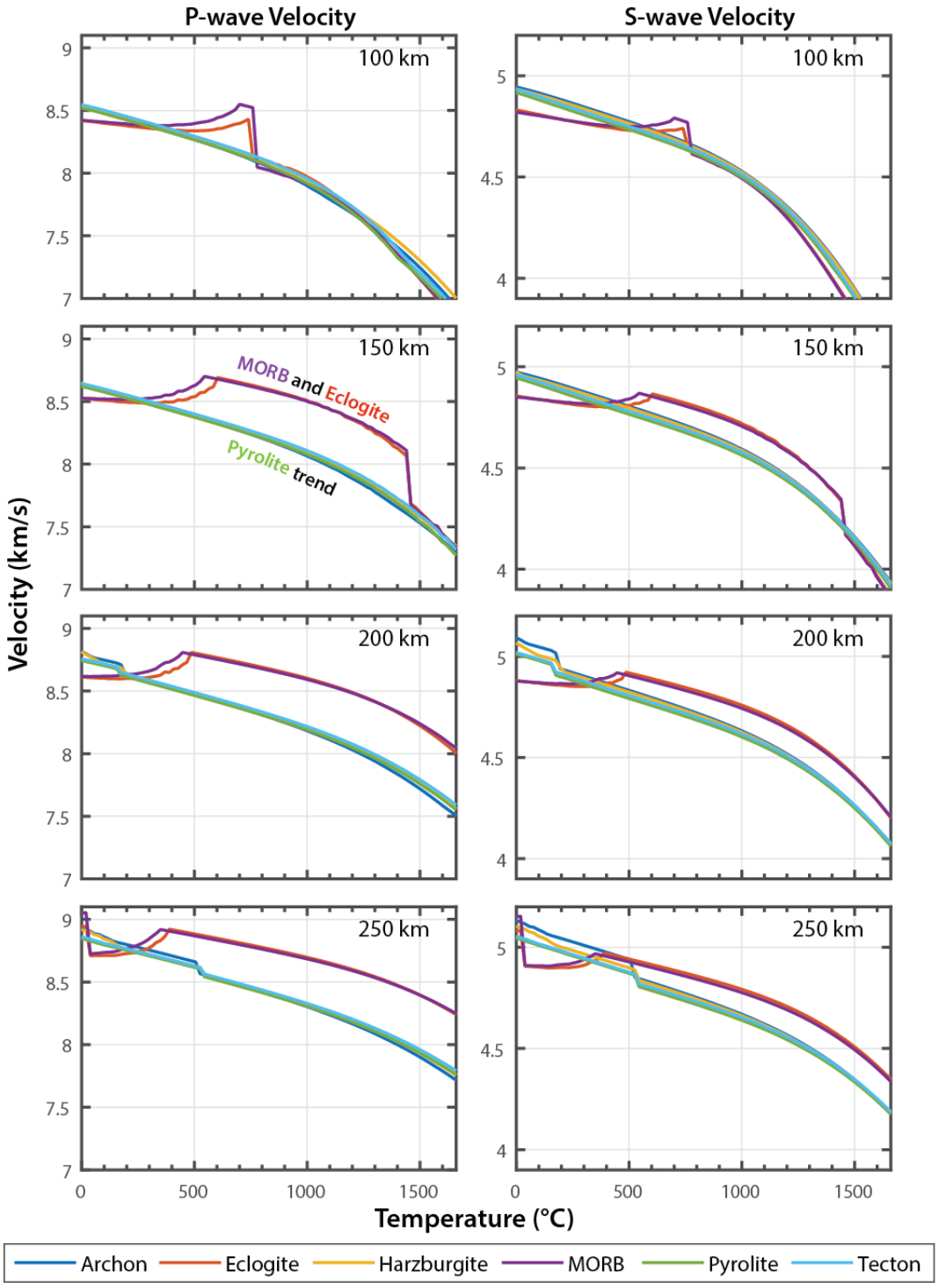

Figure 2.7 Seismic velocities as a function of temperature predicted for six mantle compositions (Table 2.2), at four depths within the upper mantle. To first-order, the mantle material can be represented by a pyrolytic composition, its velocities being comparable with all other mantle candidates. Note that increased eclogitic content results in increased P- and S-velocities of ~0.4 km s^{-1} and ~0.12 km s^{-1}, respectively.

CHAPTER 3 : DYNAMICS OF LITHOSPHERE REMOVAL

3.1 Introduction

Lithosphere removal has been proposed to have occurred within the central Andean system within the last 20 Ma as means to explain the lack of thick mantle lithosphere (and lower crust) beneath much of the Altiplano-Puna plateau, the origin of low velocity zones in the shallow mantle beneath the plateau, and the widespread mafic volcanism at the surface. To date, previous models have provided insights on the mechanism for densification of the lower crust and/or mantle lithosphere within mostly idealized and generic systems, and how this may drive lithosphere removal (e.g. Göğüş and Pyslywec, 2008; Krystopowicz and Currie, 2013; Wang *et al.*, 2015). However, most of these studies do not include the dynamics of an active subduction zone setting.

In this chapter, a series of numerical model experiments are presented that examine the dynamics of mantle lithosphere removal beneath orogenically thickened crust of an active subduction zone. As mentioned in Chapter 2, these experiments are carried out within an established steep-angle (30-40°) subduction zone system, and examine lithosphere removal over a period of 10 – 20 Ma; this is consistent with the timeframe for removal proposed for the central Andes (e.g. Garzione *et al. 2006; 2008*). The removal experiments themselves investigate removal via large-scale delamination (section 3.3) and drip-like Rayleigh-Taylor (RT)-type instabilities (section 3.4), both relying primarily on a density inversion to trigger removal. The parameter space of each removal case is examined in order to better illuminate coupling between processes within the system, and to highlight possible controlling factors of each style of removal (sections 3.3.3, 3.4.3). The intent of this work is not to assess the tectonic or petrological mechanism that leads to the initiation and development delamination or RT-type instabilities, as this has been studied elsewhere (e.g. Morency and Doin, 2004; Krystopowicz and Currie, 2013). Rather, the conditions are set-up to trigger these removal events, and focus is placed on the overall style, timing of removal after the initiation conditions are met (this chapter), as well as the near-surface dynamics (discussed in Chapter 5). Although over 100 models were carried out in this study, only a selection of representative models will be discussed in detail. All model times are reported in m.y. of elapsed model time, where an elapsed time of 0 m.y. corresponds to the beginning of the removal experiments (i.e. the start of Phase 4).

3.2 Reference model

Figure 3.1 shows the evolution of the reference model, *Model Ref1*, in which there is no imposed dense body and no purposeful removal triggered. Continental material remains stationary with little continental lithosphere thinning throughout the majority of the evolution of model, until the last 2 m.y., when the crustal material in close proximity to the trench undergoes pure shear shortening. This results in slight lithosphere thickening and surface uplift by 20 m.y. Continental mantle lithosphere close to the descending oceanic slab is continuously removed, being entrained by the viscous drag created by thermal convective circulation within the sublithospheric mantle (SLM). As the slab shallows, experiencing a decrease in subduction angle from 45° to 30°, and as low pressures are generated by mantle wedge corner flow, ablation increases. Trench position does not shift throughout this shallowing. Finally, the thermal structure experiences some changes coinciding with the shortening during the last 2 m.y. of the 20 m.y. runtime. Of note, the geothermal gradient of the plateau increases, with the Moho of the plateau increasing in temperature from 846°C to 905°C. This is due to conductive heating of the lithosphere by the underlying mantle wedge corner flow.

3.3 Models of delamination removal

3.3.1 Origin of the mantle lithosphere instability

As previous studies have noted, large-scale removal of dense mantle lithosphere via delamination cannot begin until some process breaks through the mantle lithosphere, allowing SLM to contact the crust and mantle lithosphere to peel back as an intact slab (e.g. Schott and Schmeling, 1988; Meissner and Mooney, 1998; Göğüş and Pysklywec, 2008). Possible processes capable of that intrusion include zones of rheological weakness caused by local extension, erosion by mantle plumes, local convective instabilities, or an inherent lateral compositional or rheological variation across the region. The gravitational instability itself can stem from a local perturbation in lithosphere thickness or density structure, especially in close proximity to the transition between the plateau and craton within an orogeny; for example, instability may be triggered by lithosphere thickening due to craton underthrusting (e.g. Sobelev *et al.*, 2006). Additionally, compositional contrasts resulting from inherent heterogeneities or localized eclogitized zones (due to magmatic or metamorphic processes) can generate dense root anomalies that can serve to trigger removal (see section 1.4.1).

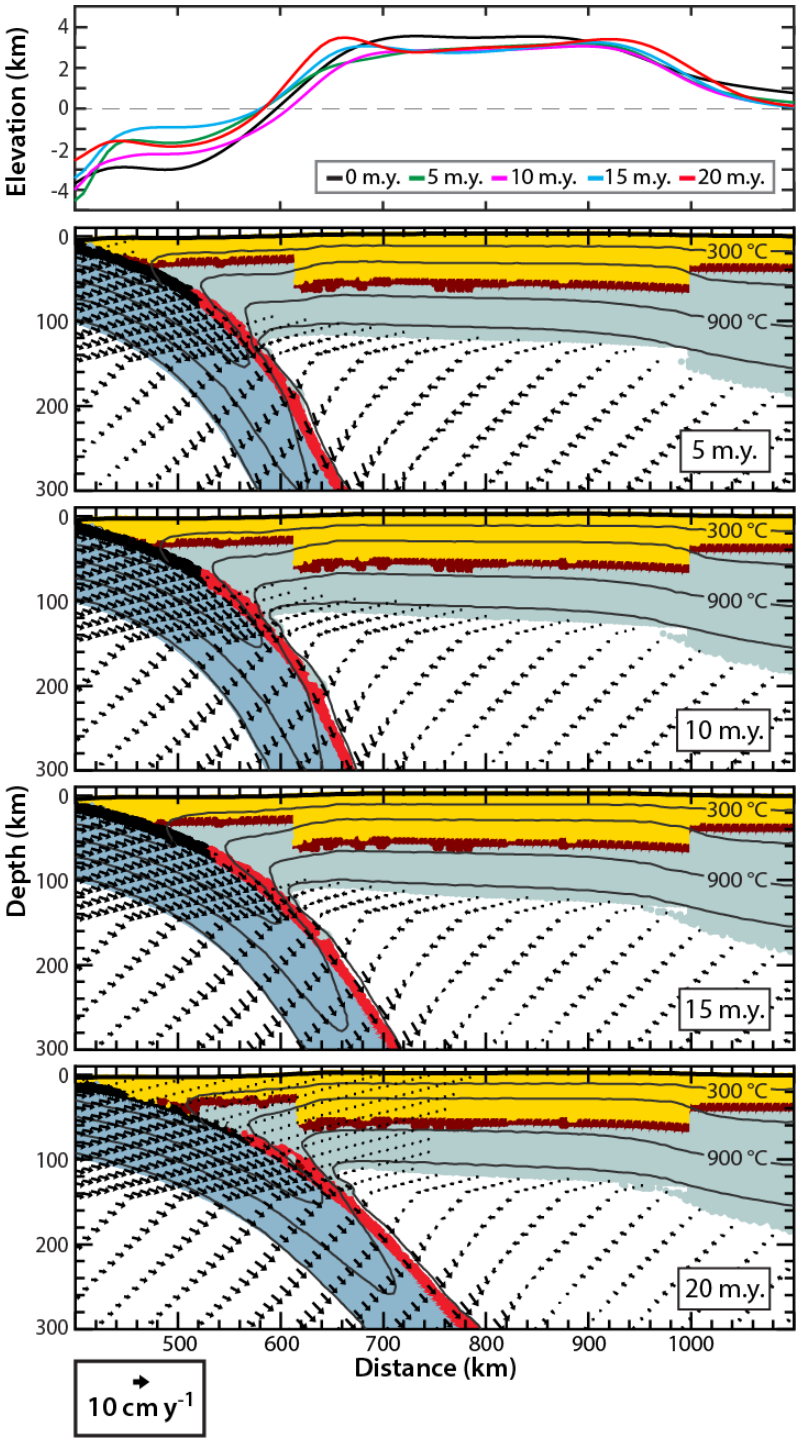

Figure 3.1 Evolution of reference model Ref1, in which there is no dense body placed within the continental mantle lithosphere. Surface elevation and model geometries are shown for 5, 10, 15, and 20 m.y. Material is removed via ablation, with some compressional deformation transmitted inboard in the latter stages of the model, resulting in minor shortening of the Pre-Cordillera region by 20 m.y. Refer to Figures 2.1, 3.2, or 3.8 for material colour coding.

3.3.2 Dynamics of removal

Models within this section are set up in order to induce the coherent large-scale delamination of the mantle lithosphere found beneath the plateau. *Model D1* depicts the style of removal observed as mantle lithosphere peels away from the overlying crust, utilizing both a imposed weak zone and a dense root in order to trigger the instability. *Model D2* provides an example of what the imposed weak zone represents, which simulates delamination that arises due to the removal of a dense root and the subsequent formation of a detachment point induced by the mantle wedge flow. This model serves to constrain the context of the imposed weak zone, and provides an estimation of the time it could take to generate such a zone without imposing it within the model. Finally, *Model D3* depicts a different style of removal exhibited as the strength of the orogen, across the entire extent of the plateau, is varied. Refer to Figure 3.2 for material colour coding as well as the geometries of the imposed roots within each model referred to in this section.

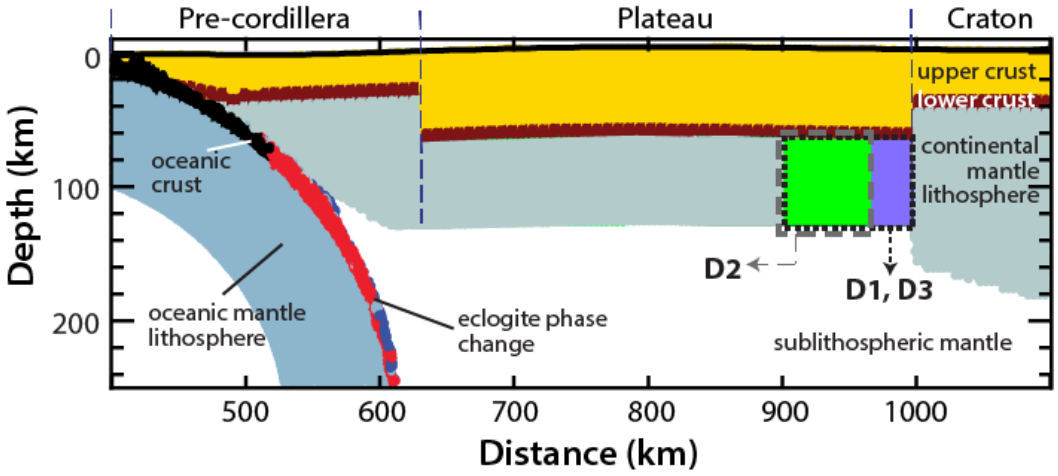

Figure 3.2 Schematic diagram of the subduction system and the imposed root and weak zone geometries for delamination models. *Model D1* and *D3* utilize both a dense root (green) and a low viscosity weak zone (LVZ) (purple). *Model D2* investigates the use of solely imposing a dense root (green) to initiate large-scale delamination.

3.3.2.1 Initiation of delamination via the imposition of a weak low viscosity zone (LVZ)

Figure 3.3 shows *Model D1*, a model of mantle lithosphere delamination. *Model D1* is identical to *Model Ref1* except for the imposition of a 64 km wider dense root that extends the LAB to the base of the mantle lithosphere. The root density is 100 kg m^{-3} greater than the surrounding mantle lithosphere and SLM (3250 kg m^{-3}). Note the dense root has the same scaling factor (refer to section 2.2.1), f=10, as that of the surrounding mantle lithosphere. Removal is triggered by the presence of this dense root in combination with weak material above and at the right side of the dense root. As delamination likely occurs at the Moho (e.g. Bird, 1979), previous studies have imposed a weak zone assigned a constant viscosity layer beneath the Moho interface in order to facilitate removal of the underlying material (e.g. Göğüş and Pyslywec, 2008, Wang and Currie, 2015). In *Model D1*, however, the base of the crust serves as the decoupling agent. Here, the crustal thermal structure (Moho temperature of 807°C) and the imposed rheology (dry Maryland diabase with f=0.1) mean that the deep crust is weak enough to allow decoupling. In addition, a weak zone placed on the right side of the root is needed in order to trigger the initial detachment, referred to hereafter as a low viscosity zone (LVZ). This LVZ may represent an inherited feature from earlier terrane accretion, a lateral compositional variation or thermal contrast as the lithosphere transitions into the stable craton, or a convective instability. It is assigned a constant viscosity of 10^{19} Pa·s in order to induce detachment, this corresponds to the minimal viscosity within upper mantle conditions (10^{19} – 10^{21} Pa·s; Karato, 2010).

The initiation of removal is defined as the time at which the point of detachment with the base of the crust is established (Figure 3.3a). By 2 m.y. of model runtime, the dense root and mantle lithosphere begin to coherently peel away from the overlying crust. Note that the point of detachment migrates towards the trench during detachment; this process is added to by shearing of the mantle lithosphere by mantle wedge flow. Viscous coupling between the root and the adjacent mantle lithosphere initially keeps the dense root attached to the delaminating slab of material, acting to drive its retreat. However, the negative buoyancy exerted by the root overcomes this coupling resulting in the foundering of the root after 3 m.y. Even after this, removal continues uninterrupted owing to the negative buoyancy of the cool mantle lithosphere and the SLM flow. Removal is completed within 7.5 m.y., corresponding to 9 m.y. runtime. The final stage of mantle lithosphere removal is for the material to fall and become entrained by the descending oceanic slab and associated wedge flow; this occurs at 8 m.y.

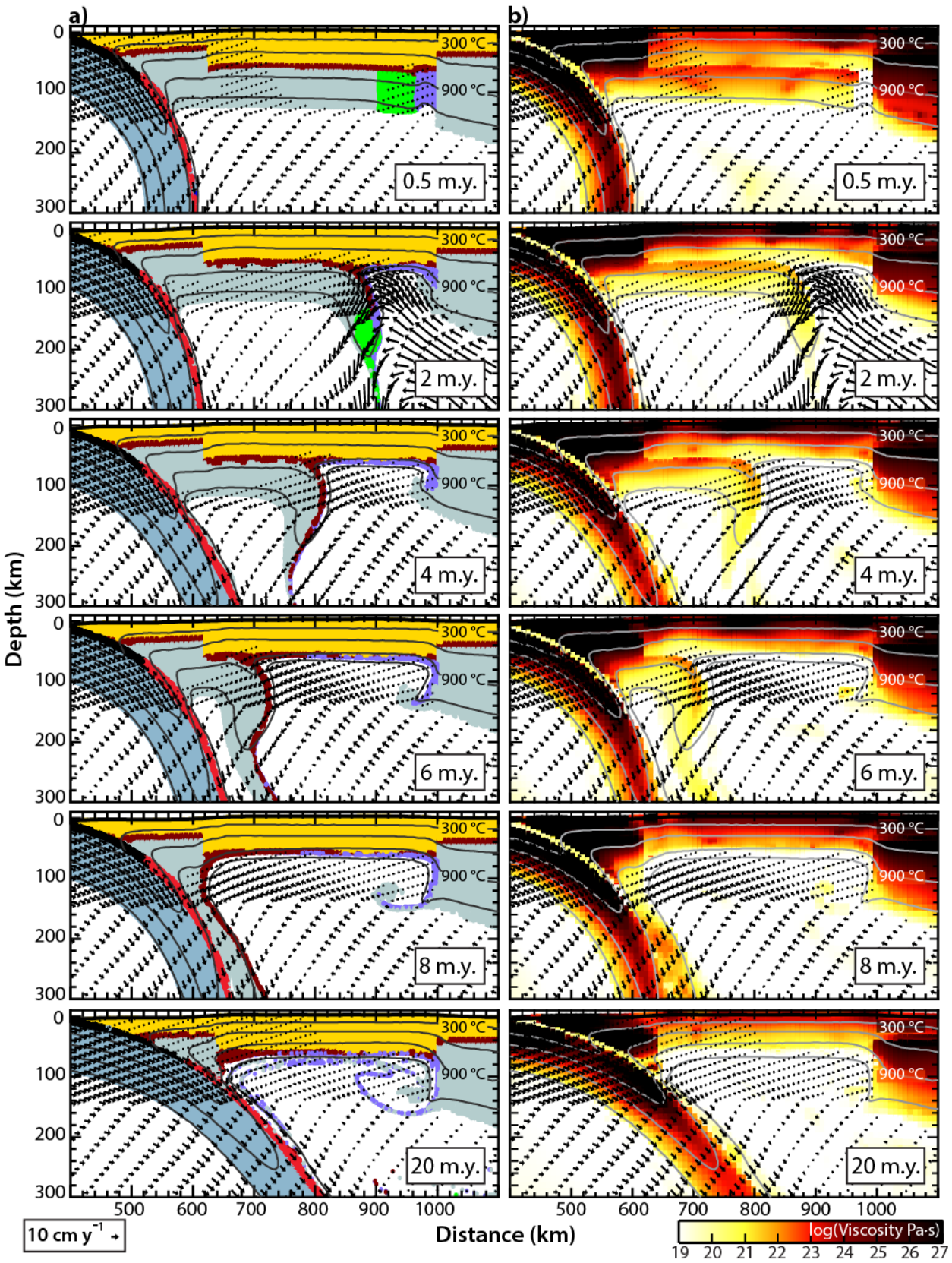
a)
b)
Depth (km)
0
100
200
300
300 °C
900 °C
0.5 m.y.
2 m.y.
4 m.y.
6 m.y.
8 m.y.
20 m.y.
500
600
700
800
900
1000
Distance (km)
10 cm y^{-1}
log(Viscosity Pa·s)
19
20
21
22
23
24
25
26
27

Figure 3.3 Delamination *Model D1*, **a)** model material distribution and **b)** the viscosity structure at the given model times. The removal style is classified as retreating delamination as lithosphere peels away from the crust at a retreating detachment point. After 3 m.y., the dense anomaly detaches, yet removal continues and is completed within 7.5 m.y. period. Refer to Figures 2.1 or 3.2 for material colour coding.

The delamination progresses rapidly, resulting in 300 km wide region of thin lithosphere created between 1.5 and 6 m.y. As the continental lithosphere slab is removed, the SLM upwells and comes into contact with the overlying crust. This results in the heating of the plateau, causing an overall increase to the geothermal gradient of the plateau, and a subsequent decrease in the viscosity structure of the remaining thick felsic crust (Figure 3.3b). This affects the area around the point of detachment as the mantle lithosphere peels away, creating a transient zone of decreased strength that moves trenchward with the migrating detachment point. Following the removal of the mantle lithosphere, the viscosity structure of the crust throughout the plateau section of the model overall decreases after 20 m.y., as a result of heating.

3.3.2.2 Initiation of multi-staged delamination due to a convective instability

As delamination cannot begin until a point of detachment is achieved, models are run to examine the conditions under which delamination may be triggered by a gravitational instability alone. For this, the LVZ in the mantle lithosphere is removed, and instability is initiated by only the presence of a dense root of mantle lithosphere (64 km wide). This dense root can also be considered as a block of perturbed mantle lithosphere that is locally thicker, and therefore has a greater integrated density, than the surrounding lithosphere. In either scenario, the dense region is gravitationally unstable, leading to further thickening over time and then removal as a RT 'drip' (e.g. Houseman and Molnar, 1997; Molnar and Houseman, 2004).In *Model* D2, the root is 125 kg m^{-3} more dense than the surrounding mantle material, and it has a wet olivine scaled (Karato and Wu, 1993) by f=1.

Figure 3.4 shows *Model D2*, which undergoes multiple phases of lithosphere removal: first the dense root is gravitationally removed in a 'drip-like' manner, and this is followed by the formation of a detachment point in the area formally occupied by this root. Therefore, *Model D2* can be thought of as depicting the origins of the weak zone emplaced in *Model D1*, which if not imposed could take millions of years to form as *Model 2* reveals. The initial piecewise removal of mantle lithosphere matures into a point of detachment within 18 m.y., with convective erosion slowly removing enough mantle

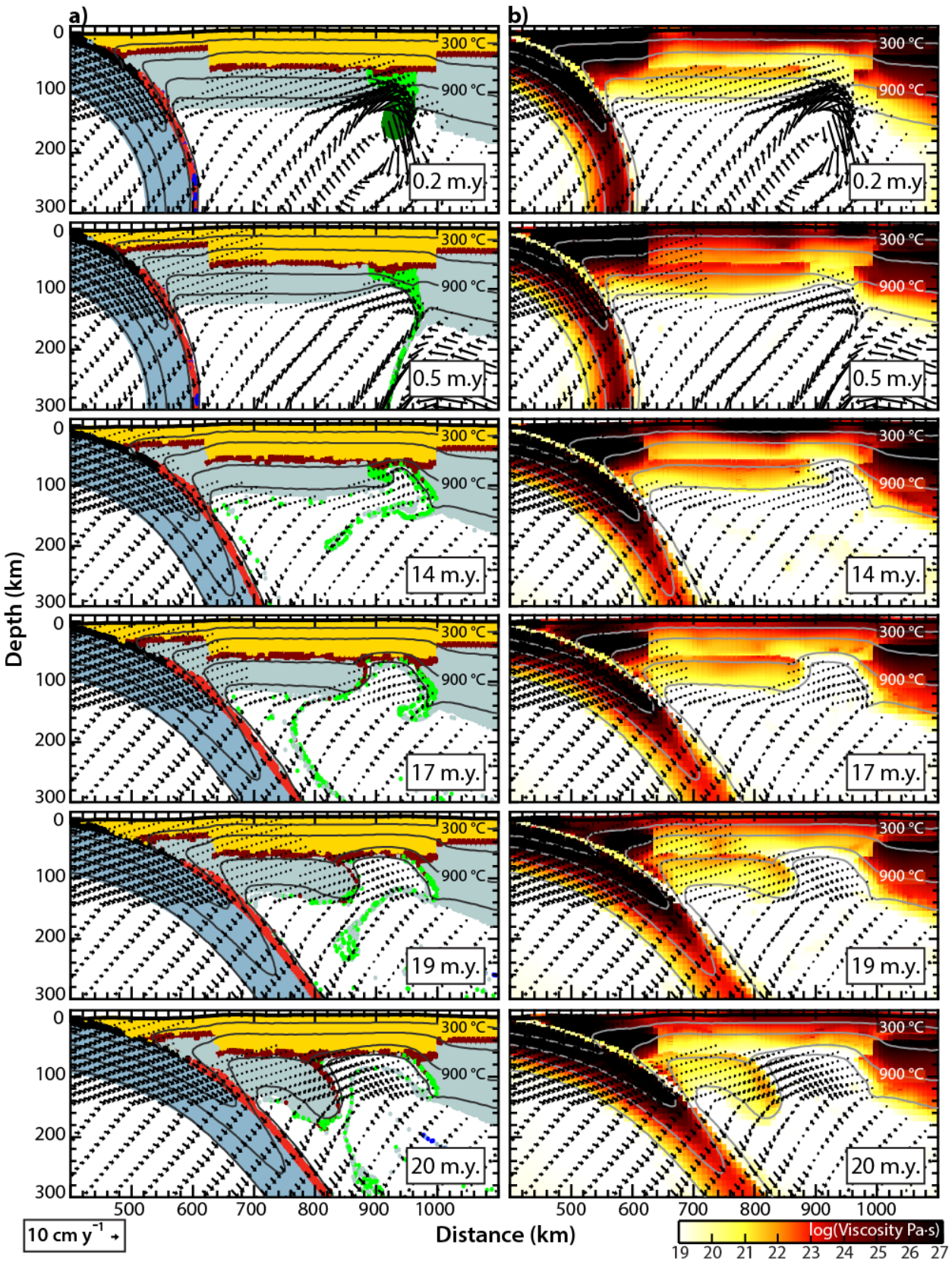
a)
b)
Depth (km)
0
100
200
300
300 °C
900 °C
0.2 m.y.
0.5 m.y.
14 m.y.
17 m.y.
19 m.y.
20 m.y.
500
600
700
800
900
1000
Distance (km)
10 cm y^{-1}
log(Viscosity Pa·s)
19 20 21 22 23 24 25 26 27

Figure 3.4 Delamination M*odel D2*, **a)** model material distribution and **b)** the viscosity structure at the given model times. Removal proceeds in two stages: the imposed column of dense material (3375 kg m^{-3}) is removed in the form of a RT 'drip', followed by convective erosion creating a point of detachment along the base of the Moho that initiates delamination. Removal under these conditions requires more than 20 m.y. years to accomplish. Figures 2.1 or 3.2 for material colour coding.

lithosphere within the gap to create a conduit to the lower crust. This then allows for the remaining mantle lithosphere to coherently decouple through delamination. The style of removal proceeds in a similar retreating style observed in *Model D1*, with the point of detachment migrating trenchward and the advection of SLM to the base of the crust. Notably, the secondary stage of removal is triggered due to circulation within the SLM induced by the descending oceanic slab. Removal of the entire mantle lithosphere under these conditions requires more than 20 m.y. to accomplish, compared to 7.5 m.y. in *Model D1*.

3.3.3 Parameterization of delamination style removal

In order to examine the dynamics of delamination, a number of model experiments are carried out focusing on varying the density and the rheology of the imposed root, the viscosity of the weak zone, and the rheological structure of the orogen. The main purpose is to investigate the timing and dynamics of removal once the prescribed parameter conditions are met, rather than a detailed assessment of the origin of the density anomaly or weak zone.

3.3.3.1 Variations in root density and weak zone (LVZ) viscosity

In order to examine the sensitivity of the density inversion required to initiate removal within the model set-up, a range of imposed root-mantle density contrast values between 0 – 150 kg m^{-3} is tested. The assigned density values reflect the average bulk density of the imposed root, with the increase in density reflecting the presence of an increased amount of eclogite. The density of eclogitized crust can vary with preliminary composition and degree of eclogitization, therefore, an eclogite-mantle density contrast of +150 kg m^{-3} represents ~50 % eclogitization of the impose dense block, assuming a density of mafic eclogite of 3550 kg m^{-3} (e.g. Austrheim *et al.*, 1997; Bousquet *et al.*, 1997). In addition to varying the root density, the viscosity of the LVZ was also change in order to assess how these two

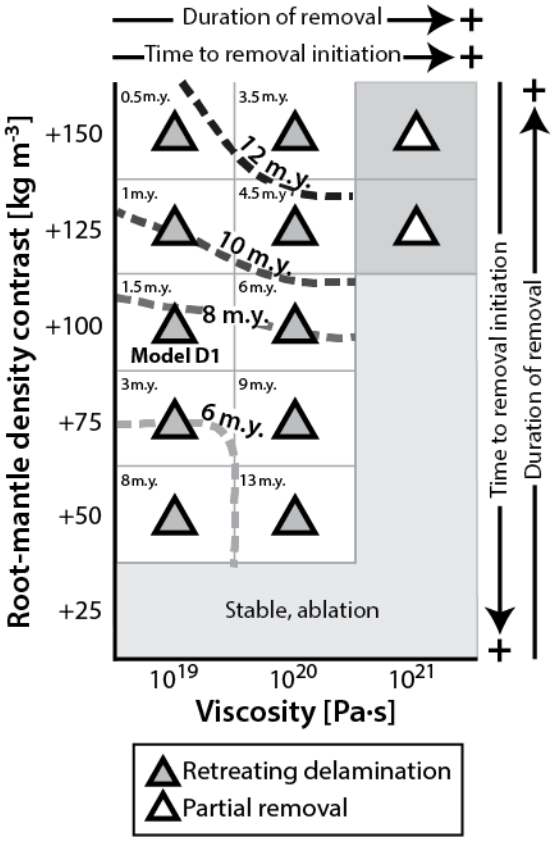

Figure 3.5 Model behaviour for variations in viscosity of LVZ and density contrast between the imposed root and the surrounding mantle. Shaded areas discern different styles of removal, indicated either by the symbol of the block or by its label. The light grey zone represents models that remain stable throughout model evolution (i.e. no delamination, but continued subduction-induced ablation) and triangles are models that exhibit delamination. Dashed lines show the time (since the imposition of the dense anomaly) for removal of >90% of orogen mantle lithosphere. Labels in the top left corner of each box indicates the time (since the imposition of the dense anomaly) for the point of detachment to form.

factors affect the removal process. Figure 3.5 summarizes the results of these parameter tests. In order for a detachment point to develop and delamination to occur, the root must be 50 kg m^{-3} more dense than the surrounding mantle and the LVZ viscosity must be less than 10^{21} Pa·s. At low density contrasts or high viscosities, large-scale removal does not occur and the system remains stable, with minor removal through ablation and small-scale drips occurring at high density contrasts. In models with delamination, the style is consistently a retreating delamination, with the detachment point migrating trenchward and relying on the lower crust as the decoupling agent as depicted in Figure 3.3. The

initiation of removal (i.e. formation of a detachment point) varies from 0.5 to 13 m.y. and the duration of removal varies from 5.5 to 13 m.y. The time of initiation is earliest in models with a dense root and weak LVZ. The rate of the removal is highest when the dense root remains viscously coupled to the mantle lithosphere peeling back; this more readily occurs with lower density contrasts. At higher densities, the root decouples from the mantle lithospheric slab within 3 m.y. of removal onset, causing the integrated negative buoyancy that drives the delamination to decrease. Densities $\geq$125 kg m^{-3} show roots decoupling within less than 1 m.y. after removal is triggered, increasing the duration of delamination to 10 to 13 m.y., compared to 5.5 to 9 m.y. for densities between 50 and $\leq$ 125 kg m^{-3}.

3.3.3.2 Variations in root and mantle lithosphere strength

The composition of the mantle lithospheric varies primarily with the age of the last major tectono-thermal event in the overlying crust (Griffin *et al.*, 1999). As the modern Andean tectonic setting was established in the mid-late Cenozoic, corresponding to the Andes rising significantly in the last 50 – 30 million years (e.g. Isacks, 1988; Allmendinger, 1997; Horton *et al.*, 2001), the mantle lithosphere beneath the plateau and the corresponding orogen is likely only mildly depleted relative to the underlying SLM (Griffin *et al*., 1999; 2009). The viscous strength of the mantle lithosphere is expected to vary with degree of hydration, temperature, and composition, with increased strength for drier, cooler and more mafic conditions. Both the aforementioned as well as compositional heterogeneities may affect the buoyancy and rigidity of the lithosphere of the plateau mantle lithosphere, which will affect removal behaviour. Therefore, the rheological structure of the mantle lithosphere of the orogen/plateau as well as the root was varied, both prescribed the same strength (Figure 3.6). Variations in strength are tested by scaling the base wet olivine rheology (Karato and Wu, 1993) from f=2 to f=20, with the reference model (*Model Ref1*, Figure 3.1) having f=10.

Figure 3.6 summarizes model behaviour for these variations in mantle lithosphere strength (including the root) with varying root density contrasts; all models have a LVZ with a constant viscosity of 10^{19} Pa·s. Models with delamination exhibit retreating delamination, as depicted in Figure 3.3. The duration of removal decreases with increased mantle lithosphere strength, with the most immediate removal occurring within 5 m.y. at f=20. Therefore, removal proceeds more quickly when the mantle lithosphere and the root are both relatively depleted and dehydrated. The duration of removal is shortest for the strongest mantle lithosphere owing to increased viscous coupling between the root and the delaminating slab. The longer time the dense root remains an active participant in driving the

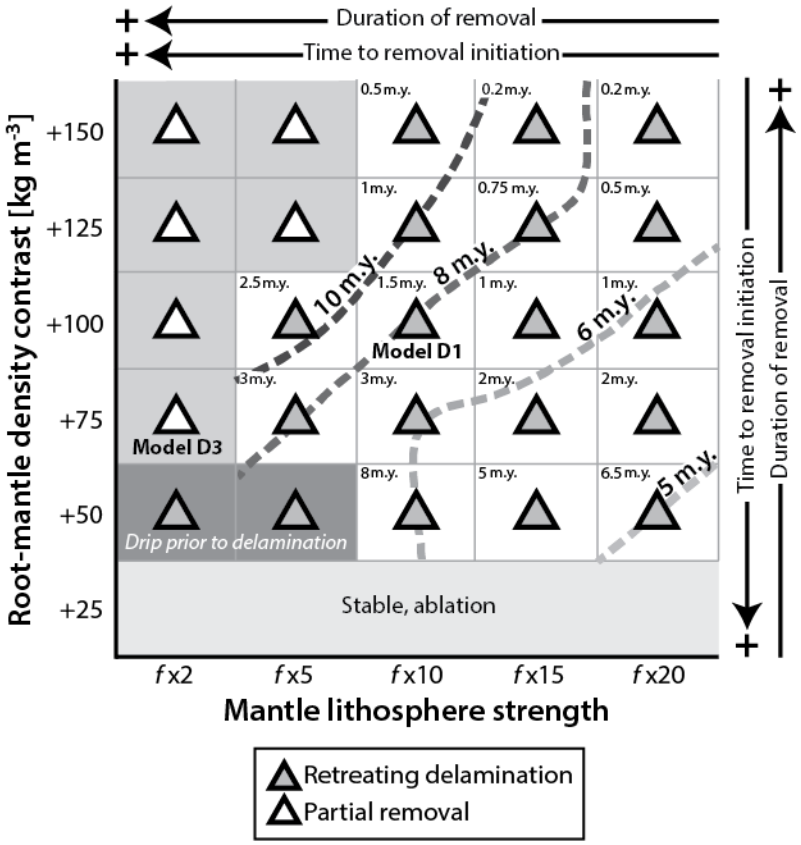

Figure 3.6 Model behaviour for variations in mantle lithosphere strength and density contrast between the root and the surrounding mantle. Shaded areas discern different styles of removal, indicated either by the symbol of the block or by its label. The light grey zone represents models that remain stable throughout model evolution (i.e. no delamination, but continued subduction-induced ablation) and triangles are models that exhibit delamination. Dashed lines show the time (since generation of the point of detachment) for removal of >90% of orogen mantle lithosphere. Labels in the top left corner of each box indicate the time (since the imposition of the dense anomaly) for the point of detachment to form.

retreating delamination (i.e., at higher strength), the shorter the duration of removal becomes. This viscous coupling between the root and surrounding mantle lithosphere is also affected by root density, which is ideally 50 to 100 kg m^{-3} denser than the underlying SLM (see previous section 3.3.2.1).

As mantle lithosphere becomes weaker than *f*=5, removal evolves from coherent delamination to more 'drip-like' detachment of the root and partial removal of the mantle lithosphere as a whole. Figure 3.7 shows *Model D3*, which exhibits this partial removal of the mantle lithosphere. The decreased strength of the mantle lithosphere means that lower crust decoupling layer and the LVZ are not clear zones of

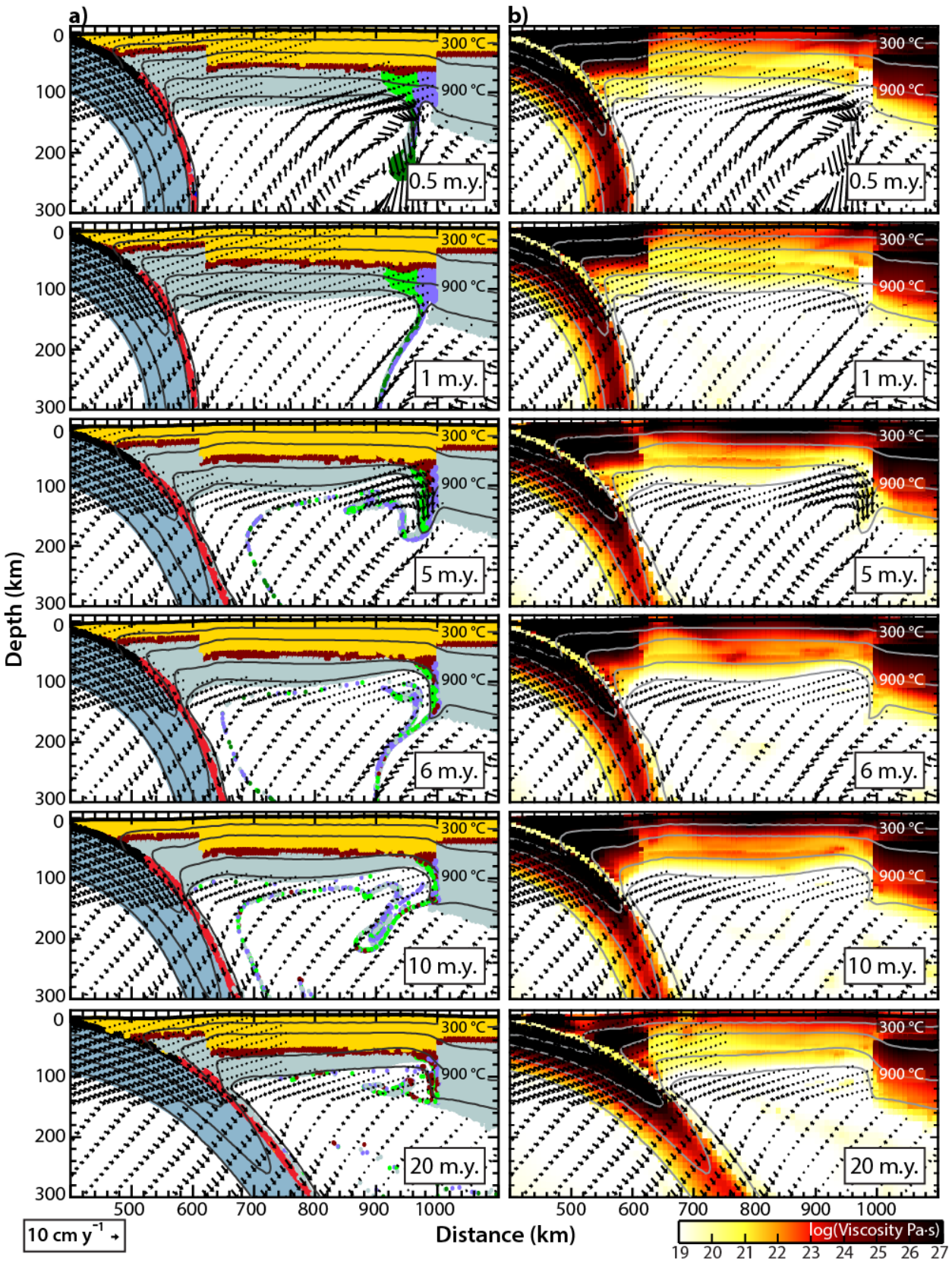
a)
b)
Depth (km)
0
100
200
300
300 °C
900 °C
0.5 m.y.
1 m.y.
5 m.y.
6 m.y.
10 m.y.
20 m.y.
500
600
700
800
900
1000
Distance (km)
10 cm y^{-1}
log(Viscosity Pa·s)
19 20 21 22 23 24 25 26 27

Figure 3.7 Delamination *Model D3*, **a)** model material distribution and **b)** the viscosity structure at the given model times. Removal proceeds in a 'drip-like' detachment of the dense root and partial removal of the mantle lithosphere as a whole. This occurs in response to the weaker overall rheology structure assigned to the mantle lithosphere beneath the plateau. This creates a wedge like geometry of mantle lithosphere within the span of 6 m.y. Figures 2.1 or 3.2 for material colour coding.

weakness, as seen in *Model D1* (Figure 3.3b). In addition, the weaker rheology leads to foundering of the dense anomaly. These two effects mean that a coherent slab of delaminating lithosphere does not readily form.

It is important to note that models that exhibit large-scale removal do so through trenchward retreating delamination. Two styles of delamination were identified by Krystopowicz and Currie (2013), occurring when the strength of the mantle lithosphere was varied. The stationary delamination style is not observed in the models in this study despite testing a wide range of mantle lithosphere strengths. Krystopowicz and Currie (2013) focused on delamination triggered by lower crustal eclogitization in a compressional system lacking an active subduction zone. In contrast, the models here include subduction and the associated mantle wedge flow. It is interpreted that within the presence of corner wedge flow and without a mechanism to readily decouple the mantle lithosphere beneath the plateau from the adjacent material, it is difficult to induce stationary delamination.

3.4 Models of Rayleigh-Taylor-type (RT) removal

3.4.1 Origin of the mantle lithosphere instability

The next set of models investigates the alternate style of lithosphere removal: Rayleigh-Taylor-type (RT) instabilities. Such instabilities require no specific structural weakness beyond a dense region imposed within the lithosphere that is gravitationally unstable with respect to the underlying mantle and possess a rheology conducive to flow. These models include high density material located in the mantle lithosphere of the orogen in order to drive gravitational instabilities. As discussed in Chapter 1 (section 1.4.1), these density anomalies can occur in the mantle lithosphere due to melt differentiation, an eclogite phase change with increasing temperatures and pressures, or a lithospheric thickness perturbation.

3.4.2 Dynamics of removal

Model RT1 and *RT2* investigate the RT removal style of by imposing a singular root beneath the lower crust at varying distance from the subducting slab. *Model RT3* and *RT4* provide examples for what occurs if the base of the mantle lithosphere beneath the imposed root is locally perturbed by SLM flow or through locally higher temperatures associated with magma emplacement; this is done by assigned a weaker rheology to the mantle lithosphere immediately below the root. *Model RT5* and *RT6* impose two roots beneath the lower crust and examine the coupled feedback between the roots and its implication for lithospheric removal on a large-scale. Similarly, *Model RT7* and *RT8* impose multiple roots, this time spanning the entire of the mantle lithosphere. Refer to Figure 3.8 for material colour coding as well as the geometries of the imposed roots within each model referred to in this section.

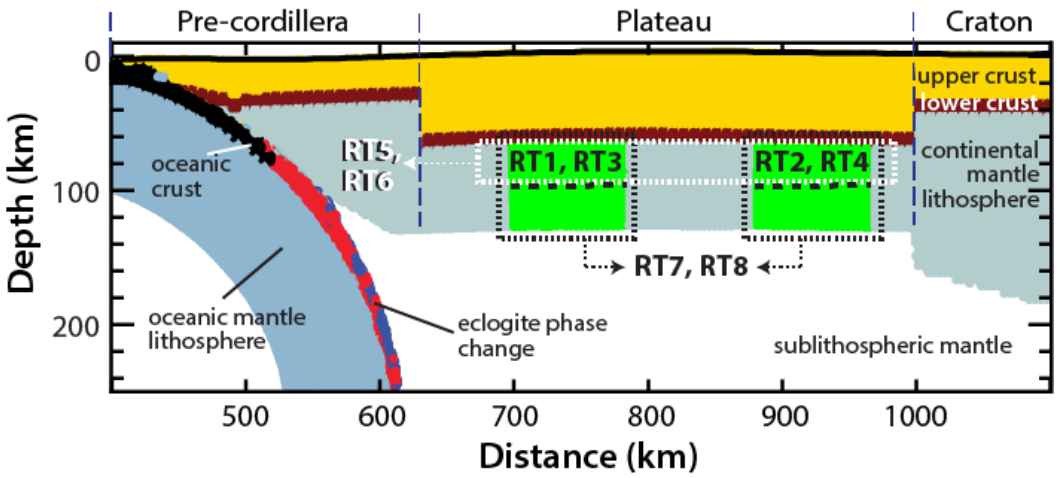

Figure 3.8 Schematic diagram of the subduction system and the imposed root geometries for Rayleigh-Taylor-type models. *Model RT1 – RT4* impose a singular root (green) either in close proximity to the subducting slan or adjacent to the craton boundary. *Model RT5* and *RT6* impose multiple roots (green) beneath the lower crust with varying rheologies. Finally, *Model RT7* and *RT8* impose multiple roots (green) that span the entire thickness of the mantle lithosphere.

3.4.2.1 Removal dynamics of a single root

Figure 3.9a, and b depicts *Model RT1* and *Model RT2*, respectively, with both models investigating RT removal. Both *Model RT1 and Model RT2* are identical to the reference model, *Model Ref1* (Figure 3.1), except for the imposition of a dense root anomaly beneath the Moho interface. This block is 100 kg m^{-3} greater than the surrounding mantle material (3250 kg m^{-3}), and spans 64 km in width while extending half way through the mantle lithosphere (70 km to 100 km depth). Note the dense root in these models are both assigned the rheology of wet olivine (Karato and Wu, 1993) with f=1 reflecting conditions of increased hydration, temperature, or volatiles; this approximates the expected weaker conditions associated with magmatic processes. The rheology of the root controls the onset of instability, with stronger roots resulting in later initiation time (Currie *et al.*, 2015; Wang and Currie, 2015). *Model RT1* highlights dynamics that may occur as a high-density root forms below the frontal arc of a Cordilleran subduction system, whereas *Model RT2* has a root closer to the craton which is assumed to be the product of a lateral heterogeneity in composition, back-arc magmatism (Coira et al., 1982; Allmendinger *et al.*, 1997; Kay and Coira, 2009; Salisbury *et al.*, 2014), or an inherited region of possible magmatic residuum formed during an earlier phase of low-angle subduction (DeCelles *et al.*, 2009; Ducea *et al.*, 2015). In both models, removal of the root is driven by the local gravitational instability generated by the density contrast between the root and the underlying mantle material.

The initiation of root removal is defined as the time at which the base of the root region is perturbed from a planar horizon. This is achieved more rapidly in *Model RT1* (Figure 3.9a), owing to the in influence of subduction-induced mantle wedge flow. Although mantle flow does not make direct contact with the root, the shearing of the base of the mantle lithosphere acts to perturb the entire column. This is a similar observation as that discussed in Currie *et al.* (2015), which focused on foundering of arc-related RT-type removal along the base of the mantle lithosphere. In *Model RT1,* the root begins to descend 1 m.y. after its imposition, with the drip becoming noticeable at 5 m.y (Figure 3.9a). As the instability grows, it continues to be viscously coupled with the surrounding mantle lithosphere causing the root to entrain the surrounding material. Once the decent of the root is triggered, root removal occurs rapidly – within 2 m.y. Once the root begins to 'drip', it becomes entrained by mantle wedge flow and is carried toward the subducting slab. After 7 m.y., the root is fully removed and the subsequent influx of SLM into the opening causes local heating of the continent. This opening creates its own convection cell 8 m.y. after the removal of the root, resulting in convective erosion and the reshaping of the opening into a more rectilinear shape.

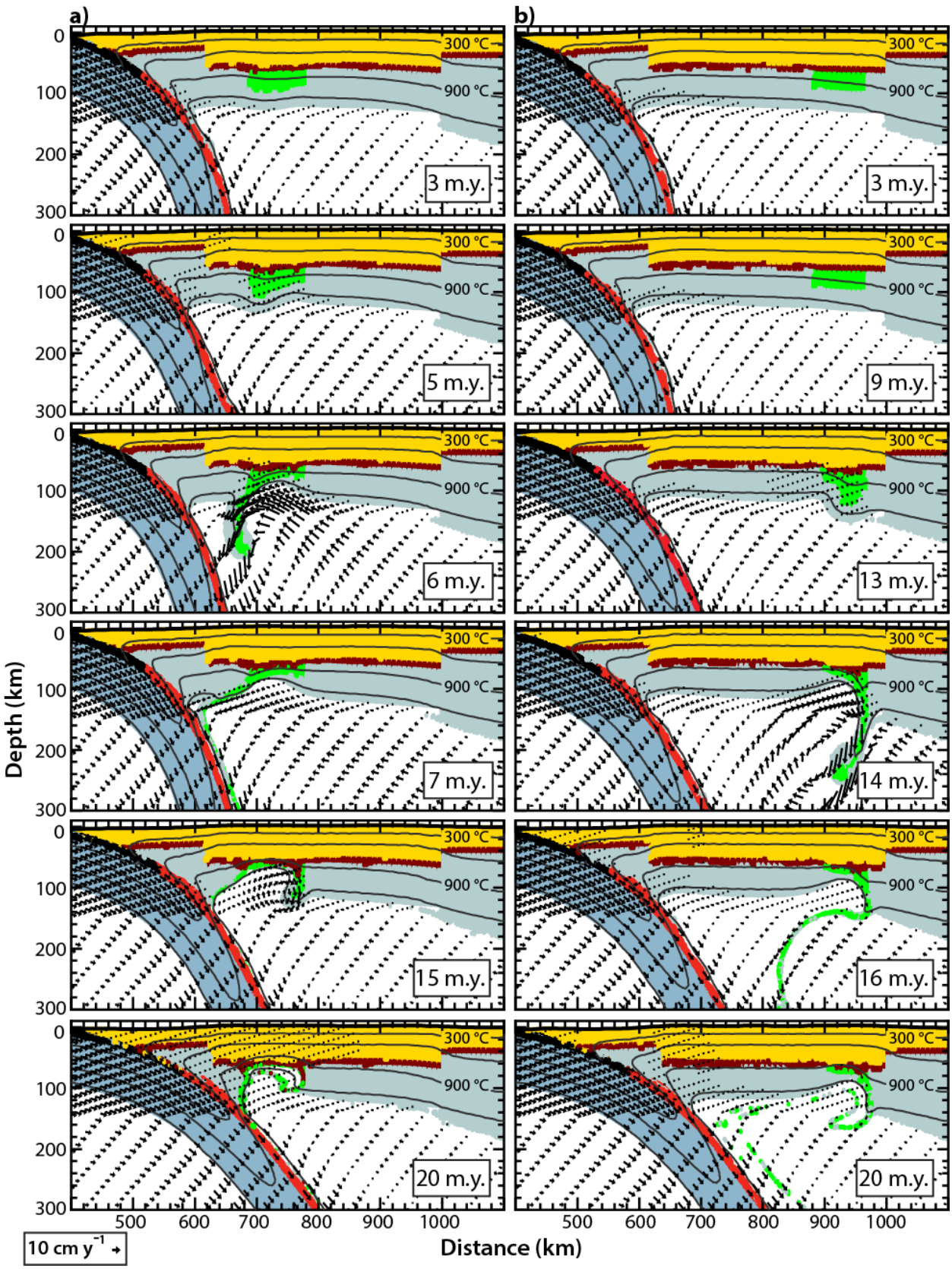
a)
b)
Depth (km)
0
100
200
300
300 °C
900 °C
3 m.y.
5 m.y.
6 m.y.
7 m.y.
15 m.y.
20 m.y.
9 m.y.
13 m.y.
14 m.y.
16 m.y.
500
600
700
800
900
1000
Distance (km)
10 cm y^{-1}

Figure 3.9 Model material distribution for **a)** *Model RT1* and **b)** *Model RT2* at the given model times. Root removal proceeds in a 'drip-like' manner, with *Model RT1* initiating more rapidly due to the influence of mantle wedge flow. Both 'drips' entrain adjacent mantle lithospheric material, creating discrete gaps within the mantle lithosphere of the orogen. Refer to Figures 2.1 and 3.8 for material colour coding.

In comparison, removal occurs much more slowly in *Model RT2*, in which the root is placed further in the back-arc (Figure 3.9b). Due to its closer proximity to the craton, its removal is not initially triggered by mantle wedge corner flow in the same way observed in *Model RT1*. In *Model RT2*, the root begins descending 8 m.y. after its imposition, 7 m.y. later than its counterpart in *Model RT1*, and becomes noticeable at 13 m.y. Viscous coupling causes the root to entrain surrounding mantle lithosphere as it falls, with the majority of the root removed by 16 m.y. The 'drip' creates a secondary cell of circulation within the SLM, rotating in the opposite direction to the mantle wedge causing the 'drip' to be pushed along the edge of the cratonic mantle lithosphere. Once removal of the root is triggered, it occurs rapidly – within 2 m.y. However, subsequent advection of SLM is not as vigorous as in *Model RT1*, and the opening that removal of the root creates remains relatively unchanged.
Similar initiation trends based on root placement can be observed in *Models RT3* and *RT4*, and are summarized in Figure 3.10a and b, respectively. These models are identical to *Model RT1* and *RT2,* however, they include a weaker rheology for the mantle lithosphere underlying the imposed root, f=1 (compared to f=10 in *Models RT1* and *RT2*). The weaker rheology means that the base of the mantle lithosphere is more readily perturbed by the subduction-induced flow within the SLM. Removal of the proximal root is initiated first (*Model RT3*, Figure 3.10a), triggered after 2 m.y. after the imposition of the root. The root perturbation is sheared by the subduction-induced flow, resulting in the removal of the base of the mantle lithosphere beneath the root to be removed in the combined style of ablation and 'drips'. The majority of the imposed root is not entrained, and begins to form a secondary perturbation along its exposed base at 5 m.y. The root is not removed coherently, as was observed in *Model RT1*, but is removed within two stages of 'drips': the first stage occurring by 6 – 7 m.y., and the secondary stage induced at 14 – 15 m.y. by a secondary cell of mantle flow within the empty site of the trenchward root. The secondary drip is formed by 15 m.y. and continues to reshape the void created by the removal of the root into a more rectilinear shape by 20 m.y.

In *Model RT4*, in which the root is in the back-arc region, the perturbation that forms beneath the root develops with little influence from mantle flow (Figure 3.10b). Removal of the root occurs once

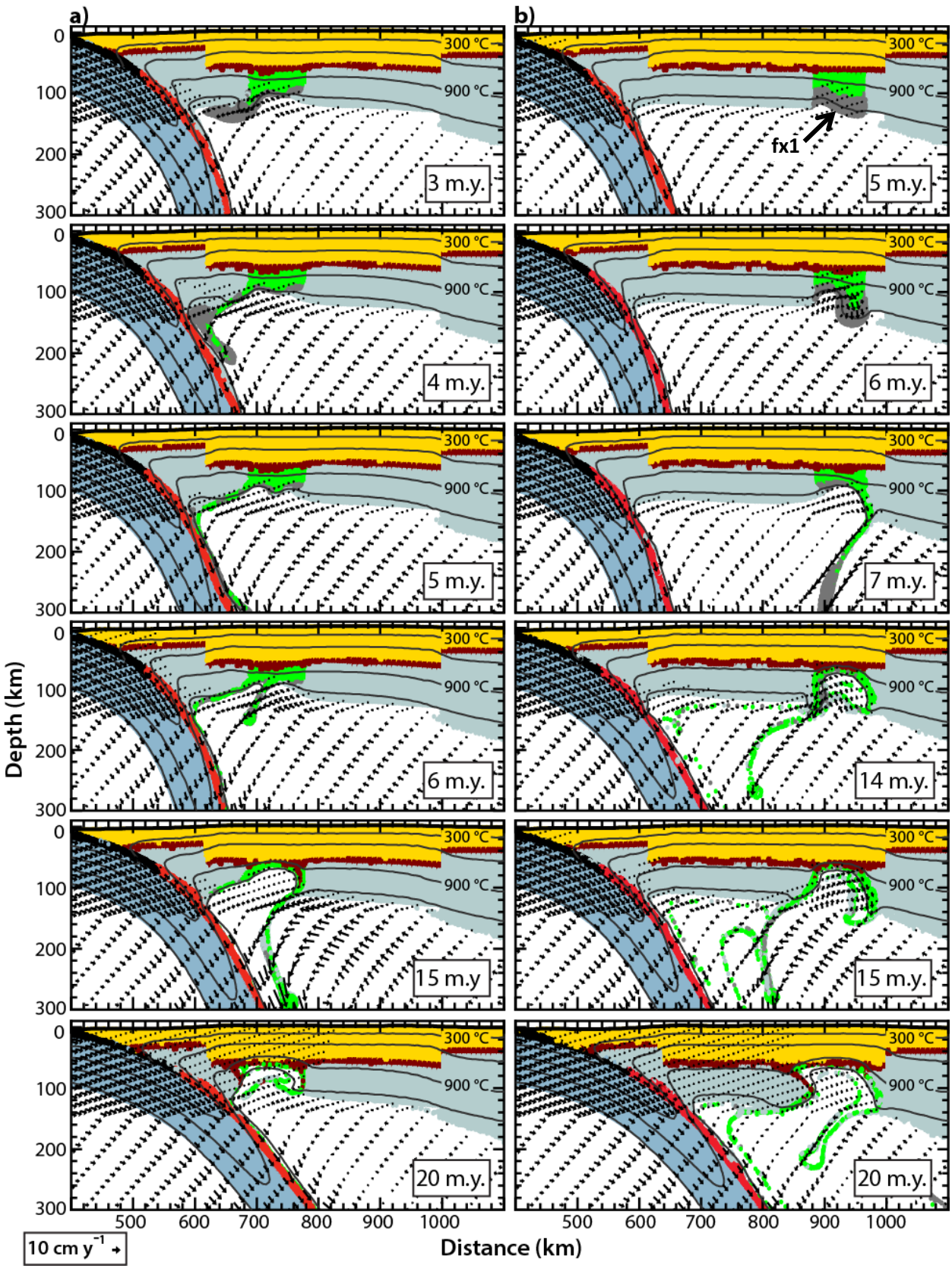
a)
b)
300 °C
900 °C
fx1
3 m.y.
5 m.y.
4 m.y.
6 m.y.
5 m.y.
7 m.y.
6 m.y.
14 m.y.
15 m.y
15 m.y.
20 m.y.
20 m.y.
Depth (km)
0
100
200
300
500
600
700
800
900
1000
Distance (km)
10 cm y^{-1}

Figure 3.10 Model material distribution for **a)** *Model RT3* and **b)** *Model RT4* at given model times. In both models, the underlying mantle lithosphere (dark grey) beneath the imposed root is reduced in strength by rheology scaling. Root removal proceeds in a 'drip-like' manner, with *Model R3* initiating more rapidly due to the influence of mantle wedge flow. However, removal does not result in viscous coupled entrainment of adjacent material. Refer to Figures 2.1 and 3.8 for material colour coding.

the weak underlying mantle lithosphere material is gravitationally removed, and this results in the creation of a conduit for the 'drip' removal of the root itself along its cratonward edge. In contrast to *Model RT3*, removal occurs continuously, between 7 and 14 m.y., with constant removal triggered by local SLM circulation. As in the previous models, the site of the root is reshaped into a more rectilinear shape, and, in particular for *Model RT4*, a point of detachment along the Moho is formed conducive to subsequent delamination. However, as in section 3.3.2.2, removal of the entire mantle lithosphere under these conditions requires more than 20 m.y. to accomplish.

3.4.2.2 Summary of RT results – Singular roots

Overall *Model RT1* and *RT2* exhibit the gradual instability of the dense roots resulting in the local perturbation of the base of the mantle lithosphere, the wavelength of which measures ~64 km. This results in a differential pressure profile along said interface, and removal proceeds due to a release of potential energy culminating in a gravitational 'drip'. In both model, the descending root alters the flow patterns in the surrounding mantle, with subsequent secondary convective cells forming in the voids created by the removed material. Both roots have high viscous coupling to the surrounding material, resulting in their coherent removal. In general, decreasing the strength of the underlying mantle lithosphere (*Models RT3* and *RT4*, Figure 3.10) causes its base to be more readily perturbed by the subduction-induced mantle wedge flow. The amplitude of this perturbation is exaggerated in comparison to *Models RT1* and *RT2* (Figure 3.9), as the mantle lithosphere beneath the root is weaker. This exaggerates the gravitational instability along the base of the lithosphere, causing the removal of the deep lithosphere prior to removal of the dense root, and in some cases, exposing the base of the root directly to the SLM flow (*Model RT3*). Increasing the distance of the root from the descending oceanic slab decreases the shearing exerted on the root; however, once a gap is produced within the mantle lithosphere, mantle flow is sufficient enough to begin to decoupling the remaining mantle lithosphere as a coherent piece along the Moho, requiring longer than 20 m.y. to complete. Ultimately,

the position of the root relative to the descending slab controls the timing of removal initiation, which decreases for roots closer to the slab, and the strength of the underlying lithosphere mantle material affects the style of removal, resulting in large drips with increased strength.

3.4.2.3 Removal dynamics of multiple roots

Figure 3.11a and b depicts *Model RT5*, and *RT6,* respectively. Both *Model RT5* and *RT6* are identical to the reference model, *Model Ref1* (Figure 3.1), except that a dense root is placed beneath the Moho. This block is 100 kg m^{-3} more dense than the surrounding mantle material (3250 kg m^{-3}), and extends halfway through the mantle lithosphere (70 to 100 km depth). The roots in *Model RT5* and *RT6* have the rheology of wet olivine (Karato and Wu, 1993) scaled by f=10 and f=1, respectively. These models serve to compare the effects of root strength, with *f=10* used to demonstrate a strong, possibly more dehydrated, root. Moreover, these two models are set-up to examine the dynamics of two dense roots beneath the orogenically thickened crust. These models thus expand upon the dynamics of single roots examined previously. Note for ease of reference, the root closest to the descending slab (x=730 km) is referred to as the proximal root, with the root closest to the craton (x=930 km) called the distal root.

Model RT5 (Figure 3.11a) exhibits no complete removal, as the increased strength of the root resists instability. Notably, even the perturbation of the base of the mantle lithosphere by the mantle wedge corner flow does not perturb the proximal root as was observed effective in *Model RT1*. Only after 20 m.y., when the model exhibits some shallowing in the subducting slab, does the proximal root begin to show destabilization. Contrastingly, *Model RT6* (Figure 3.11b) shows that same proximal root beginning to descend 5 m.y. after its imposition, just as in *Model RT2*. *Model RT6* also shows the root pulling adjacent mantle lithosphere as it removes as a 'drip'. The root is entrained by the mantle wedge flow as it descends, flowing along the subducting slab. The proximal root is removed within 2 m.y. once triggered, corresponding to 7 m.y. after the imposition of the root. Removal of the proximal root in turn initiates the removal of its distal counterpart, occurring 10 m.y. after the imposition of the both roots. The distal root is destabilized due to the combined effects of the influx of SLM within the empty proximal site and its own negative buoyancy. The distal root is removed within 3 m.y., and is replaced with localized lower crustal thickening. Due to continued secondary SLM flow cell within the proximal root site, a netward cratonward force is exerted on the remaining mantle lithosphere. As a result, no region of thinned lithosphere is created at the site of the distal root, while the proximal site undergoes

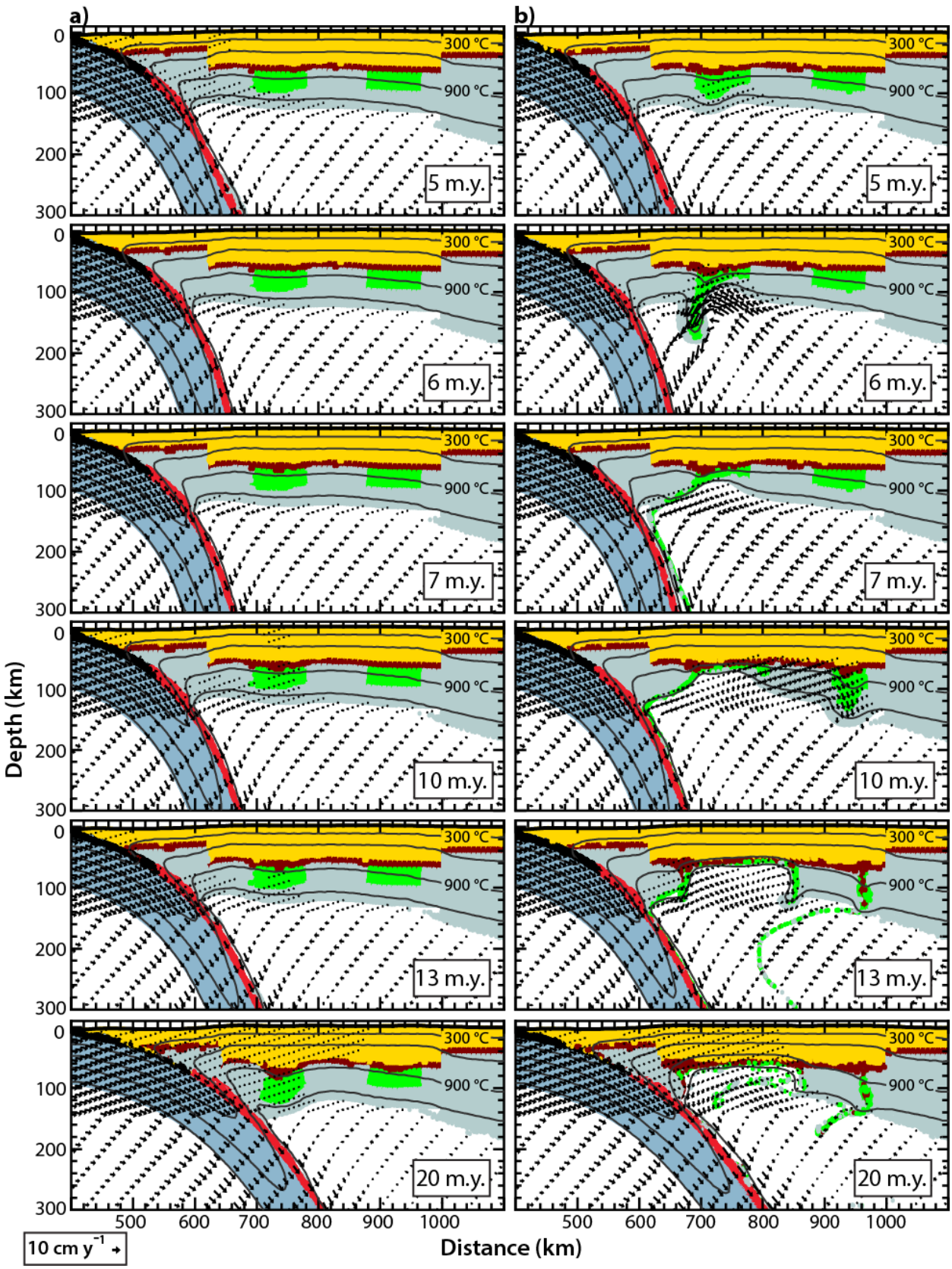
a)
b)
300 °C
900 °C
5 m.y.
6 m.y.
7 m.y.
10 m.y.
13 m.y.
20 m.y.
Depth (km)
0
100
200
300
500
600
700
800
900
1000
Distance (km)
10 cm y^{-1}

Figure 3.11 Model material distribution for **a)** *Model RT5* and **b)** *Model RT6* at given model times. The roots in *Model RT5* and *RT6* have the rheology of wet olivine (Karato and Wu, 1993) scaled by *f*=10 and *f*=1, respectively. Removal proceeds in a 'drip-like' manner in *Model RT6*, with the removal of the root closest to the subducting slab causing the initiation of the removal of the root closer to the craton. Note for ease of reference, the root closest to the descending slab (x=730 km) will be referred to as the proximal root, with the root closest to the craton (x=930 km) will be referred to as the distal root. Refer to Figures 2.1 and 3.8 for material colour coding.

consequent widening. The local secondary cell causes convective erosion and the reshaping of the proximal opening into a more rectilinear shape, similar to what is observed in *Model RT1*.This morphology is maintained until the end of model runtime at 20 m.y.

Figure 3.12a and b show *Models RT7* and *RT8*, respectively. Both *Models RT7* and *RT8* are similar to *Model RT5* and *RT6* in set-up, but the two roots extend across the entire thickness of the mantle lithosphere instead of being restricted solely to the upper portion. Roots have wet olivine rheologies, with *Model RT7* and *RT8* scaled by *f*=10 and *f*=1, respectively. *Model RT7* (Figure 3.12a) shows that removal occurs in two stages, with the basal portion of the proximal and distal roots readily 'dripping' within 1 – 3 m.y. after imposition. Its trajectory is affected by the rate of its descent. As the 'drip' descends rapidly, the mantle wedge corner flow has a minimal effect, leading to a sub-vertical trajectory, unlike the dynamics observed in *Model RT1* and *Model RT2*. The root removal acts to thin the entire width of the lower lithosphere, allowing the upper portion of the roots, which have a higher viscosity due to lower temperatures, to begin to descend. The proximal upper root is perturbed by mantle wedge flow and thus its instability initiates first at 10 m.y. Due to viscous coupling, the root pulls adjacent lithospheric material with it, resulting in the local thickening of the lower crust and the overall thinning of the mantle lithosphere. Upon its completion at 17 m.y., the initiation of the distal upper root takes place in a similar manner, and the net result is wholescale removal of the plateau mantle lithosphere within 20 m.y. Notably, the stresses associated with root removal result in deformation of the overlying crust, causing lower crustal flow into the area above the 'drip'.

Conversely, *Model RT8* (Figure 3.12b) shows that weaker roots cause removal to be carried out in a single stage, which is later perturbed by secondary cells of SLM circulation. The lower portions of the roots descend vertically and detach within 1 m.y., with the more proximal root initiating first within 0.2 m.y. Both lower portions of the roots descend as large 'drips', falling too quickly to be affected by the mantle wedge corner flow. This changes, however, as the roots continue to 'drip' and the windows

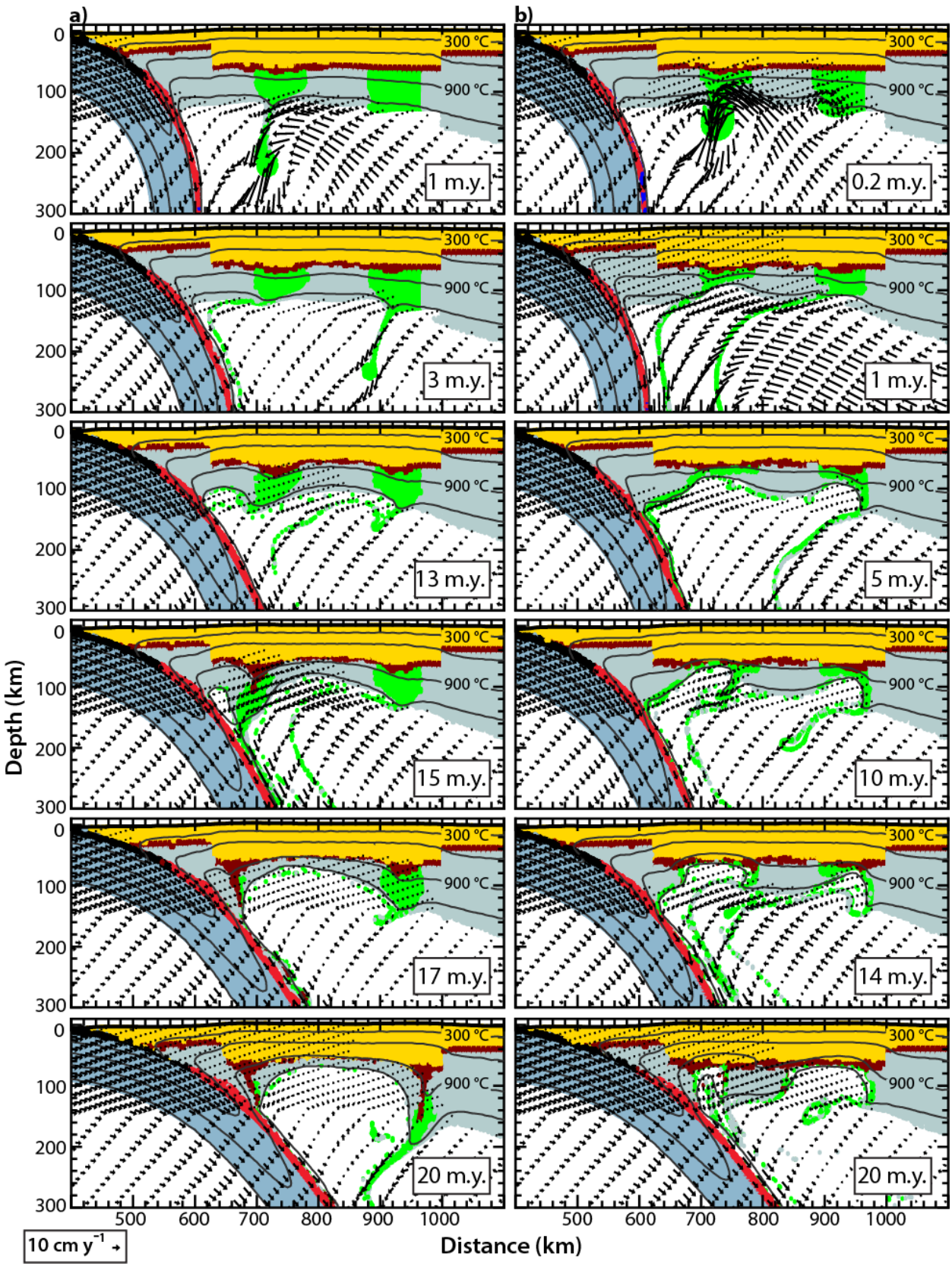
a)
b)
Depth (km)
Distance (km)
0
100
200
300
500
600
700
800
900
1000
300 °C
900 °C
1 m.y.
0.2 m.y.
3 m.y.
1 m.y.
13 m.y.
5 m.y.
15 m.y.
10 m.y.
17 m.y.
14 m.y.
20 m.y.
20 m.y.
10 cm y-1

Figure 3.12 Model material distribution for **a)** *Model RT7* and **b)** *Model RT8* at given model times. *Model RT7* and *Model RT8* have roots that extend the full thickness of the mantle lithosphere, with the rheology of wet olivine (Karato and Wu, 1993) scaled by f=10 and f=1, respectively. Refer to Figures 2.1 and 3.8 for material colour coding.

created within the mantle lithosphere experience an influx of SLM. Continuous removal develops once it is triggered, and the upper portions of the root are effectively gone within 5 m.y. As the roots are weak (f=1), they do not induce flow in adjacent material. Rather, discrete openings are formed as secondary convective cells within the SLM reshape the proximal and distal sites, in tandem, into more rectilinear shapes. This occurs within 10 m.y. SLM flow at the base of the mantle lithosphere causes the distal site to widen, and the proximal site to compress. After 20 m.y. two discrete gaps exist, one within the arc region (proximal site) and a large one at the distal edge of the orogen (distal site). The combination of the removal of two dense roots acts to remove the plateau mantle lithosphere in a piecewise manner, resulting in an asymmetric distribution of material.

3.4.2.4 Summary of RT results – Multiple roots

Feedbacks between the dynamics of multiple roots of various strengths ultimately result in complex final geometries. When two roots of lower strength (f=1) exist beneath the lower crust (*Model RT6)*, cascade destabilization ensues as removal of one root serves as the catalyst to remove its counterpart. The combined effects of subsequent SLM flow post-removal enhances the extent of local removal exhibited by the proximal root site, a direct consequence of being in close proximity to the subducting slab. When both roots extend through the entire thickness of the mantle lithosphere (*Model RT8)*, removal proceeds in a quasi-simultaneous manner resulting in symmetric openings within the mantle lithosphere. These openings lower the overall strength of the plateau mantle lithosphere, allowing shearing by mantle wedge flow to increase the amount of removal of the distal root site. In comparison, multiple roots of increased strength (f=10) and small thickness do not undergo removal (*Model RT5)*, as the density of the roots is not large enough to overcome the viscous strength of the roots. However, if the roots extend to the base of the lithosphere (*Model RT7)*, the lower parts of the root are weak and dense enough to undergo gravitational instability; this then enables further instabilities that remove the shallower root material. Removal of both roots proceeds following the same dynamics as observed in the corresponding singular root models (*Model RT1* and *RT2*), with the removal of both roots resulting in the large-scale removal of the plateau mantle lithosphere. Therefore,

in general, the combined dynamics of roots of lower strength (*f*=1) result in an overall piecewise (i.e. localized) removal style and a lithospheric substructure with isolated zones of SLM upwelling, while roots of increased strength (*f*=10) can result in wholesale (i.e. large-scale) removal and an overall thinned plateau mantle lithosphere.

3.4.3 Parameterization of RT style removal

In order to examine RT style of removal, a series of model experiments are carried out to assess the effects of the density and rheology of the imposed root, and the rheological structure of the orogen. The main purpose is to investigate the timing and style of removal once the prescribed parameter conditions are met, rather than a detailed assessment of the origin of the density inversion.

3.4.3.1 Variations in root density and rheology

The first set of models examine the effect of root density and rheology on the dynamics of RT removal. Variations in root strength are tested by scaling the base wet olivine rheology by *f*=1 to *f*=10; these are altered together along with the density of the root over a range of 25 to 150 kg m^{-3} more dense than the surrounding mantle (which remains constantly scaled *f*=10). The scaling of the root serves to approximate the variations in the root strength due to minor variations in compositional, water content, strain rates or deformation mechanism, or the presence of melt. Therefore, this sensitivity analysis provides insights on the timing and dynamics of removal with the emplacement of a localized zone of increased lithosphere hydration (which affects strength) and density.

Figure 3.13 summarizes the results of these tests. Greater root density contrasts relative to the mantle result in an earlier onset and shorter duration of removal, with the same trend exhibited for roots with a weaker rheology. Density contrasts of $\geq$75 kg m^{-3} can result in the proximal root becoming gravitationally unstable, despite its strength. In contrast, density contrasts of $\geq$125 kg m^{-3} are required to destabilize the distal root, occurring within the 20 m.y. model runtime only when the root is weak. Figure 3.13 also highlights the effect proximity to the subducting slab has on removal on the root: the influence of subduction-induced mantle wedge flow decreases with increased distance from the descending slab, delaying the initiation of removal. Note in these models, the flow of the SLM does not make direct contact with the root (Currie *et al.*, 2015); rather, the perturbation created at the base of the lithosphere due to continuous ablation serves to trigger removal. The proximal root initiates within 2 – 12 m.y. and removal is completed within 2 – 10 m.y. In comparison, the more distal root initiates

within 4 – 12 m.y. and is removed within 4 – 12 m.y. The limiting factor controlling the timing of removal at both root positions is its strength: stronger and more depleted conditions result in initiation periods that exceed the 20 m.y. model runtime, or no removal at all. When directly comparing roots of equal density and strength, both root positions exhibit similar trends in removal duration; however, the proximal root more readily descends, and, as a result, removal occurs for a larger range of parameters.

3.4.3.2 Variations in root and mantle lithosphere strength

Root removal also depends on mantle lithosphere strength as the root must descend through the mantle lithosphere. Figure 3.14 summarizes model test that vary the strength of the plateau mantle lithosphere in tandem with that of a single root, varying both by scaling factors of f=1 to f=20; the root density is 3350 kg m^{-3} in all models. The single root is imposed in the same proximal-distal manner as seen in *Models RT1* through to *RT4* in order to emphasize the influence of root position on both the timing of removal onset and its overall duration. In the case of both root positions, decreased root strength results in earlier onset and smaller duration of removal, which is further enhanced by increased density contrast. As was observed in Figure 3.13, proximal roots are removed more readily than their distal counterparts. Note that, in the case of the proximal root, an increase in removal duration of 2 m.y. can be steadily observed as strength of one parameter (the root or surrounding mantle lithosphere) is increased twofold while the other (the surrounding mantle lithosphere or root) remains fixed. Removal is inhibited only when both the root and mantle lithosphere are strong.

Figure 3.14 depicts three styles of removal for both roots: i) roots of increased strength surrounded by weak mantle lithosphere remove via localized delamination, decoupling from the overlying crust as a coherent piece (Figure 3.14c), and as the strength of the mantle lithosphere increases removal proceeds in a 'drip-like' Rayleigh-Taylor-type instability, ii) viscous coupling of the root with adjacent mantle material increases as both weaken, resulting in delocalized removal and the overall thinning of the mantle lithosphere, and iii) as both root and surrounding mantle strengthen removal becomes localized, resulting the foundering of the lowermost root, followed by later removal of the shallow portion by SLM flow. Examples of the localized delamination are provided in Figure 3.14c and d, where the root coherently peels back from the overlying crust. Before removal is underway, the descending strong root causes the weak surrounding plateau mantle to locally deflect, creating a 'step' features that influences SLM flow towards the descending slab. The proximal root removes towards the descending oceanic slab, whereas the distal root hinges back towards the craton. These trajectories are

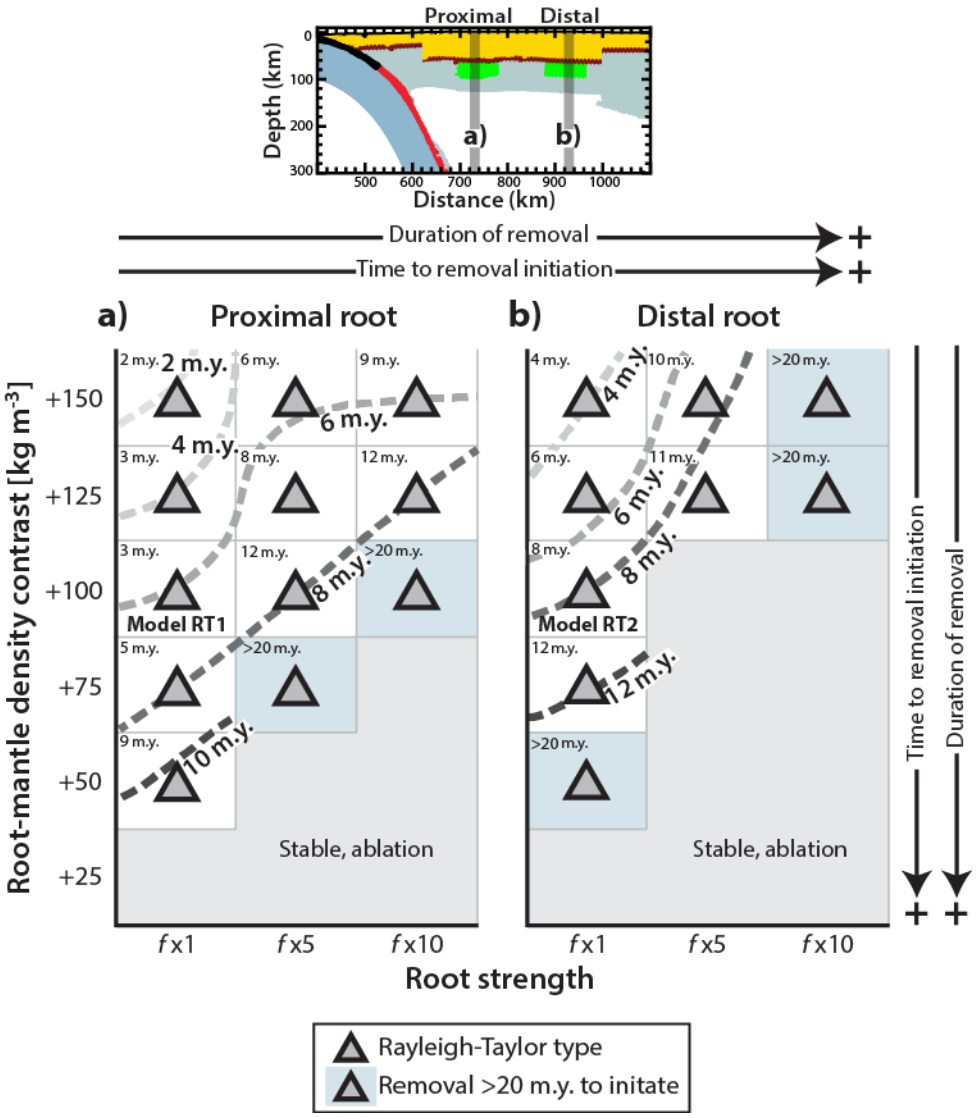

Figure 3.13 Model behaviour for variations in density, strength of the imposed root, and its location. Regime diagrams for **a)** proximal, and **b)** distal root positions relative to the subducting oceanic slab. Shaded areas discern different styles of removal, indicated either by the symbol of the block or by its label. The light grey zone represents models that remain stable throughout model evolution (i.e. no RT removal, but continued subduction-induced ablation) and triangles are models that exhibit RT removal. Dashed lines show the time (since the imposition of the dense anomaly) for removal of >90% of the root. Labels in the top left corner of each box indicate the time (since the imposition of the dense anomaly) for removal to initiate, defined as the base of the root deviating from a planar horizon.

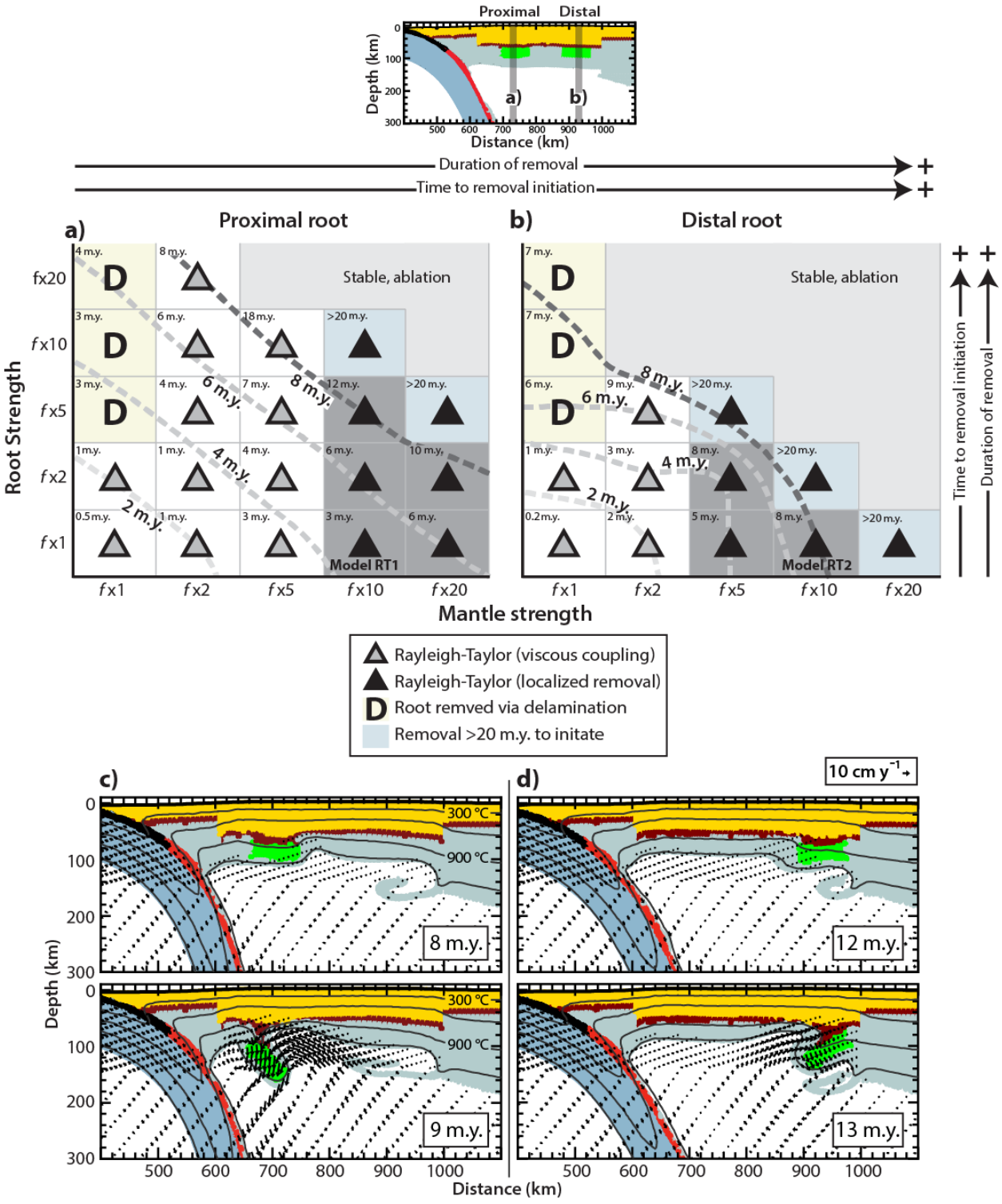

Figure 3.14 Model behaviour for variations in root strength carried with the strength of the surrounding mantle lithosphere, and root location. Regime diagrams for **a)** proximal, and **b)** distal root positions relative to the subducting oceanic slab, with roots prescribed a density 100 kg m^{-3}

denser than mantle material. Shaded areas discern different styles of removal, indicated either by the symbol of the block or by its label. The light grey zone represents models that remain stable throughout model evolution (i.e. no RT removal, but continued subduction-induced ablation) and triangles are models that exhibit RT removal. Dashed lines show the time (since the imposition of the dense anomaly) for removal of >90% of the root. Labels in the top left corner of each box indicate the time (since the imposition of the dense anomaly) for removal to initiate, defined as the base of the root deviating from a planar horizon. **c)** Model material domain of the proximal root and **d)** the distal root (root and mantle lithosphere assigned f=10 and f=1, respectively) depicting its localized delamination. Refer to Figures 2.1 and 3.8 for material colour coding.

the same observed in *Models R1* to *R4*, however, the increased root strength allows coherent removal rather than 'drips'. The descent of the proximal root prevents extensive ablative removal of the plateau mantle lithosphere contrasting the overall thinned mantle lithosphere shown Figure 3.14d. Note crustal flow causes the localized thickening of the lower crust above the foundering root in these small-scale delamination models. Finally, the trajectory of the root's descent is affected by the strength of the surrounding mantle lithosphere; where RT removal occurs (Figure 3.14) the root detaches subvertically when the surrounding mantle lithosphere is weak ($f \leq 5$), or is entrained by SLM flow that is either subduction-induced or generated as a consequence of the removal process (reflective of its proximal or distal position, respectively).

3.5 Summary of model results

The modelling results from Sections 3.3 and 3.4 are summarized as follows:

3.5.1 Models of delamination removal:

1. The onset of retreating delamination occurs earlier as the strength of the mantle lithosphere increases, and the density of the imposed root decreases; both factors allow the root to remain viscously coupled to the lithosphere as it peels back which enhances the negative buoyancy of the delaminating slab. Delamination is completed within 5 – 12 m.y. Shorter durations are achieved as plateau mantle lithosphere strengthens reflecting a more dehydrated state, root density is 50 to 100 kg m^{-3} more dense than surrounding mantle, and the LVZ is below 10^{21} Pa·s (Figures 3.5, 3.6)
2. Delamination requires a weak zone in order to allow a conduit from the SLM to the lower crust to form. A LVZ expedites the coherent removal of the mantle lithosphere (*Model D1*, Figure 3.3); however, a point of detachment along the Moho can also be generated after the foundering of a dense root, which creates a gap within the mantle lithosphere that the subduction-induced flow

can exploit (*Model D2* Figure 3.4*,* and *RT4* Figure 3.10*b*). Without a LVZ, delamination takes longer than 20 m.y. to complete. Furthermore, models in this study demonstrate only one style of delamination – retreating (*Model D1,* Figure 3.3).

3.5.2 Models of RT gravitational instabilities

3. RT instabilities of greater density contrasts positioned in close proximity to the subducting slab are more readily destabilized. Shearing by the mantle wedge flow serves to trigger the instability, occurring more rapidly both in terms of onset and overall duration. Regardless of root position, RT instabilities are removed within 2 – 12 m.y after initiation with shorter times for increased root density and decreased root strength (Figure 3.13). Note that weaker surrounding plateau mantle lithosphere lowers these removal durations to a range of 1 – 9 m.y., with earlier onsets also registered.
4. The style in which RT type instabilities remove is dependent on the relative contrast in root strength and the surrounding mantle lithosphere. Removal proceeds more readily as both the mantle lithosphere and the imposed root decrease in strength. Notably, localized coherent removal (via small-scale delamination) is triggered as the root strengthens and the surrounding mantle weakens (Figure 3.14).
5. The trajectory of descending roots is affected by the rate at which they 'drip', which is controlled by their density contrast, rheology and location relative to the subducting slab. Roots in close proximity to the subducting slab tend to be entrained by the mantle wedge flow (Figure 3.9a, Figure 3.10a), whereas more distal roots generate their own clockwise cell of mantle flow causing them to 'drip' cratonward (Figure 3.9b, Figure 3.10b). However, sub-vertical descent is exhibited by roots, regardless of their position, for root density contrasts greater than 75 kg m^{-3} and decreased plateau mantle lithospheric strength.
6. The presence of multiple roots within the mantle lithosphere results in constructive feedback affecting removal dynamics, where the foundering of the proximal root serves to destabilize the more distal counterpart. The coupled effects of both strong roots and surrounding mantle lithosphere can result in the widespread and complete removal of the plateau mantle lithosphere (Figure 3.12a). Else, when the root is weak compared to the surrounding mantle lithosphere, localized gaps occur within the plateau mantle lithosphere, that are further modified by subduction-induced flow (Figure 3.11a and b).

CHAPTER 4 : COMPARISON TO THE CENTRAL ANDES

4.1 Introduction

Lithospheric removal has long been recognized as an important process in the formation of the Andes. However, the cause, scale, timing and surface expression remain controversial. Instabilities in the lithosphere leading to its removal can be triggered by magmatic arc processes that produce an igneous eclogitic root, and crustal shortening and thickening that lead to a metamorphic eclogitization of a mafic lower crust (e.g. Elkins-Tanton, 2007, Krystopowicz and Currie, 2013); superimposed on this is the moderate density increase in the lithosphere due to its low temperature compared to the underlying mantle. As a result, removal can include parts of the lower crust as well as the mantle lithosphere. Recent studies have put emphasis on the effect of lower crustal eclogitization on large-scale delamination and local-scale Rayleigh-Taylor-type instabilities (e.g. Krystopowicz and Currie, 2013; Wang *et al.*, 2015). This section will discuss the implications of the model results based on previous geological and geophysical observations, subdivided by region. For reference, Figure 4.1 summarizes how the Altiplano-Puna plateau is subdivided for the interest of this study, which reflects latitude ranges that

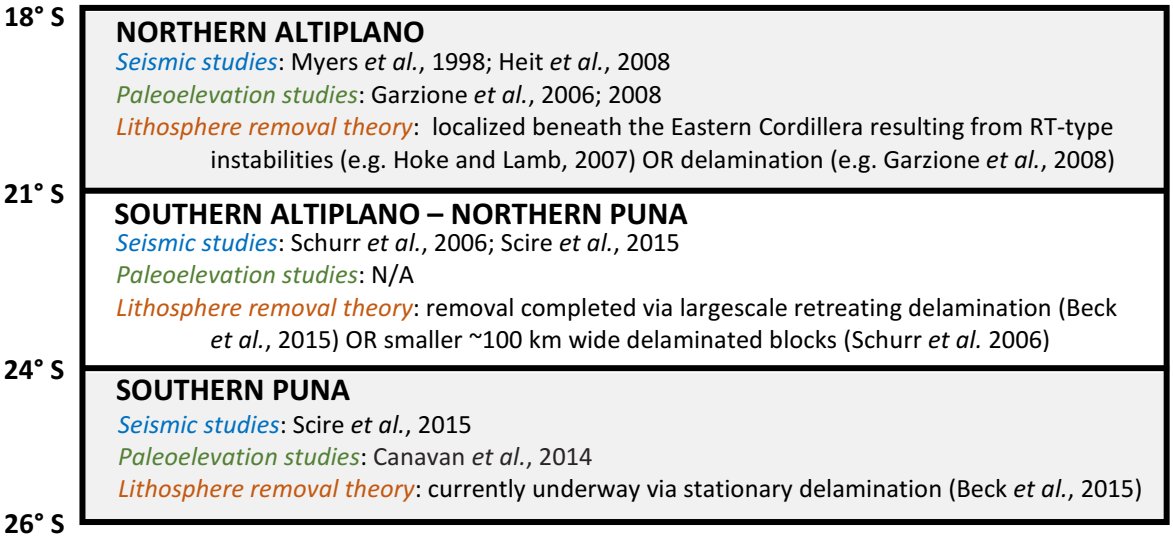

Figure 4.1 Latitude subdivisions of the Altiplano-Puna plateau for the interest of this study, based on study areas of previous studies as well as differences in the proposed mechanisms of lithosphere removal.

have been previously discussed in central Andean literature as having distinct lithosphere removal styles (e.g. Garzione *et al*., 2006; 2008; Heit *et al.* 2008; Kay and Coira, 2009; Beck *et al.*, 2015; Lamb, 2016).

4.2 Removal within the northern Altiplano (18°-21°S)

Numerous geophysical studies have investigated the lithospheric structure of the central Andes, revealing spatially heterogeneous mantle lithosphere thus inferring spatially variable styles of removal. In the northern Altiplano (18°-21°S), it is suggested that subcrustal lithosphere has been removed in a piecewise manner (e.g. Myers *et al.*, 1998; Yuan *et al.* 2002; Beck and Zandt, 2002; Heit *et al.*, 2008). Two distinct zones of low velocity in the shallow mantle are observed (Figure 4.2a and b), one being under the volcanic arc and the other located beneath the Eastern Cordillera (65-66°W). The former is attributed to fluids and crustal melts associated with a removed block of mantle lithosphere, being possibly initiated by the ascending fluids released from the subducting plate (Heit *et al.*, 2008; Yoon *et al.*, 2009), and the latter is interpreted as a likely zone of partial melt (12-18 km depth; Leidig and Zandt, 2003). The character of the upper mantle also exhibits zones of low velocity at ~100 – 190 km depth near 66° W in Figure 4.2b; this coincides with the area where receiver functions show a thinner lithosphere relative to adjacent areas (Beck and Zandt, 2002; Heit *et al.*, 2007; Ryan *et al.*, 2016). As a result, this low velocity zone is interpreted as SLM replacing foundered mantle lithosphere. The overall northern Altiplano lithospheric substructure resembles that modelled in *Model RT8* (Figure 4.2c), resulting from the removal of two dense roots via RT instabilities. These imposed roots could be thought of as being related to arc- and rear-arc- magmatism, with possible origins pertaining to the cyclicity in slab dip (Kay *et al.*, 1999; James and Sacks, 1999; Allmendinger *et al.,* 1997; Hoke and Lamb, 2007; Kay and Coira, 2009; DeCelles *et al.*, 2009).

In particular, magmatism has been present along much of the central Andes throughout the Mesozoic and Cenozoic, resulting in the creation of major stratovolcanoes, widespread ignimbrites, and back-arc volcanism (Trumbull *et al*., 2006; Hoke and Lamb, 2007; Kay and Coira, 2009). Arc volcanism in the northern Altiplano region of the orogen had been steady before 25 Ma, after which mafic to felsic magmatic activity occurred across the Altiplano region, covering a broad zone up to 300 km behind the arc (Figure 4.3) (Trumbull *et al.*, 2006; Kay and Coira, 2009; Beck *et al.*,2015); starting 20 - 15 Ma, the western arc-front and the overall volcanic distribution narrowed to its present-day 50 km wide zone (Worner *et al.*, 2000; Trumbull *et al.*, 2006). In general, the occurrence of back-arc magmatism is

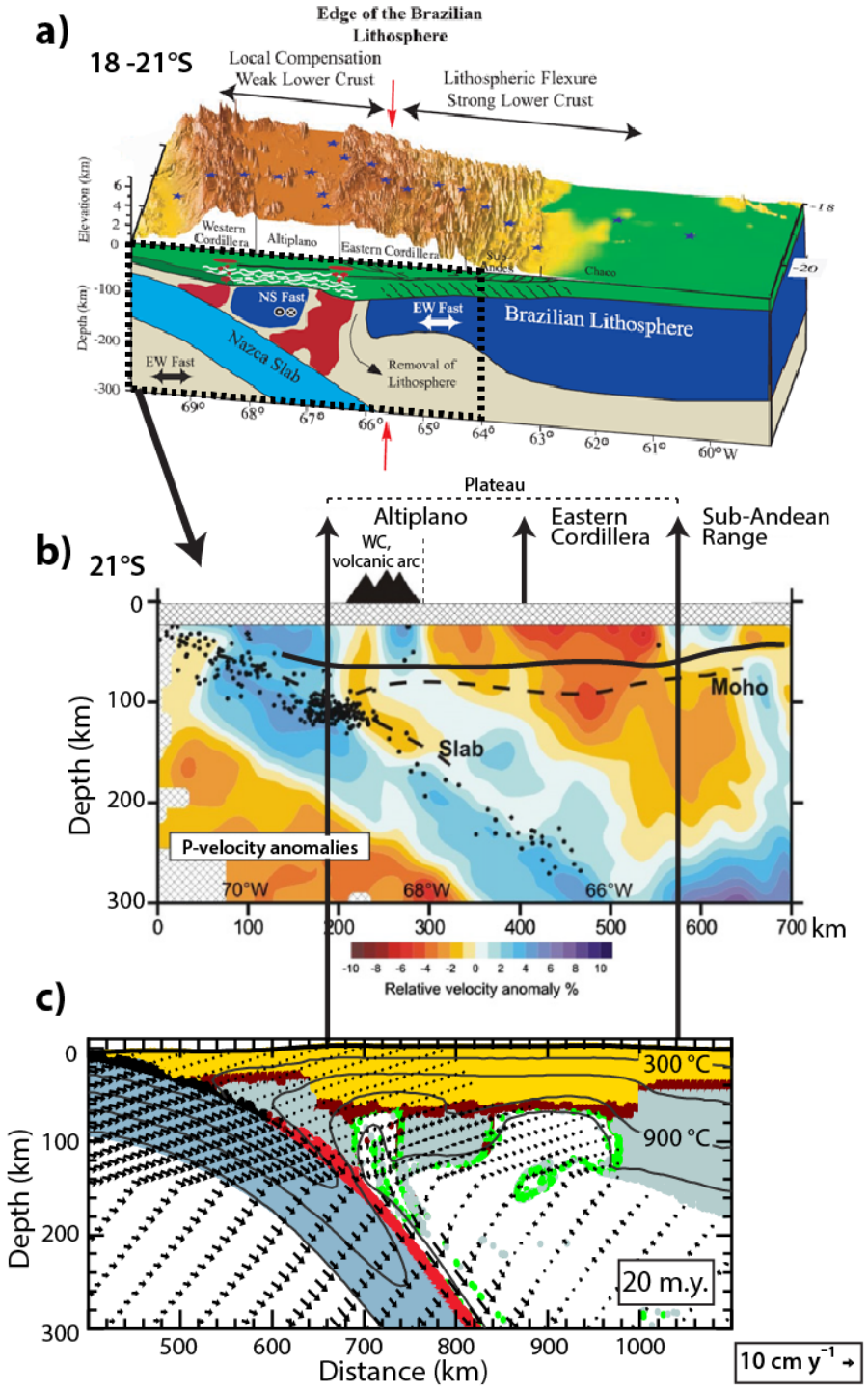

Figure 4.2 Geophysical studies reflecting piecewise removal of the mantle lithosphere beneath the Altiplano. **a)** Conceptual block model modified from Beck and Zandt (2002), combining their receiver function analysis and with the tomographic insights from Myers *et al.* (1998). Two localized zones of mantle lithosphere removal were identified between 18° - 21° S. **b)** P-wave tomographic image modified from Heit *et al.* (2008). The dash line is the Moho from

S-wave receiver functions from Heit *et al.* (2007), and the solid line is the Moho from Elger *et al.* (2005), similar to that identified in Yuan *et al.* (2002). Piecewise removal is also suggested to explain the low velocities. Refer to text for discussion. **c)** Model result from *Model RT8*, corresponding to 20 m.y. model runtime. Constructive feedback between multiple weak roots results in stable gaps within the mantle lithosphere from this study. This is the favoured model that best represents the current substructure beneath the Altiplano. Refer to Figure 2.1 and Figure **3.8** for material colour coding.

thought to be variable in the central Andes, and is possibly related to processes of plateau formation or changes in geometry of the subduction slab and the overlying lithosphere (see sections 1.2 and 1.3.1) (e.g., Allmendinger *et al.*, 1997; Coira *et al.*, 1993; Kay *et al.*, 1999; Hoke and Lamb, 2007).

To that point, Hoke and Lamb (2007) and Lamb (2016) proposed a model that linked the progressive steeping of the descending oceanic slab with mantle wedge flow and volcanism in order to explain the piecewise removal style observed within the mantle lithosphere of the northern Altiplano (Myers *et al.*, 1998; Beck *et al.*, 2002; Yuan *et al.* 2002; Heit *et al.*, 2008) (Figure 4.4, 4.2a and b). Figure 4.4 summarizes this model, which involves a lull in magmatic activity caused by a period of flat slab subduction between 35 – 25 Ma, which hydrated the overlying mantle lithosphere. The subsequent removal steeping of the subducting slab serves to re-establish the frontal arc. Therefore, Hoke and Lamb (2007) suggested that the main features of the lithospheric structure beneath the northern Altiplano, including the thin regions of mantle lithosphere identified in deep seismic imaging (Figure 4.2a and b), have existed for the last 25 Ma. In their model, water released from the flat slab hydrates the overlying mantle lithosphere and weakens it to the point of initiating large-scale removal events (James and Sacks, 1999). Lamb (2016) suggests that stresses generated by the steepening slab would strip away the lower portion of the lithosphere. However, here we discuss removal that can arise due to the presence of unstable dense eclogitic roots within the mantle lithosphere in the context of the proposed conceptual model of Hoke and Lamb (2007) and Lamb (2016).

Although flat slab subduction was not explicitly modelled in the current study, *Model RT8* (Figure 3.12b) reveals that localized zones of thin lithosphere may arise through gravitational removal of multiple dense roots. The roots in *Model RT8* can be assumed to either be proximal and distal zones of partial melt generated from the adiabatic decompression of mantle material or related to melt differentiation (e.g. Lee *et al.*, 2006; DeCelles *et al.*, 2015). *Model RT8* depicts the quasi-simultaneous removal of weak imposed roots within the lithosphere, occurring within 5 m.y. This removal results in

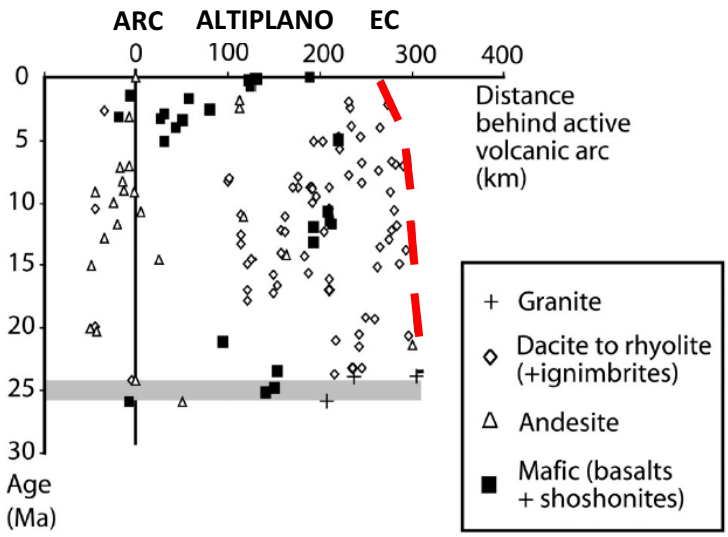

Figure 4.3 Summary of arc volcanism and ignimbrites in the northern Altiplano of the central Andes (16°to 22°S) plotted as a function of age against distance perpendicular to the active arc. Arc and widespread behind arc volcanism started abruptly at 25 Ma, after which there has was continual felsic to mafic volcanism extending up to 300 km behind the arc. Dash red line = eastern limit of magmatism. Modified from Lamb (2016).

two symmetric openings within the mantle lithosphere, the shape of which are largely maintained for the next 15 m.y (Figure 4.2c), being only slightly modified by the mantle wedge flow. Notably, the longevity of the substructure in *Model RT8* is consistent with the proposed conceptual model of Hoke and Lamb (2007), which states that the same substructure has existed for the last ~25 Ma. The resulting configuration of the mantle lithosphere within *Model RT8* (Figure 4.2c) agrees with deep seismic imaging beneath the northern Altiplano (Figure 4.2a and b), revealing evidence of localized lithosphere thinning.

If the removal of the roots are truly coeval with slab steepening, as the slab peels away from the overriding plate the influence of the subduction-induced shear force on the continent would migrate as well. The propensity for lithosphere removal would migrate as well. This could result in removal being triggered at the distal edge of the plateau first and reduce the size and density contrast of the root necessary for removal, as supported in Figure 3.13. Therefore, a similar structure as produced in *Model RT8* could be recreated with multiple roots emplaced below the Moho (more reflective of ponded partial melt) with removal of a distal root before the proximal root, opposite to the order observed within *Model RT6* (Figure 3.11b). Removal of each root could be individually completed within 2-10 m.y, (Figure 3.13a).

Note that, in contrast to Hoke and Lamb (2007), Kay and Coira (2009), and Lamb (2016), other authors (e.g. Trumbull *et al.*, 2006) suggest that a period of flat slab subduction is not needed in order to

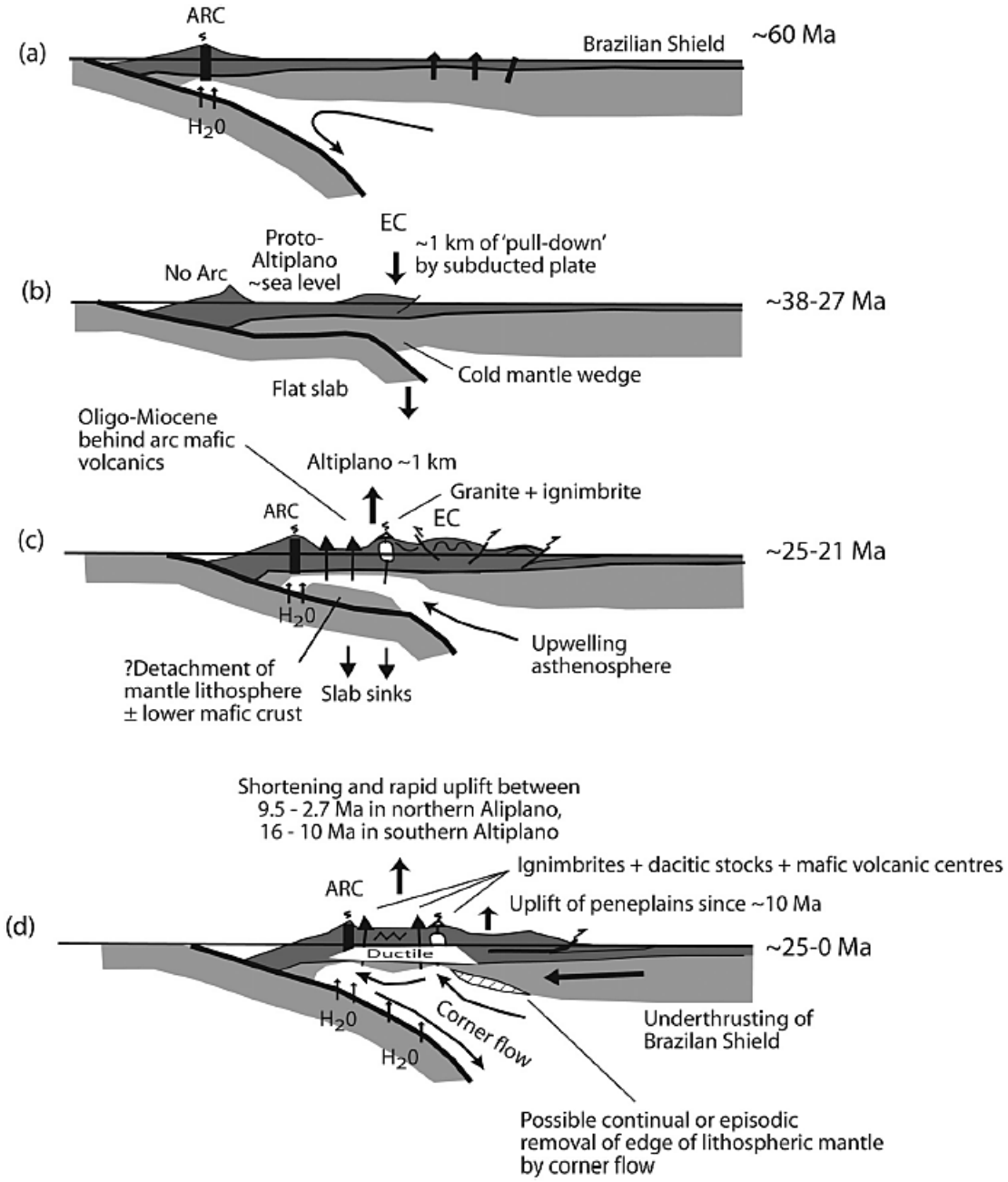

Figure 4.4 Conceptual model relating subduction geometry and mantle lithsophere removal to explain present-day lithospheric substructure. The model comprises of **a)** volcanic activity was predominantly confined to the arc region 60 Ma, **b)** between 38 – 27 Ma, the northern Altiplano region experienced a 10 m.y. period of magmatic quiescence that has been postulated to be linked to a period of 'flat slab' subduction, **c)** arc together with back-arc volcanism resumed abruptly between 25 – 21 Ma associated with the steepening of the subducting slab and the removal of part of the overlying mantle lithosphere, and **d)** the modern configuration of the mantle lithosphere being the maintained substructure from the previous stage of removal. From Lamb (2016).

explain the cratonward migration of the arc-front (Figure 4.3), rather it arose due to the subduction-induced erosion of the western edge of the South American plate. So although flat slab subduction was not incorporated into the *Model RT8*, the model nonetheless provides insight into the current substructure beneath the northern Altiplano.

4.3 Removal within the southern Altiplano and northern Puna (21°-24°S)

There is a widespread consensus that the mantle lithosphere has been completely removed below the southern Altiplano and the northern Puna plateaux. Both Schurr *et al.* (2006) and Scire *et al.* (2015) imaged large low velocity zones in the shallow mantle beneath seismically slow crust (Ward *et al.*, 2013). The low velocity zones are interpreted as a large region of upwelled mantle material and the crustal feature is associated with the Altiplano-Puna magma body (Beck *et al.*, 2015) (Figure 4.5a). Schurr *et al.* (2006) imaged local zones of high velocities, sitting atop the descending oceanic slab. These zones have similar seismic signature to the underlying oceanic slab, and were interpreted as eclogitzed lithosphere that had foundered from the upper plate. Furthermore, the position and size (~100 km across) fits with the material possibly being derived from beneath La Pacana caldera region (68°W, 23°S), which possibly was destabilized due to a dense eclogite-rich root (Schurr *et al.*, 2006; Kay and Coira, 2009). As put forward by *Beck et al.* (2015), large-scale westward-directed removal can be triggered by eclogitization of the lower crust (Krystopowicz and Currie, 2013), and can explain the present-day thin lithosphere in this region. Furthermore, Beck *et al.* (2015) used the spatial pattern of volcanism in the region to support their case. Their study proposed that retreating delamination, and the resulting migrating zone of upwelling asthenosphere, could explain the trenchward migration of Cenozoic back-arc volcanism in the northern Puna (Figure 4.6).

The models in this study show that widespread thinning of the mantle lithosphere is accomplished most readily through delamination. As seen in *Model D1* (Figure 3.3), as delamination proceeds, the slab of continental mantle lithosphere detaches as a coherent piece, after which hot SLM material upwells coming into direct contact with the overlying crust. Once initiated, removal via delamination can be carried out within 5 – 15 m.y. In the last 4 m.y. of *Model D1*, the detached lithosphere temporarily clog up the mantle wedge corner (Figure 3.3, 6 – 8m.y.), most likely impeding arc magmatism. As a result, the delamination models cannot completely reconcile the lull in frontal arc activity identified by previous studies that lasted more than 10 m.y. (Figure 4.6) (e.g. Trumbull *et al.*, 2006; Kay and Coira, 209; Beck *et al.* 2015). As other authors have suggested (e.g. Trumbull *et al.*, 2006),

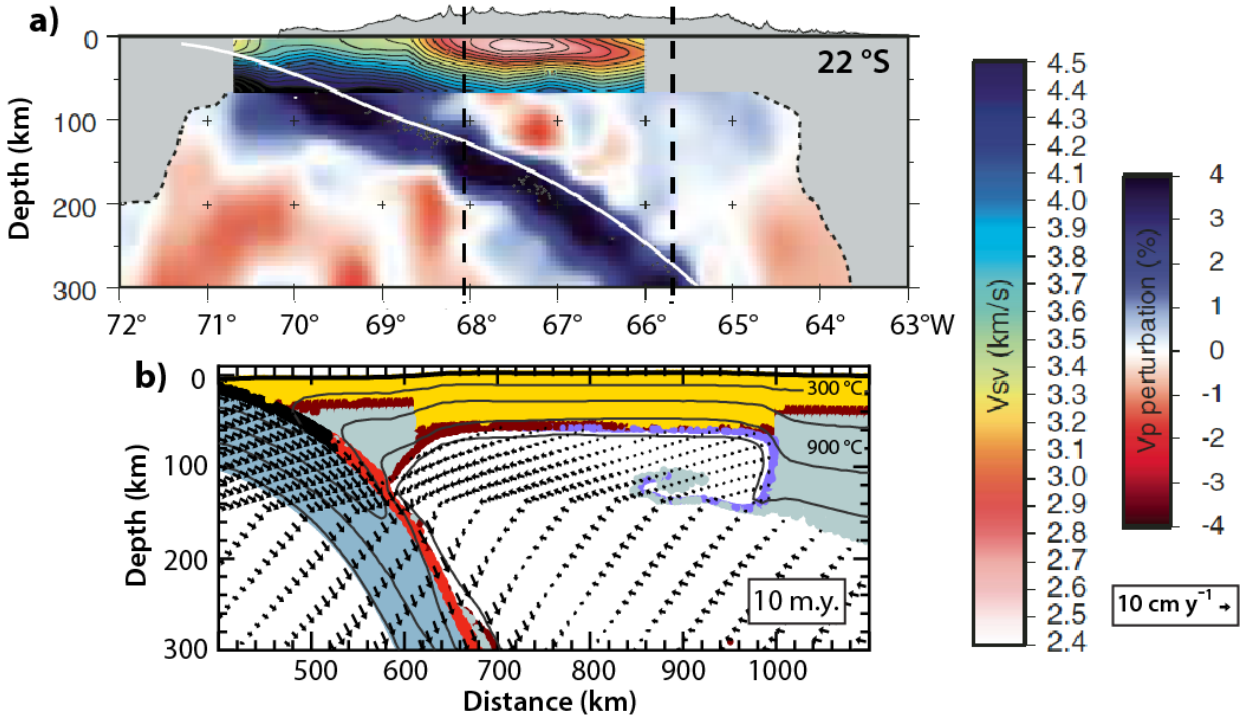

Figure 4.5 **a)** Ambient noise tomography shear-wave velocity model for the crust (Ward *et al*., 2013), and P-wave tomography model for the mantle at 22° S (Scire *et al*., 2015). Mantle lithosphere is interpreted to be completely removed resulting in a large low velocity zones beneath seismically slow crust. Modified from Beck *et al.* (2015). **b)** *Model D1*, at 10 m.y. This model is most consistent with the current structure beneath the southern Altiplano, with the thin lithosphere resulting from retreating delamination. Note that point of detachment along the Moho may have been generated by removal of a single dense root located in the back-arc region, as observed in *Model D2 and RT4*. Refer to Figure 2.1 or 3.2 for material colour coding.

this apparent lull could merely affect slight changes in subduction geometry due to continued ablation of the upper plate. However, Beck *et al.* (2015) notes that increase in back-arc magmatism responsible for its eventual areal expansion occurred between 20 – 10 Ma. This period marks the start of activity in the Altiplano-Puna volcanic centre and conceivably corresponds to the time over which the mantle lithosphere is thought to have decoupled form the overlying crust. Notably, models in this study show that delamination can be accomplished well within this 10 m.y. period, averaging 6 m.y. in duration.

Unlike in the models of Krystopowicz and Currie (2013), *Model D1* utilizes a dense root within the mantle lithosphere to drive removal, which is expedited with the presence of an imposed weak zone

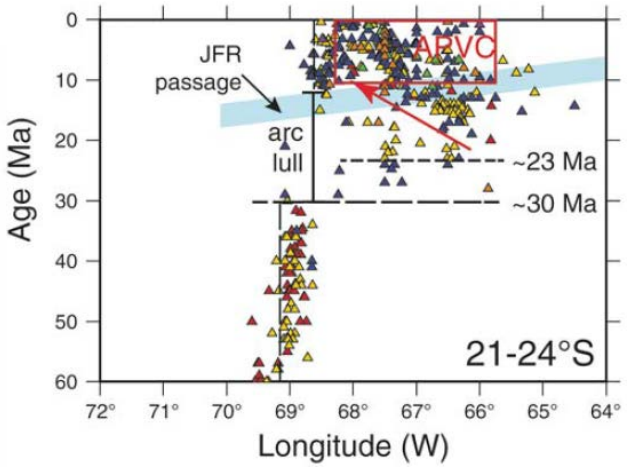

Figure 4.6 Summary of arc volcanism and ignimbrites in the central Andes as a function of age between 21°S and 24°S. Symbols are colour coded for magma type; red— intrusives; gold—lava, breccia, and dome deposits; blue—pyroclastic, ash, tuff, and ignimbrite deposits; green—calderas; orange— stratovolcanoes and cones; purple—monogenic centers. Blue bar shows the passage of the Juan Fernandez Ridge (JFR). Note the gap in arc volcanism and the onset of widespread back-arc volcanism. The red box shows the Altiplano-Puna volcanic complex (APVC). From Beck *et al.* (2015).

in the mantle lithosphere. However, as observed within *Model D2* (Figure 3.4) and *Model RT4* (Figure 3.10b), large-scale delamination can be initiated through gravitational removal of a single dense root; foundering in this manner creates a conduit to connect the SLM to the weak lower crust, triggering delamination. In this interpretation, the overall style of removal does not change, but the initial location of detachment coincides with the position of the root. The removal of the root creates a localized cratonward gap within the mantle lithosphere of the plateau most likely causing an increase in local back-arc volcanism. This would be followed by a trenchward migration in magmatism as delamination is triggered. It should be noted that the majority of delamination models show that the detached lithosphere founders as a large coherent slab. Nevertheless, both the densification of the lower crust (Krystopowicz and Currie, 2013; Beck *et al.,* 2015), and the existence of a singular dense root within the mantle lithosphere can serve as triggers to initiate large-scale westward delamination.

However, the size of the mantle lithospheric blocks imaged by Schurr *et al.* (2006) at ~23° - 24°S (~100 km wide) suggests removal may not have involved a coherent slab of mantle lithosphere, but the removal of one or more coherent roots. The models in this study show that weakened (i.e. hydrated) plateau mantle lithosphere can promote increased ablation, and strong (i.e. depleted) dense roots

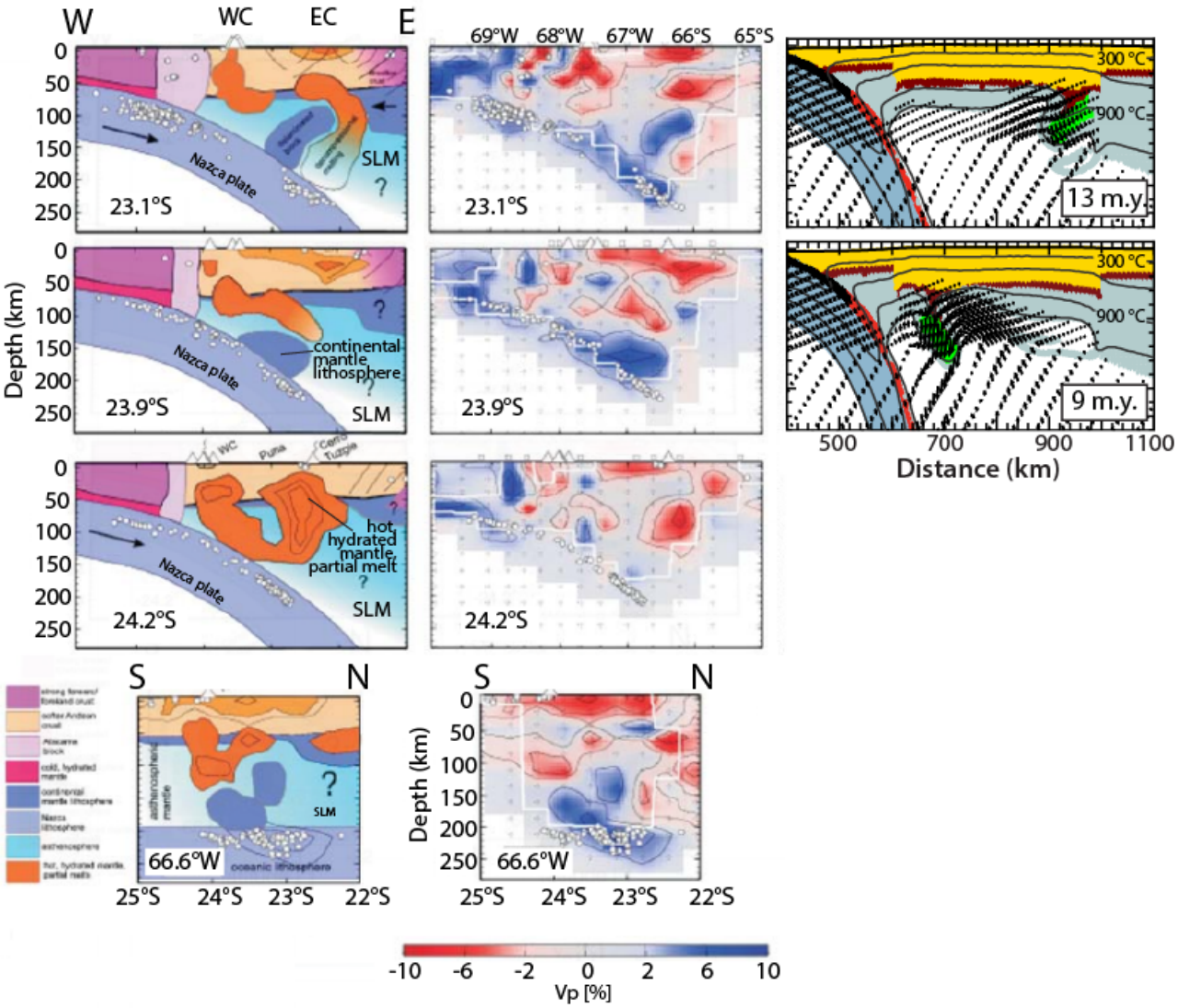

Figure 4.7 Cross-sectional tomographic images of the southern Altiplano and northern Puna plateaux, between 23° and 24°S. From left to right, conceptual models are provided to explain the tomographic observations, the tomography is shown as P-wave velocity perturbations, and models from this study are shown for comparison (refer to Figure 2.1 and Figure **3.8** for material colour coding, and Figure 3.14c and d for further discussion). Note that low velocity anomalies are associated with hot decompressional melt resulting from upwelling sublithospheric mantle (SLM), and high velocity anomalies are associated with blocks of detached continental mantle lithosphere. Modified from Asch *et al.* (2006).

within this mantle lithosphere detach coherently (Figure 3.14c and d, 4.7). As the root peels back from the overlying plate, there is a corresponding rapid influx of SLM which largely agrees with the geometry of the low velocity zones imaged by Schurr *et al.* (2006) (Figure 4.7). Note, although Beck *et al.* (2015) propose large-scale retreating delamination at these latitudes, they credit this removal style to weak northern Puna mantle lithosphere; this is the same ambient condition that permits the coherent removal of strong roots in this study (Figure 3.14c and d). As removal of a single root can both trigger large-scale coherent removal of the continental mantle lithosphere (*Model D2*, Figure 3.4) and explain the presence of ~100 km wide lithospheric blocks (Figure 3.14c and d), root destabilization within weak plateau mantle lithosphere may be a able to reconcile both these tomographic observations. Recall models in this study show the removal of one root can trigger the destabilization of another (e.g. *Models RT6* and *RT7*); therefore, destabilization of multiple roots may be a valid interpretation of the removal of the southern Altiplano and northern Puna when considered in 3D (e.g. North-South line from Schurr *et al.,* 2006; Ash *et al.*, 2006) (Figure 4.7).

4.4 Removal within the southern Puna (24°-26°S)

Beck *et al.* (2015) has proposed two styles of large-scale delamination within the Puna region, with the southern region being influenced by stationary removal owing to localized increased strength of the mantle lithosphere (Krystopowicz and Currie, 2013). This style of removal is supported by the eastward migration of the volcanic front towards the Eastern Cordillera recorded in the southern Puna at 35 Ma, contrasting the westward trend seen in the north. Recall that stationary delamination involves removal of the mantle lithosphere as a coherent slab beneath the site of initiation. Beck *et al.* (2015) suggest that this occurred in a cratonward direction to explain present-day tomography images of the southern Puna mantle lithosphere (Figure 4.8a).

This style of removal was not observed in the models in this study that include an active subduction zone. Despite varying the strength of the mantle lithosphere and the imposed root, stationary delamination could not be induced. Note that even benchmark models including a LVZ along the trenchward edge of the plateau mantle lithosphere did not serve to decouple the mantle lithosphere from the adjacent coastal mantle material. It is interpreted that within the presence of corner wedge flow (exerting a trenchward shearing on the base of the continent), stationary delamination is unlikely.

Alternatively, the presence of multiple dense roots beneath the Moho in *Model RT6* induces lithosphere removal, resulting in a lithospheric structure that resembles that currently observed in the

southern Puna (Figure 4.8). The removal of the root within the arc region of the plateau, which triggers first, results in the local upwelling of SLM, possibly corresponding to the low velocity zone imaged in Figure 4.8a. Later instability of a second distal root occurs through cratonward flow, pulling with it adjacent material that is viscously coupled (Figure 4.8b). This process occurs within 10 m.y. after the onset of instability. This style does not require spatial disparity in mantle lithosphere strength from south to north within the Puna, as suggested by Beck *et al.* (2015); rather it requires localized compositional heterogeneities that create weak dense zones that are readily able to flow. Notably, *Model RT6* predicts the distal root is removed within 3 m.y., and the system evolves to create a prominent gap within the site of the first more proximal root (Figure 3.11b). This model, therefore, does not predict large-scale removal of the mantle lithosphere, as stationary removal would imply.

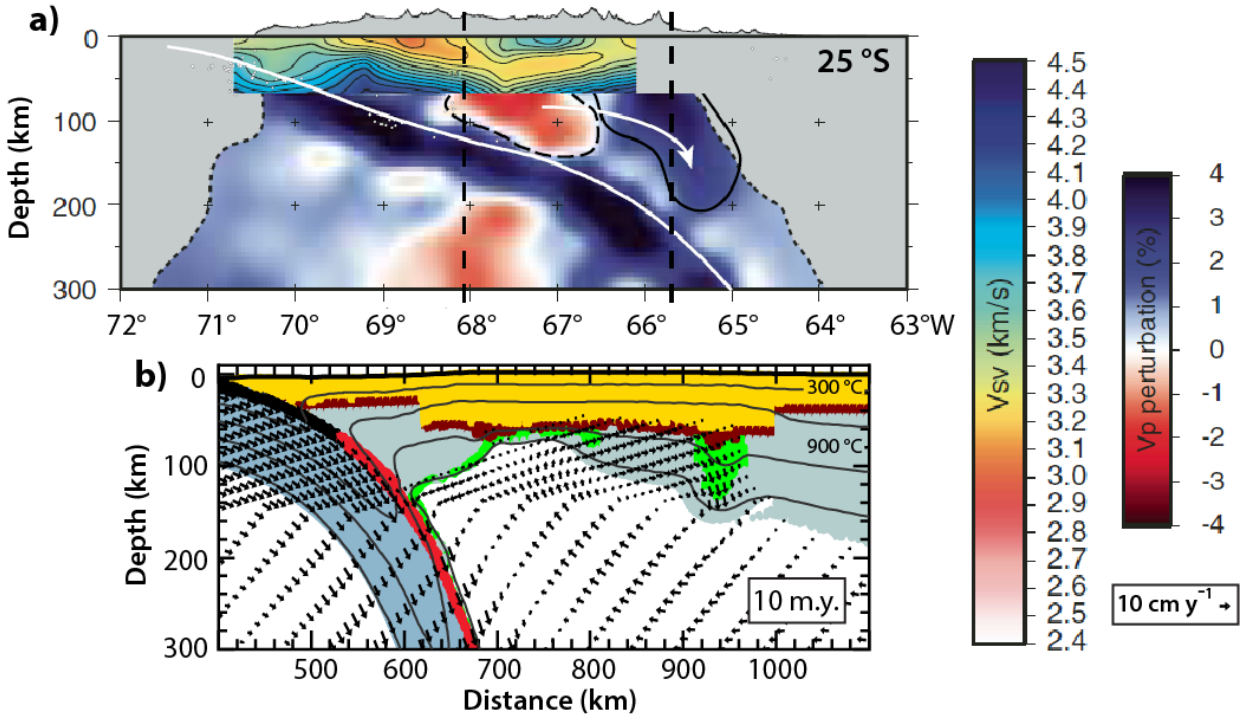

Figure 4.8 **a)** Ambient noise tomography shear-wave velocity model for the crust (Ward *et al.*, 2013), and P-wave tomography model for the mantle at 25° S (Scire *et al.*, 2015). Modified from Beck *et al.* (2015). **b)** *Model RT6* at 10 m.y. This model best represents the current structure beneath the southern Puna, providing an alternate explanation to the stationary delamination model suggested by Beck *et al.* (2015). Multiple weak roots are imposed beneath the Moho, with the more proximal root to the subducting slab triggered for removal first, followed by removal of the more distal root. Refer to Figure 2.1 and 3.8 for material colour coding.

CHAPTER 5 : SURFACE EXPRESSION AND SEISMIC VELOCITY STRUCTURE OF LITHOSPHERE REMOVAL

5.1 Introduction

As geophysical imaging of the lithosphere only provides constraints on present-day conditions, other diagnostic features must be identified in order to support occurrences of lithospheric removal. To that point, ongoing and historic removal can be inferred through the examination of regional topography and its corresponding geologic record. However, surface processes (e.g. erosion), lithospheric deformation, and transient mantle flow can also affect surface elevation, and the interaction between all these factors can make it difficult to discern lithosphere removal. In addition, the geologic record may be incomplete owing to erosion. Moreover, timescales of removal events are relatively short in geological timescales (0.2 – 12 m.y.), as demonstrated in Chapter 3, making it fleeting and sometimes undetectable in the record of the structural, geochemical, and sedimentary. However, in the central Andes there are several pieces of evidence to support removal: i) the migration pattern of mafic magmatism (Trumbull *et al.*, 2006; Kay and Coira, 2009), ii) the isotopic paleoelevational signatures (Garzione *et al.*, 2006; 2008), and iii) hinterland basin formation and uplift that cannot be linked to orogenic deformation (Carrapa *et al.*, 2011; DeCelles *et al.*, 2015). Notably, the historic spatial pattern of regional magmatism is often used as a key observation, as it indicates a rapid thermal change in the deep lithosphere (Kay and Kay, 1993). Moreover surface lavas provide thermal and compositional information of their source region, and, therefore, may be used to constrain the removal mechanism and its corresponding scale and timing (e.g. Kay *et al.*, 1994; Ducea, 2011).

Insights into the topographic signature of removal can be obtained from numerical models, as previous studies have shown (e.g. Gögus and Pysklywec, 2008; Wang *et al.* 2015). However, these models often negate the influence of regional mantle dynamics associated with the overall tectonic setting, such as the subduction of an oceanic slab; therefore, these previous studies may not fully address the surface signature of removal and how it may be superimposed on small- and large-scale mantle convective effects. For example, as shown in Chapter 3, mantle wedge flow readily affects removal dynamics, which in turn can affect the resulting surface expression.

The numerical experiments carried out in this study employ a stress free upper boundary, allowing surface topography to develop self-consistently above the destabilizing mantle lithosphere. This chapter will discuss the evolution of surface topography in the numerical models discussed in Chapter 3 (section 5.2), with emphasis placed on the models identified as best suited to represent the current lithospheric structure of the central Andes (Chapter 4). Particular attention will be paid to the timescale over which the surface elevation changes, as this is a topic of much debate (e.g. Garizone *et al.*, 2006; 2008; Hoke and Lamb, 2007; Lamb, 2011).

Additionally, in section 5.3, models are presented in terms of their corresponding seismic structure. While geology can speak to historic removal events and provide insights into consequent paleoaltimetry changes, seismic tomography is the main constraint on current lithospheric structure beneath the central Andes (e.g., Myers, *et al.*, 1998; Schurr *et al.*, 2006; Heit *et al.*, 2008, Scire *et al.*, 2015). Zones of lithospheric removal are inferred from seismic anomalies, with zones of high and low velocity interpreted to correspond to cold foundering lithosphere and hot upwelling sublithospheric mantle (SLM), respectively. However, deep seismic images can only provide a snapshot of present-day lithosphere configuration, and therefore the geodynamic models in this study can serve to provide insights into the origins of the identified velocity anomalies, most notably thermal contributions. Chapter 4 makes an initial comparison between models in this thesis to lithosphere structures previously interpreted in other studies (e.g. Figure 4.2, 4.5, 4.7, 4.8) to previous tomographic studies, while section 5.3 will allow a more direct comparison of velocity perturbations produced by these models.

5.2 Topographic expression of removal

5.2.1 Overprinting topographic signature from tectonic and geodynamic effects

Within an active subduction zone, the presence of the dense slab and the induced down-going mantle flow generated by the descending slab causes the depression of the surface. This results in a small amplitude (up to 1 – 2 km) and long wavelength (few 100 to several 1000 km) deflection, and is sometimes termed dynamic topography (e.g. Braun, 2010; Flament *et al.*, 2012). Furthermore, mantle flow can trigger removal events such as large-scale delamination, or smaller-scale Rayleigh-Taylor-type instabilities (e.g. Conrad and Molnar, 1997; Houseman and Molnar, 1997; Elkins-Tanton, 2007). Lithosphere removal of any type results in the upwelling of low density SLM and, therefore, alters the surface expression, largely due to isostatic adjustment from replacing dense mantle lithosphere with less dense material (e.g. Gögus and Pysklywec, 2008; Wang *et al.* 2015). Removal also leads to heating of

the remaining lithosphere, which decreases its density and thus increases its buoyancy, enhancing surface uplift. An additional complication is that lithosphere removal itself induces stresses on the overlying curst, and if the crust is weak (e.g. due to a felsic composition or high temperature), it may be deformed; if the crust is thickened or thinned, the elevation will adjust to isostatically balance the new crustal thickness (e.g. Neil and Houseman, 1999; Wang and Currie, 2017). Further lithosphere removal can crate secondary cells of mantle flow (as observed in Chapter 3), such that upward flow induces surface uplift and downward flow induces subsidence. Therefore, the observed surface deflection consists of an isostatic component (lateral density variations) and dynamic components (stresses associated with lithosphere destabilization and large- and small-scale mantle flow).

5.2.2 Reference model

Model Ref1 is the reference model, in which there is no dense root and no gravitational removal occurs. Figure 5.1 shows the elevation profile for this model at different times, demonstrating that the plateau maintains an average 3 km elevation for much of the model run, except for the last 2 m.y., when crustal material begins to undergo pure shear shortening. This results in slight lithosphere thickening and surface uplift by 20 m.y. Mantle lithosphere close to the descending oceanic slab is continuously removed through ablation and the entire continent sits above a convection cell induced by subduction (mantle wedge corner flow). These factors induce vertical stresses on the continent that act to deflect the surface, imposing an additional topographic signature. The subduction effects cause the slight deflection of the plateau elevation from 3.4 km (0 m.y.) to 2.8 km (5 m.y.), i.e. subsidence of 600 m. Moreover, the orogenic load of the plateau causes the flexural depression of the craton, resulting in the development of a foreland basin. The elevation profile in Figure 5.1 is therefore the expected elevation profile for an orogen with no lithosphere removal. In subsequent sections, models with lithosphere removal are discussed; any variations in the elevation between these models and *Model Ref1* are therefore related to local lithosphere dynamics.

5.2.3 Delamination removal models

Figure 5.2 shows *Model D1* which exhibits the coherent removal of mantle lithosphere in the form of retreating delamination. The imposed root is 100 kg m^{-3} denser than the surrounding mantle material, and its negative buoyancy results in the regional deflection of the initial elevational profile (Figure 5.2a). The surface near the dense root first undergoes ~0.4 km of subsidence and then exhibits

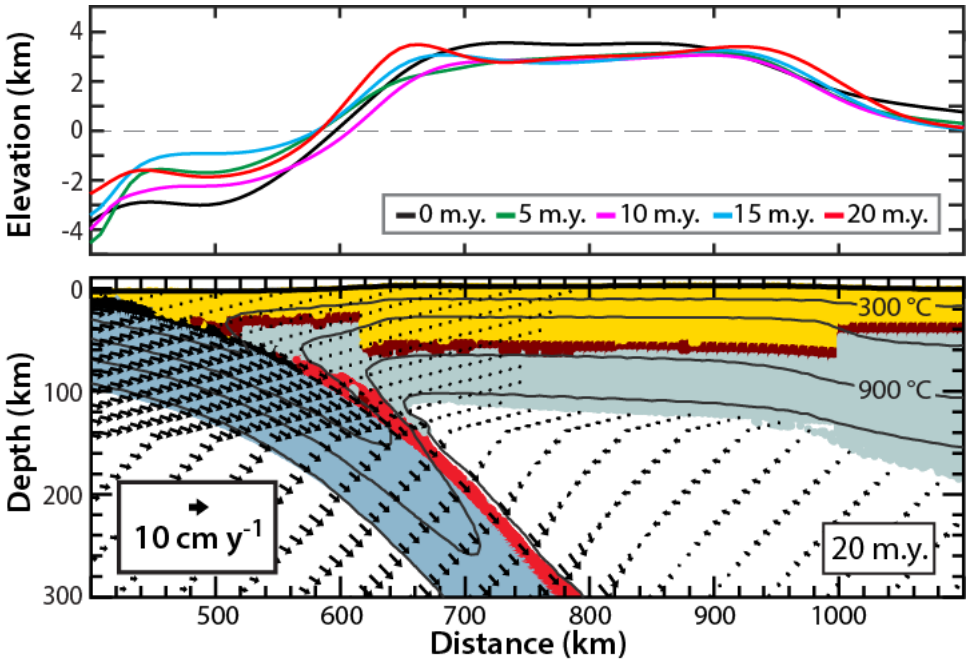

Figure 5.1 Surface elevation profiles at 0, 5, 15, 20 m.y. (top) and *Model Ref1* at 20 m.y. (bottom). This is the reference model for a Cordilleran orogen with no lithosphere removal. Refer to Figure 2.1 material colour coding.

rapid uplift (2.6 km to 3.48 km) as the root detaches at 2 m.y (Figure 5.2b), the gravitational instability of the root itself serving to trigger the delamination. The mantle lithosphere coherently peels back, transiently decoupling from the overlying crust as the point of detachment migrates trenchward. After removal is triggered by 1.5 m.y., delamination proceeds rapidly and is completed by 9 m.y. The elevation profiles show that a wave of surface uplift migrates behind the point of detachment (Figure 5.2a). As delamination proceeds, the surface deflection is asymmetric, with regions overlying the point of detachment being locally depressed followed by uplift; as a result, Figure 5.2b shows slightly raised elevations after mantle lithosphere is locally removed, peaking at ~3.6 km, 0.8 km higher than the reference model. After delamination, thermal relaxation and isostatic restoration result in an average plateau elevation of ~3.3km. This is approximately 0.5 km higher than the reference model with no lithosphere removal (Figure 5.1). Note that after 17 m.y., the plateau undergoes an additional ~0.5 km of uplift as it begins to shorten; this is outside the timeframe of interest in this study.

The elevation change caused by the coherent removal of the plateau mantle lithosphere via retreating delamination is affected by both its overall strength as well as the density of the root.

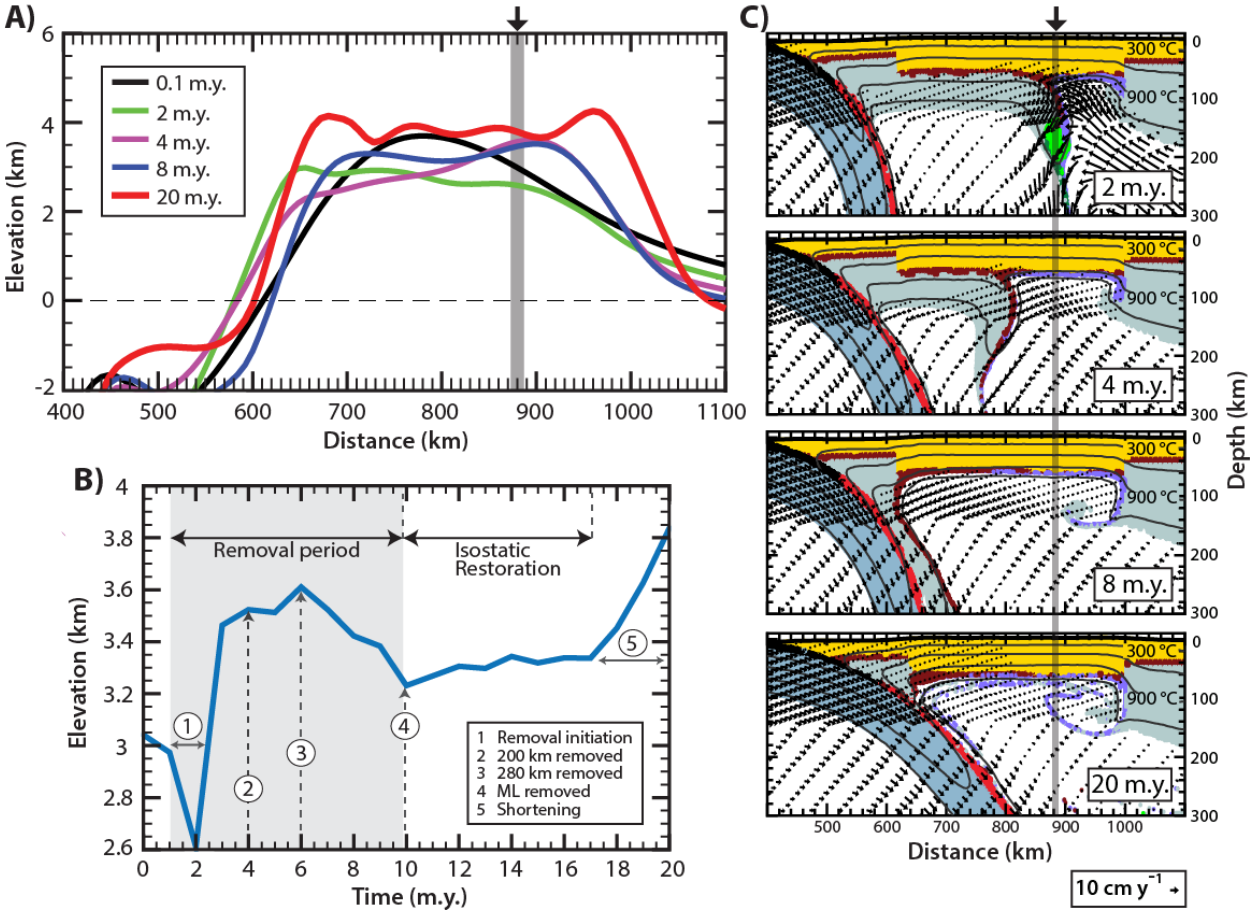

Figure 5.2 **A)** Elevation profiles for *Model D1*, exhibiting retreating delamination. **B)** Time series of the elevation at x=880 km, indicated by the grey line in both A) and C). **C)** Model domain at the time shown in A). Refer to Figure 2.1 and Figure **3.2** material colour coding.

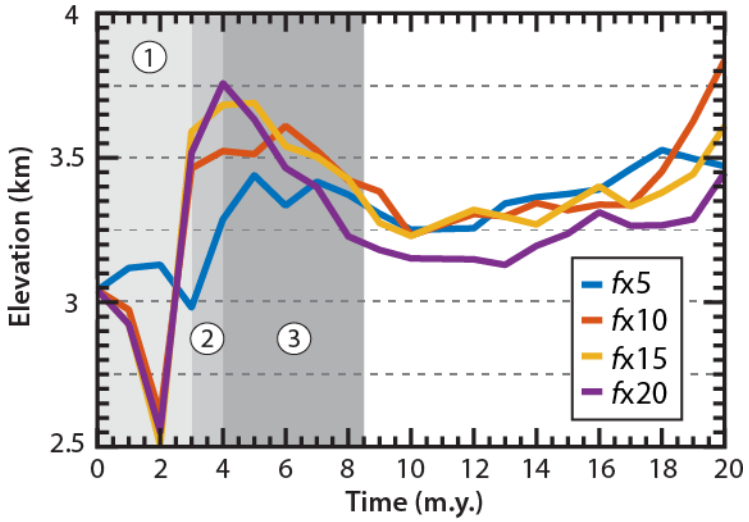

Figure 5.3 Elevation change at x=880 km (see Figure 5.2A and C) for delamination models with different mantle lithosphere strengths; *Model D1* has *f*=10. All models have a root that is 100 kg m^{-3} more dense than the mantle. Refer to text for explanation.

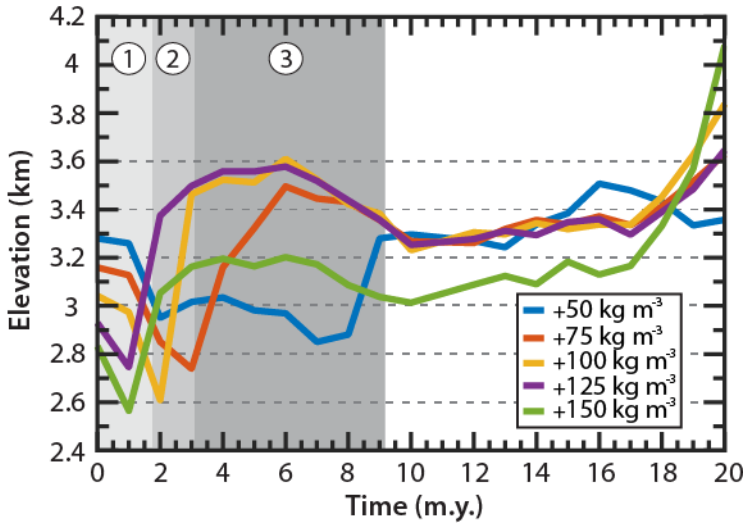

Figure 5.4 Elevation change at x=880 km (see Figure 5.2A and C) for delamination models with different root density contrasts with respect to the mantle; *Model* D1 has a density contrast of 100 kg m^{-3}. In all models, the mantle lithosphere viscous scaling factor is *f*=10. Refer to text for explanation.

Figure 5.3 shows the elevation variation at x=880 km for models in which the root density contrast is 100 kg m^{-3} and the mantle lithosphere strength is changed by varying the viscous scaling factor *f*; in *Model D1*, the mantle lithosphere has *f*=10. Although the duration and onset of removal is affected by changes in mantle lithospheric strength (see section 3.3.3.2), a similar pattern of elevation changes is observed as each model undergoes delamination. The negative buoyancy of the root is responsible for the maximum deflection of the surface (Figure 5.3 (1)), the amplitude of which is lower for weaker mantle lithospheres. The maximum uplift following root removal is greater and more rapid for higher strengths (Figure 5.3 (2)): 0.4 km compared to 1.25 km for *f*=5 and *f*=20, respectively. Figure 5.4 shows the elevation changes for models in which the root density is changed from 50 to 150 kg m^{-3}, where *Model D1* has a root density contrast of 100 kg m^{-3}; all models use a scaling factor of *f*=10 for the mantle lithosphere. The net elevation change is most affected by the bulk density of the imposed root, where greater density contrasts cause earlier removal onsets and the greatest surface deflections (Figure 5.4 (1)). The maximum uplift following root removal is larger and more rapid for higher density contrasts (2): 0.2 km compared to 1 km for 50 kg m^{-3} and 100 kg m^{-3}, respectively. However, greater density contrasts also limits the time the root is viscously coupled to the adjacent mantle lithosphere being delaminated and affects the surface expression of its removal dynamics (refer to Chapter 3 for discussion). For both Figure 5.3 and 5.4, after the root is removed, the remaining lithosphere isostatically and thermally re-establishes equilibrium (see (3)).

5.2.4 Rayleigh-Taylor-type removal models

Previous studies of Rayleigh-Taylor (RT) -type instabilities have demonstrated that feedbacks between the 'drip' and crustal deformation being are controlling factors capable of modifying the surface profile (e.g. Neil and Houseman 1999; Pysklywec and Beaumont, 2004; Wang and Currie, 2017). RT instabilities commonly induce surface subsidence as the 'drip' is removed, (Bindschadler and Parmentier, 1990; Houseman et al., 2000). Finite strain trajectories produced in these models indicate the 'drip' induces traction along the base of the crust as well as downward viscous drag that together pull the Moho and overlying crust down. However, if the crust is weak, the stresses can induce internal deformation of the crust as the 'drip' descends. As a result, the crust can thicken as the 'drip' descends, causing the surface uplift after an initial period of subsidence; if the crust is sufficiently weak, the area above the drip may become a topographic high during removal (Neil and Houseman, 1999; Wang *et al.*, 2015; Wang and Currie, 2017). However, these previous studies focused on localized removal events

representing the hinterland only, and did not incorporate the effects of an active subduction zone. The following sections discuss the elevation changes resulting from removal of single and multiple dense roots, emplaced within the mantle lithosphere, for an active convergent tectonic setting.

5.2.4.1 Single roots

Figure 5.5 shows the elevation profiles for *Models RT1* and *RT2*, which exhibit small-scale removal of mantle lithosphere due to the emplacement of single dense roots wither proximal (*RT1*) or distal (*RT2*) to the descending oceanic slab. In both models, the imposed root is 100 kg m^{-3} denser than the surrounding mantle material and scaled by *f*=1; the negative buoyancy of the root results in the local deflection of the initial elevational profile, evident at 6 m.y. and 13 m.y. for the proximal and distal root, respectively. Emplacement of a single root results in slightly asymmetric elevation profiles, and it is evident from Figure 5.5 that the uplift caused by removal of the root is localized to the overlying region. In both cases, root removal results in almost immediate uplift of ~0.5 km within 1 m.y., which is later enhanced by a clockwise cell of mantle circulation within the site of the removed root (Figure 3.9a (15 m.y.) and b (16 m.y.). The local cell derives from mantle wedge flow and is confined to the gap within the mantle lithosphere, and the upward flow causes further uplift, resulting in a total uplift ~1 km in elevation for both models. The localized cells of mantle circulation can explain zones of seemingly undercompensated crust (i.e. surface elevation is higher than expected for crustal thickness); these represent areas of positive dynamic topography.

As discussed in section 3.4.3.1, the onset and duration of removal is affected by the density of the root, with increased density resulting in more rapid removal regardless of root position. As a result, the rate of uplift that occurs in response to the removal of a RT-type instability is dependent on the root density contrast, and in turn the duration of removal. A comparison of the surface elevations produced by models with various root density assignments (Figure 5.6) shows that the change in elevation triggered by the removal of the root occurs at increasingly delayed rates as root density decreases. This is a direct consequence of the increasing removal onsets and durations observed with lower root density contrasts (Figure 3.13). These longer onset times delay the formation of the secondary cell of SLM; for example, proximal root density contrasts of 100 kg m^{-3} and 50 kg m^{-3} show removal initiated by 3 m.y. and 9 m.y., respectively, but only the former sees the formation of the cell within the 20 m.y. runtime (at 15 m.y.). As a result lower density contrasts are not as readily affected by the dynamic influence of the upward mantle flow, reflected in their lower elevations. Density also affects the wavelength of the

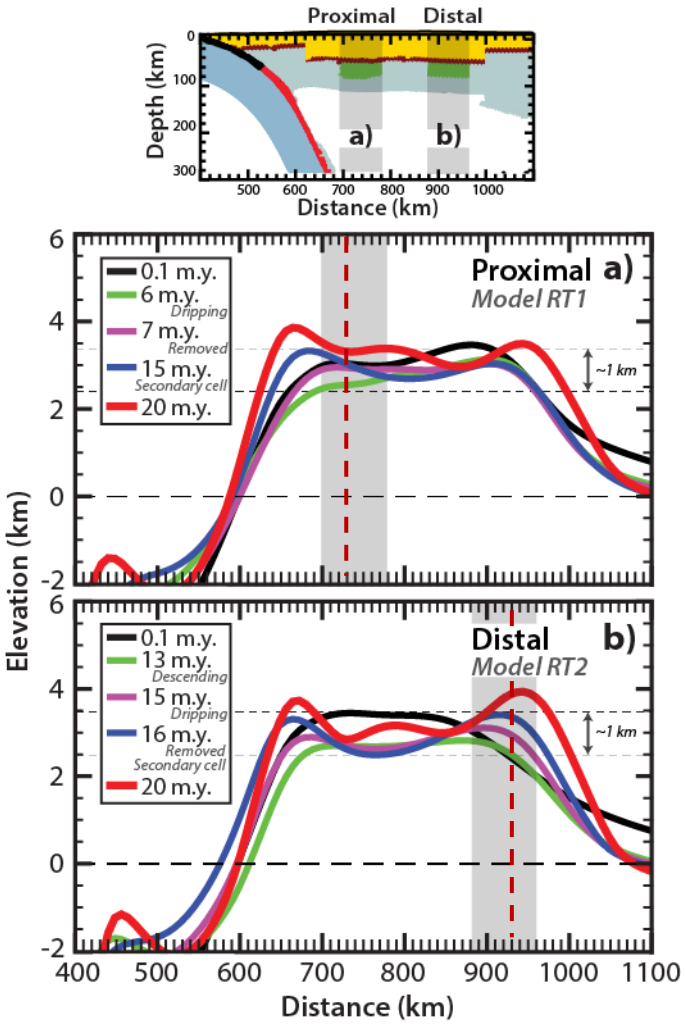

Figure 5.5 Elevation profiles for a single root removed as a RT instability. **a)** Profiles for the proximal root, placed closer to the trench, corresponding to *Model RT1*. **b)** Profiles for the distal root, placed in closer to the craton, corresponding to *Model RT2*. Dashed red lines refer to locations a) x=730 and b) x=930, used in Figure 5.6.

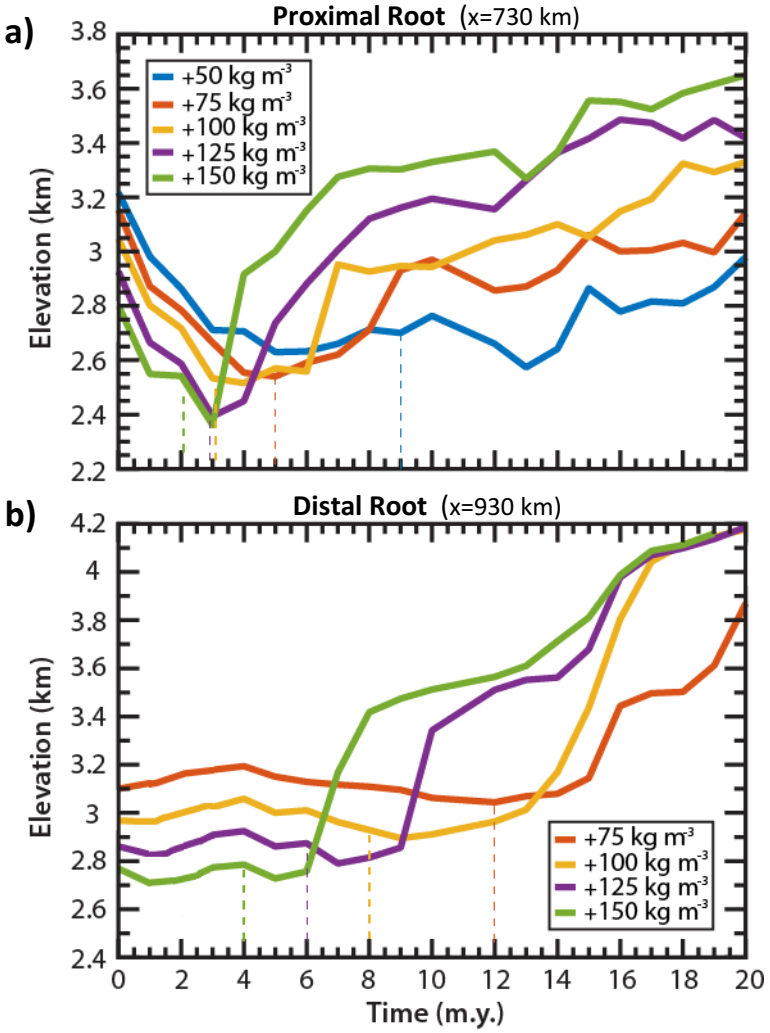

Figure 5.6 Elevation changes for Rayleigh-Taylor models with different root density contrasts with respect to the mantle at **a)** x=730km and **b)** x=930 km (refer to Figure 5.5 for locations along regional profile); *Models RT1* and *RT2* both have a density contrast of 100 kg m^{-3}. In all models, the mantle lithosphere viscous scaling factor is f=10. Dash lines indicate onset of removal, as indicated in Figure 3.13. Refer to text for explanation.

surface deflection with greater root density resulting in greater subsidence; for example, a density contrast of 150 kg m^{-3} and 50 kg m^{-3} produce deflections spanning >200 km and less than 100 km, respectively. Moreover, model tests reveal stronger mantle lithosphere also results in delayed surface uplift post root removal, regardless of root position, reflecting the fact that the root is removed in two stages (see section 3.4.3.2).

5.2.4.2 Multiple roots

The existence of multiple dense roots within the mantle lithosphere results in more complex removal dynamics leading to more complicated lithospheric structure and surface expressions. These are affected by size, density, and rheology of the imposed roots (see section 3.4.3). Figure 5.7 shows *Model RT6*, which consists of two roots beneath the Moho, 100 kg m^{-3} denser than the adjacent mantle material and with a rheology scaling factor of f=1; the mantle lithosphere scaling factor is f=10. The negative buoyancy of the roots causes an initial regional subsidence of >0.6 km within 3 m.y. This is subsequently modified by the removal of the proximal root which destabilizes first due to mantle wedge flow. As the root is removed, the surface remains as a topographic low (<0.1 km uplift). After removal, the surface directly above this root locally rebounds by 0.5 km within 2 m.y. The initial uplift is due to the removal of the dense root; this is enhanced by the associated upwelling as mantle replaces the root. The distal root is then removed at 11 m.y. This causes uplift of 0.5 km in the region above this root, owing to both the root removal and mantle upwelling (Figure 5.7a). Removal of the distal root also influence the elevation near the site of the proximal root, as it creates mantle upwelling here and causes uplift of 0.35 km (Figure 5.7b). After removal of both roots, mantle flow causes further lithosphere thinning at the proximal site; this generates a secondary cell of circulation that flows in the opposite direction to the mantle wedge flow (Figure 5.7c). This causes this site to continue to experience uplift at a steady rate. Overall, this site experiences a net elevational change of 1 km within 15 m.y.; after this, the elevation is affected by shortening.

Figure 5.8 shows the evolution of surface elevation for *Model RT8*. This model is identical to *Model RT6* (Figure 5.7) except for the dimensions of the two roots that span the entire thickness of the plateau mantle lithosphere. Removal proceeds more rapidly in *Model RT8*, with the lower portions of the roots foundering in a quasi-simultaneous manner, and regional uplift of ~0.3 km occurring within the first 1 m.y. Figure 5.7B and 5.8B show similar uplift curves above the proximal and distal foundering root, respectively, varying only due to the difference in removal onset. However, the proximal root in

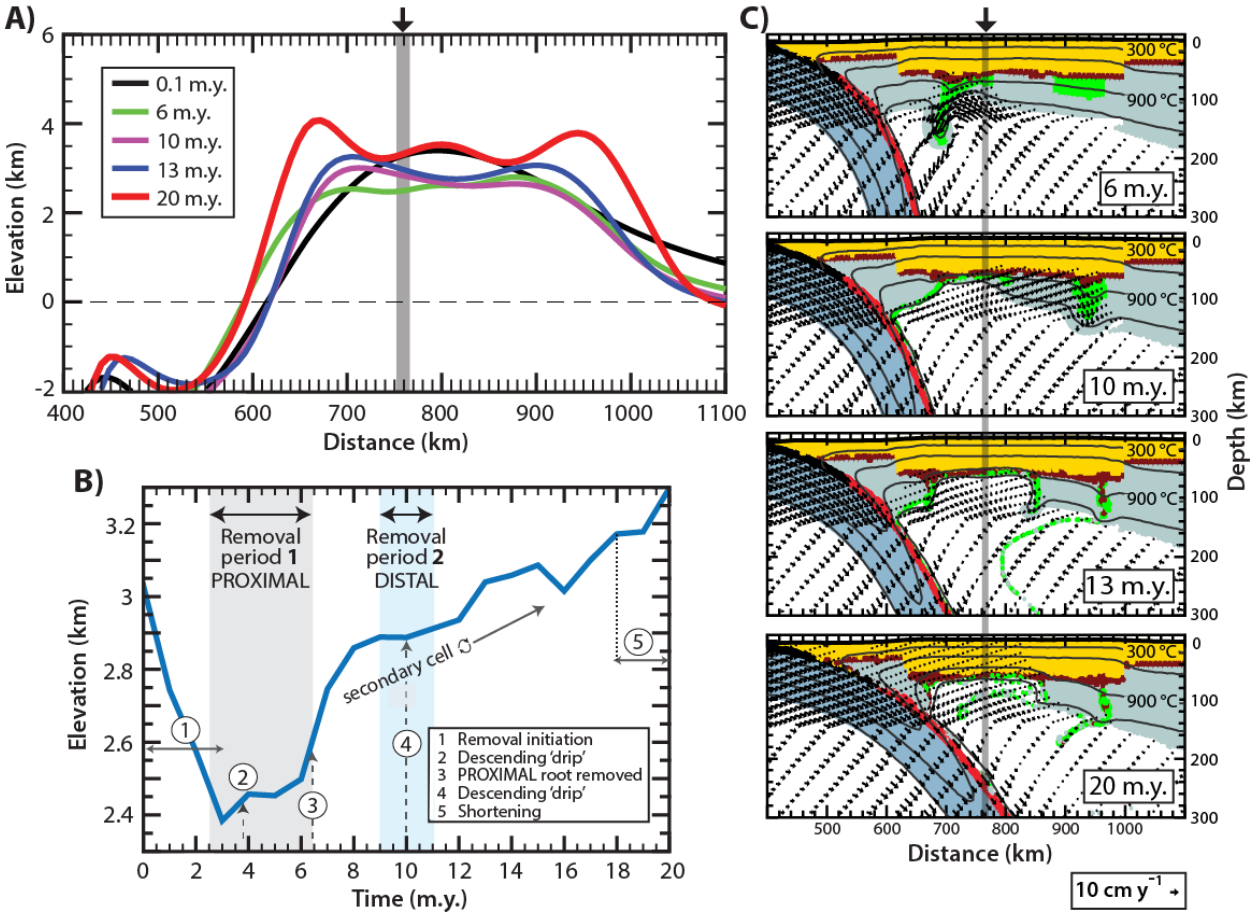

Figure 5.7 Evolution of *Model RT6*, where multiple dense roots (*f*=1, ρ=3350kg m^{-3}) are emplaced beneath the Moho. **A)** Elevation profiles shown for 0.1, 6, 10, 13 and 20 m.y. **B)** Evolution of elevation at x=760 km, indicated by the grey line in A), and C). **C)** Model domain at the time shown in A). Refer to Figure 2.1 and Figure **3.8** for material colour coding.

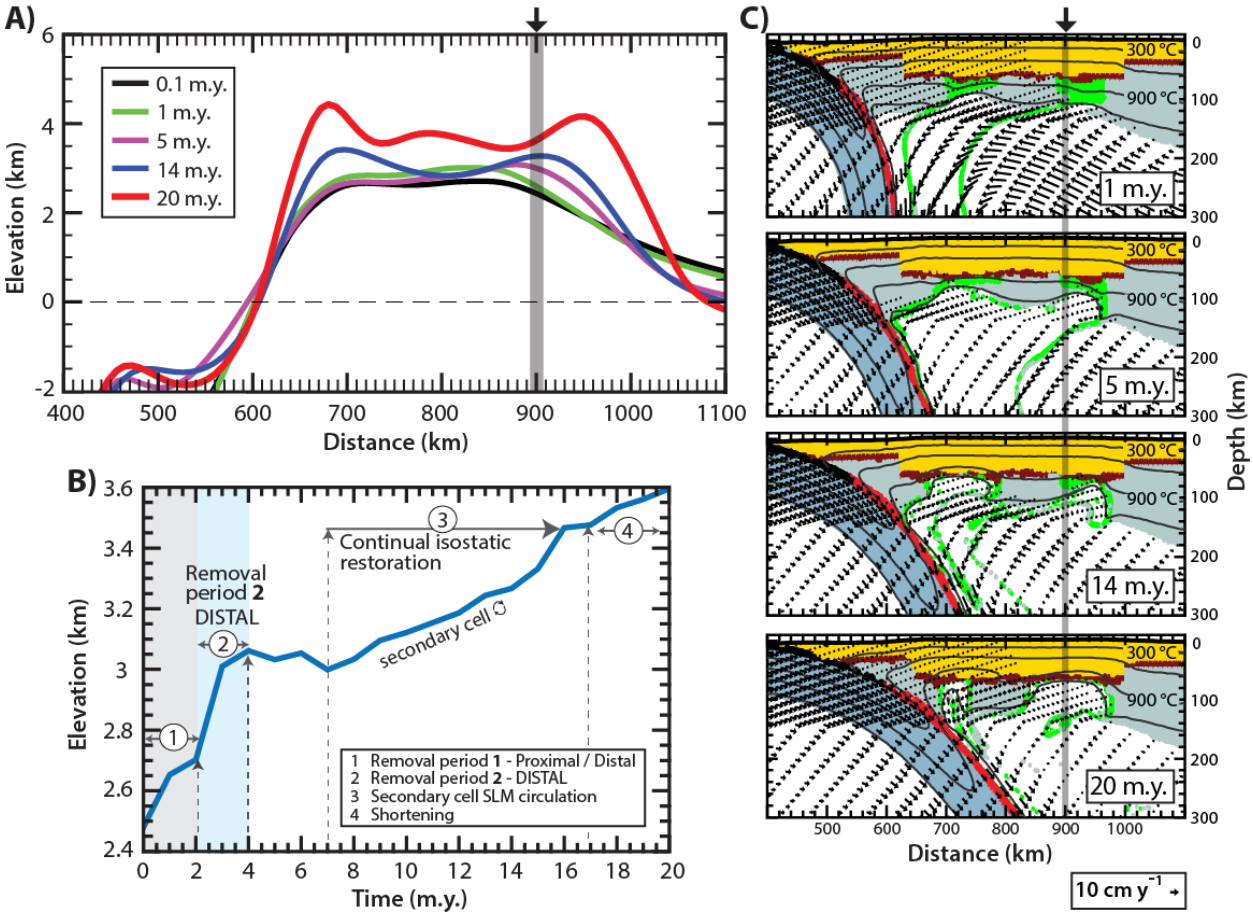

Figure 5.8 Evolution of *Model RT8*, where multiple dense roots (f=1, ρ=3350kg m^{-3}) are emplaced beneath the Moho and span the entire thickness of the mantle lithosphere. **A)** Elevation profiles shown for 0.1, 1, 5, 14 and 20 m.y. **B)** Evolution of elevation at x=904 km, indicated by the grey line in A), and C). **C)** Model domain at the time shown in A). Refer to Figure 2.1 and Figure **3.8** for material colour coding.

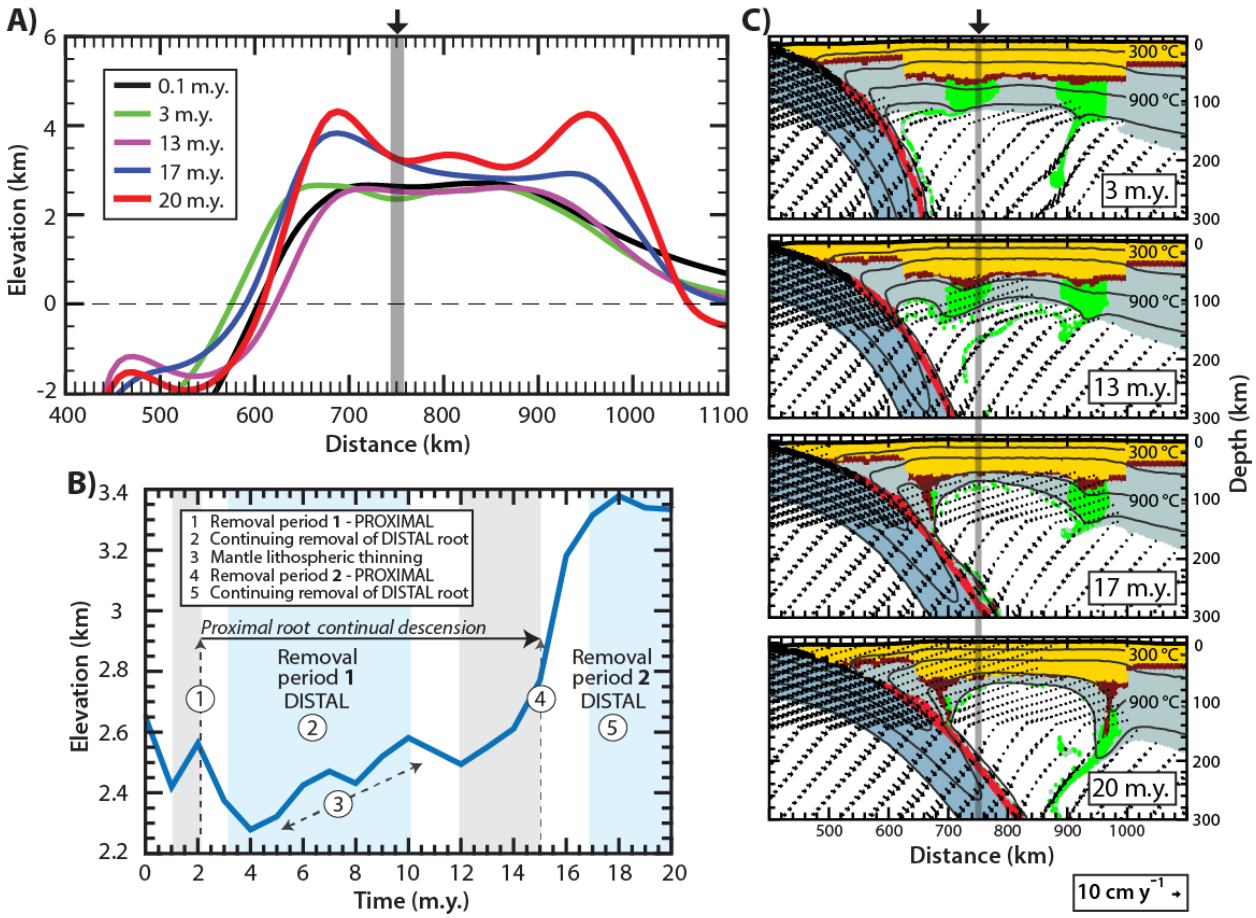

Figure 5.9 Evolution of *Model RT7*, where multiple dense roots (f=10, ρ=3350kg m^{-3}) are emplaced beneath the Moho and span the entire thickness of the mantle lithosphere. **A)** Elevation profiles shown for 0.1, 3, 13, 17 and 20 m.y. **B)** Evolution of elevation at x=752 km, indicated by the grey line in A), and C)**. C)** Model domain at the time shown in A). Refer to Figure 2.1 and Figure **3.8** for material colour coding.

Model RT8 does not experience as much immediate uplift, resulting in a more symmetric regional profile, until the SLM cell forms and enhance uplift above the empty distal root site post-removal. Overall *Model RT8* experiences a similar net elevational change to *Model RT6* despite having different final lithosphere structures, with uplift of ~ 1.2 km occurring within 16 m.y. due isostatic adjustment and dynamic topography post root removal.

Figure 4.8 shows the evolution of *Model RT7* to demonstrate how root rheology affects the removal process and its surface expression. In these models, the two dense roots have the same rheology as the surrounding mantle (scaling factor of *f*x10). As discussed in section 3.4.2.3 and 3.4.2.4, removal of these roots induces thinning of the entire plateau mantle lithosphere (Figure 5.9c). The system undergoes symmetric removal, albeit unsynchronized, of the dense roots. Viscous drag induces flow in adjacent mantle lithosphere, resulting in the thinning of the mantle lithosphere as roots descend. Thinning is enhanced by the subsequence mantle upwelling. These dynamics are reflected in the surface elevation profiles (Figure 5.9a and b). On a regional scale, there is minimum uplift (<250 km) during the removal of the roots; the plateau remains at a fairly constant elevation with no clear sites of localized deflection. Thus there is little to no surface expression in initial stages of lithosphere thinning, likely because of viscous coupling between the strong roots and adjacent mantle lithosphere. This is followed by rapid surficial uplift starting at 15 m.y. coincident with the full removal of the proximal root and ongoing descent of the distal root. At 17 m.y., the surface topography of the plateau is regionally asymmetric, with elevations reaching 3.8 km closer to the trench and 2.9 km closer to the craton. This is because the area closer to the craton is still underlain by high density root and mantle lithosphere. Overall, this model demonstrates that surface uplift can occur asymmetrically if there are multiple dense roots that are removed at different times, and may appear as a migrating wave of uplift, especially if the roots are strong and viscously coupled to the mantle lithosphere. In this model, the uplift occurs first on the trench side of the plateau (near proximal root) and then on the craton side (near distal root). This sequence is similar the uplift pattern that may be expected for large-scale delamination that proceeds from the trench to craton (c.f. Figure 5.2 for delamination in the opposite direction). This means that it may not be possible to unequivocally identify the style of removal using only surface topography records.

5.2.5 Modelling summary: Surface expression of lithosphere removal

The surface expression resulting from various types of lithospheric removal can be summarized as the follows:

1. Delamination results in asymmetric elevation, with uplift starting on the craton side of the plateau and proceeding trenchward as the dense mantle lithosphere is removed as a coherent slab. This style of removal results in a transient local elevation maxima as the surface experience rebounds following the abrupt detachment of the root, and is enhanced by mantle upwelling following detachment. Models in this study have a net uplift of 0.5 – 0.7 km, with greater uplift for higher density roots.
2. Rayleigh-Taylor-type instabilities can generate viscous drag that induces crustal flow as the gravitational unstable dense root descends. However, the models within this study show no significant thickening during root removal. As a result, removal is characterized by localized subsidence as the root destabilizes and 'drips', followed by uplift. Changes in the surface elevation are limited to the zone overlying the destabilizing root, producing a slight transient asymmetric uplift profile. The direction of this asymmetry is dependent on the trajectory of the foundering root, and, therefore, root position relative to the subducting slab: in closer proximity to the slab uplift proceeds trenchward, whereas roots closer to the craton show uplift proceeding cratonward.
3. RT- type removal of a single root results in ~ 1 km uplift, localized above the destabilized root. The uplift signature comprises of the rebound resulting from the removal of the root itself (isostatic uplift), typically occurring within 1 m.y. once triggered, and continuous dynamic uplift generated by the isolated mantle convective cells that form within the resultant mantle lithospheric gaps (dynamic uplift) (Figure 5.10). Uplift occurs more rapidly with decreased mantle lithosphere strength and increased density of the root.
4. Multiple roots result in a more complicated topographic signature, as the surface elevation undergoes multiple stages of regional and local adjustments. Elevational profiles undergo multiple stages of regional and local adjustments. Roots with a weak rheology have a longer stage of uplift (occurring over 15 m.y.), and the average net change remains constant at ~1 km. Contrastingly, stronger roots exhibit a regionally asymmetric surface signature similar to that produced by retreating delamination. However, the surface expression of removal is delayed, preceded by a period of apparent inactivity and followed by a period of rapid uplift (between 13

and 17 m.y.); this uplift results in ~1 km elevation change. In both cases, the elevational change is the result of both isostatic adjustment post root removal, and the effect of mantle flow within the empty root sites generating a positive topographic signature (Figure 5.10).

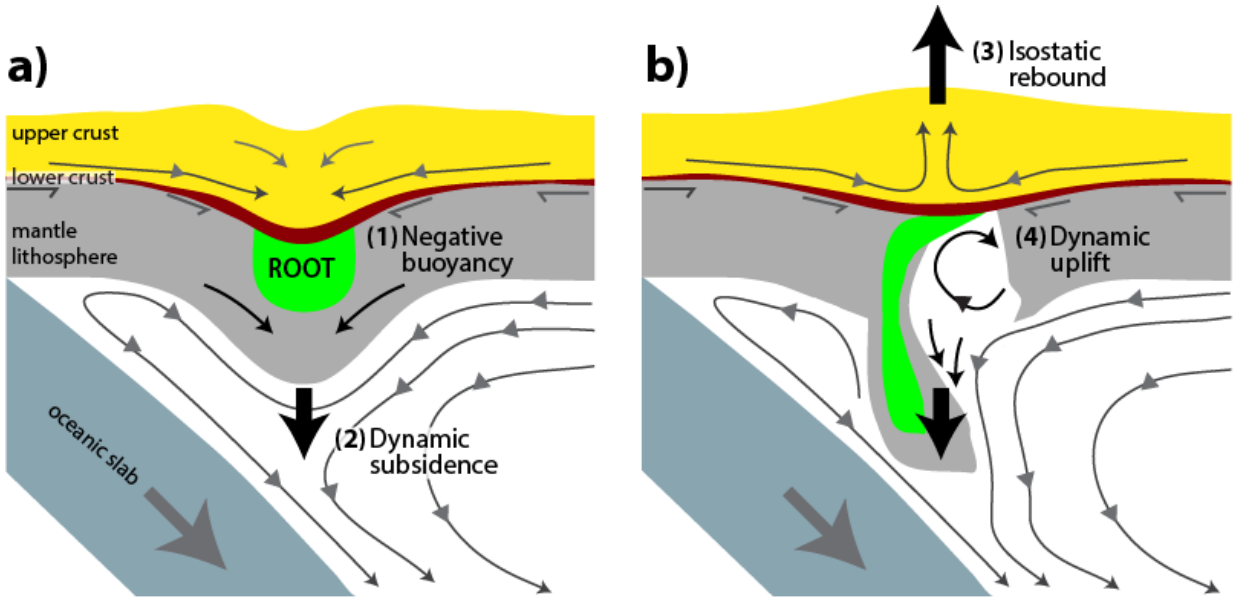

Figure 5.10 Schematic diagrams summarizing **a)** the descent of a gravitationally unstable root, and **b)** the isostatic adjustment post-removal during an episode of mantle lithosphere foundering. Dynamic topography induced by vertical flow enhances the initial subsidence and the subsequent uplift as the root is removed (provided that a localized region of thin lithosphere is able to confine a secondary cell of sublithospheric mantle circulation). From the models within this study, uplift is enhanced by 0.3 – 1 km by dynamic topography.

5.3 Modelled seismic structure

Seismic tomography images of the shallow mantle are often used to identify sites of lithosphere removal (e.g., Myers, *et al.*, 1998; Schurr *et al.*, 2006; Heit *et al.*, 2008, Scire *et al.* 2015). In order to assess how lithosphere removal may be reflected in the seismic velocity structure of the mantle, the geodynamic models in this study have been converted to P-wave and S-wave seismic velocity images, using the method described in section 2.7.2. For this, the temperatures and pressures in the mantle region of the models are mapped to seismic velocity, assuming a pyrolytic mantle composition. Both absolute P- and S-wave velocity plots are generated, as well as velocity anomaly maps. The seismic

anomalies are calculated relative to the average velocity at each depth (e.g. van Wijk *et al.*, 2010), and thus they show the velocity perturbation relative to the regional velocity structure.

Common features predicted in all converted models include those captured in tomography studies: high seismicity velocities within the cool descending oceanic slab and mantle lithosphere (especially the thick craton lithosphere), and low velocity zones in the hot mantle wedge. These features are consistent with the strong temperature control on seismic velocities. Note that the velocity conversions shown here do not include the effects of compositional variations. Chemical depletion of craton lithosphere is expected to have only a minor effect on the velocities (Figure 2.7; see also Goes *et al.*, 2012). However, the presence of eclogite or melt will affect the velocities; it is expected that higher eclogitic content and increased melt percentage would enhance the high and low velocity anomalies, respectively. In particular, increased eclogitic content within the root used to trigger removal would register increased P- and S- velocities of ~0.4 km s^{-1} and ~0.12 km s^{-1}, respectively, compared to the plots shown below.

Overall, low velocity zones that arise due to the subduction zone setting are represented in all the models (Figures 5.11, 5.12, 5.13, and 5.14) including mantle wedge flow (V_p = 7.8 – 8.1 km s^{-1}, V_s = 4.75 km s^{-1}) and slab rollback flow (V_p = 7.75 km s^{-1}, V_s = 4.35 km s^{-1}). In particular, Figure 5.11 shows the converted seismic structure for the delamination model *Model D1*. As the mantle lithosphere coherently decouples from the overlying crust, the detached mantle lithosphere registers as a high velocity anomaly that grows in length as more material peels away, generating 1 – 3 % increased velocities for P- and S- waves. The subsequent ascension of hot SLM appears as low P- and S- wave velocity anomalies with magnitudes of of 5 – 8%, that weaken as the system comes into thermal equilibrium.

Figure 5.12 shows the converted seismic structure for the Rayleigh-Taylor model *RT6*, in which two weak dense roots (3350 kg m^{-3}, f=1) are imposed beneath the Moho. Cold mantle lithosphere descends as the roots become increasingly unstable due to enhanced negative buoyancy. The 'drips' are cool relative to the surrounding mantle and therefore they appear as high velocity zones that are 1- 3 % faster than the surrounding both P- and S- waves. The anomalies would be larger if compositional effects (i.e., eclogite) were included. The temperature variations from small-scale convection within the empty proximal root site are large enough to be detected as strong S-wave anomalies (6-10% slower), and as weaker P-wave anomalies (4-6% slower). Similar features are observed for the other Rayleigh Taylor models, *Models RT7* and *RT8* (Figures 5.13 and 5.14). A notable difference in these models is that hot basal material from the mantle lithosphere is removed first, and the thermal contrast from the

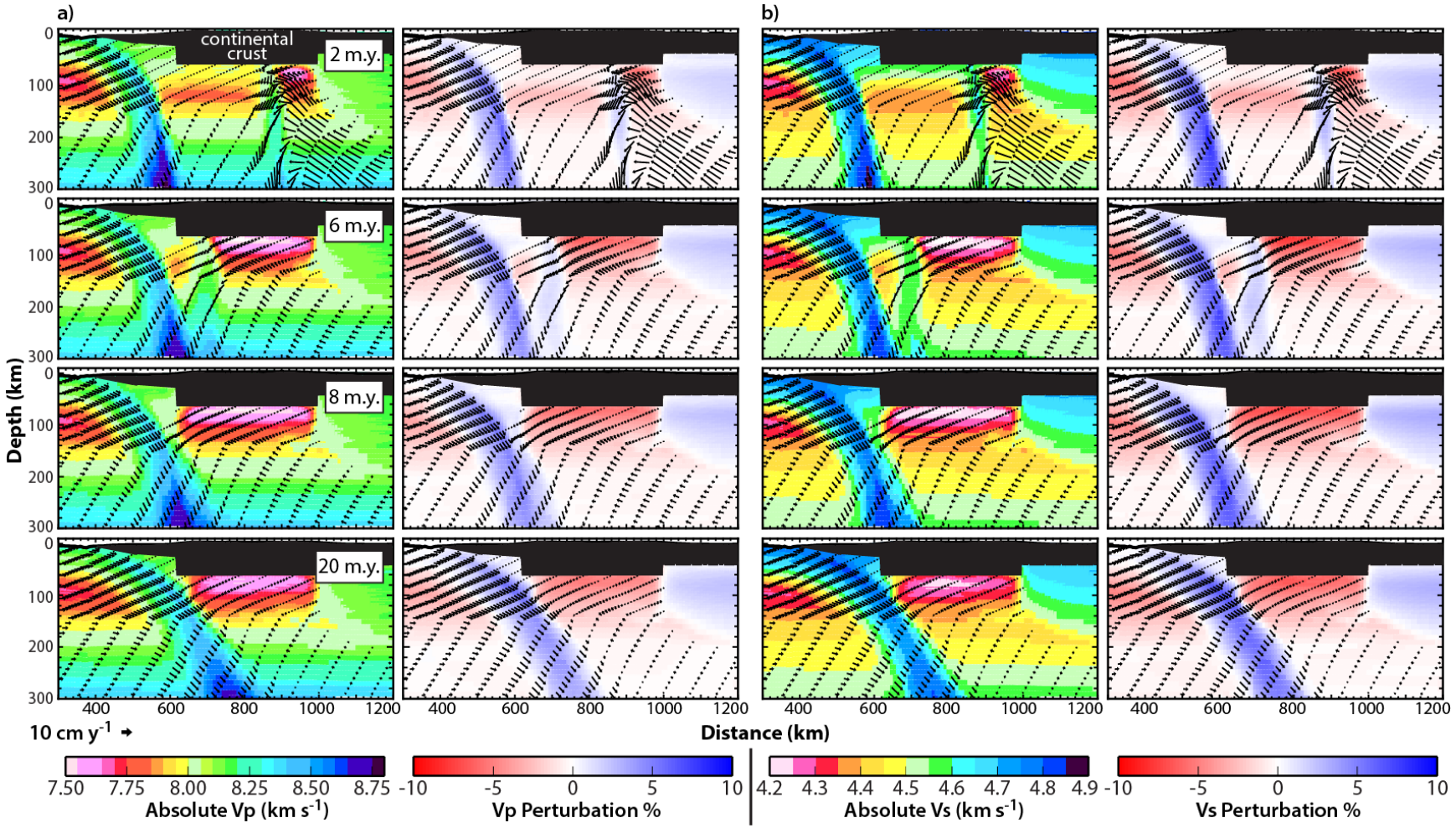

Figure 5.11 Predicted seismic structure for the delamination *Model D1* (imposed LVZ prescribed 10^{19} Pa·s with dense root of 3350 kg m^{-3}) for a constant pyrolytic composition, shown at times of 2, 6, 8, and 20 m.y. Both absolute **a)** P- and **b)** S- wave velocities are shown, as well as the velocity anomalies relative to the average velocity at each depth. See Figure 3.3 for model material and temperature structure. The continental crust is plotted in black as the velocity conversion only considers mantle structure.

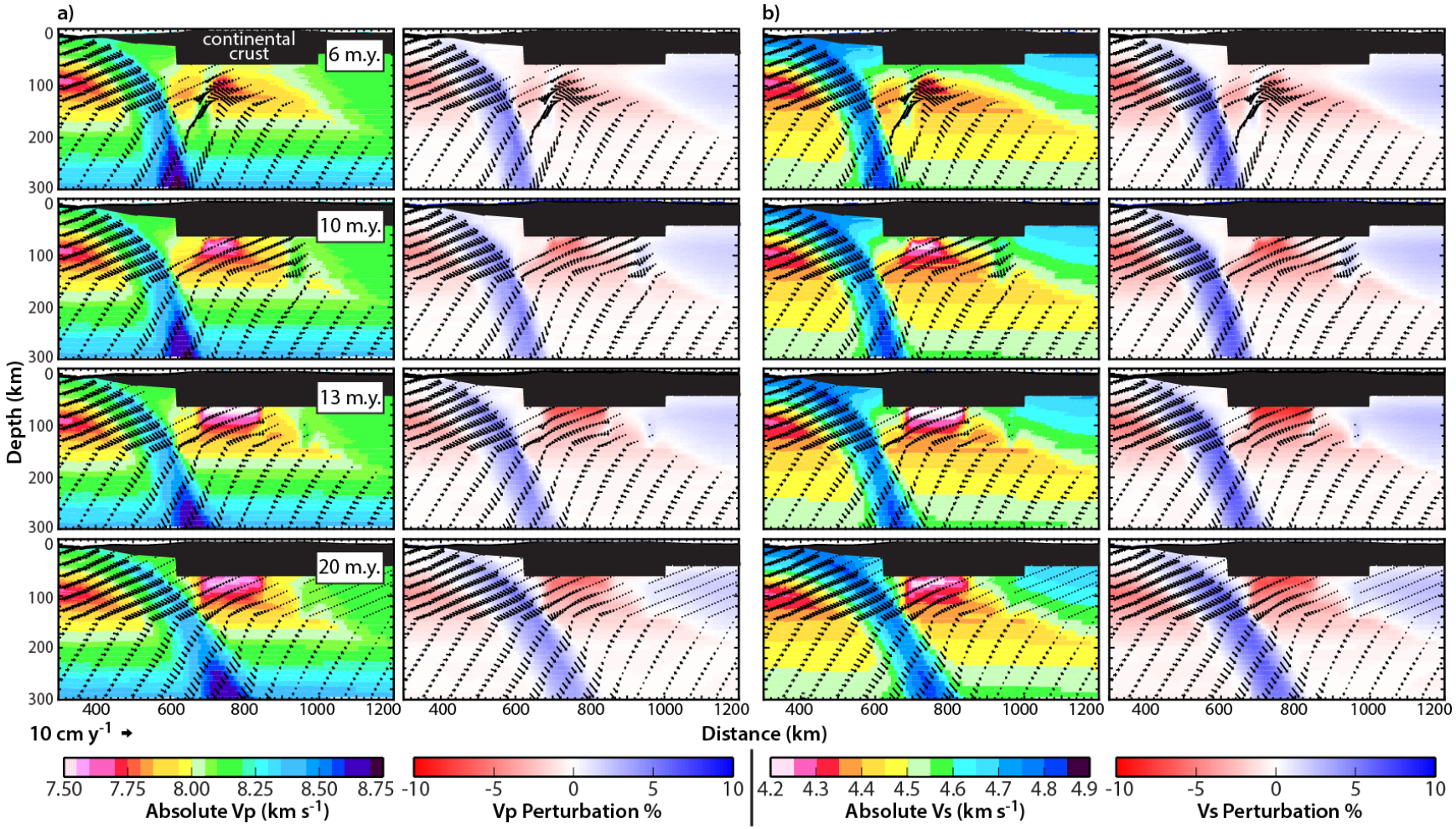

Figure 5.12 Predicted seismic structure for the Rayleigh-Taylor *Model RT6* (two dense roots imposed beneath the Moho, 3350 kg m^{-3} scaled f=1) for a constant pyrolytic composition, shown at times of 6, 10, 13, and 20 m.y. Both absolute **a)** P- and **b)** S- wave velocities are shown, as well as the velocity anomalies relative to the average velocity at each depth. See Figure 3.11b for model material and temperature structure. The continental crust is plotted in black as the velocity conversion only considers mantle structure.

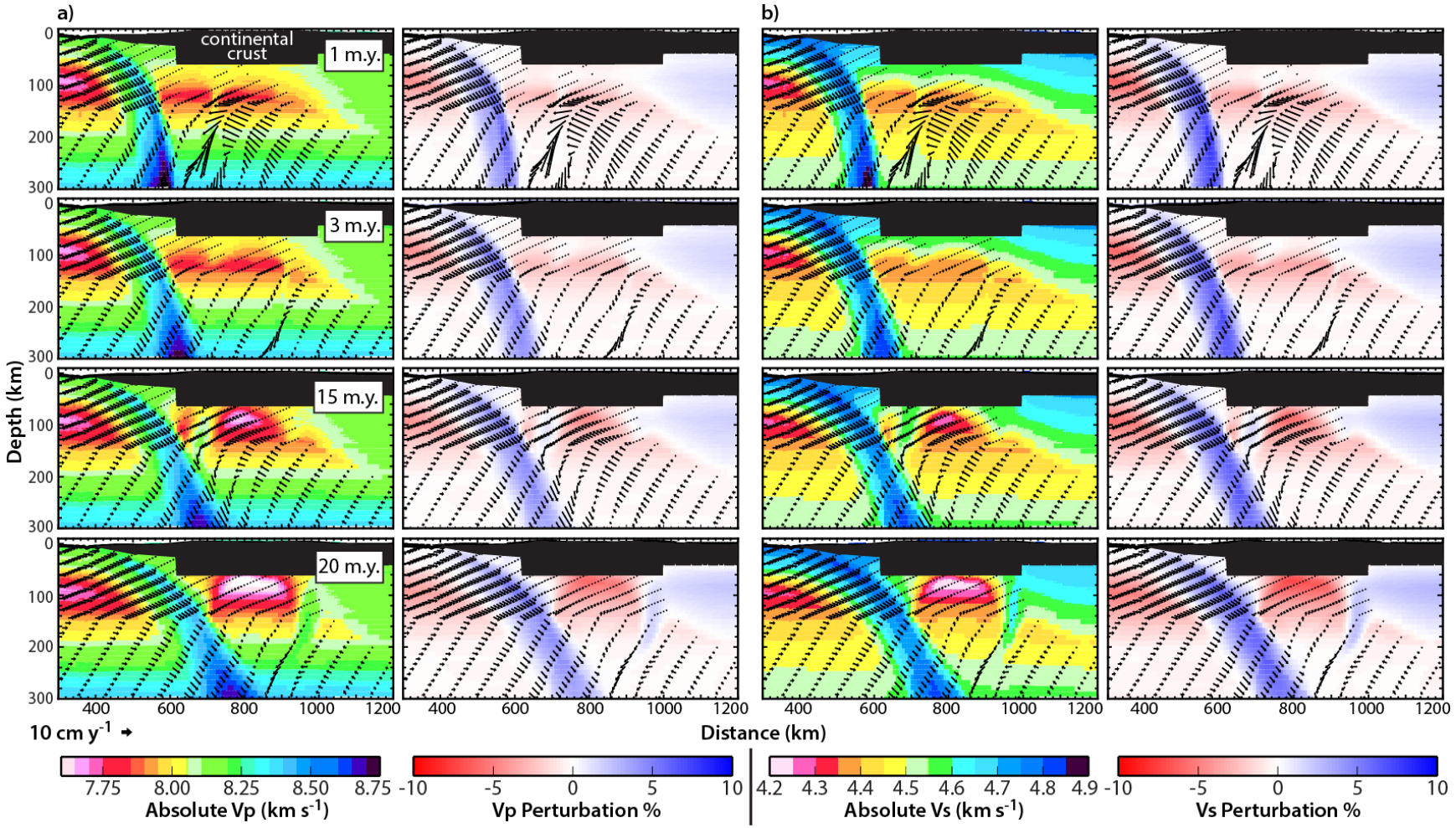

Figure 5.13 Predicted seismic structure for the Rayleigh-Taylor *Model RT7* (two dense roots imposed beneath the Moho, 3350 kg m^{-3} scaled f=10) for a constant pyrolytic composition, shown at times of 1, 3, 15, and 20 m.y. Both absolute **a)** P- and **b)** S- wave velocities are shown, as well as the velocity anomalies relative to the average velocity at each depth. See Figure 3.12a for model material and temperature structure. The continental crust is plotted in black as the velocity conversion only considers mantle structure.

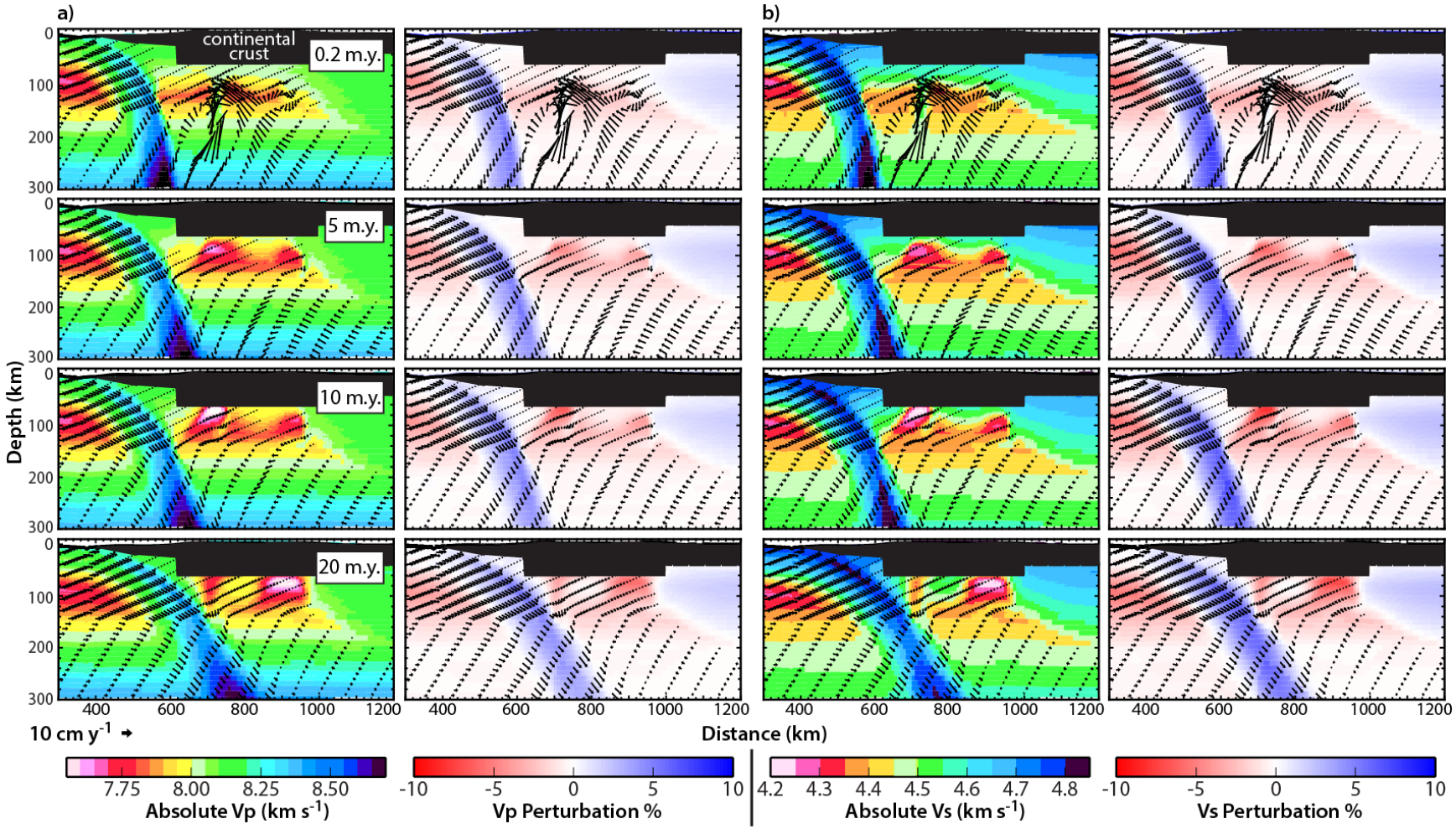

Figure 5.14 Predicted seismic structure for the Rayleigh-Taylor *Model RT8* (two dense roots imposed beneath the Moho, 3350 kg m^{-3} scaled f=1) for a constant pyrolytic composition, shown at times of 0.2, 5, 10, and 20 m.y. Both absolute **a)** P- and **b)** S- wave velocities are shown, as well as the velocity anomalies relative to the average velocity at each depth. See Figure 3.12b for model material and temperature structure. The continental crust is plotted in black as the velocity conversion only considers mantle structure.

removed material alone does not produce a prominent seismic anomaly. To that point, the upper portions of the roots, originating from shallower depths and cooler temperatures, still generate large high velocity anomalies. Moreover, the removal dynamics of *Model RT8* generate staggered convective cells, initially existing within the proximal site (at 10 m.y.) and subsequently forming in the distal site (at 20 m.y.) (Figure 5.14). As a result, the strongest low velocity anomaly exits within the empty root site that has the active SLM cell, producing strong S- and weak P-wave anomalies similar to those noted for *Model RT6*.

5.4 Implications for the central Andes

The amount and timing of regional elevation changes within the central Andes remains a topic of debate, and constraints on both can provide insights into the processes responsible for the formation of plateaus in non-collisional settings. Recent regional reconstructions of the paleoelevation of the Altiplano-Puna plateau (e.g. Garzione *et al.*, 2006; 2008; Canavan *et al.*, 2014) suggests uplift proceeded unevenly across the region. Moreover, recent deep seismic imaging of the current lithospheric structure reveals spatial heterogeneity, with indications that lithospheric removal has played a fundamental role in its evolution (e.g. Heit *et al.*, 2008; Beck *et al.*, 2015; Scire *et al.*, 2015; Ryan *et al.*, 2016). Previous studies focussing on topography analysis (e.g. Steinberger, 2007), have suggested that the Andean topography cannot be supported only by the distribution of tectonic loads or lateral variations in crust and mantle lithosphere properties, thus introducing the concept of dynamic topography as playing a key role in the elevation of the central Andes.

This section will discuss the modelling results of this thesis in relation to these geological and geophysical observations (primarily surface elevation and seismic velocity structure) concerning the timing and amount of regional uplift of the central Andes. This discussion extends the discussion of the previous chapter (Chapter 4) that focused on the dynamics of removal and its implications for lithospheric structure, and focuses on the areas that are constrained by estimates of paleoelevation (i.e. northern Altiplano (18°-21°S) and southern Puna (24°-26°S)). Refer to Figure 4.1 for region subdivisions.

5.4.1 Uplift within the northern Altiplano (18°-21°S)

Estimates of paleoelevations in the northern Altiplano are provided by the stable isotope analysis of Garzione *et al.* (2006; 2008). They proposed that rapid wholesale removal of the mantle lithosphere underlying the northern Altiplano is responsible for a 1.5 – 2.5 km uplift in the last 10.3 – 6.8

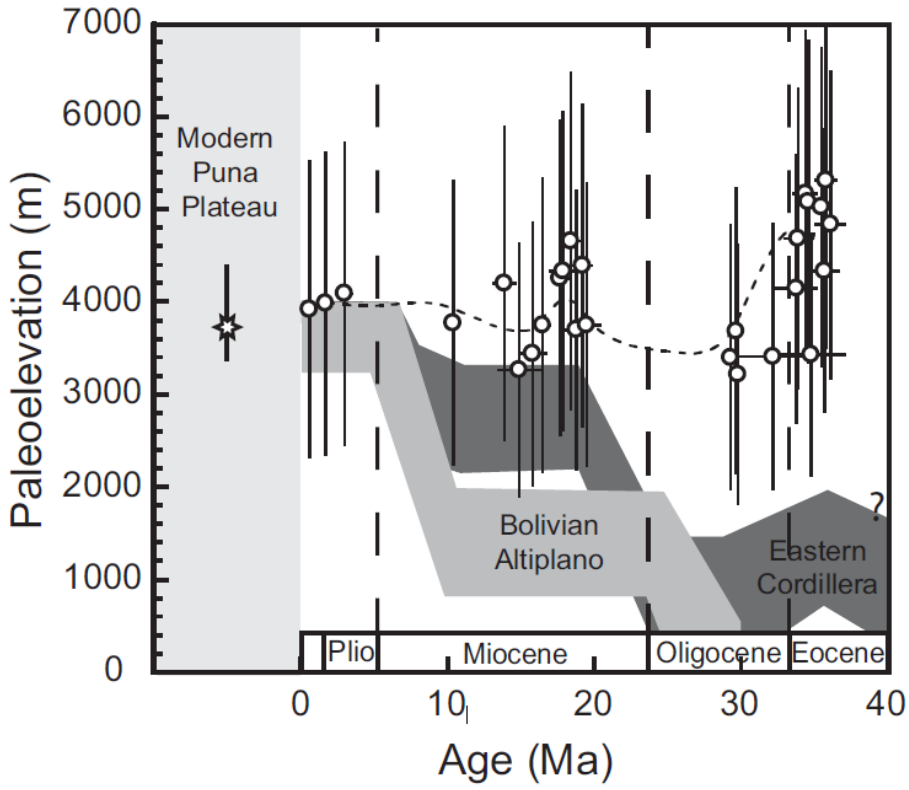

Figure 5.15 Complied estimates of paleoelevations for the central Andean plateau from Canavan *et al.* (2014). Paleoelevation estimates for the Puna are given in discrete point, with error bars corresponding to 2σ. Dark and light grey bands show paleoelevation estimates for separate portions of the northern Altiplano, from Leier *et* al. (2013) and Garzione *et al.* (2008) respectively.

Ma (Figure 5.15). Regional reconstructions by Garizone *et al.* (2008) suggest elevations of <2 km in the northern Altiplano persisted until this rapid uplift at ~10 Ma. Specifically, Garizone *et al.* (2008) propose removal via coherent delamination to explain this rapid and extreme uplift. The numerical models in the current study show that the overall uplift resulting from delamination averages 0.5 – 0.7 km (Figures 5.3 and 5.4). Note that the models show a transient and localized topographic maximum that occurs as an initial isostatic response to detaching mantle lithosphere (e.g. observed in Figure 5.2b between 2 – 4 m.y.); however, this does not permanently affect the plateau elevation, but does result in 0.5 – 1 km rapid uplift that persists for ~2 – 4 m.y of the 6 – 8 m.y. long removal process. This localized uplift persists for a longer period with increased root density (Figure 5.4), which also increases the time delamination takes to complete (refer to section 3.3.3). Therefore, the delamination models in this study support the timeline of uplift of 4 m.y. proposed by Garizone *et al.* (2006; 2008) in a localized capacity,

but not its overall elevation change. Large transient surface uplift derived from delamination in this study is not a lasting feature and would not be able to explain permanent uplift greater than 0.7 km. Instead, the models suggest that another process in combination with possible lithosphere removal is responsible for the uplift observed within the northern Altiplano. For example, Barke and Lamb (2006) have shown that the distribution of observed Late Cenozoic crustal shortening in the Altiplano can account for ~2 km of uplift across the region since ~10 Ma. This ~2km could then be enhanced by removal producing 0.5 – 0.7 km uplift, if the entire mantle lithosphere were removed by delamination.

Models in this study show that there are mechanisms other than delamination that result in large-scale lithosphere thinning and surface uplift. Notably, wholesale removal of the underlying mantle lithosphere of the plateau region was achieved in *Model RT7* through the emplacement of multiple strong dense roots that destabilize via gravitational instabilities (Figure 5.9). Removal in this scenario proceeds in a multi-staged fashion, with the strong roots generating greater viscous drag as they descend, thus entraining adjacent material and leading to the overall thinning of the mantle lithosphere. This is key, as the quasi-synchronized descent of the roots creates two symmetric cells of SLM circulation resulting in dynamically supported topography and surface uplift of 0.9 – 1.2 km above the distal and proximal root sites, respectively, which occurs as removal proceeds. Unlike the model of large-scale delamination, the configuration of the mantle lithosphere throughout the removal process is conducive to the production of localized SLM cells that exert a net upward on the overlying crust, enhancing uplift. Without the effect of positive dynamic topography, the wholesale removal of the 60 km thick mantle lithosphere would result in half the surface uplift (~0.6 km), as shown by *Model D1* (Figure 5.2). There are other aspects of *Model RT7* that also better agree with the paleoaltimetry put forward by Garzione *et al.* (2008), including the >10 m.y. of relatively low surface elevations of ~2.5 km during initial stages of removal (Figure 5.15), followed by rapid regional uplift throughout a period of 4 -5 m.y. (Figure 5.9a). The rapid uplift is coincident with the final removal of the roots; however, its resultant regional uplift of 1.2 km is still less than the 1.5 – 2.5 km suggested by Garzione *et al.* (2008). Note that crustal shortening is not explicitly modelled here, which could lead to further uplift.

However, deep seismic imaging of the current lithospheric structure does not support wholesale removal of the mantle lithosphere beneath the northern Altiplano (e.g. Myers *et al.*, 1998; Heit *et al.*, 2008). The heterogeneous velocity structure of the shallow mantle suggests that there may only be localized areas with thin lithosphere (Figures 4.2 and 5.16a,). As discussed in Chapter 3, *Model RT8* (Figures 5.8 and 5.16c) best represents the interpreted northern Altiplano structure. In this model, two

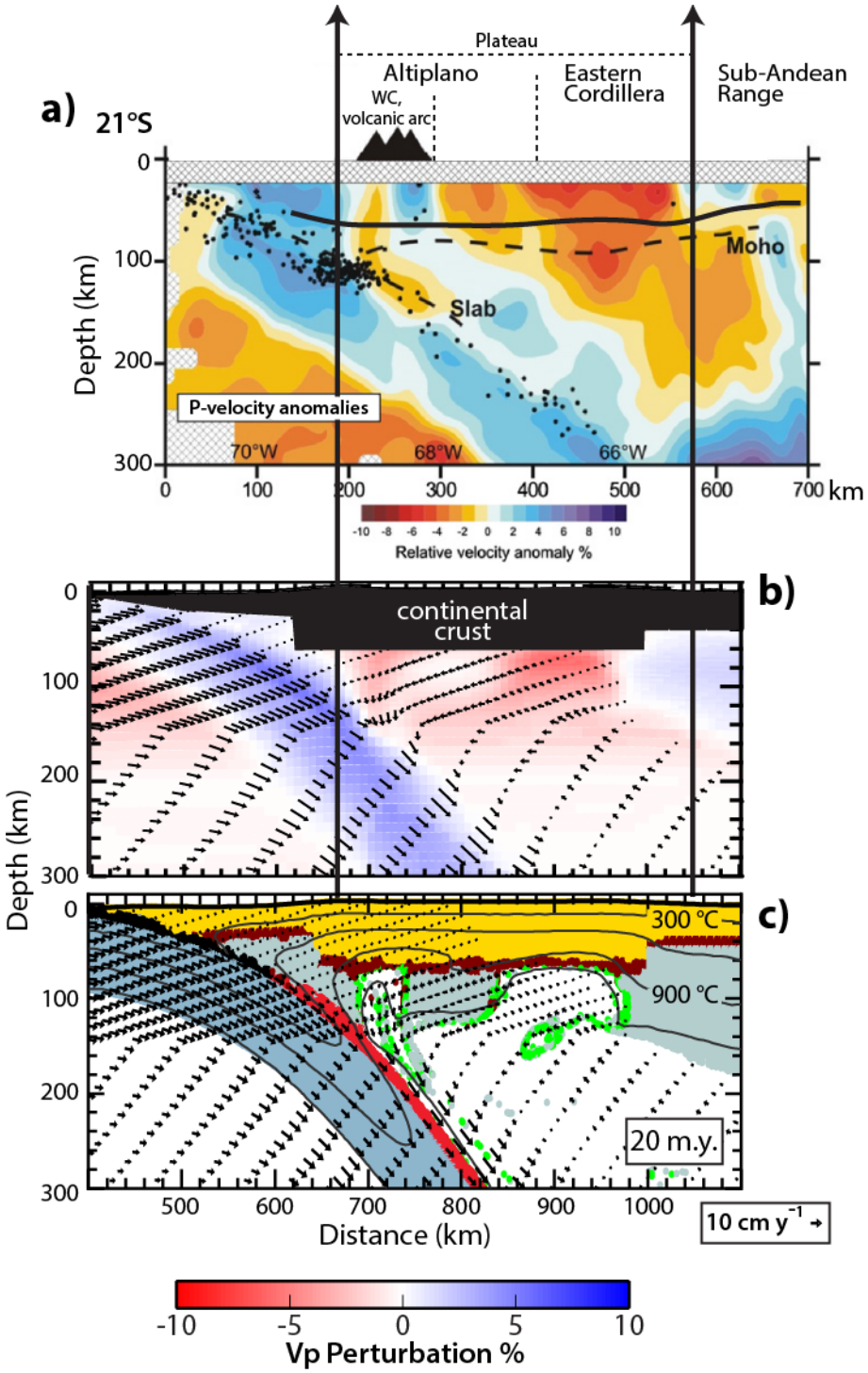

Figure 5.16 **a)** P-wave tomography image of the northern Altiplano modified from Heit *et al.* (2008). The dash line is the Moho from S-wave receiver functions from Heit *et al.* (2007), and the solid line is the Moho from Elger *et al.* (2005). **b)** The predicted P-wave velocity anomalies and c) the material and thermal structure of *Model RT8* at 20 m.y. Refer to text for discussion, and Figure 2.1 and Figure 5.10 for material colour coding.

weak, dense roots are emplaced beneath the Moho, where the roots span the entire thickness of the mantle lithosphere. The weak rheology of these roots may reflect compositional changes or the effects of higher temperatures (not explicitly modelled here) associated with magma emplacement. The plateau in this model undergoes a net 1.1 km uplift within 15 m.y. Notably localized rapid uplift of 0.7 km is achieved above the distal root site within the first 4 m.y. (Figure 5.8b). This is then followed by gradual regional uplift, enhanced by dynamically supported topography, resulting in an additional 0.4 km uplift within the next 10 m.y. (Figure 5.8b). Once again, even with the secondary influence of mantle flow, the net 1.1 km uplift in *Model RT8* is less than the 1.5 – 2.5 km proposed by Garzione *et al.* (2008) (Figure 5.15). However, the predicted seismic structure of *Model RT8* is able to reconcile upper mantle velocity anomalies to a certain degree, with the empty root sites registering as low velocity anomalies (Figure 5.16b). Namely, the proximal and distal sites register as P-wave velocity anomaly of 2-3% and 2-6%, respectively. This falls within the P-wave velocity anomaly range identified by Heit *et al.* (2008) of 1-2% (at ~68°W, ~ 100 km depth) and 2-5% (at ~66°W, ~ 100 km depth), also respectively (Figure 5.16a). As a result, the predicted seismic structure of *Model RT8* supports a thermal contribution to the low velocity zones identified by Myers *et al.* (1998) and Heit *et al.* (2008) (Figure 5.16b, c), which in *Model RT8* result from the upwelling SLM post lithosphere removal.

5.4.2 Uplift within the southern Altiplano and northern Puna (21°-24°S)

There are no current estimates of paleoelevations within the southern Altiplano and northern Puna. However, seismic images suggest large-scale mantle lithosphere thinning and/or removal (Figure 4.5a) across the extent of the plateau at these latitudes. As discussed in the previous section (5.4.1), both the foundering of multiple strong dense roots (*Model* RT7) and coherent delamination (*Model D1)* cause widespread thinning of the mantle lithosphere. Removal as a result of either mechanism would lead to surface uplift. Based on the model results in this current study: *Model RT7* resulting in rapid uplift of 1.2 km within a 4 m.y. timespan, and delamination causing 0.5 – 0.7 km uplift within 6 – 8 m.y.

5.4.3 Uplift within the southern Puna (24°-26°S)

Unlike the northern Altiplano, there is no evidence of large-magnitude uplift of the southern Puna (24° – 26°S) during the Miocene (Canavan *et al.*, 2014). Paleoelevation estimates from stable isotope analysis of the southern Puna indicate that high elevations (~3.8 - 4 km) have existed since at least 36 Ma (Canavan *et al.*, 2014) (Figure 5.15). This suggests the proposed ongoing removal of the

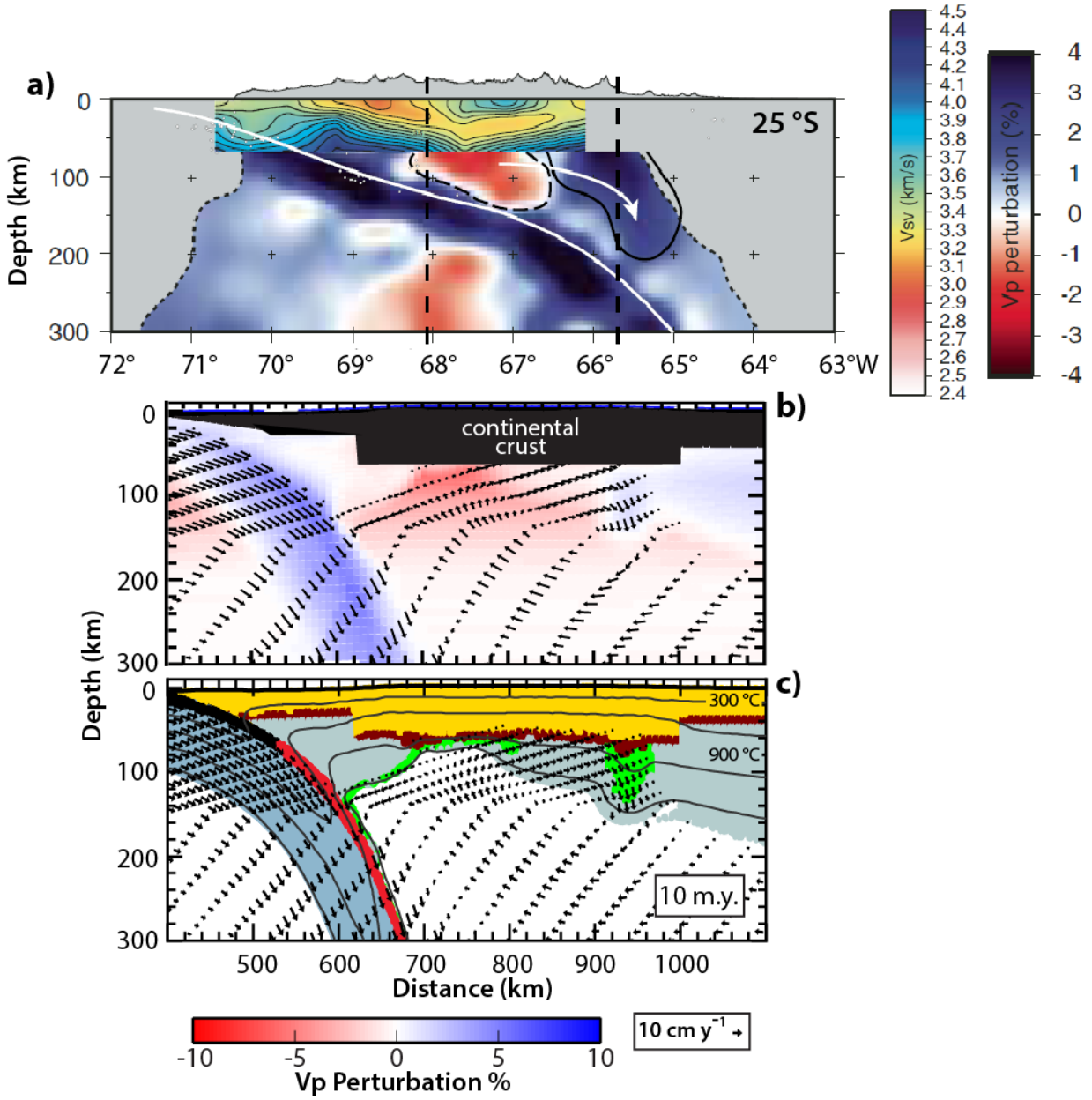

Figure 5.17 **a)** Cross-section of a compiled seismic tomography for the southern Puna (25°S), consisting of an ambient noise tomography shear-wave velocity model for the crust (Ward et al., 2013), and P-wave tomography model for the mantle (Scire *et al.*, 2015). Modified from Beck *et al.* (2015). **b)** The predicted P-wave velocity anomalies and c) the material and thermal structure of *Model RT6*, corresponding at 10 m.y. Refer to text for discussion, and Figure 2.1 and Figure 5.10 for material colour coding.

mantle lithosphere is likely disconnected from the main cause of the high elevations observed today. Notably, the stationary delamination that is proposed by Beck *et al.* (2015) for the southern Puna was not explicitly modelled in this study. However, an alternate removal scenario consisting of multiple dense weak roots removed via RT instability, *Model RT6* (Figure 5.7), can also explain the present-day lithosphere structure. Recall in this model the dense roots are 100 kg m^{-3} denser than the adjacent mantle material and with a rheology scaling factor of f=1; the mantle lithosphere scaling factor is f=10. The present-day structure is best captured by the 10 m.y. timestep output of the model, depicting the entrainment of the mantle lithosphere from the centre of the plateau by the descending distal root (Figure 5.17c). The regional topography remains relatively stable leading up to 10 m.y., with only local uplift of ~0.2 km above the proximal root after it is removed around 6 m.y. (Figure 5.7a). This is enhanced by 10 m.y. by a further 0.3 km uplift caused by upwelling mantle flow. *Model RT6* suggests that the regional average elevation has remained relatively constant leading up to the 10 m.y. lithosphere structure, experiencing only local elevational changes of ~0.5 km. However, this localized uplift of 0.5 km still falls well within the error bounds of paleoelevation estimates for the Puna plateau (Figure 5.15). Notably, if the ongoing removal beneath the Puna plateau is the result of multiple weak, dense roots, *Model RT6* predicts it will experience ~0.3 km further uplift due to continued dynamic mantle flow in the next 4 m.y. The predicted seismic structure of *Model RT6* is in fair agreement with the upper mantle velocity anomalies identified by Scire *et al.* (2015) (Figure 5.17a and b). In particular, the distal root appears as a shallow high velocity zone; note that the predicted velocity anomaly would be larger if an eclogite composition were included in the calculations. Furthermore, removal of the proximal root creates an area of upwelling hot mantle, corresponding to a low P-wave velocity anomaly of 2-5%, similar to identified by Scire *et al.* (2015).

CHAPTER 6 : CONCLUSIONS

6.1 Model insights into lithospheric removal beneath the central Andean plateau

Lithosphere removal and its role in modifying the structure and topography of the central Andes are topics still currently unresolved, both in terms of the manner of removal and its overall timing. High elevations observed within the central Andes (~3 – 4 km) cannot be readily reconciled with the current lithospheric structure imaged by numerous geophysical surveys which indicate that the mantle lithosphere is thin to absent across the Altiplano-Puna plateau, despite crustal thicknesses of 60 – 70 km (e.g. Myers *et al.*, 1998; Beck and Zandt, 2002; Schur *et al.*, 2006; Heit *et al.* 2008; Scire *et al.*, 2015; Ryan *et al.* 2016). Many previous geodynamic models investigating lithosphere removal have not incorporated an active subduction zone setting, and rather focus on models more representative of hinterland applications (e.g. Göğüş and Pyslywec, 2008; Krystopowicz and Currie, 2013; Wang *et al.*, 2015). Thus, this thesis provides insights into 1) the dynamics behind the static picture of the lithosphere provided by geophysical surveys (e.g. seismic tomography), 2) the factors that control the timing of the proposed removal events, and 3) the topographic response to lithosphere removal, all within an active subduction zone setting representative of the central Andean system. The purpose of this thesis is to study the resulting dynamics of mantle lithosphere removal, not to assess the tectonic or petrological mechanisms that lead to the development of gravitational instabilities, as this has been studied elsewhere (e.g. Morency and Doin, 2004; Krystopowicz and Currie, 2013). Models in this study use imposed density anomalies (i.e. roots) to drive lithosphere removal, representing local lithosphere thickening, magmatic differentiation, or a compositional phase change. Focus is placed on the overall style and timing of removal after the initiation conditions are met, as well as the consequent surface dynamics (i.e. uplift). The main conclusions that can be drawn from the results of the model experiments are:

1. Overall, an active subduction zone modulates the dynamics of lithosphere removal and modifies the resulting lithospheric substructure. Note that the down-going oceanic slab does not act as a barrier to lithospheres removal. In fact, subduction-induced flow aids the removal process, perturbing the lithosphere and entraining the foundering material to remove it from the system.

2. Subduction-induced ablation occurs within all models, entraining mantle material more efficiently as the mantle lithosphere underlying the plateau weakens (i.e. under hydrated and warmer conditions).
3. The models provide insights into the dynamics of two different styles of removal and how they modify the lithosphere structure. In particular:

i) Dynamics of removal via delamination

Retreating delamination, across a ~400 km wide region, results in the coherent removal of the mantle lithosphere within 5 – 12 m.y., occurring more rapidly with decreased density of the imposed root (50 to 100 kg m^{-3} more dense than surrounding mantle) and increased strength of the mantle lithosphere (i.e. reflecting a more dehydrated state). Lower root density in particular allows the root to remain viscously coupled to the mantle lithosphere as it peels back, which in turn enhances the negative buoyancy of the delaminating slab. Moreover, delamination requires that the mantle lithosphere can decouple from the overlying crust, and that there is a conduit through the mantle lithosphere to connect the sublithospheric mantle to the decoupled interface; such a conduit may reflect a local area of reduced strength (e.g. inherited structure) or can be created by a localized gravitational instability. The orogenically thickened crust of the central Andes is conducive to the existence low viscosity zone at its base owing to the thick felsic crust (~60 km) and high temperature in the deep crust. In general, delaminated mantle lithosphere detaches towards the subducting slab, aided by shearing from mantle wedge corner flow; however, dense roots positioned past the arc region are able to generate cells of sublithospheric mantle flow opposing the wedge flow, resulting in their cratonward detachment and small-scale delamination (~100 km wide region). Notably, this small-scale delamination is triggered as the root strengthens and the surrounding mantle weakens.

ii) Dynamics of removal via Rayleigh-Taylor type instabilities

Rayleigh-Taylor-type instabilities (i.e. ‘drips’) within the mantle lithosphere are removed faster than the aforementioned delamination models, being removed within 2 – 12 m.y. The duration of removal is directly dependent on the properties of the root, occurring more rapidly within increased density and decreased strength. The tectonic setting directly influences the manner in which instabilities detach from the overlying plate, as the subduction-driven mantle wedge flow

acts to initiate removal. In addition, mantle flow modifies the resulting mantle lithosphere configuration post-removal as upwelled mantle causes convective erosion in the empty root sites. Dense roots in closer proximity to the descending slab (~ arc region) are more readily triggered and entrained by the down-going mantle wedge flow, whereas roots further inland more readily generate their own cell of mantle circulation causing them to 'drip' against the direction of the corner flow. Moreover, the presence of multiple roots, representative of possible lateral compositional heterogeneities or zone of partial melt, results in dynamic feedbacks capable of both wholesale- (i.e. large-scale) and piecewise- (i.e. localized) removal of the mantle lithosphere. In particular, in the context of strong mantle lithosphere, the coupled effects of multiple strong roots result in widespread regional removal, whereas weakened roots generate localized gaps within the mantle lithosphere.

3. **The surface expression of mantle lithosphere removal**

Regardless of the manner in which removal proceeds, topographic uplift does not exceed 1.2 km in the models in this study. In general, the removal style is readily detectable via its surficial expression: i) Delamination results in asymmetric elevation profiles, with ~1.1 km initial rebound that migrates with the point of lithosphere detachment; this transient maximum thermally re-equilibrates after delamination is completed resulting in 0.5 – 0.7 km net uplift. ii) Rayleigh-Taylor (RT) -type 'drips' result in localized net uplift of 1 km. Changes in the surface elevation are limited to the zone overlying the destabilized root, producing a slight transient asymmetric uplift profile. The direction of this asymmetry is dependent on the trajectory of the foundering root, and, therefore, root position relative to the subducting slab: in closer proximity to the slab uplift proceeds trenchward, whereas roots closer to the craton show uplift proceeding cratonward. In the presence of an active subduction zone, secondary cells of sublithospheric mantle circulation form in the areas of removed lithosphere, adding a dynamic component to the elevation that serves to enhance the uplift. The positive dynamic topography is more readily observed above sites that have undergone RT-type removal, as the isolated gaps within the mantle lithosphere site serve to confine the flow.

In this study, generally mantle lithosphere removal results in topographic uplift. However, under certain conditions, removal can proceed with little to no indication at the surface. Specifically, when multiple dense, strong roots are emplaced across the width of the plateau and remove in

a multi-stage manner, a prolonged negative buoyancy force is exerted on the surface; therefore, the regional topography can remain deflected during the initial stages of removal (i.e. removal can sometimes be associated with apparent subsidence). As a result, paleoelevation estimates and present-day topography may not irrevocably reflect historic or current removal dynamics.

4. **Implication for the central Andes**

The spatial heterogeneity of the mantle lithosphere imaged beneath the central Andean plateau can be reconciled by lateral compositional and rheological contrasts that induce lithosphere removal. However, regardless of the manner of removal, the resulting surficial uplift is limited to ~1 km, suggesting the modern topography of the Altiplano-Puna plateau is likely a compounded result of removal, dynamic topography, and crustal shortening (e.g. Barke and Lamb, 2006); note that the current models are not designed to study crustal shortening. In particular:

i) The northern Altiplano Plateau (18°- 21°S)

Paleoelevation estimates reveal rapid uplift of 1.5 – 2.5 km between 10 – 6.8 Ma (Garzione *et al.*, 2006; 2008). This rapid uplift is interpreted to be an isostatic adjustment in response to large-scale removal of the entire plateau mantle lithosphere. Models of delamination in this study do not agree with this interpretation showing a net 0.5 – 0.7 km uplift after coherent removal of the plateau mantle lithosphere. Furthermore, tomographic images reveal localized low velocity anomalies, likely representing zones of upwelled sublithospheric mantle (e.g. Myers *et al*., 1998; Heit *et al.*, 2008). This snapshot of the current lithosphere structure suggests only localized removal has occurred beneath the northern Altiplano, and does not agree with proposed paleoaltimetry. As shown in this study, the current lithosphere structure can be reproduced with the removal of two dense weak roots located beneath the Moho (*Model RT8*), possibly arising due to arc- and back-arc magmatism in combination with slab dip cyclicity (e.g. Kay *et al.*, 1999; Hoke and Lamb, 2007; DeCelles *et al.*, 2009). This model also predicts a seismic velocity structure able to reconcile upper mantle velocity anomalies to a certain degree, supporting the idea that the low velocity zones identified by Myers *et al.* (1998) and Heit *et al.* (2008) represent high temperature areas of thinned mantle lithosphere.

ii) The southern Altiplano Plateau and northern Puna (21°-24°S)

Seismic images suggest large-scale removal of the mantle lithosphere lid has occurred beneath the southern Altiplano and northern Puna (e.g. Schurr *et al.*, 2006; Scire *et al.* 2015). This is interpreted from a regional low seismic velocity zone observed beneath the tectonically thickened crust corresponding to upwelled sublithospheric mantle post removal. Based on a trenchward regional magmatic evolution that occurred since ~15 Ma, Beck *et al.* (2015) propose large-scale coherent removal of the mantle lithosphere via retreating delamination. Models in this study show that widespread thinning of the mantle lithosphere is indeed accomplished most readily through delamination, with an average duration of 6 m.y. and 0.5 – 0.7 km increase in elevation. However, the removal of multiple strong roots via Rayleigh-Taylor-type 'drips' across the extent of the plateau (*Model RT7*) also results in the wholesale removal of the mantle lithosphere, within 17 – 20 m.y. However, the Rayleigh-Taylor model causes a greater topography change of 1.2 km uplift within a 4 m.y. timespan. Estimates of paleoelevation are currently unavailable for this region, and are required to further constrain the timing and style of removal.

iii) Implications for removal in the southern Puna (24°-26 °S)

Lithosphere removal is interpreted to be currently underway in the southern Puna due in large part from the interpretation of deep seismic images (e.g. Scire *et al.*, 2015). In particular localized low seismic velocity anomalies observed beneath the plateau are attributed to upwelling sublithospheric mantle. In this study, the dynamic feedbacks generated by Rayleigh-Taylor style of removal of multiple dense roots beneath the Moho (*Model RT6)* generates a lithospheric structure resembling that currently observed in the southern Puna (e.g. Beck *et al.*, 2015; Scire *et al.*, 2015). The model exhibits a relatively constant average elevation of ~3.1 km, experiencing only local elevational changes of ~0.5 km as each root founders. This longevity of a constant high elevation despite ongoing removal largely agrees with the conclusions of Canavan *et al.* (2014); their study maintains that high elevations of 3 – 4 km have persisted since 36 Ma in the southern Puna, and are probably not connected to largescale lithosphere removal. The RT model also predicts a seismic velocity structure able to reconcile the seismic velocity anomalies identified by Beck *et al.* (2015) and Scire *et al.* (2015) within the upper mantle, supporting the interpretation

of the high and low velocity anomalies as being a detached block of mantle lithosphere and upwelled sublithospheric mantle, respectively. Notably, the proposed RT model predicts that the lithosphere removal currently underway in the southern Puna will result in 0.3 km dynamic uplift in the next 4 m.y.

6.2 Future work

The results of the geodynamic models presented in this thesis show promising agreement with the seismic observations of the current lithospheric structure and elevation history of the central Andes. However, further work is required to investigate other important modulating processes and reconcile the models with observations not incorporated in the current study. For example, further refinement of the material assignments (i.e. rheology and density), which currently reflect bulk conditions, could serve to modulate uplift and deformation; this is particularly true for the crust where variations in composition could lead to local changes in density and strength. Furthermore, the inclusion of shortening of the lithosphere throughout the evolution of the model would allow for trench advancement and retreat, as well as an opportunity to investigate the influence of craton underthrusting on the dynamics of the orogen. The latter has been suggested to be currently underway in the central Andes (e.g. Beck and Zandt, 2002) and may trigger lithospheric removal (e.g. Sobolev *et al.*, 2006). Of course, the addition of surface processes (i.e. sedimentation, erosion) would modify the surficial expression of removal as it would act to redistribute material, thus altering the isostatic response of the system. Therefore, inclusion of erosional and depositional processes would provide a more complete picture of preserved indications of topographic changes as removal proceeds.

As down-going lithosphere can retain its separate thermal and mechanical identity to considerable depths, a descending oceanic plate, such as the Nazca plate, can penetrate the transition zone into the lower mantle, albeit perhaps first experiencing a period of stagnation (e.g. Scire *et al.*, 2015). Test models that extended the model domain to 900 km depth were carried out as part of this study in order to test the influence of the closed and impermeable basal boundary on the model dynamics. No large change in dip angles (<12°) at depths <300 km were observed; however, it remains unclear if this boundary creates unwanted effects on slab dynamics. In particular, previous studies show that the cold central core of the oceanic slab should remain stronger and thus be able to sustain and transmit stresses (e.g. Riedel and Karato, 1997), possibly directed up-dip. In turn, this could affect the evolution of the overriding plate, resulting in trench advance/retreat that would especially affect the

models if crustal shortening was incorporated. However, this transference of stress at depth may be modulated by phase changes within the slab; the olivine-spinel phase change at ~410 km depth results in significant weakening by up to 4 -5 orders of magnitude for slab temperature below 630°C due to a reduction in grain size (e.g. Riedel and Karato, 1997; Billen, 2010). In terms of rheological adjustments, diffusion creep is believed to dominate at in the deep mantle, depths ~660 km (e.g. Karato, 2010), and should be implemented in these extended models. Moreover, the presence of metastable olivine as well as the latent heat produced by the polymorphic phase changes within the slab as it enters the transition zone (410 – 660 km) would also affect the stress and thermal field of the system. Future models should then also include transition zone phase changes in order to capture its effects on the density and viscosity structure of both the slab and surrounding mantle, and, subsequently, its influence on lithosphere removal events occurring within the overriding plate.

The model results presented in this thesis can be further analyzed to extend upon the products discussed in Chapter 5. For example, the evolution of pressure-temperature conditions of the crust and mantle during lithosphere removal can be used to provide insights into magmatic activity in terms of decompression melting or melting of components as they are heated (e.g. Wang and Currie, 2015); such an analysis would also offer constraints on conditions of contact metamorphism.

Finally, models exploring a third dimension should be considered. Note that all numerical models in this study employ a 2D model domain with the assumption of plane strain. This 2D approach can appropriately capture the period of interest of this study, specifically the past 20 Ma of central Andean evolution, as it has experienced quasi-perpendicular convergence (Somoza, 1998). However, 2D models do constrain the mantle wedge flow and deforming lithosphere to the model plane, which may affect removal dynamics. A 3D model would introduce a volume parameter to root removal dynamics. To first-order, it is likely the unstable root would destabilize and remove faster for equivalent parametrizations investigated in this study. This reflects the growth of the instability involving surrounding material. It is important to note, however, heterogeneities in the surrounding mantle material (i.e. local increases in strength, hydration, mantle lithosphere thickness), as well as irregularities in sublithospheric mantle flow, would undoubtedly complicate removal dynamics. For example, in 3D wedge flow may be diverted around perturbations in the overriding lithosphere (e.g. Hasenclever, *et al.*, 2011) which would reduce its ability to perturb and entrain the foundering root of mantle lithosphere, possibly resulting in increased onsets of removal. Therefore, inclusion of a third

dimension, or purposeful north-south cross-sectional models, must be carried out in order to further enhance the understanding of lithosphere removal for a Cordilleran orogeny such as the central Andes.

REFERENCES

Abers, G.A., van Keken, P.E., Kneller, E.A., Ferris, A., and Stachnik, J.C., (2006). The thermal structure of subduction zones constrained by seismic-imaging: Implications for slab dehydration and wedge flow. Earth and Planetary Science Letters, v. 241, p. 387-397.

Allmendinger, R., Jordan, T., Kay, S.M., and Isacks, B., (1997). The evolution of the Altiplano-Puna Plateau of the central Andes. Annual Review of Earth and Planetary Sciences, v. 25, p. 139–174, doi:10.1146/annurev.earth.25.1.139.

Arcay, D., (2012). Dynamics of interplate domain in subduction zones: influence of rheological parameters and subducting plate age. Solid Earth, v. 2, p. 467-488, doi:10.5194/se-3-467-2012.

Asch, G., Schurr, B., Bohm, M.C., Haberland, C., Heit, B., Kind, R., Wolbern, I., Yuan, X., Bataille, K., Comte, D., Pardo, M., Viramonte, J., Rietbrock, A., and Giese, P., (2006). Seismological studies of the central and southern Andes, *in* Oncken, O., Chong, G., Franz, G., Giese, P., Goetze, H.-J., Ramos, V., Strecker, M., and Wigger, P., eds., The Andes: Active Subduction Orogeny: Berlin, Springer, Frontiers in Earth Sciences, p. 443–457.

Assumpção, M., James, D., Snoke, A., (2002). Crustal thicknesses in SE Brazilian shield by receiver function analysis: implications for isostatic compensation. Journal Geophysical Research, v. 107(B1), doi:10.1029/2001JB000422.

Austrheim, H., (1991). Eclogite formation and dynamics of crustal roots under continental collision zones. Terra Nova, v. 3, p. 492-499.

Austrheim, H., Erambert, M., and Engvik, A. K., (1997). Processing of crust in the roots of the Caledonian continent collision zone: the role of eclogitization, *in* Touret, J.L.R., and Austrheim, H., eds., Collision Orogens: Zones of Active Transfers between crust and mantle, Tectonophysics, v. 273, p. 129-153.

Baby, P., Rochat, P., Mascle, G., and Herail, G., (1997). Neogene shortening contribution to crustal thickening in the back arc of the central Andes. Geology, v. 25, p. 883–886, doi:10.1130/0091-7613(1997)025<0883:NSCTCT>2.3.CO;2.

Babeyko, A.Y., Sobolev, S.V., Vietor, T., Oncken, O., and Trumbull, R.B., (2006). Numerical study of weakening processes in the central Andean back-arc, *in* Oncken, O., Chong, G., Franz, G., Giese, P.,

Goetze, H.-J., Ramos, V., Strecker, M., and Wigger, P., eds., The Andes: Active Subduction Orogeny: Berlin, Springer, Frontiers in Earth Sciences, p. 495–512.

Barke, R., and Lamb, S., (2006). Late Cenozoic uplift of the Eastern Cordillera, Bolivian Andes. Earth and Planetary Science Letters, v. 249, p. 250-267.

Beaumont, C., Nguyen, M.H., Jamieson, R.A., and Ellis, S., (2006). Crustal flow modes in large hot orogens, *in* Law, R.D., Searle, M.P., and Godin, L., eds., Channel Flow, Ductile Extrusion, and Exhumation of Lower-Mid Crust in Continental Collision Zones: Geological Society, London, Special Publication 268, p. 91–145.

Beck S. L. and Zandt, G., (2002). Nature of orogenic crust in the central Andes. Journal Geophysical Research, v. 107, p. 2230, doi:10.1029/2000JB000124.

Beck, S. L., Zandt, G., Myers, S. C., Wallace, T. C., Silver, P. G., and Drake, L., (1996). Crustal-thickness variations in the central Andes. Geology, v. 24, p. 407-410.

Beck, S. L., Zandt, G., Ward, K. M., and Scire, A., (2015). Multiple styles and scales of lithospheric foundering beneath the Puna Plateau, central Andes. Geological Society of America Memoirs, 212, MWR212-03.

Becker, T.W., and Faccenna, C., (2009). A review of the role of subduction dynamics for regional and global plate motions, *in* Lallemand, S., and Funiciello, F., eds., Subduction Zone Geodynamics: Springer-Verlag Berlin Heidelberg, doi:10.1007/978-3-540-87974-9.

Behn, M.D., Hirth, G., and Elsenbeck II, J.R., (2009). Implications of grain size evolution on the seismic structure of the oceanic upper mantle. Earth and Planetary Science Letters, v. 282, p. 178-189.

Bianchi, M., Heit, B., Jakovlev, A., Yuan, X., Kay, S.M., Sandvol, E., Alonso, R.N., Coira, B., and Kind, R., (2012). Teleseismic tomography of the southern Puna plateau in Argentina and adjacent regions. Tectonophysics, v. 586, p. 65-83.

Bindschadler, D.L, and Parmentier, E.M., (1990). Mantle flow tectonics: The influence of a ductile lower crust and implications for the formation of topographic uplands on Venus. Journal of Geophysical Research, v. 95, p. 21,329-21,344.

Bird, P., (1979). Continental delamination and the Colorado Plateau. Journal of Geophysical Research, v. 84, p. 7561–7571.

Bird, P., (1998). Kinematic history of the Laramide Orogeny in latitudes 35°-49° N, western United States. Tectonics, v. 17(5), p. 780-801.

Bird, P., (1991). Lateral extrusion of lower crust from under high topography in the isostatic limit. Journal of Geophysical Research: Solid Earth (1978–2012), v. 96(B6), p. 10275-10286.

Billen, M.I., (2008). Modeling the Dynamics of Subducting Slabs. Annual Review of Earth and Planetary Sciences, v. 36, p. 325–256, doi:10.1146/annurev.earth.36.031207.124129.

Billen, M.I., (2010). Slab dynamics in the transition zone. Physics of the Earth and Planetary Interiors, v. 183, p. 296-308.

Billen, M.I., and Gurnis, M., (2001). A low viscosity wedge in subduction zones. Earth and Planetary Science Letters, v. 193, p. 227-236.

Bos, B., and Spiers, W., (2002). Frictional-viscous flow of phyllosilicate-bearing fault rock; microphysical model and implications for crustal strength profiles. Journal of Geophysical Research, v. 107, doi:10.1029/2001JB000301.

Bousquet, R., Goffe, B., Henry, P., Le Pichon, X., and Chopin, C., (1997). Kinematic, thermal and petrological model of the central Alps: Lepontine metamorphism in the upper crust and eclogitisation of the lower crust. Tectonophysics, v. 273, p. 105 – 127.

Bown, J.W., and White, R.S., (1994). Variation with spreading rate of oceanic crustal thickness and geochemistry, Earth and Planetary Science Letters, v. 121, p. 435–449.

Braun, J., (2010). The many surface expressions of mantle dynamics. Nature Geoscience, v. 3, p. 825-833, doi:10.1038/ngeo1020.

Buiter, S.J.H., Babeyko, A.Y., Ellis, S., Gerya, T.V., Kaus, B.J.P., Kellner, A., Schreurs, G., Yamada, Y., (2006). The numerical sandbox: comparison of model results for a shortening and an extension experiment: analogue and numerical modelling of crustal-scale processes, *in* Buiter, S.J.H., and Schreurs, G., eds., Analogue and Numerical Modelling of Crustal-Scale Processes. Geological Society, London, Special Publications, v. 253, p. 29–64.

Burov, E.B., (2011). Rheology and strength of the lithosphere. Marine and Petroleum Geology, v. 28, p. 1402-1443.

Cammarano, F., Deuss, A., Goes, S., and Giardini, D., (2005). One-dimensional physical reference models for the upper mantle and transition zone: Combining seismic and mineral physics constraints. Journal of Geophysical Research, v. 110, doi:10.1029/2004JB003272.

Cammarano, F., Goes, S., Vacher, P., and Giardini, D., (2003). Inferring upper-mantle temperatures from seismic velocities. Physics of the Earth and Planetary Interiors, v. 138, p. 197-222.

Canavan, R.R., Carrapa, B., Clementz, M.T., Quade, J., DeCelles, P.G., and Schoenbohm, L.M., (2014). Early Cenozoic uplift of the Puna Plateau, Central Andes, based on stable isotope paleoaltimetry of hydrated volcanic glass. Geology, doi:10.1130/G35239.1.

Cande, S.C. and Leslie, R.B., (1986). Late Cenozoic tectonic of the Southern Chile Trench. Journal of Geophysical Research, v. 91, p. 471–96.

Carrapa, B., Bywater-Reyes, S., DeCelles, P.G., Mortimer, E., and Gehrels, G.E., (2011). Eocene-Miocene synorogenic basin evolution in the Eastern Cordillera of northwestern Argentina (25°–26°S): Regional implications for Andean orogenic wedge development, Basin Research, v. 23, p. 1–20.

Cobden, L., Goes, S., Cammarano, F., and Connolly, J.A.D., (2008). Thermochemical interpretation of one-dimensional seismic reference models for the upper mantle: evidence for bias due to heterogeneity. Geophysical Journal International, v. 175, p. 627-648.

Coira, B., Davidson, J., Mpodozis, C., and Ramos, V.A., (1982). Tectonic and magmatic evolution of the Andes of Northern Argentina and Chile. Earth-Science Reviews, v. 18, p. 302-332.

Coleman, R.G., Lee, D.E., Beatty, L.B., and Brannock, W.W., (1965). Eclogites and eclogites: their difference and similarities. Geological Society of America Bulletin, v. 76, p. 483-508.

Connolly, J.A.D., (1990). Multivariable phase diagrams: An algorithm based on generalized thermodynamics. American Journal of Science, v. 290, p. 666-718.

Connolly, J.A.D., and Petrini, K., (2002). An automated strategy for calculation of phase diagram sections and retrieval of rock properties as a function of physical conditions. Journal of Metamorphic Geology, v. 20, p. 697-708.

Conrad, C.P., and Molnar, P., (1997). The growth of Rayleigh-Taylor type instabilities in the lithosphere for various rheological and density structures. Geophysical Journal International, v. 129, p. 95-112.

Currie, C.A., and Beaumont, C., (2011). Are diamond-bearing Cretaceous kimberlites related to low-angle subduction beneath western North America? Earth and Planetary Science Letters, v. 303, p. 59-70.

Currie, C.A., Beaumont, C., and Huismans, R.S., (2007). The fate of subducted sediments: A case for backarc intrusion and underplating. Geology, v. 35(12), p. 1111-1114.

Currie, C.A., Ducea, M.N., DeCelles, P.G., and Beaumont, C., (2015). Geodynamic models of Cordilleran orogens: Gravitational instability of magmatic arc roots, *in* DeCelles, P.G., Ducea, M.N., Carrapa, B., and Kapp, P.A., eds., Geodynamics of a Cordilleran Orogenic System: The Central Andes of Argentina and Northern Chile: Geological Society of America Memoir 212, p. 1–22, doi:10.1130/2015.1212(01).

Dávila, F.D., and Lithgow-Bertelloni, C., (2013). Dynamic topography in South America. Journal of South American Earth Sciences, v. 43, p. 127-144.

DeCelles, P.G., Ducea, M.N., Kapp, P., and Zandt, G., (2009). Cyclicity in Cordilleran orogenic systems. Nature Geoscience, 2(4), p. 251-257.

DeCelles, P.G., and Horton, B.K., (2003). Early to middle Tertiary foreland basin development and the history of Andean crustal shortening in Bolivia. Geological Society of America Bulletin, v. 115(1), p. 58-77.

DeCelles, P.G., Zandt, G., Beck, S.L., Currie, C.A., Ducea, M.N., Kapp, P., Gehrels, G.E., Carrapa, B., Quade, J., and Schoenbohm, L.M., (2015). Cyclical orogenic processes in the Cenozoic central Andes, *in* DeCelles, P.G., Ducea, M.N., Carrapa, B., and Kapp, P.A., eds., Geodynamics of a Cordilleran Orogenic System: The Central Andes of Argentina and Northern Chile: Geological Society of America Memoir 212, p. 459–490, doi:10.1130/2015.1212(22).

Dickinson, W.R., and Snyder, W.S., (1978). Plate tectonics of the Laramide orogeny. Geological Society of America, v. 151, p. 355–366, doi:10.1130/MEM151-p355.

Dorbath, L., Dorbath, C., Jimenez, E., and Rivera, L., (1991). Seismicity and tectonic deformation in the Eastern Cordillera and the sub-Andean zone of central Peru. Journal of South American Earth Science, v. 4, p. 13–24.

Dorbath, C., and Granet, M., (1996). Local earthquake tomography of the Altiplano and the Eastern Cordillera of northern Bolivia. Tectonophysics, v. 259, p. 117-136.

Ducea, M.N., Barton, M.D., (2007). Igniting flare-up events in Cordilleran arcs. Geology, v. 35, p. 1047–1050.

Ducea, M.N., Saleeby, J.B., and Bergantz, G., (2015). The architecture, chemistry and evolution of continental magmatic arcs. Annual Review of Earth and Planetary Sciences, v. 43, doi: 10.1146/annurev-earth-060614-105049.

Ducea, M.N., Seclaman, A.C., Murray, K.E., Jianu, D., and Schoenbohm, L.M., (2013). Mantle-drip magmatism beneath the Altiplano-Puna Plateau, Central Andes: Geology, v. 41, p. 915–918, doi:10.1130/G34509.1.

Dumitru, T.A., Gans, P.B., Foster, D.A., and Miller, E.L., (1991). Refrigeration of the western Cordilleran lithosphere during Laramide shallow-angle subduction. Geology, v. 19, p. 1145-1148.

Durek, J.J. and, Ekstrom, G., (1996). A radial model of anelasticity consistent with long period surface wave attenuation. Bulletin of the Seismological Society of America, v. 86, p. 144– 158.

Ehlers, T.A., and Poulsen, C.J., 2009, Influence of Andean uplift on climate and paleoaltimetry estimates: Earth and Planetary Science Letters, v. 281, no. 3–4, p. 238– 248, doi:10.1016/j.epsl.2009.02.026.

Elger, K., Oncken, O., and Glodny, J., (2005). Plateau-style accumulation of deformation—The Southern Altiplano. Tectonics, v. 24, doi:10.1029/2004TC001675.

Elkins-Tanton, L. T., (2005). Continental magmatism caused by lithospheric delamination. Geological Society of America Special Papers, v. 388, p. 449-461.

Elkins-Tanton, L. T., (2007). Continental magmatism, volatile recycling, and a heterogeneous mantle caused by lithospheric gravitational instabilities. Journal of Geophysical Research: Solid Earth, v. 112, doi:10.1029/2005JB004072.

Elkins-Tanton, L.T., and Hager, B.H., (2000). Melt intrusion as a trigger for lithospheric foundering and the eruption of the Siberian flood basalts. Geophysical Research Letters, v. 27(23), p. 3937-3940.

Flament, N., M. Gurnis, and R. Dietmar Müller, (2012). A review of observations and models of dynamic topography. Lithosphere, v. *5*, p. 189-210.

Forsyth, D.W., and Uyeda, S., (1975). On the relative importance of the driving forces of plate motion. Geophysical Journal of the Royal Astronomical Society, v. 43, p. 163–200.

Franz, G., Lucassen, F., Kramer, W., Trumbull, R.B., Romer, R.L., Wilke, H.-G., Viramonte, J.G., Becchio, R., and Siebel, W., (2006). Crustal evolution at the central Andean continental margin: A geochemical record of crustal growth, recycling and destruction, *in* Oncken, O., Chong, G., Franz, G., Giese, P., Gotze, H.J., Ramos, V.A., Strecker, M.R., and Wigger, P., eds., The Andes: Active Subduction Orogeny: Berlin, Springer-Verlag, Frontiers in Earth Sciences, v. 1, p. 45-64.

Fullsack, P., 1995, Arbitrary Lagrangian-Eulerian formulation for creeping flows and its application in tectonic models: Geophysical Journal International, v. 120, no. 1, p. 1-23.

Gao, W., Grand, S.P., Baldridge, W.S., Wilson, D., West, M., Ni, J.F., and Aster, R., (2004). Upper mantle convection beneath the central Rio Grande rift imaged by P and S wave tomography. Journal of Geophysical Research, v. 109, doi: 10.1029/2003JB002743.

Garzione, C.N., Hoke, G.D, Libarkin, J.C., Withers, S., MacFadden, B., Eiler, J., Ghosh, P., and Mulch, A., (2008). Rise of the Andes. Science, v. 320, p. 1304–1307.

Garzione, C.N., Molnar, P., Libarkin, J.C., and MacFadden, B.J., (2006). Rapid late Miocene rise of the Bolivian Altiplano: evidence for removal of mantle lithosphere. Earth and Planetary Science Letters, v. 241, p. 543–556.

Gleason, G.C., and Tullis, J., (1995). A flow law for dislocation creep of quartz aggregates determined with the molten salt cell. Tectonophysics, v. 247(1), p. 1-23, doi: 10.1016/0040-1951(95)00011-B.

Goes, S., Armitage, J. Harmon, N., Smith, H., and Huismans, R., (2012). Low seismic velocities below mid-ocean ridges: Attenuation versus melt retention. Journal of Geophysical Research, v. 117, doi:10.1029/2012JB009637.

Goes, S., Govers, R., and Vacher, P., (2000). Shallow mantle temperatures under Europe from P and S wave tomography. Journal of Geophysical Research, v. 105, p. 11,153-11,169.

Göğüş, O.H., and Pysklywec, R.N., (2008). Near-surface diagnostics of dripping or delaminating lithosphere. Journal of Geophysical Research, v. 113, doi: 10.1029/2007JB005123.

Griffin, W.L., O'Reilly, S.Y., Abe, N., Aulbach, S., Davies, R.M., Pearson, N.J., Doyle, B.J., and Kivi, K., (2003). The origin and evolution of Archean lithospheric mantle. Precambrian Research, v. 127, p. 19-41.

Griffin, W.L., O'Reilly, S.Y., Afonso, J.C., and Begg, G.C., (2009). The composition and evolution of lithospheric mantle: a re-evaluation and its tectonic implications. Journal of Petrology, v. 50, p. 1185-1204, doi:10.1093/petrology/egn033.

Gurnis, M., Mitrovica, J., Ritsema, J., and van Heijst, H.-J. , (2000). Constraining mantle density structure using geological evidence of surface uplift rates: The case of the African Superplume, Geochemistry Geophysics Geosystems, v. 1, doi:10.1029/1999GC000035.

Gutscher, M.A., Spakman, W., Bijwaard, H., and Engdahl, E.R., (2000). Geodynamics of flat subduction: Seismicity and tomographic constraints from the Andean margin. Tectonics, v. 19(5), p. 814–833, doi:10.1029/1999TC001152.

Hacker, B.R., (1996). Eclogite formation and the rheology, buoyancy, seismicity, and H2O content of oceanic crust, *in* Bebout, G.E, ed., Subduction: Top to Bottom: Washington, D.C., Geophysical Monograph Series., v. 96, p. 337– 246.

Hacker, B.R., Abers, G.A., and Peacock, S.M., (2003). Subduction factory 1. Theoretical mineralogy, densities, seismic wave speeds, and H2O contents. Journal of Geophysical Research, v. 108 (B1), doi: 10.1029/2001JB001127.

Hasenclever, J., Morgan, J.P., Hort, M., and Rupke, L.H., (2011). 2D and 3D numerical models on compositionally buoyant diapirs in the mantle wedge. Earth and Planetary Science Letters, v. 311, p. 53–68, doi:10.1016/j.epsl.2011.08.043.

Hayes, G.P., Wald, D.J., and Johnson, R.L., (2012). Slab 1.0: A three-dimensional model of global subduction zone geometries. Journal of Geophysical Research, v. 117, B01302, doi:10.1029/2011JB008524.

Heit, B., Koulakov, I., Asch, G., Yuan, X., Kind, R., Alcozer, I., Tawackoli, S. and Wilke, H., (2008), More constraints to determine the seismic structure beneath the central Andes at 21°S using teleseismic tomography analysis. Journal of South American Earth Science, v. 25, p. 22–36.

Heit, B., Sodoudi, F., Yuan, X., Bianchi, M., and Kind, R., (2007). An S-receiver function analysis of the lithospheric structure in South America. Geophysical Research Letters, v. 34, L14307, doi:10.1029/2007GL030317.

Herzberg, C., Raterron, P., and Zhang, J., (2000). New experimental observation on the anhydrous solidus for peridotite KLB-1. Geochemistry Geophysics Geosystems, v. 1, 2000GC000089.

Hildreth, W., and Moorbath, S., (1988). Crustal contributions to arc magmatism in the Andes of Central Chile. Contributions to Mineralogy and Petrology, v. 98, p. 455-489.

Hirth, G., and Kohlstedt, D.L., (1996). Water in the oceanic upper mantle: implications for rheology, melt extraction and the evolution of the lithosphere. Earth and Planetary Science Letters, v. 144(1), p. 93-108.

Hirth, G., and Kohlstedt, D.L., (2003). Rheology of the upper mantle and the mantle wedge: A view from the experimentalists. Inside the subduction Factory, p. 83-105.

Hoke, L., and Lamb, S., (2007). Cenozoic behind-arc volcanism in the Bolivian Andes, South America: implications for mantle melt generation and lithospheric structure. Journal of the Geological Society, v. 164(4), p. 795-814.

Horton, B.K., (2012). Cenozoic evolution of hinterland basins in the Andes and Tibet, *in* Busby, C.J., and Azor, A., eds., Tectonics of Sedimentary Basins: Recent Advances (1st ed.): Hoboken, New Jersey, Blackwell Publishing, p. 427–444.

Horton, B.K., Hampton, B.A., and Waanders, G.L., (2001). Paleogene synorogenic sedimentation in the Altiplano plateau and implications for initial mountain building in the central Andes. Geological Society of America Bulletin, v. 113(11), p. 1387-1400.

Houseman, G., Neil, E.A., and Kohler, M.D., (2000). Lithospheric instability beneath the Transverse Ranges of California. Journal of Geophysical Research, v. 105, p. 16,237–16,250, doi:10.1029/2000JB900118.

Houseman, G.A., McKenzie, D.P., and Molnar, P., (1981). Convective instability of a thickened boundary layer and its relevance for the thermal evolution of continental convergence belts. Journal of Geophysical Research, v. 86, p. 6115–6132, doi:10.1029/JB086iB07p06115.

Houseman, G.A., and Molnar, P., (1997). Gravitational (Rayleigh-Taylor) instability of a layer with non-linear viscosity and convective thinning of continental lithosphere. Geophysical Journal International, v. 128(1), p. 125-150, doi: 10.1111/j.1365-246X.1997.tb04075.x.

Houseman, G.A., and Molnar, P., (2003). Mechanisms of lithospheric rejuvenation associated with continental orogeny, *in* Miller, J.A., Holdsworth, R.E., Buik, I.S., and Hand, M., eds., Continental Reactivation and Reworking. Geological Society, London, Special Publications, v. 184, p. 13-38.

Huismans, R.S., and Beaumont, C., (2003). Symmetric and asymmetric lithospheric extension: relative effects of frictional-plastic and viscous strain softening. Journal of Geophysical Research, v. 108, doi:10.1029/2002JB002026.

Irifune, T., and Ringwood, A.E., (1987). Phase-Transformations in a Harzburgite Composition to 26 Gpa - Implications for Dynamical Behavior of the Subducting Slab. Earth and Planetary Science Letters, v. 86, p. 365-376.

Isacks, B.L., (1988). Uplift of the central Andean Plateau and bending of the Bolivian orocline. Journal of Geophysical Research - Solid Earth, v. 93, p. 3211–3231, doi:10.1029/JB093iB04p03211.

Isacks, B., and Molnar, P., (1969). Mantle earthquake mechanisms and the sinking of the lithosphere. Nature, v. 223, p. 1121-1124.

Jackson, J.A., Austrheim, H., McKenzie, D., and Priestly, K., 2004, Metastability, mechanical strength, and the support of mountain belts: Geology, v. 32, no. 7, p. 625– 628, doi: 10.1130/G20397.1.

Jackson, I., and Ridgen, S.M., (1998). Composition and temperature of the Earth's mantle: Seismological models interpreted through experimental studies of Earth materials, *in* Jackson, I., ed., The Earth's Mantle: Composition, Structure and Evolution: Cambridge Univ. Press, New York., p. 405 – 460.

James, D.E., and Sacks, I.S., (1999). Cenozoic formation of the central Andes: A geophysical perspective, *in* Skinner, B., ed., Geology and Ore Deposits of the Central Andes: Society of Economic Geology Special Publication, v. 7, p. 1–25.

Jarrard, R.D., (1986). Relations among subduction parameters. Reviews of Geophysics, v. 24(2), p. 217-284.

Jaupart, C., and Mareschal, J. -C., (1999). The thermal structure and thickness of continental roots. Developments in Geotectonics, v. 24, p. 93-114.

Jaupart, C., and Mareschal, J.-C., (2003). Constraints on crustal heat production from heat flow data, *in* Rudnuck, R., ed., Treatise on Geochemistry: The Crust, v. 3, p. 65-84.

Jull, M., and Kelemen, P.B., (2001). On the conditions for lower crustal convective instability. Journal of Geophysical Research, v. 106, p. 6423–6446, doi:10.1029/2000JB900357.

Kárason, H., and van der Hilst, R.D., (2000). Constraints on mantle convection from seismic tomography, *in* Richards, M.A., Gordon, R.G., van der Hilst, R.D., eds., The History and Dynamics of Global Plate motion, American Geophysical Union, v. 121 of Geophysical Monograph, p. 277-288.

Karato, S.I., (1981). Rheology of the lower mantle. Physics of the Earth and Planetary Interiors, v. 24(1), p.1-14.

Karato, S. I., (2010). Rheology of the deep upper mantle and its implications for the preservation of the continental roots: A review. Tectonophysics, v. 481(1–4), p. 82–98, doi:10.1016/j.tecto.2009.04.011.

Karato, S.I., Riedel, M.R., and Yuen, D.A., (2001). Rheological structure and deformation of subducted slabs in the mantle transition zone: implications for mantle circulation and deep earthquakes. Physics of the Earth and Planetary Interiors, v. 127, p. 83-108.

Karato, S.I., and Wu, P., (1993). Rheology of the upper mantle: a synthesis. Science, v. 260(5109), p. 771-778.

Kay, S.M., and Coira, B.L., (2009). Shallowing and steepening subduction zones, continental lithospheric loss, magmatism, and crustal flow under the Central Andean Altiplano–Puna Plateau. Geological of America Memoir, v. 204(11), p. 229-260, doi: 10.1130/2009.1204(11).

Kay, S. M., Coira, B., and Viramonte, J., (1994). Young mafic back-arc volcanic rocks as indicators of continental lithospheric delamination beneath the Argentine Puna Plateau, Central Andes. Journal of Geophysical Research, v. 99, p. 24,323–24,339, doi: 10.1029/94JB00896.

Kay, R.W., and Kay, S.M., (1993). Delamination and delamination magmatism. Tectonophysics, v. 219, p. 177-189.

Kay, S.M., Mpodozis, C., and Coira, B., (1999). Magmatism, tectonism and mineral deposits of the Central Andes (22°–33°S latitude), *in* Skinner, B.J., ed., Geology and Ore Deposits of the Central Andes: Society of Economic Geology Special Publication, v. 7, p. 27–59.

Kay, S.M., Mpodozis, C., (2001). Central Andean ore deposits linked to evolving shallow subduction systems and thickening crust. GSA Today, v. 11, p. 4-9.

Kay, S.M., and Mpodozis, C., (2002). Magmatism as a probe to the Neogene shallowing of the Nazca plate beneath the modern Chilean flat-slab. Journal of South American Earth Sciences, v. 15, p. 39–57, doi:10.1016/S0895-9811(02)00005-6.

King, S.D., (2001). Subduction zones: observations and geodynamic models. Physics of the Earth and Planetary Interiors, v. 127, p. 9-24.

Kirby, S., (1995). Interslab earthquakes and phase changes in subducting lithosphere. Reviews of Geophysics, v. 33(S1), p. 287–297, doi:10.1029/95RG00353.

Kirby, S. H., Engdahl, E.R., and Denlinger, R., (1996). Intraslab earthquakes and arc volcanism: Dual physical expressions of crustal and uppermost mantle metamorphism in subducting slabs, *in* Bebout, G.E., Scholl, D.W., Kirby, S.H., and Platt, J.P., Subduction: Top to Bottom, Geophysical Monograph Series, v. 96, p. 195 –214.

Kirby, S., Hemingway, B.S., and Lee, R., (1990). Anomalous fracture and thermal behavior of hydrous minerals. Geophysical Monograph Series, v. 56, p. 119–126.

Kley, J., (1996). Transition from basement involved to thin-skinned thrusting in the Cordillera Oriental of southern Bolivia. Tectonics, v. 15, p. 763– 775.

Krystopowicz, N. J., and Currie, C. A., (2013). Crustal eclogitization and lithosphere delamination in orogens. Earth and Planetary Science Letters, v. 361, p. 195-207.

Lamb, S., (2016). Cenozoic uplift of the Central Andes in northern Chile and Boliva – reconciling paleoaltimetry with the geological evolution. Canadian Journal of Earth Science, v. 53, p. 1227-1245.

Lamb, S., (2011). Did shortening in thick crust cause rapid Late Cenozoic uplift in the northern Bolivian Andes?. Journal of the Geological Society, v. 168(5), p. 1079– 1092, doi:10.1144/0016-76492011-008.

Lamb, S., and Hoke, L., (1997). Origin of the high plateau in the central Andes, Bolivia, South America. Tectonics, v. 16, p. 623–649, doi:10.1029/97TC00495.

Leech, M., (2001). Arrested orogenic development: eclogitization, delamination and tectonic collapse. Earth and Planetary Science Letters, v. 185, p. 149-159.

Lee, C.-T. A., Luffi, P., and Chin, E.J., (2010). Building and destroying continental mantle. Annual Review of Earth and Planetary Sciences, v. 39, p. 59-90, doi: 10.1146/annurev-earth-040610-133505.

Lee, C.-T. A., Cheng, X., and Horodyskyj, U., (2006). The development and refinement of continental arcs by primary basaltic magmatism, garnet pyroxenite accumulation, basaltic recharge and

delamination: insights from the Sierra Nevada, California. Contributions to Mineral and Petrology, v. 151, p. 222-242, doi:10.1007/s00410-005-0056-1.

Leidig, M., and Zandt, G., (2003). Highly anisotropic crust in the Altiplano-Puna volcanic complex of the central Andes, Journal of Geophysical Research, v. 108, doi: 10.1029/2001JB000649.

Leier, A., McQuarrie, N., Garzione, C., and Eiler, J., (2013). Stable isotope evidence for multiple pulses of rapid surface uplift in the central Andes, Bolivia. Earth and Planetary Science Letters, v. 371-372, p. 49-58, doi:10.1016/j.epsl.2013.04.025.

Liu, S., (2014). Flattening the slab: Farallon plate subduction and the Laramide orogeny. Master's thesis, University of Alberta.

Mackwell, S.J., Zimmerman, M.E., and Kohlstedt, D.L., (1998). High temperature deformation of dry diabase with application to tectonics on Venus. Journal of Geophysical Research, v. 103, p. 975–984, doi:10.1029/97JB02671.

Manea, V., and Gurnis, M., (2007). Subduction zone evolution and low viscosity wedges and channels. Earth and Planetary Science Letters, v. 264, p. 22-45.

Manea, V., Pérez-Gussinyé, M. and Manea, M., (2012). Chilean flat slab subduction controlled by overriding plate thickness and trench rollback. Geological Society of America, v. 40(1), p. 35-38, doiL10.1130/G32543.1.

McQuarrie, N., Horton, B.K., Zandt, G., Beck, S., and DeCelles, P.G., 2005, Lithospheric evolution of the Andean fold-thrust belt, Bolivia, and the origin of the central Andean plateau: Tectonophysics, v. 399, p. 15–37, doi:10.1016/j.tecto.2004.12.013.

McKenzie, D., Daly, M.C., and Priestley, K., (2015). The lithospheric structure of Pangea. Geology, v. 43(9), p. 783-786, doi:10.1130/G36819.1.

Meissner, R.O., and Mooney, W.D., (1998). Weakness of the lower continental crust; a condition for delamination, uplift, and escape. Tectonophysics, v. 296, p. 47–60.

Minster, J.B., and Anderson, D.L., (1981). A model of dislocation-controlled rheology for the mantle. *Philosophical transactions* of the Royal *Society* of *London, v. 299, p. 319-356.*

Molnar, P., Freedman, D., and Shih, J.S.F., (1979). Lengths of intermediate and deep seismic zones and temperatures in downgoing slabs of lithosphere. Geophysical Journal of the Royal Astronomical Society, v. 56, p. 41–54.

Molnar, P., and Houseman, G.A., (2004). The effects of buoyant crust on the gravitational instability of thickened mantle lithosphere at zones of intracontinental convergence. Geophysical Journal International, v. 158(3), p. 1134-1150, doi: 10.1111/j.1365-246X.2004.02312.x.

Molnar, P., Houseman, G.A., and Conrad, C.P., (1998). Rayleigh-Taylor instability and convective thinning of mechanically thickened lithosphere: effects of non-linear viscosity decreasing exponentially with depth and of horizontal shortening of the layer: Geophysical Journal International. v. 133(3), p. 568-584.

Mora, A., Parra, M., Strecker, M.R., Kammer, A., Dimaté,C., and Rodriquez, F., (2006). Cenozoic contractional reactivation of Mesozoic extensional strcutures in the Eastern Cordillera of Colombia. Tectonics, v. 25, doi:10.1029/2005TC001854.

Morency, C., and Doin, M.-P., (2004). Numerical simulations of the mantle lithosphere delamination. Journal of Geophysical Research, v. 109, B03410, doi:10.1029/2003JB002414.

Mpodozis, C., and Allmendinger, R.W., (1993). Extensional tectonics, Cretaceous Andes, northern Chile (27°S). Bulletin of the Geological Society of America, v. 105, p. 1462–1477.

Mpodozis, C., and Ramos, V., A., (1989). The Andes of Chile and Argentina, *in* Ericksen, G.E., Cañas Pinochet, M.T., and Reinemund, J.A., eds., Geology of the Andes and its Relation to Hydrocarbon and Mineral Resources: Circum–Pacifi c Council for Energy and Mineral Resources Earth Science Series, v. 11, p. 59–90.

Müller, R.D., Sdrolias, M., Gaina, C., and Roest, W.R., (2008). Age, spreading rates, and spreading asymmetry of the world's ocean crust. Geochemistry Geophysics Geosystems, v. 9(4), doi:10.1029/2007GC001743.

Myers, S., Beck, S., Zandt, G., and Wallace, T., (1998) Lithospheric-scale structure across the Bolivian Andes from tomographic images of velocity and attenuation for P and S waves. Journal of Geophysical Research, v. 103, p. 21,233–21,252.

Neil, E. A., and Houseman, G.A., (1999). Rayleigh-Taylor instability of the upper mantle and its role in intraplate orogeny. Geophysical Journal International, v. 138, p. 89–107.

Oncken, O., Hindle, D., Kley, J., Elger, K., Victor, P., and Schemmann, K., (2006). Deformation of the Central Andean upper plate system—Facts, fiction and constraints for plateau models, *in* Oncken, O., Chong, G., Franz, G., Giese, P., Gotze, H.J., Ramos, V.A., Strecker, M.R., and Wigger, P., eds., The Andes: Active Subduction Orogeny: Berlin, Springer-Verlag, Frontiers in Earth Sciences, v. 1, p. 3–27.

Peacock, S.M., (1993). The importance of blueschist-eclogite dehydration reactions in subducting oceanic crust. Geological Society of America Bulletin, v.105, p. 684-694.

Piñán-Llamas, A., and Simpson, C., (2006). Deformation of Gondwana margin turbidites during the Pampean orogeny, north-central Argentina. Geological Society of America Bulletin, v. 118(9/10), p. 1270–1279.

Pollack, H., and Chapman, D., (1997). Mantle heat flow. Earth and Planetary Science Letters, v. 34, p. 174-184.

Pope, D.C., and Willett, S.D., (1998). Thermal-mechanical model for crustal thickening in the central Andes driven by ablative subduction. Geology, v. 26(6), p. 511-514.

Pysklywec, R.N., and Beaumont, C., (2004). Intraplate tectonics: Feedback between radioactive thermal weakening and crustal deformation driven by mantle lithosphere instabilities. Earth and Planetary Science Letters, v. 221, p. 275–292, doi:10.1016/S0012-821X(04)00098-6.

Pysklywec, R.N., Beaumont, C., and Fullsack, P., (2002). Lithospheric deformation during the early stages of continental collision: Numerical experiments and comparison with South Island, New Zealand. Journal of Geophysical Research, v. 107, doi:10.1029/2001JB000252.

Ramos, V.A., (1988). Tectonics of the Late Proterozoic – Early Paleozoic: a collisional history of Southern South America. Episodes, v. 11(3), p. 168-174.

Ramos, V.A., (2009). Anatomy and global context of the Andes: Main geologic features and the Andean orogenic cycle, *in* Kay, S.M., Ramos, V.A., and Dickinson, W.R., eds., Backbone of the Americas: Shallow Subduction, Plateau Uplift, and Ridge and Terrane Collision: Geological Society of America Memoir, 204, p. 31–65, doi:10.1130/2009.1204(02).

Ramos, V.A., and Folguera, A., (2009). Andean flat-slab subduction through time, *in* Murphy, J.B., Keppie, J.D., and Hynes, A.J., eds., Ancient Orogens and Modern Analogues: Geological Society of America Special Publications 327, doi:10.1144/SP327.3.

Ranalli, G., (1987). Rheology of the Earth, Deformation and flow processes in geophysics and geodynamics, Allen & Unwin, Boston, 386 pp.

Ray, J.S., Mahoney, J.J., Duncan, R.A., Ray, J., Wessel, P., and Naar, D.F., (2012). Chronology and geochemistry of lavas from the Nazca Ridge and Easter Seamount Chain: a ~30 myr hotspot record. Journal of Petrology, v. 53, p. 1417-1448, doi:10.1093/petrology/egs021.

Riedel, M.R., and Karato, S.I., (1997). Grain-size evolution in subducted oceanic lithosphere associated with the olivine-spinel transformation and its effects on rheology. Earth and Planetary Science Letters, v. 148, p. 27-43.

Rubie, D.C., and Ross, C.R., (1994). Kinetics of the olivine-spinel transformation in subducting lithosphere: experimental constraints and implications for deep slab processes. Physics of the Earth and Planetary Interiors, v. 86, p. 223-241.

Ryan, J., Beck, S., Zandt, G., Wagner, L., Minaya, E., and Tavera, H., (2016). Central Andean crustal structure from receiver function analysis. Tectonophysics, v. 682, p. 120-133.

Saleeby, J.B., Ducea, M.N., Clemens-Knott D., (2003). Production and loss of high-density batholithic root, southern Sierra Nevada California. Tectonics, v. 22, doi:10.1029/2002TC001374.

Saleeby, J., Le Pourhiet, L., Saleeby, Z., and Gurnis M., (2012). Epeirogenic transients related to mantle lithosphere removal in the southern Sierra Nevada region, California, part I: Implications of thermomechanical modeling. Geosphere, v. 8(6), p. 1286-1309.

Salisbury, M.J., Jicha, B.R., de Silva, S.L., Singer, B.S., Jimenez, N.C., and Ort, M.H., (2011). Ar-40/Ar-39 chronostratigraphy of Altiplano-Puna volcanic complex ignimbrites reveals the development of a major magmatic province. Geological Society of America Bulletin, v. 123, p. 821–840, doi:10.1130/B30280.1.

Salisbury, M.J., Kent, A.J.R., Jiménez, N., and Jicha, B.R., (2014). Geochemistry and Ar40/Ar39 geochronology of lavas from Tunupa volcano, Bolivia: Implications for plateau volcanism in the central Andean Plateau. Lithosphere, v. 7(2), p. 95-107, doi:10.1130éL399.1.

Schmidt M.W., Poli S. (1998). Experimentally based water budgets for dehydrating slabs and consequences for arc magma generation. Earth and Planetary Science Letters, v. 163, p. 361–379.

Schott, B., and Schmeling, H., (1988). Delamination and detachment of a lithospheric root. Tectonophysics, v. 296, p. 225-247.

Schurr, B., Rietbrock, A., Asch, G., Kind, R., and Oncken, O., (2006). Evidence for lithospheric detachment in the central Andes from local earthquake tomography: Tectonophysics, v. 415(1), p. 203-223, doi: 10.1016/j.tecto.2005.12.007.

Scire, A., Biryol, C.B., Zandt, G., and Beck, S., (2015). Imaging the Nazca slab and surrounding mantle to 700 km depth beneath the central Andes (18°S to 28°S), *in* DeCelles, P.G., Ducea, M.N., Carrapa, B., and Kapp, P.A., eds., Geodynamics of a Cordilleran Orogenic System: The Central Andes of

Argentina and Northern Chile: Geological Society of America Memoir 212, doi:10.1130/2015.1212(02).

Sempere, T., (1995). Phanerozoic evolution of Bolivia and adjacent regions, *in* Tankard, A. J., Suárez R.S., and Welsink, H.J., eds., Petroleum basins of South America: AAPG Memoir v. 62, p. 207–230.

Sibson, R.H., (1990). Conditions for fault-valve behaviour, *in* Knipe, R.J. and Rutter, E.H., eds., Deformation Mechanisms, Rheology and Tectonics. Special Publication Geological Society of London, v. 54 p. 15-28.

Silver, P.G., Russo, R.M., and Lithgow-Bertelloni, C., (1998). Coupling of South American and African plate motion and plate deformation. Science, v. 279, p. 60–63.

Sisson, T.W., and Bronto, S., (1998). Evidence for pressure-release melting beneath magmatic arcs from basalt at Galunggung, Indonesia. Nature, v. 391, p. 883–886.

Sobolev, S.V., Babeyko, A.Y., Koulakov, I., Oncken, O., and Vietor, T., 2006, Mechanism of the Andean orogeny: Insight from the numerical modeling, *in* Oncken, O., Chong, G., Franz, G., Giese, P., Goetze, H.-J., Ramos, V., Strecker, M., and Wigger, P., eds., The Andes: Active Subduction Orogeny: Berlin, Springer-Verlag, Frontiers in Earth Sciences, p. 509–531.

Sobolev, S.V., Zeyen, H., Stoll, G., Werling, F., Altherr, R., and Fuchs, K., (1996). Upper mantle temperatures from teleseismic tomography of French Massif Central including effects of composition, mineral reactions, anharmonicity, anelasticity and partial melt. Earth and Planetary Science Letters, v. 139, p. 147-163.

Sodoudi, F., Yuan, X., Asch, G., and Kind, R., (2011). High-resolution image of the geometry and thickness of the subducting Nazca lithosphere beneath northern Chile. Journal of Geophysical Research, v. 116, doi:10.1029/2010JB007829.

Somoza, R., (1998). Updated Nazca (Farallon)–South America relative motions during the last 40 My: implications for mountain building in the central Andean region. Journal of South American Earth Sciences, v. 11, p. 211–15.

Spence, W. (1987). Slab pull and the seismotectonics of subducting lithosphere, Rev. Geophys., 25, 55 – 69.

Springer, M., 1999. Interpretation of heat-flow density in the central Andes. Tectonophysics, v. 306(3), p. 377-395.

Springer, M., and Förster, A., (1998). Heat-flow density across the central Andean subduction zone, Tectonophysics, v. 291, p. 123-139.

Steinberger, B., (2007). Effects of latent heat release at phase boundaries on flow in the Earth's mantle, phase boundary topography and dynamic topography at the Earth's surface. Physics of the Earth and Planetary Interiors, v. 164, p. 2-20.

Stern, R.J., (2002), Subduction zones, *Rev*. *Geophys*., *40*(4), 1012, doi: 10.1029/2001RG000108.

Stixrude, L., and Lithgow-Bertelloni, C., (2011). Thermodynamics of mantle minerals – II. Phase equilibria. Geophysical Journal International., v. 184, p. 1180-1213.

Stolper, E. and Newman, S., (1994). The role of water in the petrogenesis of Mariana Trough magmas. Earth and Planetary Science Letters, v. 121, p. 293-325.

Sun, S.S., (1982). Chemical composition and origin of the Earths primitive mantle. Geochimica Et Cosmochimica Acta, v. 46, p. 179-192.

Tao, W.C., and O'Connell, R.J., (1992). Ablative subduction: A two-sided alternative to the conventional subduction model. Journal of Geophysical Research, v. 97, p. 8877–8904, doi:10.1029/91JB02422.

Tassara, A., (2006). Factors controlling the crustal density structure underneath active continental margins with implications for their evolution. Geochemistry Geophysics Geosystems, v. 7, Q01001, doi:10.1029/2005GC001040.

Tassara, A., and Echaurren, A., (2012). Anatomy of the Andean subduction zone: Three-dimensional density model upgraded and compared against globalscale models. Geophysical Journal International, v. 189, p. 161–168, doi:10.1111/j.1365-246X.2012.05397.x.

Trumbull, R.B., Riller, U., Oncken, O., Schueber, E., Munier, K., and Hongn, F., (2006). The time-space distribution of Cenozoic arc volcanism in the Central Andes: A new data compilation and some tectonic considerations, *in* Oncken, O., Chong, G., Franz, G., Giese, P., Goetze, H.-J., Ramos, V., Strecker, M., and Wigger, P., eds., The Andes: Active Subduction Orogeny: Berlin, Springer-Verlag, Frontiers in Earth Sciences, v. 1, p. 29-44.

Turcotte, D. L., and Schubert, G., (2002). Geodynamics (second edition): Cambridge, UK, Cambridge University Press, 456 p.

Uyeda, S. and Kanamori, H. (1979). Back-arc opening and the model of subduction. Journal of Geophysical Reseach, v. 84, p. 1049–1061.

Van der Pluijm, B. and Marshak, S., (2004). Earth Structure (second edition): New York, W. W. Norton & Company, 656 p.

van Hunen, J., van der Berg, A.P., and Vlaar, N.J., (2002). The impact of the South-American plate motion and the Nazca Ridge subduction on the flat subduction below Peru. Geophysical Research Letters, v. 29, doi:10.1029/2001GL014004.

van Hunen, J., van der Berg, A.P., and Vlaar, N.J., (2004). Various mechanisms to induce present-day shallow flat subduction and implications for the younger Earth: a numerical parameter study. Physics of the Earth and Planetary Interiors, v. 146, p. 179-194.

van Keken, P.E., (2003). The structure and dynamics of the mantle wedge. Earth and Planetary Science Letters, v. 215, p. 323-338.

Van Wijk, J., Van Hunen, J., and Goes, S., (2008). Small-scale convection during continental rifting: Evidence from the Rio Grande rift. Geology, v. 36(7), p. 575-578.

Van Wijk, J. W., Baldridge, W. S., Van Hunen, J., Goes, S., Aster, R., Coblentz, D. D., Grand, S. P., and Ni, J., (2010). Small-scale convection at the edge of the Colorado Plateau: Implications for topography, magmatism, and evolution of Proterozoic lithosphere. Geology, v. 38(7), p. 611-614.

Valera, J.L., Negredo, A.M., and Jimenez-Munt, L., (2011). Deep and near-surface consequences of root removal by asymmetric continental delamination. Tectonophysics, v. 502, p. 257–265.

Wang, H., and Currie, C.A., (2015). Magmatic expressions of continental lithosphere removal. Journal of Geophysical Research: Solid Earth, v. 120, p. 7239-7260, doi: 10.1002/2015JB012112.

Wang, H., Currie, C. A., and DeCelles, P. G., (2015). Hinterland basin formation and gravitational instabilities in the central Andes: Constraints from gravity data and geodynamic models. Geological Society of America Memoirs, v. 212, p. 387-406.

Ward, K., Porter, R., Zandt, G., Beck, S., Wagner, L., Minaya, E., and Tavera, H., (2013). Ambient noise tomography across the central Andes. Geophysical Journal International, doi:10.1093/gji/ggt166.

Warren, C.J., Beaumont, C., and Jamieson, R.A., (2008). Formation and exhumation of ultra-high-pressure rocks during continental collision: Role of detachment in the subduction channel, Geochemistry Geophysics Geosystems, v. *9*, Q04019, doi: 10.1029/2007GC001839.

White, R.S., McKenzie, D., and O'Nions, R., (1992). Oceanic crustal thickness from seismic measurements and rare earth element inversions. Journal of Geophysical Research, v. 97, p. 19,683– 19,715.

Whitman, D., Isacks, B.L., and Kay S.M., (1996). Lithospheric structure and along-strike segmentation of the Central Andean Plateau: seismic Q, magmatism, flexure, topography and tectonics. Tectonophysics, v. 259, p. 29-40.

Willett, S.D. (1999). Orogeny and orography: the effects of erosion on the structure of mountain belts. Journal of Geophysical Research, v. 104, p. 28,957– 28,982.

Wörner, G., Hammerschmidt, K., Henjes-Kunst, F., Lezaun, J., and Wilke, H., (2000). Geochronology (40Ar/39Ar, K-Ar and He-exposure ages) of Cenozoic magmatic rocks from northern Chile (18–22°S): Implications for magmatism and tectonic evolution of the central Andes. Revista Geológica de Chile, v. 27, p. 205–240.

Yañez, G., Ranero, C.R., Von Huene, R., Díaz, J., (2001). Magnetic anomaly interpretation across the southern central Andes (32°-34°S). The role of the Juan Fernandez Ridge in the late Tertiary evolution of the margin. Journal of Geophysical Research, v. 106, p. 6325–6345.

Yoon, M., Buske, S., Shapiro, S.A., and Wigger, P., (2009). Reflection image spectroscopy across the Andean subduction zone. Tectonophysics, v. 472, p. 51-61, doi: 10.1016/j.tecto.2008.03.014.

Yuan, X., Sobolev, S.V., Kind, R., Oncken, O., Bock, G., Asch, G., Schurr, B., Graeber, F., Rudloff, A., Hanka, W., Wylegalla, K., Tibi, R., Haberland, Ch., Rietbrock, A., Giese, P., Wigger, P., Rower, P., Zandt, G., Beck, S., Wallace, T., Pardo, M., and Comete, D., (2000). Subduction and collision processes in the central Andes constrained by converted seismic phases. Nature, v. 408, p. 958 – 961.

Yuan, X., Sobolev, S.V., and Kind, R., (2002). Moho topography in the central Andes and its geodynamic implications: Earth and Planetary Science Letters, v. 199(3), p. 389-402, doi: 10.1016/S0012-821X(02)00589-7.